Transport and self-assembly of droplets in microfluidic devices

Bing-Qing Shen

UNIVERSITÉ PIERRE ET MARIE CURIE (Paris 6)

Thèse de doctorat

Spécialité:
Sciences mécaniques, acoustique, électronique & robotique de Paris
(ED 391)

présentée par

Bingqing SHEN

Transport and self-assembly of droplets in microfluidic devices
Transport et auto-assemblage de gouttes dans des systèmes microfluidiques

---

soutenance prévue le 25 septembre 2014 devant le jury composé de :

M. Yves Fouillet	rapporteur
M^{me} Véronique Schmitt	rapportrice
M^{me} Martine Ben Amar	examinatrice
M. Jean-Christophe Baret	examinateur
M. Florent Malloggi	invité
M. Patrick Tabeling	directeur de thèse
M^{me} Mathilde Reyssat	co-directrice de thèse

Institut de Mathématiques de Jussieu
175, rue du chevaleret
75 013 Paris

École doctorale Paris centre Case 188
4 place Jussieu
75 252 Paris cedex 05

Résumé

Transport et auto-assemblage de gouttes dans des systèmes microfluidiques

Résumé

Les propriétés d'un matériau sont fortement liées à l'organisation de la matière qui le constitue. Notre approche consiste à développer une nouvelle méthode de synthèse de briques élémentaires de la matière constituées d'assemblage de colloïdes à haut débit en utilisant la technologie microfluidique et à en comprendre la physique associée. Après une exploration des différentes techniques disponibles permettant la création d'assemblage de gouttes, nous avons choisi de concentrer notre étude sur un mécanisme d'assemblage piloté par les interactions dipolaires entre gouttes. Nous démontrons la possibilité de former les assemblages de gouttes (ayant des interactions adhésives entre elles) grâce à l'utilisation conjointe d'une jonction en T et d'un dispositif d'émulsification à marche (step emulsification). Nous observons une grande variété de configurations stationnaires ou oscillantes. Nous explorons l'influence des paramètres physicochimiques et hydrodynamiques sur le mécanisme d'assemblage. Enfin, nous montrons la possibilité de jouer sur la taille des gouttes et leur composition chimique pour obtenir des assemblages complexes anisotropes par cette technique. Ces briques élémentaires ouvrent une nouvelle voie pour la synthèse de matériaux microtexturés à l'échelle colloïdale.

Mots-clés

assemblage colloïdal, molécule colloïdale, microfluidique, intéraction dipolaire, auto-assemblage.

Transport and self-assembly of droplets in microfluidic devices

Abstract

The material's behaviors are strongly related to the spatial arrangement of their fundamental building blocks. In this Ph.D. work, we aim at developing a novel approach for high-throughput colloidal clusters synthesis and understanding the related physics. After having explored various different techniques to elaborate the cluster entities, we have chosen to focus our study on a hydrodynamic-assisted assembly mechanism based on dipolar interaction. Through the use of dedicated two-layer microfluidic devices and by decoupling T-junction production and step emulsification, we demonstrate the direct assembling of droplets into clusters (of the adhesive emulsions). A rich variety of configurations, either stationary or oscillatory are observed. We have investigated the effect of the hydrodynamics as well as the physicochemical conditions on the clustering process. Moreover, more complex clusters such as anisotropic ones have been successfully generated by integrating some additional functionalities to our microfluidic chips. These features are potentially interesting to access new microstructured colloidal materials.

Keywords

cluster, colloidal molecule, microfluidics, dipolar interaction, self-assembly.

Contents

Chapter 1

Introduction

1.1 Colloidal assembly

1.1.1 General introduction

The material's behaviors are strongly related to the spatial arrangement of their fundamental building blocks. From the aspect of scale, these building blocks comprise atoms, molecules, macromolecules and colloidal particles.

Take carbon atoms for example, both diamond and graphite are made entirely out of carbon. However, the way carbon atoms arranged in space is completely different for these two materials. In a diamond, the carbon atoms are arranged tetrahedrally. Each carbon atom is attached to four other carbon atoms, 15.44 nanometer away with a C-C-C bond angle of 109.5°. It is a strong, rigid three-dimensional structure that results in an infinite network of atoms. Because of its tetrahedral structure, diamond also shows a great resistance to compression. The carbon atoms in graphite are also arranged in an infinite array, but they are layered. These atoms have two types of interactions with one another. In the first, each carbon atom is bonded to three other carbon atoms and arranged at the corners of a network of regular hexagons with a 120° C-C-C bond angle. These planar arrangements extend in two dimensions to form a horizontal, hexagonal array. In addition, these planar arrays are held together by weaker forces known as stacking interactions. Unlike diamond, graphite can be used as a lubricant or in pencils because the layers cleave readily. The differing properties of carbon and diamond arise from their distinct crystal structures.

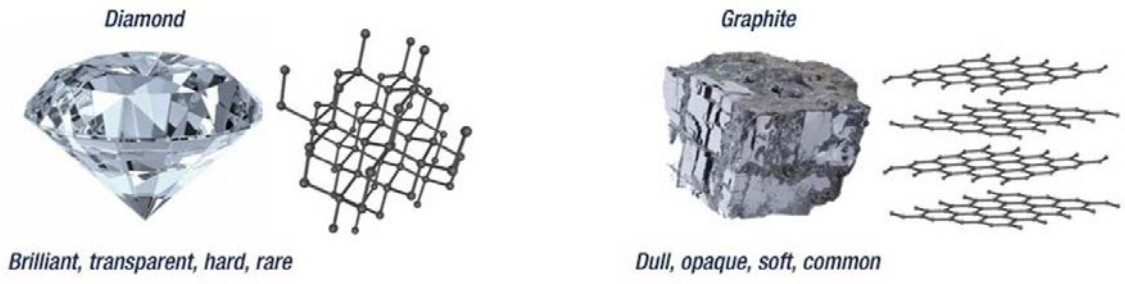

Figure 1.1: In diamond, the carbon atoms are arranged tetrahedrally and every carbon atom is connected to four other carbon atoms. In contrast, the carbon atoms in graphite are bound together mostly crosswise in sheets that lie on top of one another.

Colloidal spheres can be viewed as the mesoscopic counterparts of atoms. They are

also capable of ordering into various arrangements. The assembly of colloidal spheres could construct 'supracolloidal structures' over multiple length scales. The most studied representative of assemblies is colloidal crystals. The organization in crystal-like structure could bring about collective material properties such as optical refraction, photonic bandgaps and high surface-to-volume ratios [1]. The periodic replication of refractive index, density and porosity, applications of colloidal crystals include photonic[2] [3] [4] and phononic material[5] [6] as well as macro porous material [7] [8].

Monodisperse nanometer and micrometer sized spheres in a suspension can spontaneously form close-packed colloidal crystal arrays if the free volume is restricted below a certain level [9]. Figure 1.2 shows an example of such regularly-spaced lattice of colloidal crystal. The particles used in this study are made from silica spheres with the sizes ranging from 390 nm to 1 μm. Using a method called isothermal heating evaporation induced self-assembly (IHEISA), highly ordered silica colloidal crystal films are deposited on a planar substrate without any limitations imposed by the size of silica spheres. Figure 1.2 (a) -(d) shows cross-sectional scanning electron microscopy (SEM) images of the colloidal crystal films formed by 635 nm, 850 nm, and 1 μm silica spheres. Silica colloidal crystal films show a high degree of order. Figure 1.2 (e), (f) presents color photographs of several silica colloidal crystal films deposited on a half-cut glass slide [10]. The colors arise from light diffraction (opalescence) from the colloidal arrays, due to this long-range ordering of the particles.

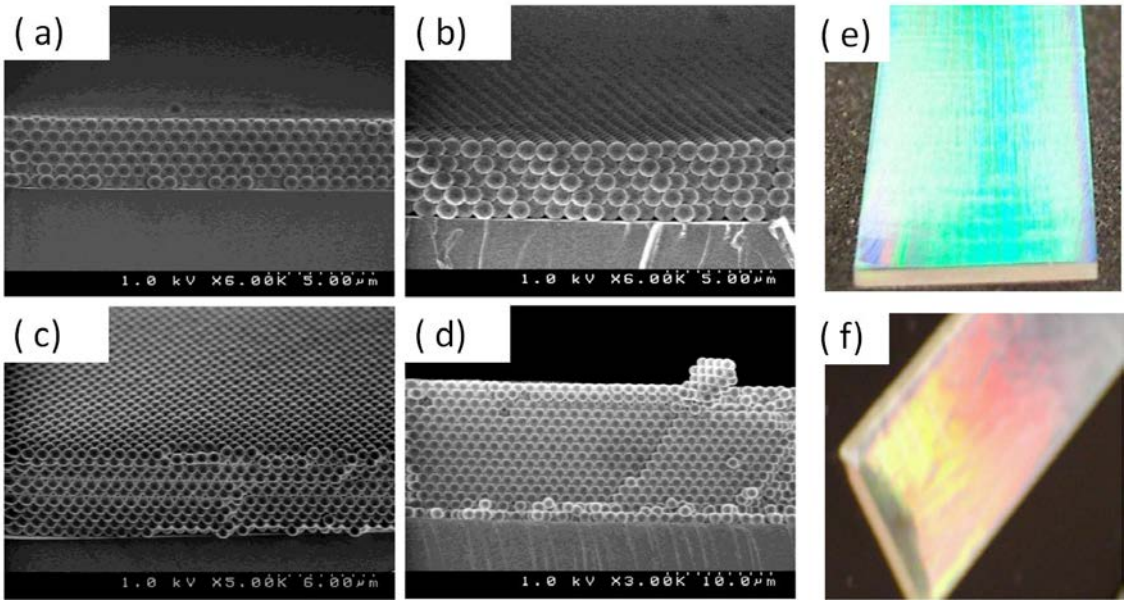

Figure 1.2: Representative SEM images of the cross sections of the silica colloidal crystal films produced by IHEISA using (a) and (c) 635 nm, (b) 850 nm, and (d) 1 μm spheres. (e) Photographs of the colloidal crystal films made out of 650 nm silica spheres deposited by IDEISA onto a glass slide support. (f) The films made out of 850 nm silica spheres. Images adapted from ref [10].

Other than silica spheres, various colloidal spheres are also demonstrated to be able to assemble into crystal structures, such as latex spheres [1][11], silicon nanocrystal (Si-NCs) [12] [13], inorganic oxides [14] and metal nanoparticles [13]. In addition, Malloggi et al.

1. Most common latex polymers are polystyrene (PS) and acrylates, e.g. poly(methyl methacrylate) (PMMA).

have investigated the assembly of droplets of colloidal size, they demonstrated that with a low volumetric fraction around 0.5, a liquid state (figure 1.3(a)) is observed, while with a higher volumetric fraction 0.74, a hexagonal crystal structure is obtained. The diffraction pattern in figure 1.3(b) corresponds to the close packing of monodisperse spheres, which is in agreement with the literature on colloids.

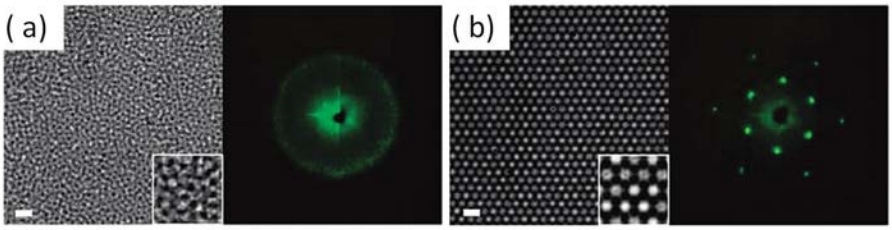

Figure 1.3: Assemblies obtained in the nanofluidic device using fluorinated oil/water + SDS 1 wt %: (a) liquid state; (b) ordered phase. To the right of each image, the corresponding diffraction pattern is shown which generated by illuminating droplet assemblies stored in the reservoir under normal incidence and with coherent light beams (a green laser with λ=532 nm). Scale bar, 5 μm. The close-up views of the various patterns are also presented in the inset. Figure adapted from [15].

Beside colloidal crystals, other typical supracolloial assemblies include 'supraballs' and colloidosome. Figure 1.4 shows an illustration of those assemblies.

Figure 1.4: Illustration of colloidal assemblies: colloidal crystals., 'supraballs' and colloidosome. Figure adapted from [1].

The 'supraballs' is used to describe compact aggregates made up from a larger number of spherical particles and a well ordered layer of particles at their surface which gives them photonic properties [16] [17][18] [19]. Figure 1.5 shows one of the examples of the 'superballs'. Negatively charged polystyrene latex microspheres with 270 nm to 630 nm in diameter were dispersed in aqueous droplets inside which the colloidal particles were gradually concentrated by drying to form 3D crystals, yielding a variety of microstructured symmetric supraparticles. Visualized by scanning electron microscopy, large domains of hexagonally packed particles can be seen on the surface and each domain incorporates hundreds to thousands of microspheres in the first visible layer (figure1.5 (a), (b)). Optical microscopy shows brightly colored reflecting patches on the surface of these balls (figure1.5 (c), (d)). The colors depend on the size of the latex particles: green and red for assemblies made of 270 nm microspheres, blue for 320 nm microspheres, and yellow-green for 630 nm microspheres [17].

The colloidosomes are another class of finite size particles assemblies with hollow capsules whose walls consist of colloidal building blocks resulting from close packings of particles on a spherical template [20]. The colloidosomes can find applications as semipermeable

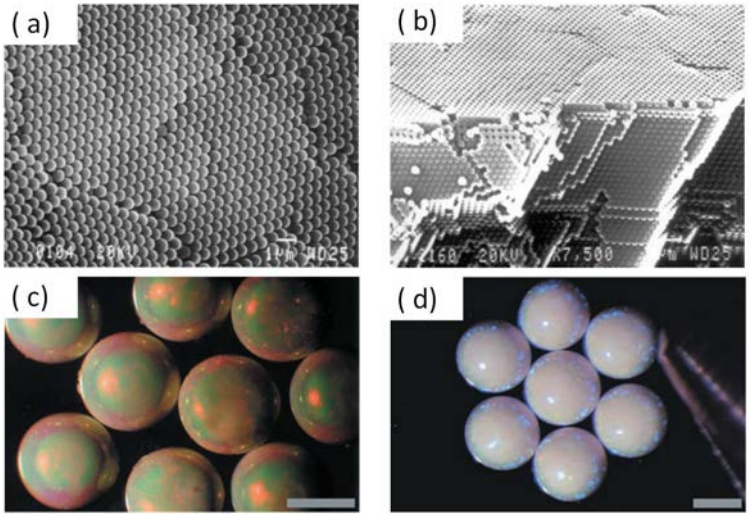

Figure 1.5: (a) A scanning electron micrograph of a typical area on the surface of the assemblies. (b) A scanning electron micrograph along the edge of a broken particle. The surface is seen at the top and the cut through the bulk is toward the bottom of the micrograph. Scale bars, 1 μm. (c) Optical micrographs of structured spherical assemblies obtained from 270 nm and (d) 320 nm latex particles. Scale bars, 500 mm. Figure adapted from [17]

capsules for drug delivery and biotechnology as well as in pharmaceutical, cosmetic, and food products with advanced structure [21]. Figure 1.6 shows examples of such supracolloial assemblies.

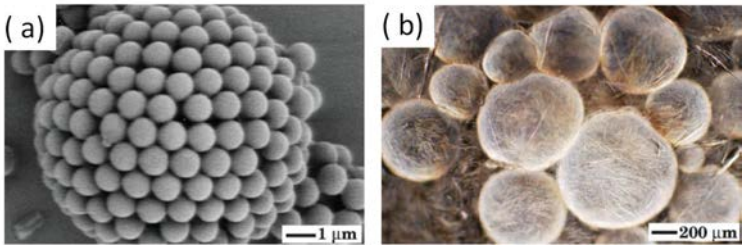

Figure 1.6: Examples of colloidosome supraparticles. (a) Semipermeable 10μm-diameter colloidosome composed of 0.9μm diameter polystyrene spheres. Image adapted from [20]. (b) Microrod-stabilized 'hairy' colloidosomes. Image adapted from [22].

The major limit of the colloidal assemblies is that dense suspensions of identical hard spheres are known to form only a few relatively simple crystals such as face-centered cubic (fcc), hexagonal close-packed (hcp), random hexagonal close-packed (rhcp) or body-centered cubic (bcc) arrays because the equilibrium and non-equilibrium behavior of colloidal suspensions is controlled primarily by the hard repulsive interaction between the spheres. Although the diversity of crystalline packing structures can be extended when spheres of different size are assembled into dense binary colloidal crystals [23] [24] [25] [26], the kinds of lattices that can be made is somewhat limited and many structures remain difficult or impossible to make. For example, the diamond structure that we described before, was predicted to have a full three-dimensional photonic bandgap more than 20 years ago [27] [28] [29]. It still cannot be made by colloidal self-assembly because it requires

fourfold coordination and such low-coordination state are thermodynamically unstable. The preparation of diamond colloidal architectures was achieved by nanorobtic manipulation [30] (see figure1.7). Particle-by-particle construction is highly time-consuming and thus limited in terms of the number of particles that can be assembled per hour.

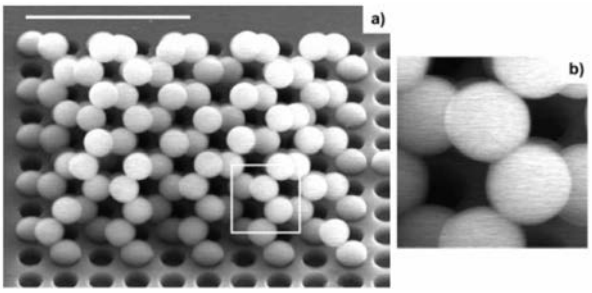

Figure 1.7: Five-layer diamond lattice directly grown in the {001} orientation. (a) Structure made of 165 silica spheres of 0.9 μm of diameter. (b) Detail of a contact point between two silica beads. Pictures are tilted 45° to show {011} facets. Scale bar, 5 μm. Figure adapted from [30].

One most straightforward strategy to elaborate more complex crystal structures is to break down the desired structure into subunits with tailored symmetries and valences that enable their directed self-assembly into the final target structure. It is proposed building them by packing the clusters, i.e. the finite packings, instead of building materials by packing individual spheres together [31].

1.1.2 Clusters: colloidal molecules

Clusters of spheres have received significant interest. The colloidal cluster is an aggregate of a small number of constituent particles with well defined sizes, shapes and symmetries. Many experimental studies have been carried out with spherical colloids as the model system to enrich our understanding on various physical phenomena that range from phase transition to particles-particle interaction [32] [33] [34] [35]. For example, small clusters of colloidal microspheres have been proposed as model systems for nanocrystals which are essentially aggregates of a few particles.

As we discussed before, if spherical colloids can be treated as if they were atoms, then clusters of a small number of the same or different constituent particles can be regarded as colloidal analogues to small molecules [36] [37]. That is why Van Blaadereen introduced this elegant term of 'colloidal molecule' for describing clusters of spheres with shapes resembling space-filling models of simple molecules[38] [39]. They open unprecedented fascinating perspectives because of their unique rheological, optical, magnetic, or electric properties, which result from the assembly of functional subunits into aggregates with tailored shapes and symmetries [40] [41].

An illustration of examples of clusters and their possible assemblies are shown in figure1.8. Clusters, the finite packings of spheres, present intermediates between the single particle level and the macroscopic domain, to which colloidal crystals can be assigned. From a fundamental point of view, clusters of spheres are interesting because the basic principles behind their formation can provide new insights into the assembly, structure, and dynamics of hierarchically organized materials [42] [43] [44].

In order to facilitate the discussion, we propose several classifications of the 'colloidal molecules' and then give a general review on the typical synthetics routes to elaborate

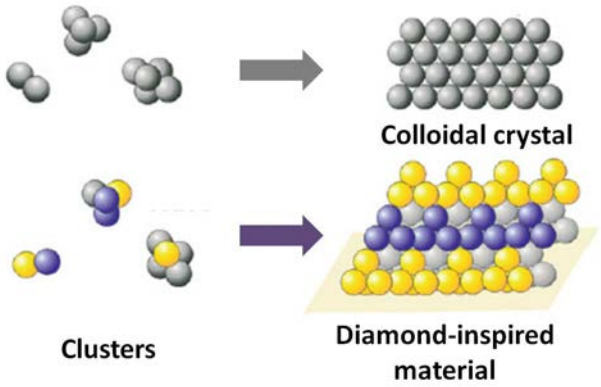

Figure 1.8: Illustration of clusters made of the same or different constituent spheres and their possible crystal assemblies. A more complex network can be realized when the clusters are heterogeneous. Figure adapted from [1].

those finite assemblies in the next part.

1.1.3 Clusters classification

Theoretical description of the new particles seems daunting in the face of their complexity [45]. Thanks to the analogy of clusters of spheres and the molecules, we could classify those clusters by VSEPR model according to the similarities between the two species. On the other hand, the anisotropy 'dimension' could also be used as a criterion for describing those building blocks.

VSEPR model

Duguet and co-worker have proposed a classification of the 'colloidal molecules' in their review, using and extending the well-known formalism of Gillespie derived from the valence shell electron pair repulsion (VSEPR) model [38]. VSEPR theory is a simple model used, in chemistry, to predict the geometry of covalently bonded compounds from the number of electron pairs surrounding their central atoms.

The 'AXE' method of electron counting is commonly used when applying the VSEPR theory where the A represents the central atom and always has an implied subscript one. The X represents the number of ligands (atoms bonded to A). The E represents the number of lone electron pairs surrounding the central atom. Figure 1.9 shows some examples of the shapes and symmetries of large, complex molecules.

Anisotropy 'dimensions'

Describing the various anisotropies of a building block based on their key parameters in terms of anisotropy 'dimensions' is another simple, potentially interesting and useful way to classify clusters. The practically infinite number of shapes and types can thus be reduced to description by a vector comprising just a few critical dimensions, each of variable amplitude [45]. The complexity of a cluster is determined by its dimensionality in anisotropy space: the higher the dimensionality is, the more complex the corresponding clusters are.

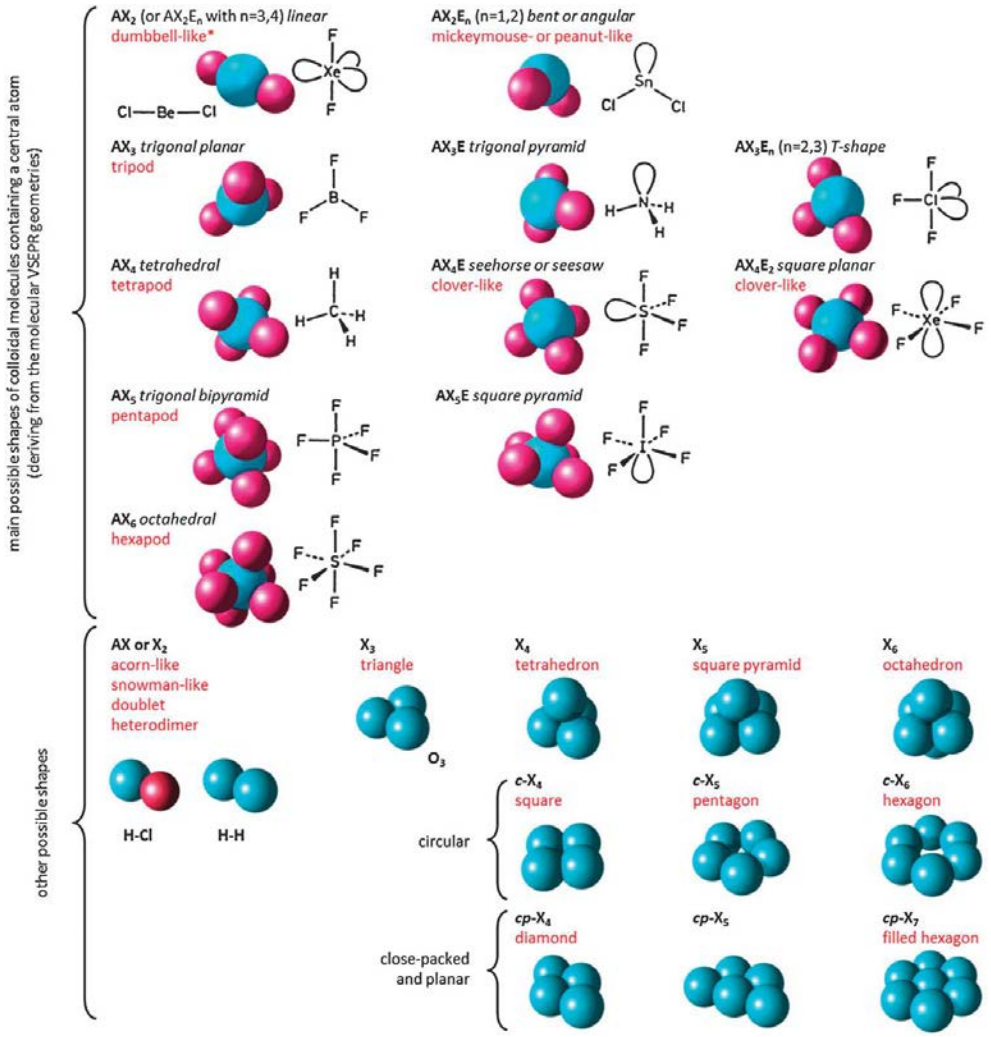

Figure 1.9: Proposition of classification for colloidal molecules based on spheres and mimicking space-filling models of simple molecules (respective atomic radii are not systematically guaranteed). The usual terms found in the literature for describing such clusters are written in red. Figure adapted from [38].

Figure 1.10 resumes key anisotropy 'dimensions' along which homologous series of clusters vary only in that dimension. Taken cluster with four constituent spheres for example: in figure 1.10 (a), the spheres adopt different arrangements from 3D (tetrahedra), 2D(rhombus) to 1D(liner chain) (from left to right); in figure 1.10 (b), the chemical composition changes in the tetrahedra cluster; the dimension presented in figure 1.10(c) quantifies the variation in chirality; the anisotropy in terms of chemical ordering and shape gradient are shown in figure 1.10 (d) and (e) respectively. This illustration is a conceptual framework based on consideration of anisotropy dimensions which may be not exhaustive. Other dimensions could be induced according to diverse applications.

1.1.4 Clusters synthesis

The preparation of clusters of particles with requisite shapes and symmetries can be realized through various synthetic routes: physical routes, chemical routes, templates strategies etc. The controlled phase separation or nucleation/ growth phenomena could

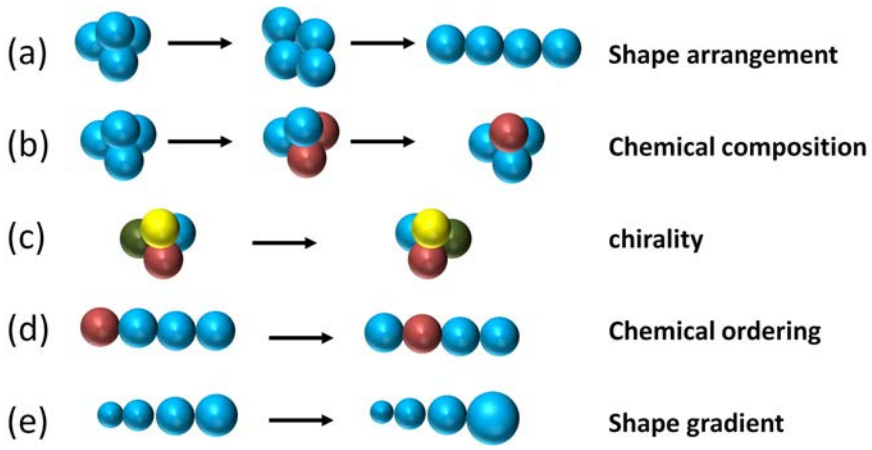

Figure 1.10: Anisotropy 'dimensions' used to describe key anisotropy attributes of clusters. Homologous series of particles as the attribute corresponding to the anisotropy axis is varied from left to right. (a) anisotropy in shape arrangement; (b) anisotropy in chemical composition; (c) anisotropy in chirality; (d) anisotropy in chemical ordering; (e) anisotropy in shape gradient.

also lead to clusters synthesis [38]. The most prominent of these approaches are briefly highlighted in the following part. More exhaustive information on this dynamically and rapidly developing research area can be found in recent review articles [41] [38] [46].

Physical routes

The depletion interaction occurs when two species of different sizes are suspended in a liquid. An effective attractive force arises between large colloidal particles that are suspended in a dilute solution of depletants, which are smaller solutes that are preferentially excluded from the vicinity of the large particles [47] [48] [49]. The depletion interaction is a powerful tool for assembly because its range and strength can be independently manipulated.

Meng et al. have investigated clusters made of 1 μm polystyrene spheres in the presence of 80 nm poly(N-isopropylacrylamide) microgel particles [50]. They used lithography to make microwells with depth and diameter of 30 μm , which are filled with the colloidal suspension. Dimers, trimers, tetramers in the form of tetrahedra and pentamers in the form of trigonal bipyramids were observed. In the case of six PS particles, octahedra and non-centrosymmetric clusters were both obtained with transition between the two states on time scales of minutes. An illustration of depletion interaction as well as some micrographs of colloidal clusters observed are shown in figure 1.11.

Pine and co-workers elaborated a directional assembling route based on the lock-and-key concept to the colloidal regime [52]. Triggered by short-range depletion attractions upon adding a non-adsorbing polymer, they demonstrated the site-specific recognition and association among bowl-shaped (lock) and spherical (key) colloidal subunits. Complex assemblies could be formed as shown in the figure 1.12.

Kraft et al. have presented an experimental realization of patchy colloidal particles based on material independent depletion interaction and surface roughness [53]. Smooth patches on rough colloids are shown to be exclusively attractive due to their different

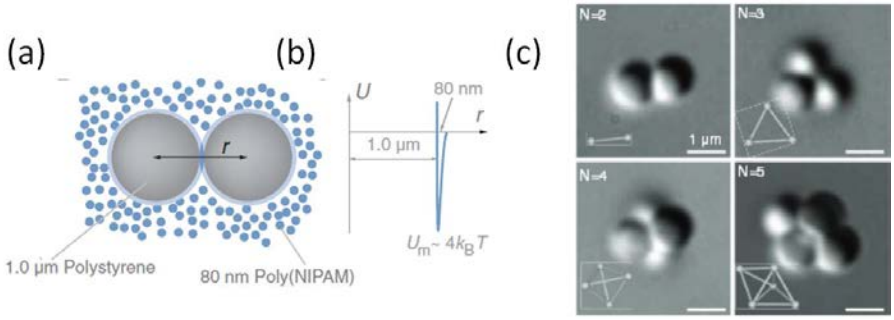

Figure 1.11: (a) A suspension of 1 μm diameter PS spheres are surrounded with 80 nm polyNIPAM microgel particles, which induce a depletion attraction as illustrated. (b) Pair potential as estimated from the V_{rij} approximation to the Asakura-Oosawa potential [51]. The interaction is strictly pairwise additive. (c) High-magnification optical micrographs of colloidal clusters in microwells with N = 2, 3, 4, and 5 particles. Scale bar, 1 μm. Figure adapted from [50].

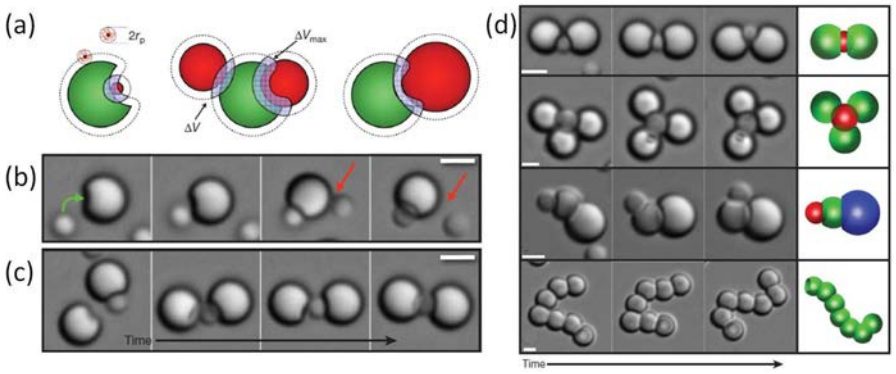

Figure 1.12: Lock-key interactions. (a) The depletion attraction potential between lock and key is proportional to the overlapping excluded volume, which attains a maximum for the configuration in which the key particle, by virtue of its size and position, precisely fits into the spherical cavity of a lock particle. (b), (c) Snapshots showing examples of depletion driven self-assembly of lock and key particles. Scale bars, 2 μm. (d) Time-lapse optical microscopy images (left three columns), and schematics (rightmost column), show the flexibility of lock-key bonds in various assemblies. The absence of irreversible chemical bonds between the building blocks allows these ball-in-socket joints to move freely. Scale bars, 2 μm. Figure adapted from [52].

overlap volumes. Association among the smooth patches is more favorable than that among the rough ones in terms of gain in free volume for the depletant, so that smooth patches are preferentially attracted to each other (see figure 1.13).

Long-range attractive forces due to the van der Waals interaction can induce clustering process in colloidal suspensions. If the electrolyte is dissolved, the ionic strength increases. The repulsive force between two colloids due to the distribution of charge on their surfaces is modeled by a screened coulombic interaction. Silica dumbbells were successfully synthesized in the micrometer range via van der Waals forces through the addition of ammonia into a suspension of silica spheres under shear [54] [55]. Similarly, colloidal homodoublets and heterodoublets have been produced from polymer colloids[56] and from micrometer scale metal particles [57] by increasing the ionic strength through adding potassium chlo-

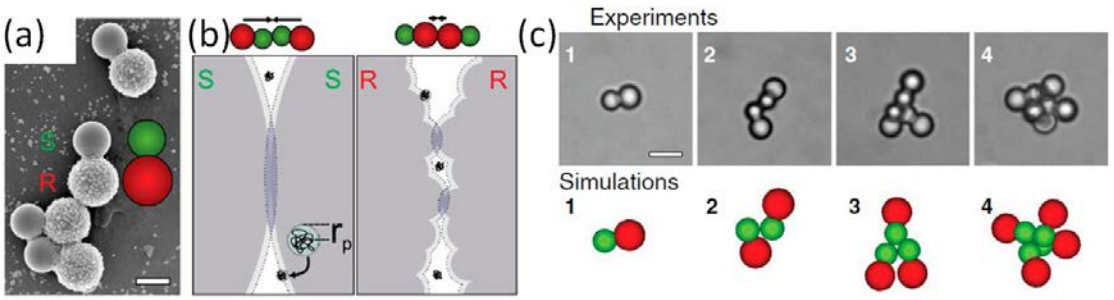

Figure 1.13: Patchy particles by roughness specific depletion interactions. (a) Colloidal model systems consisting of one sphere with a smooth and one sphere with a rough surface. Scale bars, 2 μm. (b) In the presence of small depletants, the colloidal particles are surrounded by a layer inaccessible to the depletant (dotted line). If colloidal particles approach such that their excluded volumes overlap, the depletant gains entropy, which results in a net attraction between the colloids. For two rough spheres the overlap volume is significantly reduced compared to that for smooth particles. Small arrows represent the effective forces on both colloids. (c) Typical cluster shapes obtained from colloids with attractive small smooth, and large rough (non-attractive) side containing N = 1 to N = 4 patchy particles. Upper rows show experimentally observed clusters of colloids with small, smooth side are presented. The lower, colored rows show clusters obtained from Monte Carlo simulations on dimers consisting of a rough and a smooth sphere. The smooth spheres interact by an attractive depletion potential (green) and the rough spheres interact with a hard-sphere potential (red). Scale bars, 5 μm. Figure adapted from [53].

ride (see figure 1.14).

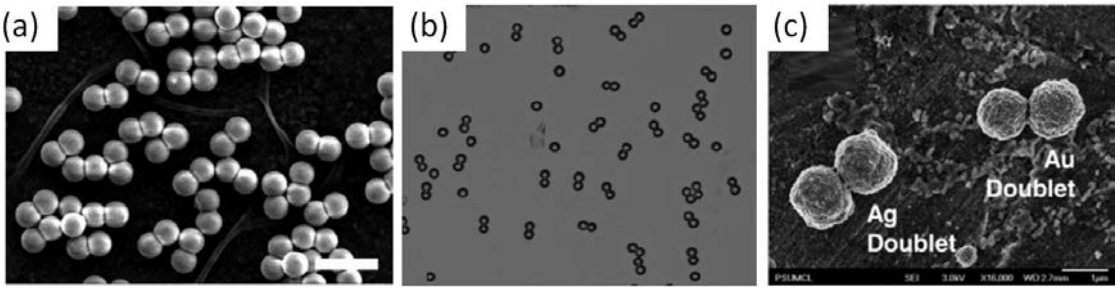

Figure 1.14: (a) SEM image of colloidal silica dumbbells. The scale bar is 4μm. Figure adapted from [54]. (b) Image of Amidine homodoublets. The singlet spheres are 2.1 μm amidine-functionalized polystyrene latex (PSL) particles. Figure adapted from [56]. (c) SEM images of synthesized metallic colloidal doublets: gold-gold and silver-silver from the gold-silver solution images. Figure adapted from [57].

Electrostatic attractive forces are also employed to favor the clustering of charged colloidal spheres. Microspheres with oppositely charged hemispheres (i.e. Janus-like particles[58] [59] [60]) were prepared and these particles spontaneously self-assemble into clusters of defined configurations due to their electrostatic interactions [61]. An example of such clusters are shown in figure 1.15.

Sacanna and co-workers have introduced a new class of spherical colloids that reversibly self-assemble into well-defined nonlinear structures by virtue of 'magnetic patches' [62]. This assembly is driven by tunable magnetostatic binding forces that originate from mi-

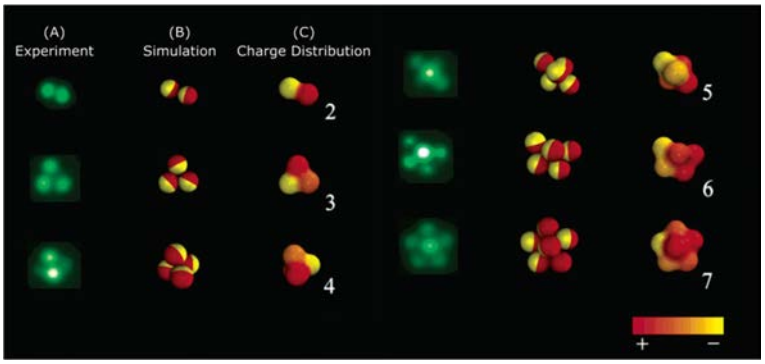

Figure 1.15: Comparison of experimental epifluorescence images (A) and Monte Carlo computer simulations (B) of the self-assembled clusters of 1 μm particles with near-equal positive and negative charges on the two hemispheres (denoted by red and yellow colors). The charge distribution in these clusters is also computed; the color goes smoothly from red to yellow depending on the inner product of the vector from the center of mass of the cluster to each colloid and the axial vector (pointing to the positive side) of this colloid (column C). Figure adapted from [38].

croscopic permanent magnets embedded underneath the surface of the particles. The resulting clusters form spontaneously in the absence of external magnetizing fields. Their geometry is determined by magnetic, steric, and electrostatic interactions. A reconfigurable structural arrangement is possible by imposing an external magnetic field which enables the clusters to unbind or change their geometry.

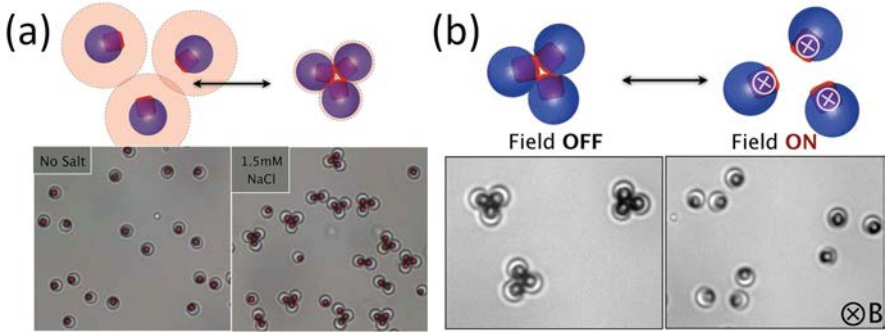

Figure 1.16: (a) When suspended in deionized water, the magnetic patchy particles are purely repulsive and singlets are observed. However, if the Debye screening length is reduced below 6 nm by means of added salt (here 1.5 mM NaCl), the patches become 'sticky' and particle clusters start forming. (b) Clusters formed at high salt concentration in zero-field can be disassembled by imposing an external magnetic field. Here planar trimers diffusing on a glass slide are quickly exposed to a 30 G field perpendicular to the substrate. The resulting parallel-aligned dipoles repel each other, causing the clusters to unbind. Figure adapted from [62].

Cluster assemblies by external fields have been also explored in many studies. The driving force of the aggregation could be induced by optical [63] [64] [65], electric [66] [67] and megnetic[68] [69] [70] interactions.

Chemical bonding routes

Clustering assisted by chemical bonding is a promising strategy to build 'colloidal molecules'. Directional interactions, such as hydrogen or covalent bonding, ligand or scaffold binding could be used to link and assemble colloidal particles together.

Highly selective interactions between colloidal particles can be realized by using DNA strands to functionalize their surfaces and borrow from biology the binding specificity encoded into the DNA sequences [71] [72] [73] [74] [75]. For example, Loweth and coworkers have elaborated assemblies of gold nanocrystals using DNA hybridization [76]. Gold nanocrystals derivatized with complementary single-stranded DNAs (ssDNAs) can be hybridized to each other to form periodic arrays. They reported the synthesis of heterodimeric and heterotrimeric 'nanocrystal molecules' in which Watson-Crick base-pairing interactions are used to control the relative spatial arrangement of Au nanocrystals. A large variety of clusters were observed, as shown in figure1.17.

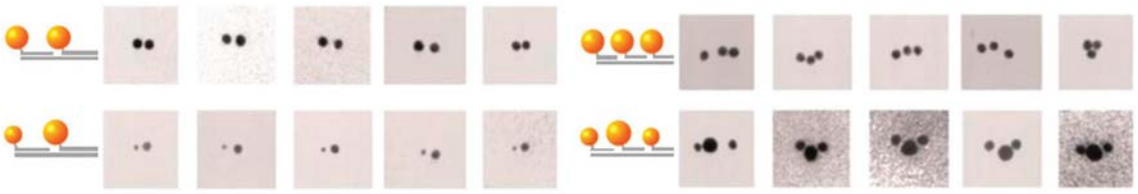

Figure 1.17: Schematic illustrations of ssDNA/Au nanoparticles hybridization and representative TEM images of obtained corresponding clusters. The size of nanocrystals is 5 or 10 nm. Figure adapted from [77].

Wang et al. have recently demonstrated the synthesis and assembly of colloidal particles with directional interactions [78]. Those particles possess various numbers of patches on the surface, N = 1-7 and higher, that adopt spherical, linear, triangular, tetrahedral, trigonal dipyramidal, octahedral or pentagonal dipyramidal symmetries. The patches are then site-specifically functionalized with oligonucleotides, enabling a reversible and controllable attraction between patches on different particles. Figure 1.18 shows some examples of these assemblies.

Synthetic phenylacetylene-based scaffolds with two, three or four thioacetyl groups were also successfully used for generating well-defined clusters of Au and Ag nanoparticles. Novak et al. have developed phenylethynyl-bridged metal nano-particle clusters from the monomeric particle starting material [79] [80] [81]. According to the molecular scaffolds, dimers and trimers were obtained (see figure 1.19).

Many other surface functionalization can provide colloids with directional interactions. The binding between inhomogeneous surface coatings can be realized by small molecules such as biotin/avidin and carbodiimide, click-chemistry [82] etc.

Template strategies

Alternative strategy towards particle clusters is based on the templates confinement. Xia et al. have reported a strategy that is based on a 2D template [83] [84] [85] [86]. Using lithographic techniques, they have demonstrated that polystyrene and silica beads could be trapped on patterned surfaces with two-dimensional arrays of cylindrical holes. The number of particles trapped in each hole as well as their arrangements could be determined by geometry and can be changed by tuning the ratios between the size of the

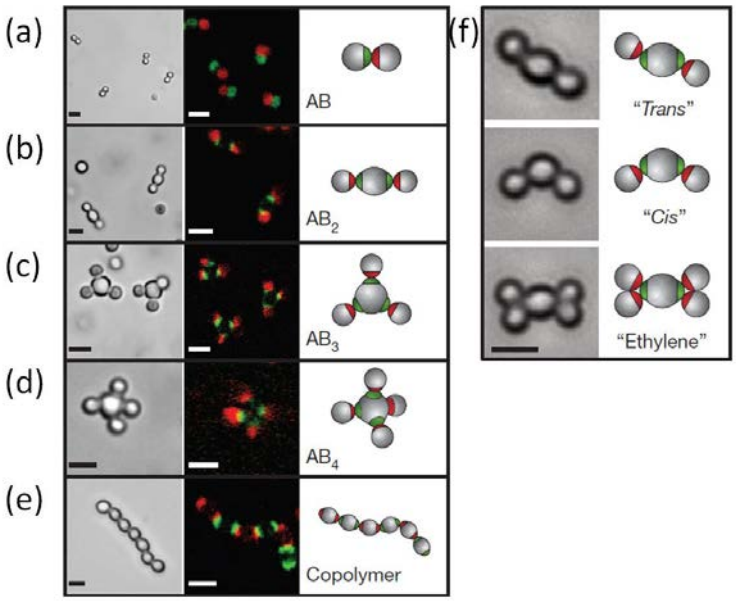

Figure 1.18: Specific directional bonding between colloidal clusters observed with optical microscopes. (a)-(e), Bright-field (left panels), confocal fluorescent (middle panels), and schematic images (right panels), show colloidal molecules self-assembled from patchy particles. (a), Complementary green and red monovalent particles form dumbbell-shaped AB-type molecules. Supracolloidal molecules AB_2, AB_3 and AB_4 are formed by mixing red monovalent with green divalent (b), trivalent (c) and tetravalent (d) particles. (e) If complementary divalent particles are mixed, linear alternating polymer chains spontaneously assemble. (f) When particles with bigger patches are used, cis- trans-like isomers can form. Introducing more monovalent particles leads to ethylene-like colloidal molecules. Images are bright-field (left panels) and schematic (right panels). Scale bars, 2 μm. Figure form [78]

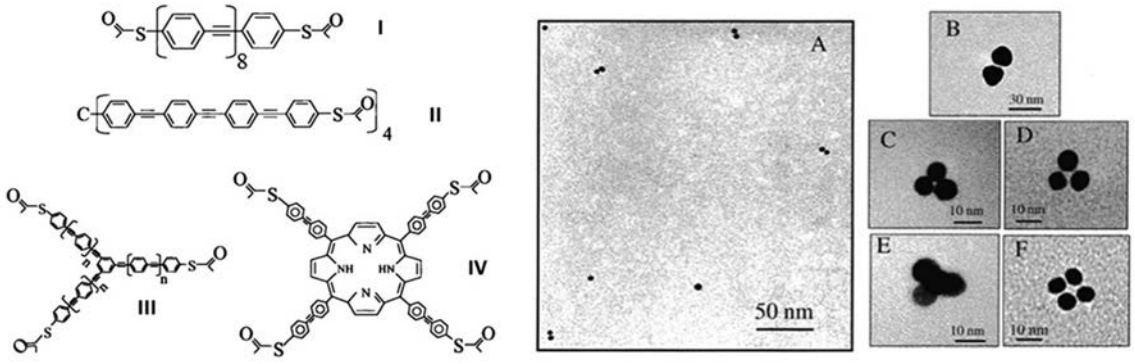

Figure 1.19: TEM images of gold nanoparticle clusters formed using linkers I (A, B), III with n = 1 (C), and III with N = 2 (D), II (E) and IV (F). Figure adapted from [77].

particles and the dimensions of the hole. After slow dewetting of a suspension on arrays of cylindrical holes, the system is heated slightly above the glass transition temperature of the colloidal material to permanently bond together the spherical particles within each hole. This approach is now commonly referred to as template-assisted self-assembly (TASA). Various templates are used to obtain cluster geometries such as dimers, tetrahedrons and

zigzag chains. More complex heterogeneous aggregates were obtained applying consecutive TASA depositions with particles of different sizes or composition, as shown in figure 1.20.

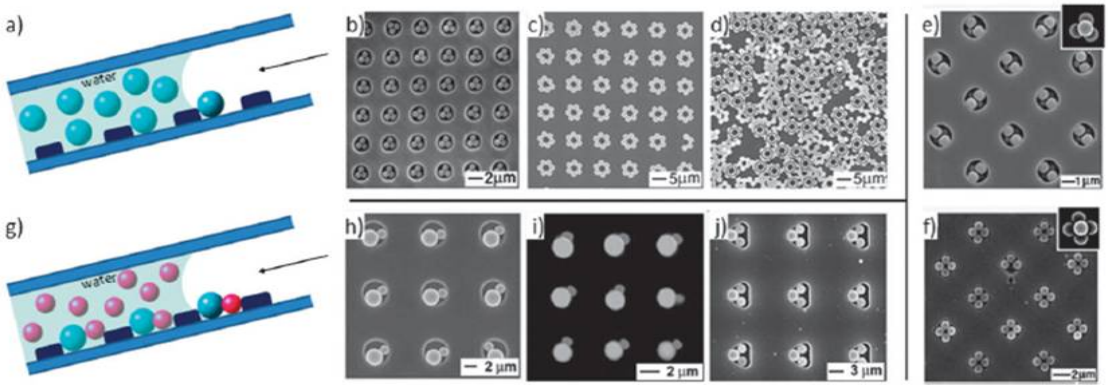

Figure 1.20: (a) Schematic representation of the experimental cell and procedure for the one-stage dewetting of spherical colloids for the production of homoclusters such as (b) triangles, (c) ,(d) hexagons, (e) tetrahedrons and (f) octahedrons; (g) schematic representation of the experimental cell and procedure for the two-stage dewetting of spherical colloids for the production of heteroclusters such as (h), (i) snowman-like and (j) mickey mouse like clusters. The spherical colloids are micron-sized PS particles and images were acquired by SEM. Figure adapted from [77].

Even through these template-directed colloidal self-assembly strategies lead to well-defined clusters with satisfying morphology yield, the amount of clusters which may be prepared per batch is restricted due to the use of two-dimensional templates [77]. Velev and co-workers used emulsion droplets as 3D templates to pack particles [87]. This strategy is based on the agglomeration of particles adsorbed on emulsion droplets. This process is driven by a significant reduction of interfacial tension; the adsorption energy of the particles is governed by their size, the interactions among them and their interactions with both fluid phases [88]. Subsequent evaporation of the dispersed phase of the emulsion causes capillary forces, which pack the particles together. This strategy was further optimized for the preparation of polystyrene colloidal clusters with a precisely-defined geometry by Manoharan et al. in 2003 [89] and then adapted by the same author and several other research groups to various colloidal systems including inorganic colloids and binary mixtures [90] [91].

Figure 1.21 (a) illustrates the original idea which consists of preparing an oil-in-water emulsion in which spherical colloids are trapped at the interface of the oil droplets. Subsequent evaporation of the oil phase forces the spheres to pack into small clusters and bind to each other via van der Waals interactions. It is observed that for a given number of spheres N, all clusters exhibited well-defined configurations, which for $N \leq 11$ minimize the second moment of the mass distribution [89] (see figure1.21 (b)).

The clusters reported so far were made from a rather limited number of different constituent particles, in most instances polystyrene (PS), poly(methyl methacrylate) (PMMA) or silica microspheres [92]. Very recently, van Blaaderen and co-workers reported on clusters built from dumbbell-shaped particles [93]. Despite its flexibility and large particle yield, a broad size distribution of the droplets as well as the statistical distribution of the particles on the droplets, would give rise to a broad range of different species of clusters. Emulsion confinement drying typically produces mixtures of clusters composed of different numbers of spheres. Therefore, a separate sorting process is often required to obtain truly

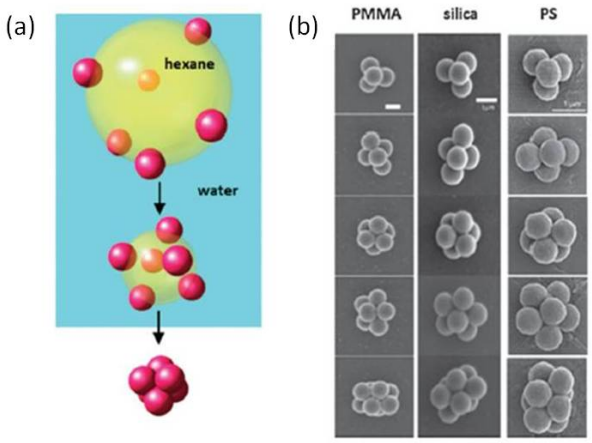

Figure 1.21: (a) Schematic representation of the fabrication of clusters by using emulsion droplets as 3D templates. (b) SEM micrographs of PMMA, silica and PS colloidal clusters obtained by 3D emulsion droplet confinement. Scale bars, 1 μm. Adapted from review [77]. Examples of clusters from the literature [92].

monodisperse suspensions.

After this overview of the different ways to create colloidal clusters, we will recall some fundamentals on microfluidics that we will use to create droplets and assemble them.

1.2 Microfluidics

In recent years, considerable progress has been made in the miniaturization field. It is now effectively possible to miniaturize all kinds of systems, such as mechanical, fluidic, electromechanical or thermal, down to submicrometric scale. The manufacture of smaller, cheaper, and more accurate devices, such as micron-size pumps, separators, and detectors are just a small sample of the contributions that microfabrication has provided.

The miniaturization and MEMS (microelectro - mechanical systems) gave birth to microfluidics in the 1990s. Microfluidics is a multidisciplinary field intersecting engineering, physics, chemistry, biochemistry, nanotechnology, and biotechnology, with practical applications to the design of systems in which small volumes of fluids will be handled [94]. Microfluidics has a promising future due to its advantages when compared with the conventional macroscopic systems. The microfluidics entails fluids at the micro-scale dimensions, which allows flexible production processes or the capacity to integrate all the steps of a complex process within a single device, the so-called 'Lab-on-a-chip' or 'Micro-total-analysis-systems' (μTAS).

In the following part, we will briefly review in particular the droplet based microfluidics and some existing assembly processes assisted with microfluidic techniques.

1.2.1 Droplet-based microfluidics

Microfluidic generation of droplets has attracted lots of interest, due to the ability of this method to produce droplets with precisely controlled sizes, shapes and internal structures. Droplet based microfluidics is a rapidly growing interdisciplinary field of research. The droplets generated via microfluidic emulsification have been used in various field, in high-throughput screening of biomaterials and the encapsulation of cells [95] [96] [97], in studies of protein crystallization [98] [99] and in the synthesis and fabrication of particles[100] [101] etc.

We begin with a brief overview of the working fluids and surfactants then we will continue with some general microfluidic emulsification methods as well as the droplet production regimes. Four categories of microfluic geometries are discussed: Coaxial devices, T-junction devices, Flow Focusing devices and Step emulsification devices. We will also give a description of some common methods of solidification and strategies for achieving microparticles from droplets.

Dispersed phase, continuous phase and surfactants

Microfluidic technologies have emerged recently as a promising new route for the fabrication of emulsions. Emulsions are a class of disperse system consisting of two immiscible liquids [102]. The liquid droplets (the disperse phase) are dispersed in a liquid medium (the continuous phase or carrier fluid).

Several classes may be distinguished: oil in water droplets (O/W), water in oil droplets (W/O) and oil in oil droplet (O/O). The latter class refers to a system of two immiscible oils such as a polar oil (e.g. propylenen glycol) and a non-polar oil (paraffinic oil). Generally, to disperse two immiscible liquids, one needs a third component, the emulsifier or surfactant. It helps to lower the interfacial energy, i.e. to facilitate the formation of new interfaces and to stabilize the formed emulsion droplets from coalescence. The choice of the surfactant is crucial in the formation of the emulsion and its long-term stability [103] [104] [105].

Droplet based microfluidics relies on the production of droplets with a controlled size and at a high frequency. Those two immiscible fluids, dispersed phase and continuous

phase, are injected into different inlets in the microfluidic devices either by flow rate, using, e.g., syringe pumps or by pressure.

Droplet production geometries

The production of droplets in a two-phase microfluidic device has mostly been explored in four types of microfluidic geometries, namely in coaxial, T-junction, flow-focusing, and step emulsification devices. Figure 1.22 provides the schematics of the typical geometries of these devices.

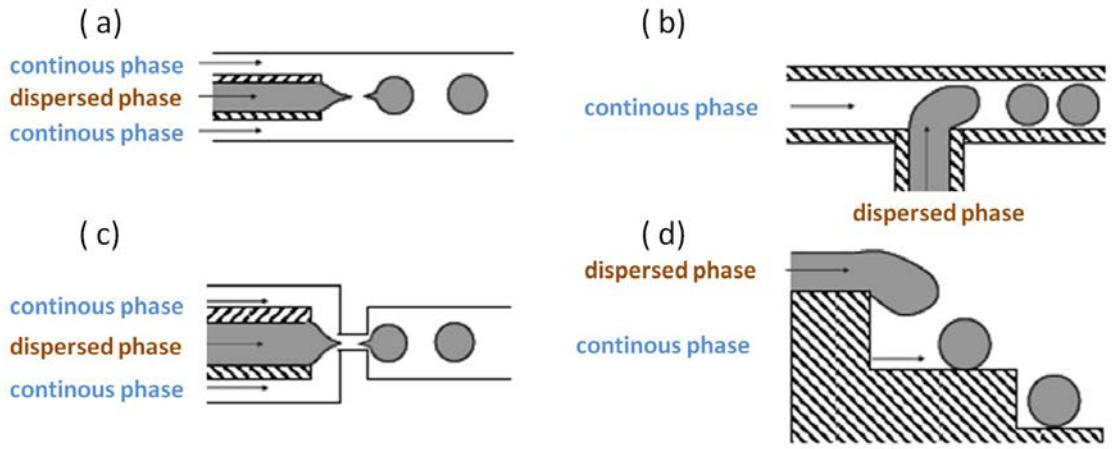

Figure 1.22: Illustration of four main microfluidic geometries used for droplet formation. (a) coaxial device, (b) T-junction, (c) flow-focusing device, and (d) step emulsification device.

Coaxial geometry

In the coaxial co-flowing device, the droplets formations are achieved with a set of concentric channels where the dispersed phase liquid is driven into the inner channel or capillary, and emerges from the end of the capillary into a parallel flowing stream of the continuous phase liquid, as shown in figure 1.22 (a). Experimental devices using the coaxial geometry are often made by inserting a smaller circular inner glass capillary tube into a larger square capillary tube [106] [107]. More recently, researchers are able to design all-PDMS coaxial channels for more rapid prototyping of devices [108]. The stream of disperse phased is subjected to a hydrodynamic force exerted by the flow field of the continuous phase.

T-junction geometry

In T-junction devices, the dispersed and the continuous phases flow through two orthogonal channels and form droplets when they meet, as shown in figure 1.22 (b). The shear forces generated by the continuous phase and the subsequent pressure gradient imposed on the dispersed phase cause the head of the dispersed phase to elongate and eventually collapse into droplets.

In this geometry, droplet size is determined by the interfacial tension between the two phases, the viscosity of the continuous phase, and the shear rate imposed on the droplet phase [109] [110].

Flow-focusing geometry

A flow-focusing microfluidic device was first demonstrated by Stone et al. [110] [111] [112] for the generation of monodispersed bubbles. In those devices, the continuous phase is injected to two outer microchannels while the dispersed phase is injected into a central microchannel, as shown in figure 1.22 (c). Those two phases are forced through a narrow region in the microfluic device (e.g. a narrow orifice) [113] [114] [115].

This geometry employs symmetric shearing by the continuous phase on the dispersed phase which enables a well controlled and stable generation of droplets. Droplet size can be manipulated by altering the capillary number, flow rate ratios of fluids, the interfacial tension between the two phases, the viscosity ratio of the droplet phase to the continuous phase, and the geometry of the flow-focusing device, e.g. the size of the orifice.

Step emulsification geometry

This process mimics membrane emulsification in a microfluidic format. These devices usually consist of terraces housing many micron-sized channels along their sides. Seki's research group pioneered the generation of droplets using terrace-like microfluidic devices [116] [117] [118] [119]. The dispersed phase is forced from an inner chamber through the channels into the surrounding chamber containing the continuous phase, as shown in figure 1.22 (d). The droplets are formed via an inflation and detachment process, as they grow and drop off the terrace into the collecting well. Several groups have studied on the derived terrace-like geometry which uses only one geometric step to trigger droplet formation of a stream of a dispersed phase surrounded by a continuous phase. This droplet break-up mechanism is called 'step emulsification' [15] [120] [121] [122] [123] [124][125]. The important feature of the step-emulsification technique is that the dispersed stream is stabilized between the two walls of a high aspect ratio channel suppressing interfacial induced instabilities. The stream of the dispersed phase abruptly breaks up into droplets at the geometric step when the stabilizing channel walls end [126].

Droplet production regimes

We have shown some typical microfluidic droplet generation geometries. Although physical mechanisms for the generation process are different for various types of microfluidic configurations, the formation of droplet is the result of the interplay between viscous stresses and capillary pressure. For different geometries of droplet production, we could briefly define two regimes [126] [127] [128] [129]:

Dripping regime

In the dripping mode, a droplet grows and eventually detaches from the tip of a nozzle or an orifice under the action of an external force.

Jetting regime

In the jetting mode, a jet of the droplet phase forms above a critical flow rate of fluids. The jet extends far from the orifice or nozzle into the continuous phase, and then breaks up to droplets due to Plateau-Rayleigh instability [2].

Those two regimes mentioned above have been commonly observed, nevertheless the droplet production regimes can be further developed with expanded classification accord-

2. The Plateau-Rayleigh instability explains why and how a falling stream of fluid breaks up into smaller packets with the same volume but less surface area. The driving force of the Plateau-Rayleigh instability is that liquids, by virtue of their surface tensions, tend to minimize their surface area. A considerable amount of work has been done recently on the final pinching profile by attacking it with self similar solutions [130] [131].

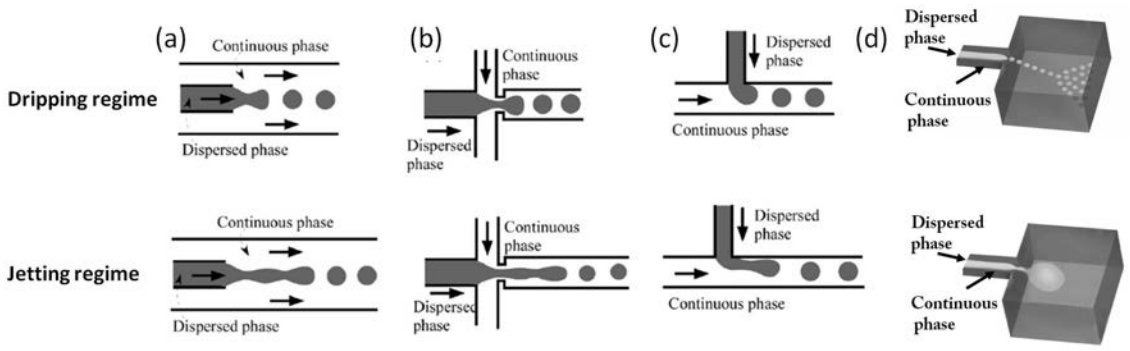

Figure 1.23: Schematic of different flow regimes in (a) coaxial, (b) flow-focusing (c) T-junction and (d) step emulsification microfluidic devices. Figures (a)-(c) adapted from [129].

ing to specific microfluidic geometries. For instance, in the T-junction geometry, monodispersed droplets could be generated under **squeezing regime** and **dripping regime**. In the squeezing regime, the generated droplet blocks the channel of the continuous phase and creates a pressure drop across the droplet. While in the dripping regime, the droplets are smaller than the dimensions of the channel of the continuous phase. We will discuss this in details in Chapter 5, Cluster production part.

Droplet solidification

Once droplets have formed, they can be used, for example, as liquid templates for particle synthesis [129]. There are various synthetic methods for the solidification of droplets. Several insightful reviews [129] [132] [133] [134] [135] covering different aspects of microfluidic particle synthesis have been published in the past few years and have focused mainly on droplet formations [127] as the basis for particle synthesis. In the following part, we will introduce some frequently used methods which transform liquid droplets generated by microfluidic emulsification to solid or gel-like polymer particles.

First, free-radical polymerization or condensation polymerization of monomers/prepolymers compartmentalized in droplets have been used to solidify the droplets and transform them into polymer particles or polymer capsules [136] [137] [138] [139] [140] [141] [142] [143] [144] [145]. The droplets contain monofunctional/multifunctional monomers and an initiator which produces highly reactive free-radical species that initiate the chain reaction. This process may be initiated thermally or by light.

Nisisako and co-workers have generated polymer particles from 1,6-hexanediol diacrylate via both UV-initiation and thermal initiation off-chip [147]. The team of Whitesides and Kumacheva developed a continuous reactor for polymer particles synthesis with a variety of shapes using flow-focusing microfluidic devices [146]. The same groups have demonstrated the preparation of gel-like polymer particles by thermal gelatin. Figure1.24 shows that both the emulsification and the polymerization compartments were integrated into a single planar microfluidic device. Various diacrylate, triacrylate and divinyl monomers were crosslinked and solidified on-chip either photochemically (by photopolymerization of monomer fluids, see figure1.24 (c), (d)) or thermally (see figure1.24 (e), (f)). Using the similar mechanism, Dendukuri et al. created solid disk-shaped and plug-shaped particles by UV-polymerizing plugs of a photopolymerizable resin (Norland optical adhesive, NOA-60) in a T-junction device [148]. Figure 1.25 shows a schematic of the system and the polymerized plugs and disks obtained.

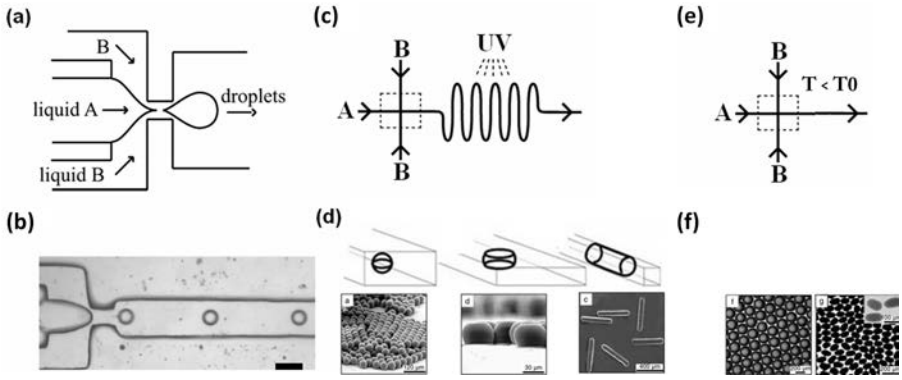

Figure 1.24: (a) A schematic representation of the flow-focusing geometry. (b) Optical microscopy images of the generation of monomer droplets. (c) Schematic representation of the devices used for producing photochemically solidified particles. The dashed rectangles mark the flow-focusing device shown in (a). The channels used for photochemical cross-linking were elongated to allow extended exposure of the droplets to UV light. (d) (Top): the shapes of droplets are defined by the confinement of microfluidic channels. (Bottom): PolyTPGDA particles with shape of microspheres, disks and rods after droplet solidification. (e) Schematic representations of the devices used for producing thermally solidified particles. The flow focusing region was kept at a temperature exceeding the gelling (or solid-liquid phase transition) temperature (T_0). The outlet channel was cooled to a temperature below T_0, and the droplets solidified as they traveled down the channel. (f) agarose disks and bismuth alloy ellipsoids produced using thermal solidification. Figure adapted from [146].

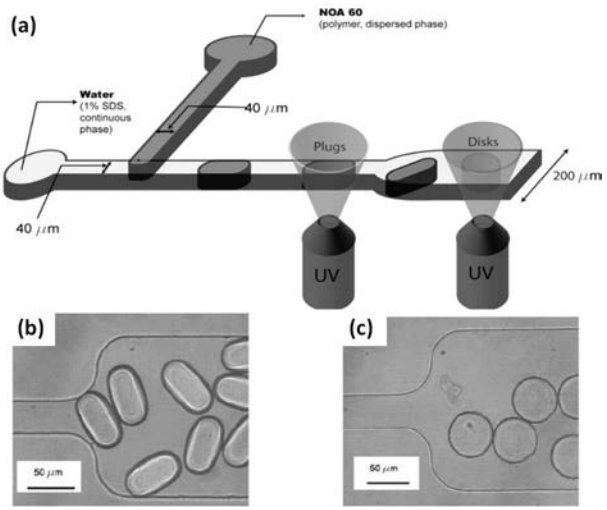

Figure 1.25: Microchannel geometry used to create plugs and disks: (a) schematic of channel with plug and disk creation zones marked; (b) polymerized plugs in the 200 μm section of the channel, 38 μm height; and (c) polymerized disks in the 200 μm section of the channel, 16 μm height. Figure adapted from [148]

Seiffert and co-workers have developed methods called 'polymeranalogous crosslinking process' in order to improve the chemical homogeneity of such solidified particles [149] [150]. Uncrosslinked polymer chains with sites for subsequent crosslinking were well prepared in advance. Semi-dilute solutions of these macromolecular precursors were later

emulsified on-chip and the crosslinking reaction was triggered. For example, poly(N-isopropylacrylamide) (pNIPAM) microparticles were synthesized with UV light using this method.

The second strategy involves the use of ionic crosslinking to generate gel-like polymer particles or capsules. This method is a solidification method often used with biological polymers. The reaction typically proceeds via the crosslinking of polyelectrolyte polymer chains with multivalent ions or small ionized molecules. One of the most common examples of this reaction is the gelation of anionic alginate with Ca^{2+} ions, which crosslink the guluronic acid blocks. Alginate gelation is commonly used for both particle and fiber synthesis [108] [151] [152] [153]

There are different approaches to elaborate spherical alginate particles, such as the coalescence of droplets separately containing the precursor polymer and the crosslinking agent [153] [154] [155] [156]; external or internal gelation where a solution of a precursor polymer is emulsified in the continuous phase (typically, a non-polar liquid), and the crosslinking agent either diffuses into the droplets from the continuous phase or is directly introduced into the droplets and be activated later to trigger the gelation of the prepolymer after emulsification [155] [157][158]. Kumacheva's research group have demonstrated that the structure of microgels (from capsules to gradient microgels to particles with a uniform structure) could be well controlled by varying the time of residence of droplets on the microfluidic chip and the concentration of the cross-linking agent in the continuous phase. Figure1.26 shows an illustration of the formation of microgels by an external gelation method and some microgels obtained with this method.

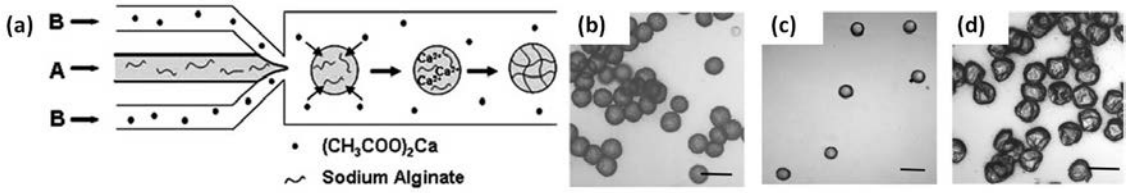

Figure 1.26: (a) Schematic drawing of the formation of microgels by an external gelation method. An aqueous solution of sodium alginate is introduced as liquid A in the central channel. A non-polar continuous phase containing a suspension of calcium acetate is introduced in the device as liquid B. Calcium acetate dissolves in the droplets and releases Ca^{2+} ions which bind to alginate molecules to form a gel. (b) Optical microscope image of calcium alginate microgels prepared through the mechanism of external gelation. (c) Micrograph of κ-carrageenan microgels obtained with external gelation. (d) Micrograph of carboxymethylcellulose microgels obtained with external gelation. The scale bar is 100 μm. Figure adapted from [155] [158].

Finally, solvent extraction/evaporation methods are also commonly used to form particles from droplets generated by microfluidic emulsification. It is useful for particles and fibers composed of uncrosslinked polymeric systems [65] [159] [160] [161]. After a precuseur solution is emulsified in microfluidic droplet generator, particles are produced by removing the solvent via in-situ extraction into a continuous phase or through evaporation in the off-chip process.

Wang and co-workers have generated toroidal particles through solidification of droplets of polymer solution in a microchannel [162]. Solidification likely proceeds through phase separation of the polymer solution as the solvent diffuses into the continuous phase. In axisymmetric laminar flow, fluids at the front and the back of the droplet in the axial direction move at the same velocity as the droplet, leading to a stagnation zone and poorer

solvent diffusion. As a result, solidification occurs in a spatially non-uniform fashion, resulting in toroidal particles. Figure 1.27 shows the monodisperse toroidal particles synthesis. The particle was prepared by solidifying a droplet of 10 wt% polysulfone dissolved in dimethylformamide solvent(DMF).

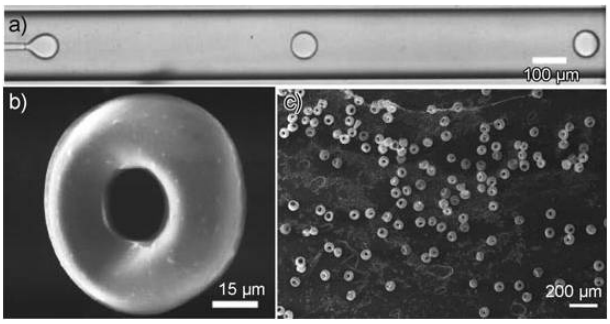

Figure 1.27: (a) Droplets of polymer solution being generated inside a microcapillary device. (b) Scanning electron microscopy (SEM) image of a typical toroidal polymer particle. (c) SEM image of toroidal polysulfone particles prepared under the same conditions as in (b). Figure from [162].

Fang et al. have elaborated silica microspheres using sol-gel polymerization triggered by the diffusion of water into the continuous dimethyl carbonate solvent (DMC). They have further explored the phenomenon of microfluidic diffusion-induced self-assembly and studied silica particle shape by tuning the parameters of geometric confinement and the local Peclet number [3] [163][164].

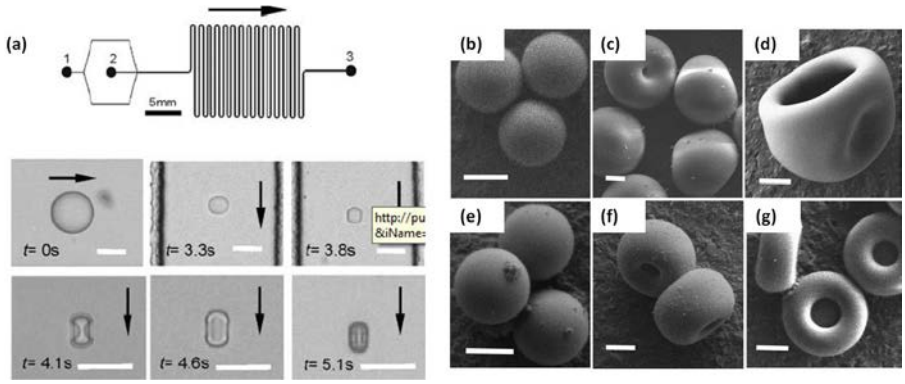

Figure 1.28: (a) Schematic of the PDMS device used for this work (top). Evolution of a droplet toward silica particle (bottom) as it travels downstream. Scale bar, 50 μm. Figure from [163]. Silica particle shapes by tuning Pe and D_0/h (D_0 is the droplet initial diameter at breakup, h is the height of channel and l is the drying length.): (b) Pe = 4.1, D_0/h =0.32, l = 84 cm; (c) Pe = 12, D_0/h = 0.62, l = 137 cm; (d) Pe = 45, D_0/h = 0.57, l = 36 cm; (e) Pe = 6.5, D_0/h = 0.97, l = 137 cm; (f) Pe = 10, D_0/h = 0.80, l =36 cm; (g) Pe = 52, D_0/h = 0.92, l = 36 cm. Scale bar, 10 μm. Figure from [164].

3. This dimensionless number is defined by the ratio of the rate of advection of a physical quantity by the flow to the rate of diffusion of the same quantity driven by an appropriate gradient.

1.2.2 Microfluidic assembly strategies

At the microscale, microfluidic technology provides a good fluid-flow control for component transport, orientation and assembly. A variety of solutions are available for manipulation and assembly of objects of interest.

Microfluidic sorter, for example, can be viewed as a gross-position step in assembly processes, by bringing a disordered dispersion of components into a desired arrangement [165]. Passive or active manipulation techniques exist that allow us to sort and address objects of interest. Hydrodynamic effects, such as hydraulic resistance can result in sorting confined objects into channel having low resistance by the pressure gradient. External fields which can be switched on and off, such as electric or magnetic fields, also provide possibilities to actuate and actively sort objects by dielectric, magnetic or electrorheological effects. Temperatures gradients, can be also employed to create flows and to displace objects by means of the thermocapillary effect [126].

The 'rails' and 'anchors' in microfluidic channels have been developed to guide, position and assemble microstructures inside fluidic channels. Chung and co-workers have introduced 'railed microfluidics' as an agile method to guide and assemble microstructures inside fluidic channels [166] [167]. The guided movement of microstructures in microfluidic channels was achieved by fabricating grooves ('rails') on the top surface of the channels and also creating complementary polymeric microstructures that fit with the grooves. Figure1.29 (a) (b) shows the concept of railed microfluidics and guiding mechanism. Similarly, Abbyad and al. presented a method to control the motion of nanolitre drops in a wide and thin microchannel, by etching fine patterns into the channel's top surface [168]. When drops are squeezed by the channel roof, their surface energy will be reduced as they enter into a local depression. The resulting gain in surface energy pulls a drop into the groove such that localized holes can be used as anchors for holding drops, while linear patterns can be used as rails to guide them along complex trajectories, as shown in figure 1.29 (c)-(f).

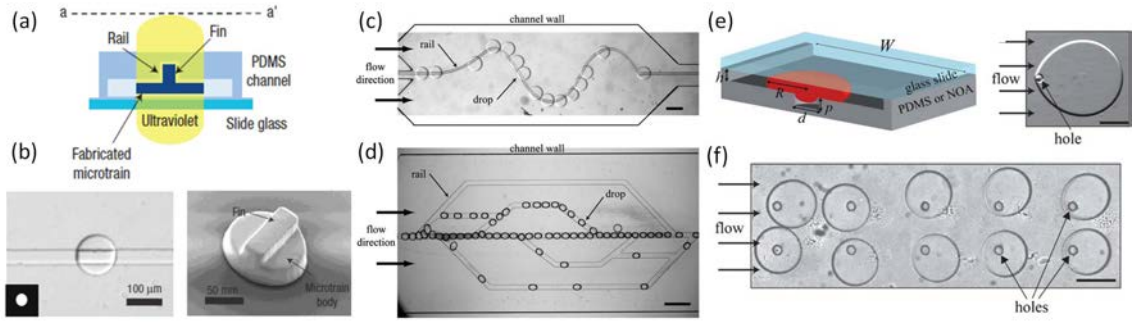

Figure 1.29: (a) Cross-section of the polydimethylsiloxane (PDMS) railed microfluidic channel and a finned microtrain cut at a-a′ from a. (b) Fabricated microtrain. (Left): the top view of the microtrain in a differential interference contrast image. The top-view shape of the microtrain is determined by a pattern specified on a digital micromirror device (inset). (Right): a corresponding scanning electron microscope image. Figure(a), (b) adapted from [166]. (c) Large water drops follow a narrow sinusoidal rail inside a Hele-Shaw channel. (d) Smaller drops of radius follow a complex network of rails with bifurcations and junctions. The scale bars represent 500 μm. (e) (Left): Sketch of the experimental device which defines the geometric parameters. (Right): A water drop anchored to a hole in the channel roof with oil flowing left to right. (f) An array of anchored droplets. The scale bar represents 250 μm. Figure(c)-(f) adapted from [168].

Xu and co-workers have developed a multiple-droplet clustering device that can perform sequential droplet trapping and storing [169]. It consists of a 10 × 12 array of clustering structures (e.g., storing well, storing chamber, trapping well, and guiding track). By applying forward and backward flows, shape-dependent droplet can be manipulated as follows: flattened droplets are trapped in each trapping well in the forward flow and in the backward flow, the trapped droplets are able to get released from the trapping well and follow the guiding tracks to their corresponding storing wells. The guided droplets float up out of the confining channel to the super stratum of the storing chamber due to interfacial energy and buoyancy effects. This forward/backward flow-based trapping/storing process can be repeated several times to cluster droplets with different contents in the storing chambers (see figure1.30).

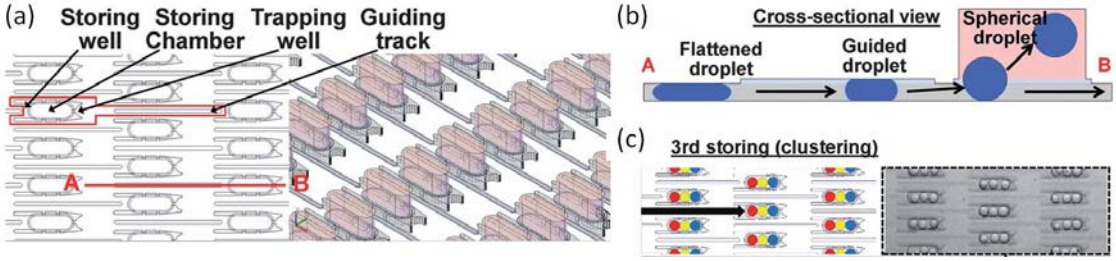

Figure 1.30: Working principle of the proposed device. (a) Top and 3D views of the multiple-droplet clustering array. A unit cell includes a storing well, a storing chamber, a trapping well, and a guiding track placed in the second column between the trapping well (in the first column) and the storing well (in the third column). (b) Cross-sectional view of A and B in (a). In the backward flow, the flattened droplet follows the guiding track, releases its interfacial energy after entering the storing chamber, and floats up to the super stratum of the chamber. Under the forward flow, the droplet stays in the chamber due to the interfacial energy and buoyancy effects. (c) Photographs of three times repeated trapping and storing for triple-droplet clustering in the microfluidic device. Scale bars, 300 μm. Figure adapted from [169].

Other self-assembly methods could be realized by the integration of micropumps and microvalves in microfluidic systems. Micropumps are responsible for generating temporal and volumetric fluid movement on-chip and they are used to reduce the amount of external hardware necessary to operate a microfluidic device. Microvalves, on the other hand, control routing, timing, and separation of fluids within a microfluidic device and are crucial for designs with complex functionality [170]. The valves can be actuated mechanically [171] [172] [173] [174], pneumatically [175][176][177][178][179][180][181][182][183], electrokinetically [184][185][186][187], by phase changes [180][181][188][189][190][191][192] or by introduction of external force [193][194].

Tolley et al. have demonstrated experimentally a semidirected fluidic assembly process in two dimensions [195]. A microfluidic chamber was equipped with several inlet and outlet ports. Systematic use of valves controlled flow through each port individually. Translation and rotation forces can be created by controlling the flow field for component manipulation. Figure 1.31 shows how sequential control of valves would drive a component through several paths, up to a successfully assembled state.

With the help of sorters, 'rails', 'anchors' and valves etc., we dispose of a lot of methods to manipulate objects of interest. However, the precise positionning of objects remains quite challenging in such systems even if microfluidic chambers have shown the capacity for controlling reconfigurable 2D fluid force fields [165] [196]. Indeed Schneider et al.

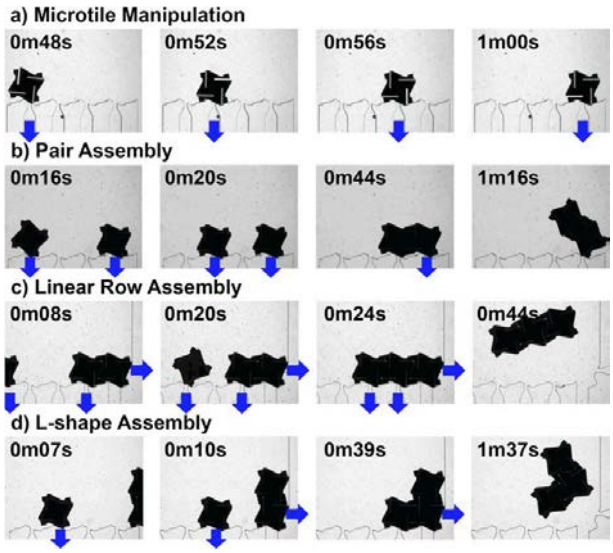

Figure 1.31: Color online Microtile manipulation and assembly. Frames taken from video micrographs of (a) an automated microtile manipulation and (b)-(d) three assembly experiments. Timed valve actuation directs pressurized flow into the microfluidic chamber and out the indicated openings. Fluid flow applies hydrodynamic forces to the microtiles, causing them to move and assemble. Alignment patterns and compliant latches cause adjacent tiles to self-align and bond together. The valving sequences determine the final structures. Figure adapted from [195].

studied laminar flow fields within a microfluidic chamber analytically [197]. They have analyzed the flow fields defined by the flow status at each inlet and outlet. The number of ports and the relative chamber size directly controlled the number of nodes at which different field vectors converge. These convergence nodes would then provide equilibrium locations for components present within the chamber. With 7 controlled flow rates, they have illustrated the algorithm by showing that a modified Hele-Shaw cell can be designed to construct the entire English alphabet from particles that irreversibly stick to each other. Figure 1.32 illustrates a sequential assembly algorithm which generates component arrays.

This theoritical work shows the possibility to form all kinds of aggregates. Nevertheless, experimentally, the exact positionning of objects is not so obvious as we will develop in the next chapters.

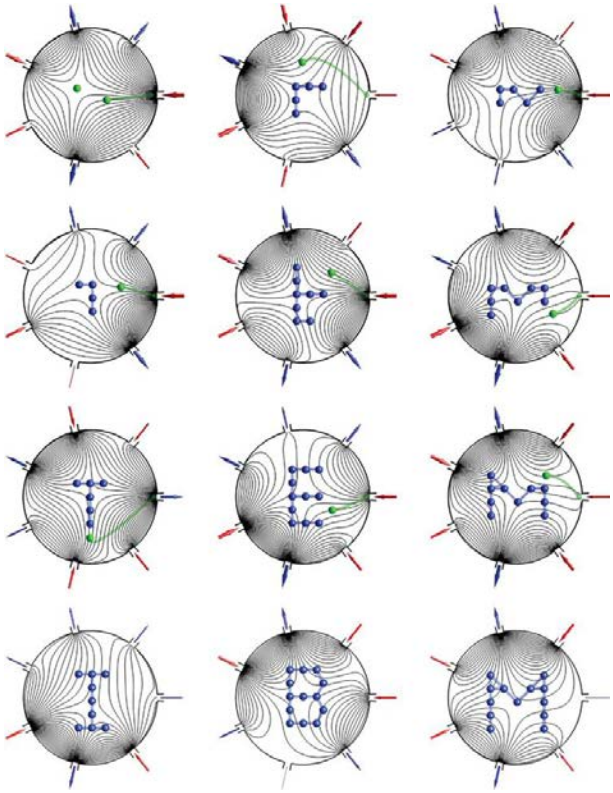

Figure 1.32: Sequentially particles are added to form aggregates of arbitrary shape. The three columns present snapshots along the assembly of three example structures presented in the last row. The required time variations of the 7 controlled flow rates are computed a priori. Figure adapted from [197].

1.3 Hydrodynamic interaction between droplets

1.3.1 Characteristics of flow

It is important to give some basics to the reader concerning microfluidics fluid mechanics for the comprehension of topics presented in the next part.

The governing equations for hydrodynamics in general and microfluics in particular are derived from the fundamental equations describing the rate of change of the flux densities of mass, momentum and energy [198]. The Navier-Stokes equations [199] [200] [201] [202][203] describe the motion of fluid substances. These equations arise from applying Newton's second law to fluid motion, together with the assumption that the stress in the fluid is the sum of a diffusing viscous term (proportional to the gradient of velocity) and a pressure term - hence describing viscous flow.

$$\rho[\frac{\partial \mathbf{v}}{\partial t} + (\mathbf{v} \cdot \nabla)\mathbf{v}] = -\nabla p + \eta \nabla^2 \mathbf{v} + \mathbf{f} \tag{1.1}$$

$$\nabla \cdot \mathbf{v} = 0 \quad \text{(incompressibility of fluids)} \tag{1.2}$$

where $\mathbf{v}$ is the flow velocity, p is the pressure, ρ is the density and η dynamic viscosity.

Eq. 1.1 is analogous to Newton's second law with inertial acceleration terms to the left and force terms on the right. The inertial acceleration term on the left consists of local acceleration, $\frac{\partial \mathbf{v}}{\partial t}$, and convective acceleration, $(\mathbf{v} \cdot \nabla)\mathbf{v}$. Local acceleration describes the change in the velocity of a fluid over time at a fixed point in space. Convective acceleration is the change in velocity as fluid moves from one place to another. The force terms consist of $-\nabla p$, the pressure gradient, and $\eta \nabla^2 \mathbf{v}$, the viscous effects. $\mathbf{f}$ represents body forces such as gravity and electrical forces. Eq. 1.2 is the continuity equation, obtained by assuming an incompressible fluid where ρ remains constant in both time and space.

The Reynolds number and the Stokes equation

With the nonlinear term in the Navier-Stokes equation $(\mathbf{v} \cdot \nabla)\mathbf{v}$, it cannot generally be solved analytically. Fortunately, the equation can be greatly simplified under specific conditions such as those found at the small length scales relevant for microfluidic devices.

The ratio between the inertial forces ($\rho(\mathbf{v} \cdot \nabla)\mathbf{V} \sim \rho\frac{v^2}{L}$) and the viscous forces ($\eta\nabla^2\mathbf{v} \sim \eta\frac{V}{L^2}$) defines the Reynolds Number:

$$Re \equiv \frac{F_{inertial}}{F_{viscous}} = \frac{\rho L V}{\eta} \tag{1.3}$$

The characteristic length L is a length scale that characterizes the system and V is often taken to be the average velocity. Re is a dimensionless number which can be ubiquitously used to predict whether and when the Navier-Stokes equation can be simplified.

In the majority of microfluidic applications the Reynolds number is not too large. For example, consider the typical flow in my study: with water as the fluid, characteristic channel dimensions in the range 10^{-6}m to 10^{-3}m and characteristic velocities in the range $10^{-6} m \cdot s^{-1}$ to $10^{-3} m \cdot s^{-1}$, Re ranges from 10^{-6} to 1 which signifies that the inertial term can be neglected and Navier-Stokes equation simplifies to the linear Stokes equation:

$$0 = -\nabla p + \eta \nabla^2 \mathbf{v} + \mathbf{f} \tag{1.4}$$

with

$$\nabla \cdot \mathbf{v} = 0 \tag{1.5}$$

Flows in Hele-Shaw cells

In microfluidics the aspect ratio of a rectangular channel can often be so large that the channel is well approximated by an infinite parallel-plates configuration. Hele-Shaw flow (named after Henry Selby Hele-Shaw) is defined as Stokes flow between two parallel flat plates separated by an infinitesimally small gap h that is much smaller than the scale of the variation of the velocity .

The representative situation of these flows is schematized in figure 1.33. The flow goes along the xy plane (parallel to the plates) and the component of velocity normal to the plane of the plates is considered to be zero.

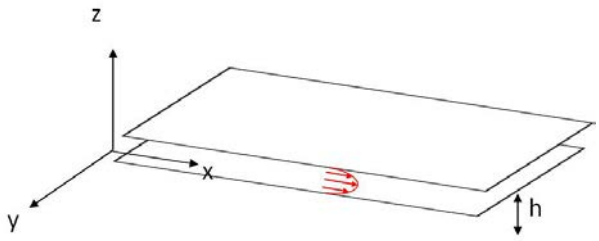

Figure 1.33: Sketch of geometry of Hele-Shaw flows, with the corresponding definition of the adapted system of coordinates.

The approximation of $\partial_z^2 \gg \partial_x^2, \partial_y^2$ (the Darcy approximation), together with the Stokes equation 1.4 leads to separation of variables, $\mathbf{u}(x, y, z) = \mathbf{v}(x, y)f(z)$, such that $f(z) = \frac{3}{2}(1-4\frac{z^2}{h^2})$ is a parabolic Poiseuille profile, and the $\mathbf{v}$ is a vector possessing two components in the planes x and y; which are functions of x and y. This relation is obtained from the equations of motion, in the limits of the Stokes approximation. They are valid in the center of the Hele-Shaw canal (far from the surfaces parallel to the axis Oz). Inserting this expression into the Stokes equation, and averaging along the direction z, we obtain the following relation

$$\mathbf{v}(x, y) = -\frac{h^2}{12\eta}\nabla P(x, y) \tag{1.6}$$

Where P is the pressure and η is the dynamic viscosity. This relation is often known as the 'Law of Darcy'. Such a law shows that in Hele-Shaw flows, the velocity field is derived from a potential proportional to the pressure. One can immediately deduce:

$$\varpi = (\mathbf{rot}\ \mathbf{v})_z = 0 \tag{1.7}$$

The vorticity associated with V is thus null everywhere. There cannot be vortices in Hele-Shaw flows. Applying the conservations of mass, we obtain the following relation:

$$\Delta P = 0 \tag{1.8}$$

showing that pressure is a harmonic function. These properties characterize Hele-Shaw flows, and in many cases allow the determination of their structures in a precise kind simple manner[94].

1.3.2 Droplets transport in fluids

Unconfined droplet in unbounded fluid

The translation of a sphere has been extensively studied. An axisymmetrical flow arises from the motion of a rigid sphere moving with constant velocity through an unbounded fluid otherwise at rest. We suppose that the radius of the sphere is R and that it moves in the positive x direction with velocity U. The problem is most amenable to treatment in spherical coordinates [203][202]. We set, in spherical coordinate, that the velocity U lies along x, thus $\varphi = 0$ and the component of $v_\theta = 0$; v_r and v_φ is independence of φ.

The velocity components of v_r and v_φ are:

$$v_r = Ucos\varphi(\frac{3}{2}\frac{R}{r} - \frac{R^3}{2r^3}) \tag{1.9}$$

$$v_\varphi = -Usin\varphi(\frac{3}{4}\frac{R}{r} + \frac{R^3}{4r^3}) \tag{1.10}$$

This solution is valid in the condition of low Reynolds numbers where the fluid is sensibly devoid of inertia. We note that these rigid spheres perturb the flow around them mediating $1/r$ long-range hydrodynamic interactions. Figure 1.34 shows the streamlines around a moving sphere and that past a sphere.

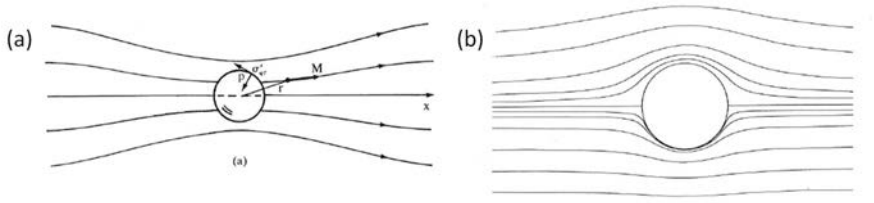

Figure 1.34: (a) Streamlines around a moving sphere at a constant velocity through an unbounded fluid otherwise at rest. (b) The upper part corresponds to streamlines for streaming flow with a constant velocity at infinity past a sphere at low *Re*. The lower part is a comparaison made with streamlines obtained in a potential flow approximation. Figure adapted from [202].

Confined droplet in Hele-Shaw cell

Let's now consider the situation where a sphere is localized between two parallel-plates, i.e. Hele-Shaw cell. Equation 1.6 asserts that the flows from high to low pressure. The pressure defines an effective 2D potential, $\phi(x, y) \equiv (-h^2/12\eta)P$. Together with the incompressibility condition Eq. 1.5, we obtain that the flow in the xy plane is described by the 2D Laplace equation:

$$\mathbf{v}(x, y) = \nabla\phi \tag{1.11}$$

$$\nabla \cdot \mathbf{v} = \nabla \cdot (\nabla\phi) = \nabla^2\phi = 0 \tag{1.12}$$

In this case of an incompressible flow, the velocity potential satisfies Laplace's equation, and potential theory is applicable. A potential flow is characterized by an irrotational velocity field, which is a valid approximation for several applications [204].

It is described by means of a velocity potential ϕ, being a function of space and time. The flow velocity v is a vector field equal to the gradient, ∇, of the velocity potential ϕ [205]:

$$\mathbf{v} = \nabla\phi \tag{1.13}$$

Consider that we have a uniform flow velocity U along x direction corresponding to the case in figure 1.33. We have an uniform flow:

$$\mathbf{v}_x = \frac{\partial\phi}{\partial x} = U = cte \tag{1.14}$$

$$\mathbf{v}_y = \frac{\partial\phi}{\partial y} = 0 \tag{1.15}$$

where

$$\phi = Ux \tag{1.16}$$

In polar coordinate system:

$$\phi = Urcos\theta \tag{1.17}$$

For the velocity potential ϕ that satisfy Laplace's equation, the results induced by all perturbations can be treated as adding simple elementary flows together with a development of multipolar sources (multipole expansion).

In the following part, we will discuss the monopole and dipole. We are first interested in the perturbation related to a flow monopole, shown in figure 1.35. A point source or sink is an infinitesimal region of space from which fluid issues radially in all directions. When the flow is directed inwardly, toward the point, it is termed a sink (Q is the flow quantity; $Q > 0$ for a source and $Q < 0$ for a sink). Point sources and sinks are abstractions which cannot be realized in nature, although they can be simulated more or less closely.

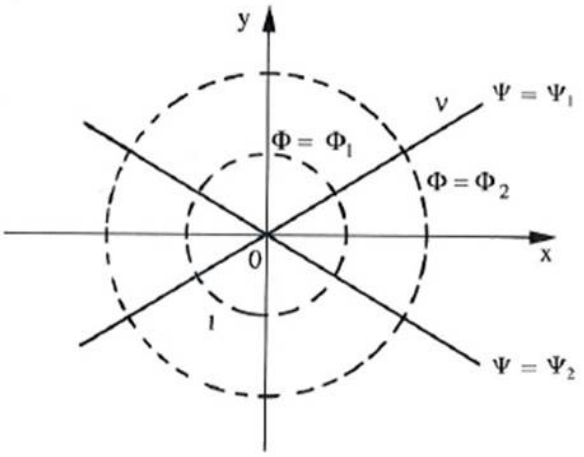

Figure 1.35: The streamlines (φ = cste) and the equal-potential line (ϕ = cste dash line) induced by a point source. Figure from [202].

Since the flow is effectively 2D in the case we consider, we use cylindrical coordinates to describe the situation where an incompressible fluid radiates from the source into an unbounded region at a volumetric flow rate Q. If we imagine a circular envelope of fluid

of radius r, having the source at its center, the radial component of velocity on its surface is given by:

$$v_r(r) = \frac{Q}{2\pi r} \tag{1.18}$$

$$v_\theta = 0 \tag{1.19}$$

Taking account the flow velocity to across a circle with its center at the origin and a radius r, we obtain by integration (Gauss's theorem):

$$\int_c \mathbf{v} \cdot \mathbf{n}\ dl = \int_0^{2\pi} r v_r d\theta = Q \tag{1.20}$$

which gives:

$$\frac{\partial \phi}{\partial r} = \frac{Q}{2\pi r} \tag{1.21}$$

by integration, we have:

$$\phi = \frac{Q}{2\pi} log(\frac{r}{r_0}) \tag{1.22}$$

we obtain the velocity components in this uniform flow field:

$$v_r = \frac{\partial \phi}{\partial r} = U cos\theta \tag{1.23}$$

$$v_\theta = \frac{1}{r}\frac{\partial \phi}{\partial \theta} = -U sin\theta \tag{1.24}$$

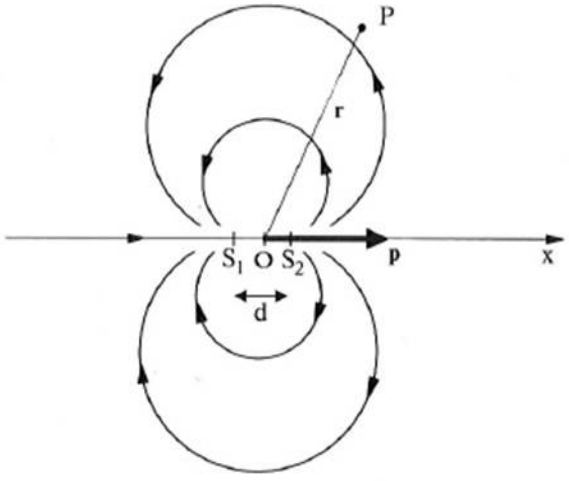

Figure 1.36: 2D Streamlines induced by both a source and a sink of equal flow rate Q. S1 and S2 situated on either side of the x axis at points equidistant from the origin. $\overrightarrow{OP}$= $\mathbf{r}$, $\overrightarrow{OS_1}$= $\mathbf{r}_1$, $\overrightarrow{OS_2}$= $\mathbf{r}_2$. Figure from [202].

Now let's consider a flow dipole which consists a sink S1 and a source S2 having the same flow rate Q with a separation d (see figure 1.36). We suppose that fluid issues from the source S2 at a volumetric flow rate Q and flows into the sink S1 at the same rate. As a

whole, the flow quantity related with this dipolar perturbation is not changed. The dipole moment of the source and sink is defined as | p | = Qd, in the vector form: $\mathbf{p} = Q\ \mathbf{S1\vec{S}2}$.

$$\phi_1 = -\frac{Q}{2\pi} log \frac{|\mathbf{r} - \mathbf{r}_1|}{r_0} \tag{1.25}$$

$$\phi_2 = \frac{Q}{2\pi} log \frac{|\mathbf{r} - \mathbf{r}_2|}{r_0} \tag{1.26}$$

The velocity potential in the position P in the presence of sink S1 and source S2 is the the sum of the two independent values, that is:

$$\phi = \phi_{s1} + \phi_{s2} = \frac{Q}{2\pi}(log \frac{|\mathbf{r} - \mathbf{r}_2|}{r_0} - log \frac{|\mathbf{r} - \mathbf{r}_1|}{r_0}) \tag{1.27}$$

With the logarithm development around r ($|\mathbf{r}| \gg |\mathbf{r}_1|$, $|\mathbf{r}| \gg |\mathbf{r}_2|$ when d $\to$ 0), we obtain the approximation:

$$\phi \cong \frac{Q}{2\pi r}(|\mathbf{r} - \mathbf{r}_2| - |\mathbf{r} - \mathbf{r}_1|) = -\frac{Qd}{2\pi}\frac{cos\theta}{r} = -\frac{pcos\theta}{2\pi r} \tag{1.28}$$

that is:

$$\phi = -\frac{\mathbf{p} \cdot \mathbf{r}}{2\pi r^2} \tag{1.29}$$

we obtain the velocity components:

$$v_r = \frac{\partial \phi}{\partial r} = \frac{pcos\theta}{2\pi r^2} \tag{1.30}$$

$$v_\theta = \frac{1}{r}\frac{\partial \phi}{\partial \theta} = \frac{psin\theta}{2\pi r^2} \tag{1.31}$$

Now, consider the uniform flow velocity U which is perturbated by a droplet of radius R with a cylinder shape. The flow disturbances can be treated as pair-wise additives and therefore the flow perturbation induced by the advected droplet can be written down as a linear superposition of dipolar singularity, we have:

$$\phi = \phi_{uniformflowfield} + \phi_{dipolarflowfield} = Urcos\theta - \frac{pcos\theta}{2\pi r} \tag{1.32}$$

$$v_r = \frac{\partial \phi}{\partial r} = (U + \frac{p}{2\pi r^2})cos\theta \tag{1.33}$$

$$v_\theta = \frac{1}{r}\frac{\partial \phi}{\partial \theta} = -(U - \frac{p}{2\pi r^2})sin\theta \tag{1.34}$$

The figure 1.37(a) shows that a potential flow is constructed by adding simple elementary flows and figure 1.37(b) is the results obtained from the group of R. Bar-Ziv[206].

To satisfy the boundary condition, we should have:

$$v(\infty) = U \tag{1.35}$$

$$v_r(r = R) = 0 \tag{1.36}$$

The first boundary condition is automatically satisfied as the the dipolar field decays as $1/r^2$ (which results in mass-dipole, i.e. source-sink pair). This is in contrast to the far

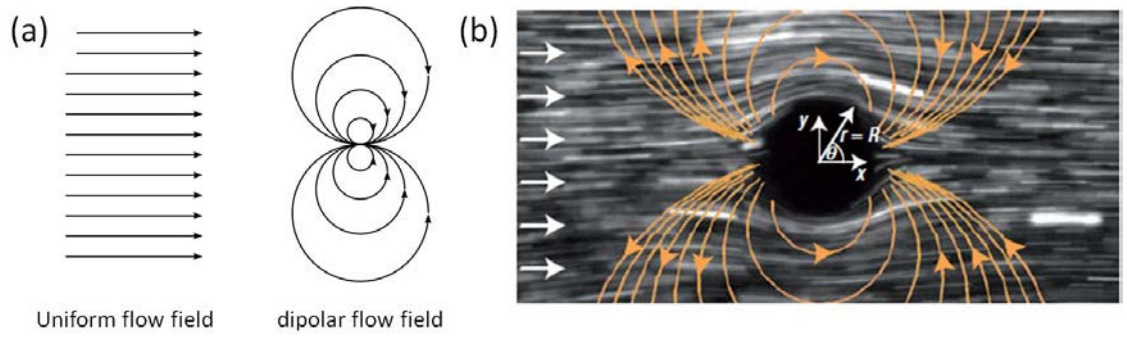

Figure 1.37: (a) A potential flow is constructed by adding simple elementary flows (uniform flow + dipolar flow) and observing the result. (b)The flow field of the carrier fluids and a droplet was visualized by fluorescent micro-beads immersed in the carrier fluids. The flow was from left to right. The beads appear as lines due to the camera exposure time, thereby illustrating the flow streamlines. Superimposed is the dipolar flow field induced by the droplet's perturbation to the flow. The dipolar field was calculated using the unconfined single-droplet potential. Figure from [206].

flow field of any small particle moving in an unbounded 3D viscous fluid, which decays as $1/r$ [207]. The dipolar flow pattern is depicted in figure 1.38(b), where it is contrasted with the flow in an unconfined medium (in figure 1.38(a)).

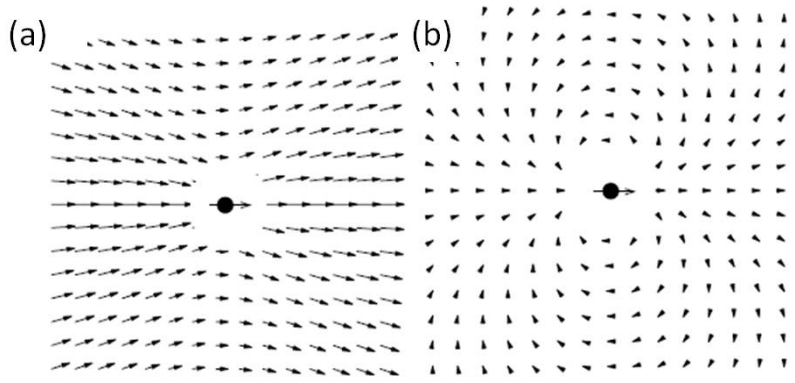

Figure 1.38: Flow velocity field away from a particle moving to the right (indicated by circle and arrow at the center), in (a) unconfined liquid (similar to figure 1.34 (a)) [203] and (b) liquid confined between two plates. Figure from [207].

The second boundary condition gives:

$$-\frac{p}{2\pi R^2} = U \tag{1.37}$$

That is :

$$\phi = Urcos\theta(1 + \frac{R^2}{r^2}) \tag{1.38}$$

1.3.3 Interaction between two or more droplets

The simplest ensemble is a train of droplets which is analog to one-dimensional crystal.

Beatus and co-worker have investigated this many-body effect using a microfluidic water-in-oil droplet generator [206] [208] [209]. Water droplets are formed at a T-junction. They produced an ordered array of droplets with radius R and constant distance a along x between adjacent droplets (figure1.39 (a)). The droplets were deformed into discs-shape and their motion was confined to 2D with friction with the floor and ceiling. They reported the emergence of collective normal vibrational modes (equivalent to acoustic 'phonons') at low Reynold's number ($\approx 10^{-4}$). The microfluidic droplet crystal exhibited longitudinal and transversal fluctuations (figure (b)-(e)). The wave dispersion relation is made by tracking the positions of droplets in time and applying a Fourier transform to obtain the power spectrum of vibrations in terms wavevector k and frequency ω.

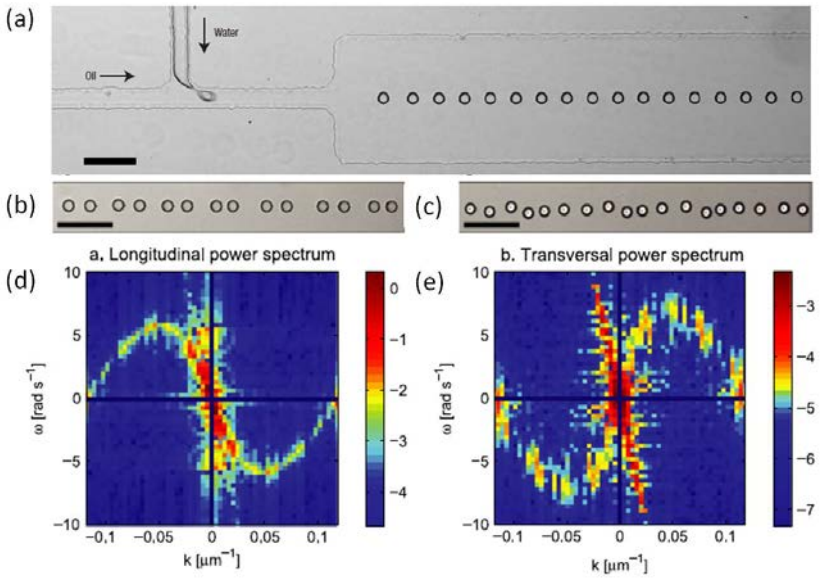

Figure 1.39: (a) A microfluidic device for generating a 1D flowing crystal of water-in-oil droplets. Uniform droplets form at the T-junction. (b), (c) Images of transversal and longitudinal acoustic waves. (d), (e) Intensity plot of the logarithm of the power spectrum of longitudinal and transversal waves as a function of wavevector and frequency (k, ϖ). Figure adapted from [206] [208] [209].

This phonons propagation gives rise to a variety of cristal instabilities. Beatus et al. identify three types of them, including **'surface' melting instability**, **zigzag instability** and **1 + 3 instability**. The two former instabilities are induced by the asymmetry at the droplet formation. Far enough from the formation zone, the crystal can be treated as approximately infinite, however, it is not the case of if droplets are located near T-junction.

The **'surface' melting instability** occurs at the droplet-formation zone on abruptly cutting the crystal by stopping water flow while maintaining oil flow. The drifting crystal then exhibits a wandering motion in the transversal direction and a longitudinal pairing wave that advances from the crystal trailing end (figure1.40 (a)). The **zigzag instability** occurs close to the droplet-formation zone as the crystal bifurcates into two parallel crystals (figure1.40 (b)).

Different from the instabilities caused by droplet formation, the **1 + 3 instability** is a local fluctuation which grows in the middle of the crystal, far from the T-junction. This phenomenon is frequently observed in experiments: as the crystal was flowing downstream from the droplet-formation area, phonons amplitude increased in time. The nonlinear effects of the dipolar interaction become significant. Interestingly, in most experiments,

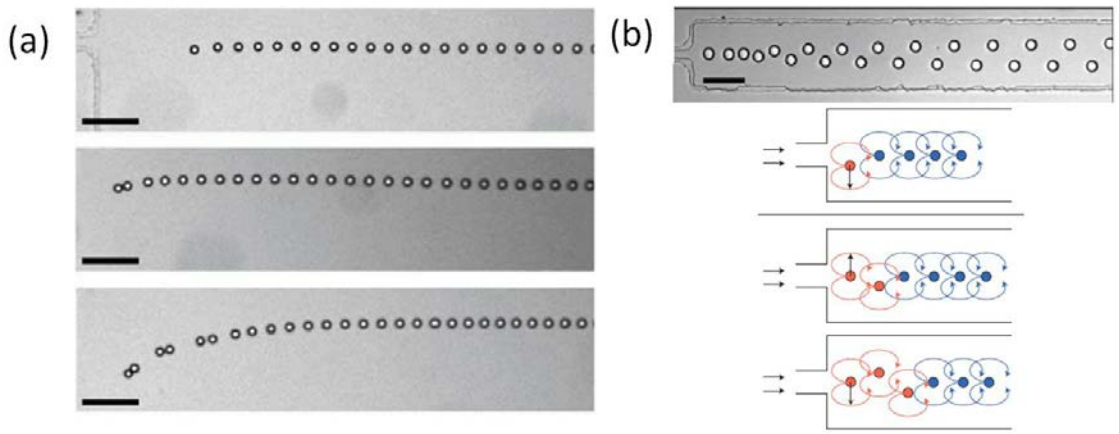

Figure 1.40: (a) Crystal 'surface' melting instability at the tailing edge that occurred upon stopping droplet formation and maintaining the flow of oil. The instability appeared as a longitudinal pairing wave and wandering motion in the transversal direction. Scale bars, 100 μm. (b) (Top): Zigzag instability close to the droplet formation area. Scale bar, 100 μm. The asymmetry at the trailing end of the crystal makes it a source of zigzag waves. (Bottom): The scheme shows a small deflection of the trailing (orange) droplet that increases due to transient force imbalance near the formation area. When the next droplet emanates, it is pushed in the opposite direction, and so on (arrows mark transversal forces). Figure adapted from [206] [208] [209].

this local fluctuation had a distinct structure of a single droplet followed by an oblique row of three droplets. The authors argue that it is essentially a result of a non-linearity, which arises both from the large amplitude and from the interaction between longitudinal and transversal modes (see figure 1.41).

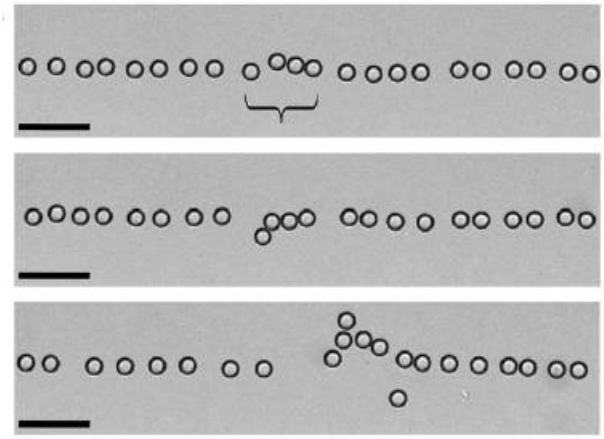

Figure 1.41: Subsequent images showing crystal breakup process with 1+3 instability, taken 0.3 s apart, of a local fluctuation in a 1D crystal (1 + 3 droplets, marked). The fluctuation grows and leads to crystal breakup. Scale bars, 100 μm. Figure adapted from [206] [208] [209].

1.4 Conclusion

We have overviewed the state-of-art of recent achievements and developments in the field of anisotropic clusters for colloidal assemblies. In particular, the synthesis of 'colloidal molecules', i.e. clusters of spheres with shapes resembling space-filling models of simple molecules, are highlighted. This brief survey has been followed by a general introduction to the microfluidics, because the microfluidic technologies has a great potential in the synthesis and assembly of such clusters (anisotropic elementary objects) with various advantages compared with traditional synthetic approaches. We also give a theoretical background related with the microfluidics concerning on the transport of objects (droplets/particles).

The next chapters are organized as follows:

The second chapter presents our strategies and microfluidic techniques to produce a small number of droplets in a periodic way. The basis of the microfabrication is given and different experimental approaches have been explored to elaborate droplet clusters using various microfluidic techniques, including valves, sorters, T-junction and step emulsification droplet generators combination.

The third chapter is dedicated to an experimental and theoretical study on the dynamics of a small number of droplets moving in Hele-Shaw cells with the help of externalized microfluidic pneumatic valves. A quantitative study is carried out on the interaction of the droplets confined in the microfluidic channel. The motion of the droplets induces dipolar flow field. This rich dynamical mechanism enlightens us to assemble droplets in a smart way.

The fourth chapter presents a novel approach to assemble droplets into clusters assisted with the hydrodynamic interaction. By the use of microfluidic devices with a T-junction combined with a step emulsification generator, the droplets can be directly assembled into clusters in a reproducible manner within Hele-Shaw microfluidic channel. Various morphologies of clusters have been observed. Theoretical and numerical study are also carried out to investigate the self-assembly mechanism.

The thesis ends with a chapter displaying perspectives towards more complex clusters. Many strategies have been successfully demonstrated to render the clusters more stable and more complex. We identify three directions: towards sticky clusters, hybrid clusters, magnetic and non magnetic clusters as well as solidifying clusters.

Chapter 2

Experimental techniques

2.1 Introduction

This study starts with the observations made in MMN's laboratory using nano/microfluidic devices by Malloggi et al. The feasibility of assembling simple droplets into clusters directly within the nano/microfluidic devices was demonstrated. With a step emulsification device, Malloggi et al. generated a train of droplets of colloidal size and observed local aggregation of droplets downstream of the reservoir channel [15].

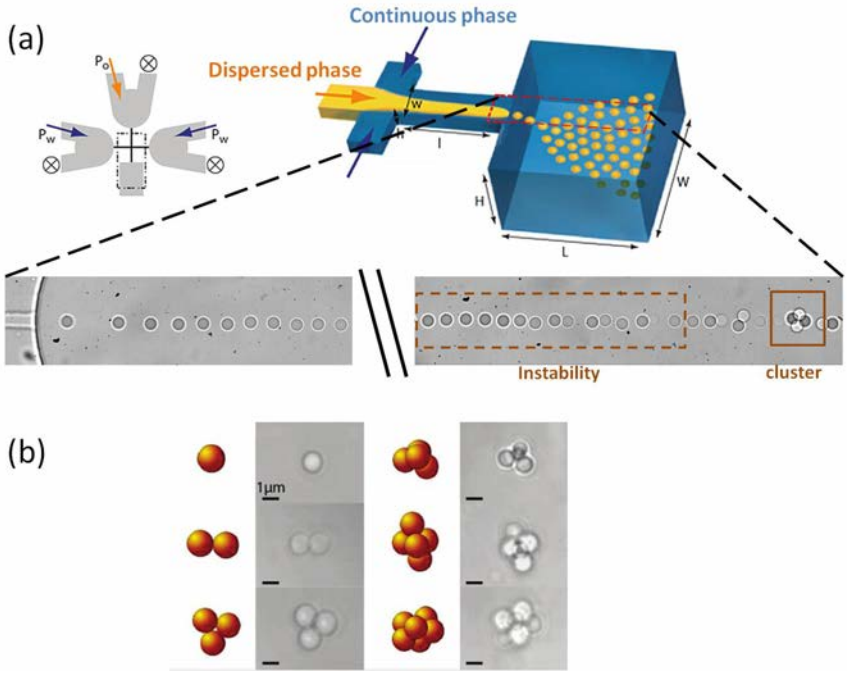

Figure 2.1: (a) Schematic illustration of a step-emulsification device. The immiscible fluids (oil (yellow) and water (blue)) are driven into U-turn microchannels (the "rivers") under fixed pressure differences. They meet in a terrace and flow into a reservoir, generating droplets. Zoom over the step area: optical micrographs of the droplet transport are shown near the step and 200 μm away from the step. An instability develops downstream and aggregation of droplets is observed. (b) Elementary clusters produced in the microfluidic system and the corresponding theoretical models [210]. Figure adapted from [15].

The experimental system of this study is sketched in figure 2.1 (a). The device includes

a nanofluidic (i.e., submicrometric) section that comprises a cross junction and a terrace connecting to a profound reservoir channel. The inlets of the nanochannel section are U-turn microchannels (rivers), along which pressure differences are imposed. Small fractions of the flows driven along these rivers are driven into the nanofluidic section. The design of the inlet channels allows us to impose well-controlled pressures at the nanofluidic section entries while avoiding dust accumulation, which causes damageable system clogging. In the nanofluidic part, the dispersed phase (yellow) meets with the continuous phase (blue) at the cross junction. In certain regimes, a train of droplets is produced, which is analogous to the one-dimensional crystal. Phonon-like instability is observed, as shown in figure 2.1 (a). This 1D cristal undergoes an instability similar to that described in Chapter 1. The droplets in this study have 4.6 μm in diameter and the height of the reservoir channel is 10.3 μm, thus the droplets occupy nearly half of the channel (R/h $\approx$ 0.5). Although they are not as confined as the case in the study of Beatus et al., [208] in which the droplet diameter is 20 μm and the channel height 10 μm, which gives R/h = 2, the 1 + 3 instability, a local fluctuation in the middle of the train is well observed. The aggregation of droplets in the downstream region leads to clusters formation. In this figure 2.1 (a), a tetrahedron droplet cluster is formed spontaneous which is highlighted with a red frame. When the flow is stopped abruptly, various assemblies of droplets depicted in figure 2.1 (b) are obtained, which correspond well to theoretical models[210].

However, this phonon-like instability takes place in a spontaneous way and is very sensitive to the perturbations of the flow conditions. It has not been possible to obtain monodisperse populations of such clusters with the present experimental system. Obtaining homogeneous populations of clusters requires the addition of a functionality to the chip.

2.2 Principal idea developed in this thesis

Our idea is to generate, in a discontinuous manner, periodically a small number of droplets instead of a train of droplets continuously. It is desirable that the assembly process is re-programmable and deterministic. The complexity of instability is reduced when it involves only a small number of droplets, thus we have better chance to control their assembly process. Finally, once clusters are formed, a second operation such as cross-linking, is necessary for them to be able to maintain their shapes.

In Chapter 1, we have briefly introduced the commonly used microfluidic droplet generators: coaxial, T-junction, flow focusing and step emulsificaton devices. Such droplet generators are classified as 'passive approach'. Those methods take advantage of the characteristic flow field in microfluidics to control the interface and capillary instability, and consequently to produce droplets. Although highly monodisperse and reproducible, with simple geometrical designs, they are not able to generate a small number of droplets periodically.

Some additional functionality integrated to the microfluidic droplet generators have been taken under consideration in order to achieve the periodic production. The existing drop-on-demand techniques include the use of valves [175] [176] [179][181] [183], piezoelectric actuators [211] [212], electrowetting [213] etc. Those methods are named as 'active approach'. Active elements allow for a more flexible droplets generation in an extended size range.

In this PhD study, we investigated the use of electrodes and externalized pneumatic valves to generate a small number of droplets periodically. Apart from the 'active approach', we also succeed in producing a small number of droplets in a reproducible man-

ner by coupling two 'passive' droplet generators. Those three approaches are illustrated in figure 2.2.

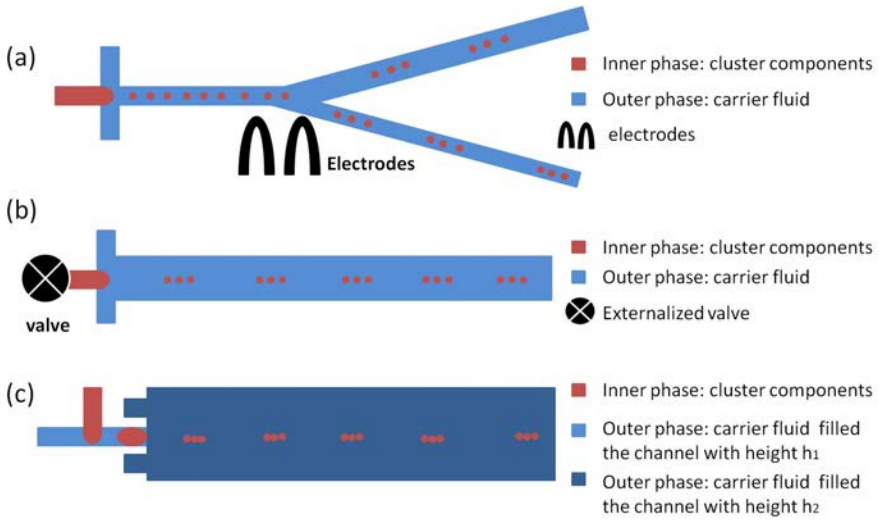

Figure 2.2: Periodical generation of 3-droplet clusters. (a) Using electrodes sorting device. When the droplets in a train flowing in the main channel arrive at the 'Y' junction, they are either directed to the upper channel or the bottom channel by groups of three.(b) Using device including externalized valves. The valve imposes an interruption of the droplet passive production (Flow focusing geometry is used in this illustration. However it works for other types of droplet generators). (c) Using device coupling T-junction and step emulsification production. Details of droplet generation mechanism will be given in Chapter 4 on cluster production part.

Once a precise small number of droplets are generated, we are interested in understanding the instability, that is the dynamics interactions between the droplets. The question arises, whether droplets could aggregate into clusters in a deterministic manner through the interactions. If so, in the following step, we would like to facilitate the 'bonding' between the elementary units. This research work aims to provide a versatile approach to produce clusters with the following features:

1. Morphology yield. The clusters synthesized are expected to have a good monodispersity for a given morphology.
2. Versatility. Through different control parameters, this approach is desired to have a rich accessible morphologies.
3. High-throughput. This approach should be able to produce large quantity of clusters in a short time to meet the industrial processes requirement.
4. Tunability. The properties of the clusters obtained should be tunable in terms of the size domain, shape, chemical composition variety etc. (as we have described in the Chapter 1 on anisotropy dimensions part).
5. Robustness and scalability. This approach should be reproducible and allows for scale up by means of parallelization of microfluidic systems for instance.

The following part will be organized as follows. We begin with recalling the basis of the microfabrication principle. Then we present preliminary results of 'discontinuous' production using electrodes and valves (figure 2.2 (a) (b)). The comparison of the two results is made, which leads us to adopt valves control to study the dynamical interaction

between a small number of droplet (Chapter 3). With the understanding in dynamics of a small number of droplet moving in Hele-Shaw cells, the results using two droplet generators coupling are presented and further interpreted in Chapter 4. The cluster 'bonding' issue is addressed in Chapter 5 in which we try to render the clusters more stable and complex.

2.3 Microfluidic device fabrication

A standard photolithography and rapid prototyping of microfluidic systems are introduced here. The whole microfabrication procedure includes design and fabricate (including sealing) microfluidic systems in an elastometric material, Poly(dimethylsiloxane) (PDMS).

Despite PDMS has many advantages (cheap, disposable, transparent etc.), its low elastic modulus sometimes becomes a significant issue for theoretical study. For example, its deformation makes it difficult to accurately predict the flow rates and flow profile in Hele-Shaw cells.

In our study, shallow microfluidic channels with high aspect ratio are often used. In order to avoid this inconvenience, in particular for droplet dynamic interaction study, we exploit also another polymer, Norland Adhesive 81 (NOA81), which has higher rigidity, to prototyping the microfluidic systems, as complementary to PDMS.

2.3.1 Fabrication of Silicon Master

Lithography masks are designed by CleWin4 and printed with high resolution (at least 3600 dpi) according to critical dimension of the design. The fabrication of silicon master is carried out in the clean room of MMN laboratory in ESPCI. The photoresist (SU8 20XX series, Microchem) is spincoated on a pre-cleaned silicon wafer and a soft bake is performed according to the manufacturer's specifications in order to remove the solvent. By varying of SU8 solvent content (viscosity) and spinning speed, the desired film thickness of the photoresist could be achieved. The desired microstructures are transferred from the mask to the photoresist by UV exposure on a mask-aligner at wavelentgh of 365 nm. After exposure, the wafer is further cured by the post-bake step in order to cross-link the exposed SU8 areas. The non-exposed SU8 areas will be removed by the developer solvent in the developing step. Final dimensions of the fabricated structures are verified with a mechanical profiler (Dektak) or an optical profiler(Veeco wyko NT9100).

The fabrication of multi-layer silicon master is based on the accumulation of single layer with alignment of microstructures. The main fabrication steps are as follows: with the UV exposure through mask 1, the first layer of microstructures is transferred to the photoresist; a second layer is achieved by the same way after an alignment of mask 2 with the structures of the first layer. The figure2.3 illustrates the fabrication process.

2.3.2 Fabrication of PDMS (Poly(dimethylsiloxane)) Systems

PDMS devices are cast from the silicon master by pouring liquid mixture of PDMS monomer (Sylgard or RTV) and 10 wt% of crosslinker onto the master and allowing for curing at elevated temperatures (70°C) for hours. The cured, solidified PDMS is then peeled off from the master. Inlets and outlets holes are punched. We plasma-bond the PDMS part to microscope glass slides to enclose the microfluidic system. Plasma oxidation has two effects. One is when the two oxidized surfaces are brought into conformal contact, an irreversible seal is formed between them. Another effect is that, silanol (Si-OH) groups introduced onto the surfaces will render the microfluidic devices hydrophilic.

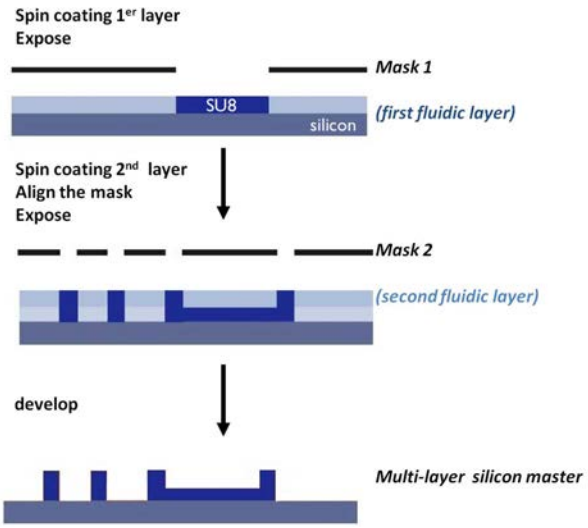

Figure 2.3: Double layer fabrication process.The multilayer structures are constructed through layer by layer exposition and alignment operations.

Sometimes we wish to have a homogenous device with all PDMS channels, especially in the case of hydrophobic systems. To make such devices, the PDMS upper part is prepared as usual and the substrate, the microscope glass slide, should be first spincoated with the liquid mixture of PDMS monomer and crosslinker following an independent curing before bonding. Once the two parts are enclosed, the systems should be placed in the oven for one day at 95°C so that they recover hydrophobicity. The general PDMS device fabrication process is shown in figure 2.4.

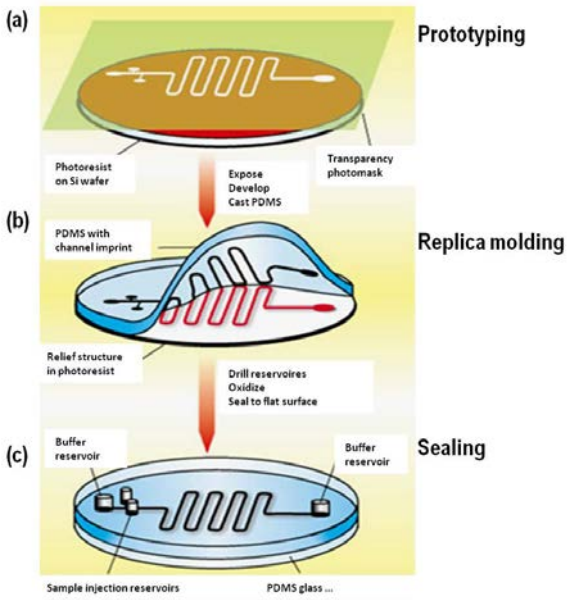

Figure 2.4: General process of PDMS device fabrication. (a) Fabrication of silicon master: Desired structures are transferred to photoresist on silicon wafer via photolithography. (b) Cast from the silicone master transfers the embossed master structures as grooves to the PDMS device. (c) PDMS device is bonded against a flat counterpart in order to create enclosed microfluidic structures.

2.3.3 Fabrication of NOA (Norland Optical Adhesive 81) Systems

Norland Optical Adhesive 81 ('NOA 81') is a commercial product, made of single component liquid adhesive that cures in seconds to a tough, hard polymer when exposed to ultraviolet light. The stickers are made by soft imprint lithography. We fabricate NOA devices following the protocol described below: a PDMS mold is made from the master as described above, then this PDMS mold is in turn used as a template to produce a PDMS stamp. After using the plasma to activate the surface, we expose the PDMS mold to gaseous 1H,1H,2H,2H-perfluorooctyl-trichlorosilane for hours in a sealed container to make sure that the PDMS layers do not permanently bond during the UV curing process afterward. This PDMS mold is placed in a vacuum to degas for at least 2 hours. The structured PDMS stamp is then gently pressed onto a drop of Norland Optical Adhesive 81 (NOA 81, Thorlabs) before exposure to a UV lamp (exposure for 7 seconds at a power of 6.5 mW cm^{-2}). A thin layer of glue remains uncured on the surface due to the presence of oxygen. The presence of oxygen inhibits the free radical polymerization due to the fact that the growing chain will react with molecular oxygen, producing an oxygen radical, which is much less reactive, thus the reaction is slowed down significantly. This inhibition allows the device to be sealed with a glass slide after a second exposure to a UV source (exposure for 30 seconds at a power of 25 mW cm^{-2}).

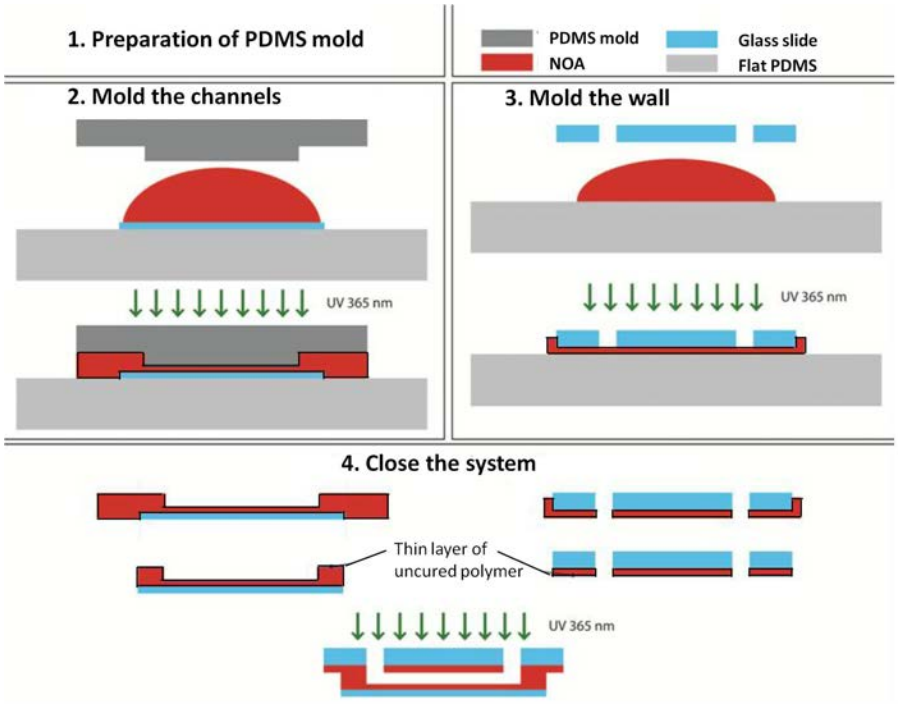

Figure 2.5: The process of microfluidic sticker NOA device fabrication which consists in four steps: preparation of PDMS stamp, mold the channnels, mold the wall and sealing of the system. Figure adapted from doctoral dissertation [214].

2.4 Attempt to use microfluidic sorters based on electrodes

Microfluidic flow sorting systems enable us to actuate the trajectory of the transported objects (cells, droplets and particles etc.) in inexpensive, efficient and reliable way. Several approaches have already been demonstrated, including deterministic lateral displacement

[215], hydrodynamic filtration [216], dielectrophoresis [217], acoustophoresis [218] [219], optical force [220].

Many microfluidic sorting devices exploit dielectrophoretic forces that depend on the volume and dielectric contrast of the sorted objects and the continuous medium. Such sorting device functions as follows[221] : the droplets are evenly spaced and periodically injected into the device forming a train. They flow to the asymmetric 'Y' sorting junction, where they can take one of two paths. Droplets flow into the wider channel by default due to its lower hydraulic resistance. When a pulse of high-voltage alternating current (AC) is applied across the electrodes adjacent to the sorting junction, the droplets are deflected into the narrower channel of the junction by dielectrophoresis (see figure 2.6). One well established application based on this dielectrophoretic (DEP) sorting is the fluorescence-activated droplet sorting (FADS) [95] [221] where a laser detection is integrated which focus on the channel at the gap between two electrodes.

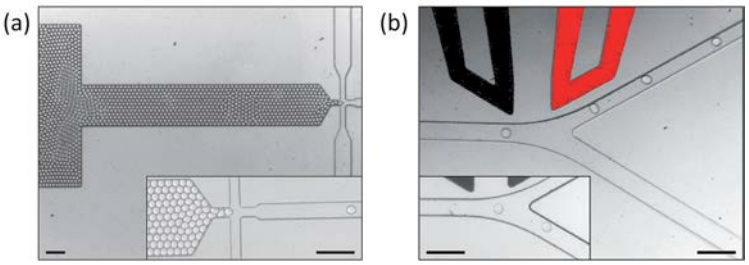

Figure 2.6: (a) A monodisperse emulsion is injected into the sorting device. The inset image shows the emulsion droplets being spaced-out with more carrier fluid. Scale bar, 1 mm. (b) Trajectories of droplets stream through the sorting junction. When an AC electric field is applied across the electrodes, the droplets are deflected into the narrow arm. In the absence of a field, the droplets flow into the wider arm owing to the lower hydraulic resistance (inset). Scale bar is 100 μm. Figure adapt from [221].

For our application, we search to deflect periodically a small number of droplets into one channel as shown in figure 2.2 (a). Based on FADS, a simplified microfluidic sorting device is made by suppressing the fluorescence laser detection system since there is only one population of droplets generated with a flow focusing junction. An additional continuous phase inlet is located in the main channel helping to space the droplets when they enter the sorting channel. The design of our system is shown in the figure 2.7.

We make PDMS microfluidic devices using standard soft lithographic methods. We design electrodes as channels within the PDMS device located in the proximity of the asymmetric 'Y' sorting junction. In the conventional approach, metallic electrodes are fabricated by injecting liquid solder into microfluidic channels, and allowing the solder to cool and solidify. This method is named 'microsolidics' [222]. We have used this technique in the beginning of our study to elaborate the microfluidic droplet sorters. We also explore another alternative method to elaborate liquid electrodes by replacing the solder by highly concentrated electrolyte solution. Thought the Electrowell, a multiple channels accessory, we can apply a voltage to liquids injected in microfluidic chips. This device imposes a difference of potential at the terminals of a microfluidic circuit. Using liquid electrodes, although the electric field has not been fully characterized, this technique provides an easier and efficient method of the electrode fabrication.

We verified that this simplified microfluidic droplet sorter deflects efficiently the droplet of interest into the desired channel. Figure 2.8 shows that in the absence of external force, the droplet flows into the upper channel owing to the lower hydraulic resistance (Channel

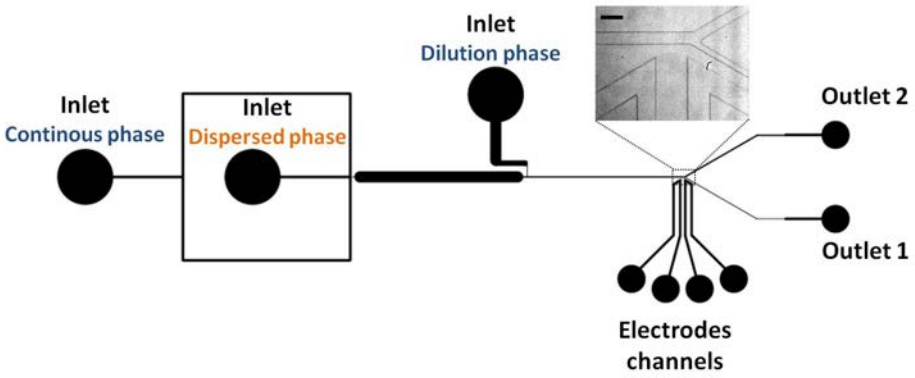

Figure 2.7: Sketch of the design of microfluidic device integrated with electrodes channels close to the asymmetric 'Y' junction. Inset showing that Outlet 1 is the channel with higher hydrodynamic resistance and Outlet 2 with lower resistance (Channel width$_{upper}$ > Channel width$_{bottom}$). The droplets flow into this branch only in the presence of an electric field. Scale bar is 30 μm.

width$_{upper}$ > Channel width$_{bottom}$). Whereas if the electric field is turned on, the droplet is directed into the narrow channel by dielectrophoresis.

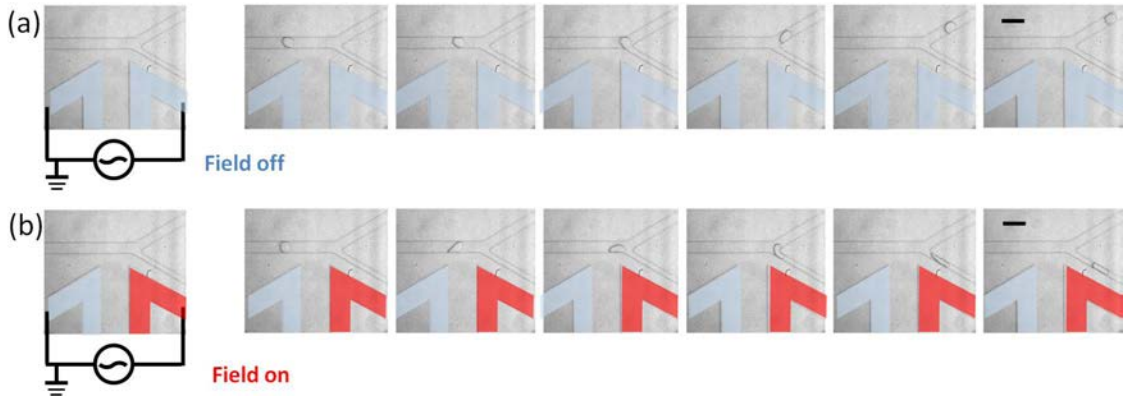

Figure 2.8: (a) When the electric field is switched off, droplet flows along the upper channel because of low flow resistance. (b) When the electric field is switched on, the droplet is driven in the the lower channel of the branch. Scale bar is 30 μm. The artificial added color is used to indicate the different states of electrodes.

We are able to program the number of cycles and the voltages applied to the electrodes to synchronize the arrival of droplets depending on flow rates, droplet size and droplet rate. In the example in figure 2.9, we could drive periodically a short train of four droplets into the narrow channel. Cycles of 1 KHz single-ended square waves are sent to the electrodes over 2 seconds. The voltage across the electrodes is 3 V_{p-p} which is amplified by a factor of 100 by a high-voltage amplifier(Trek). The cycle is repeated every 9 seconds.

To conclude, the electrode sorter provides an effective way to produce periodically a small number of droplet. However, there are some limits in this method. First of all, in order to evenly space the droplets (which is critical for periodically deflection), the train of droplets should be confined in the main sorting channel. This condition imposes that droplet size is determined by the geometrical parameters and there is not much room to tune the droplet size as we wish. Secondly, the synchronization between the arrival

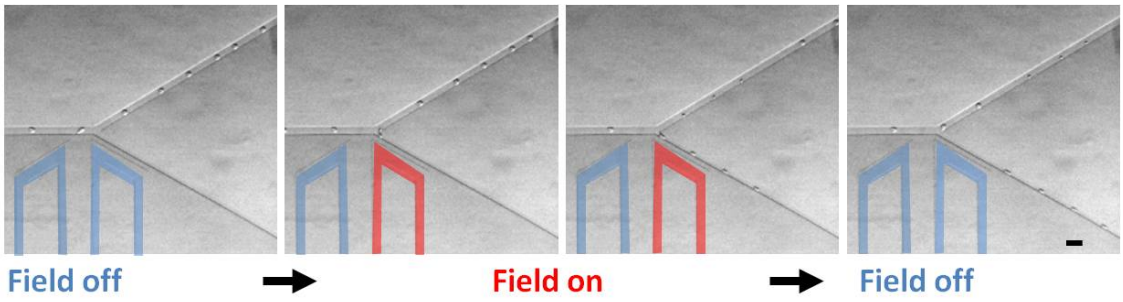

Figure 2.9: A train of droplets is flowing in the microfluidic channel. In the presence of the electric field, a small number of droplets (N = 4 in this example) is directed and sorted. Scale bar is 30 μm. The artificial added color is used to indicate the different states of electrodes.

of the droplets and the electrode working circles should be adjusted every run according to experimental conditions. As a consequence, the control over droplet spacing and the number of droplets to be deflected each time is time-consuming. Thirdly, this sorting mechanism is fluid dependent and it requires dielectric contrast between the sorted objects and the continuous medium. We cannot manipulate easily oil droplets in aqueous solution for example.

Microfluidic externalized pneumatic valves, on the other hand, offers a more flexible control over parameters such as droplet size, spacing and number as we will see. Furthermore, the working mechanism of this active control is fluid independent.

2.5 Microfluidic externalized pneumatic valves

The fluid flow in a microchannel can be controlled with the help of microvalves. By taking advantage of the elasticity of PDMS [223], the actuation of the valves for the microfluidic application can be realized with the pneumatic deformation. The fluidic channels can be closed at a precise location where an external force is applied to pinch the channels.

Among all the microfluidic valves made with elastomeric materials, Quake valves are the most commonly used. The Quake valve is a multilayer microfluidic structure, consisting of a flow channel in one layer separated by a thin elastomeric membrane from a (usually perpendicular) control channel in the layer above. The flow channel must have a rounded profile to enable the valve to close completely during actuation. The schematic of a PDMS pneumatic microvalve is shown in the figure 2.10 (a). However the Quake valves is designed for densely packed networks and complex on-chip integrated functionality. A generic device based on Quake valve to control the droplet production has been developed by Galas et al.[224]. With an active microfluidic connector, which includes a single pneumatic Quake valve, the flow of the dispersed phase can be regulated as follows. When the valve is open and then closed, a single drop is produced and the size of this drop is controlled by the opening time of the valve. The size of the droplet can be tuned by the opening time of the valve and the spacing between the droplets can be adjusted by the waiting time of the successive opening, as shown in figure 2.10 (b).

We adopt this drop-on-demand technique to produce periodically a short train of a small number of droplets (see figure 2.2 (b)). The externalized valves are stuck to a glass slide and the working fluid (dispersed phase) flows from the fluidic channel in the

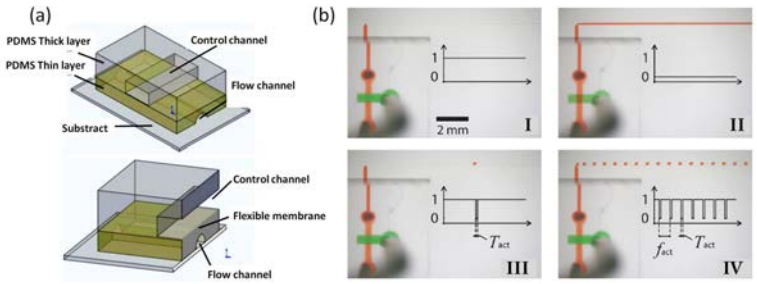

Figure 2.10: (a) The control channel passes over the flow channel. Pneumatic/hydraulic pressure in the control channel flattens the membrane valve downwards to create a seal. (b) Four pictures of the same drop-on-demand device for various actuation signals applied to the externalized valve. An aqueous solution of orange dye is injected at a T-junction in a straight channel filled with mineral oil. The valve is actuated by pressure pulses in the controlled channel (filled with water and green food dye). On each picture, the graph shows the variations of the actuation pressure with time. (I) Valve closed: the water does not flow. (II) Valve open: stable coflow of water and oil. (III) The valve is open over a time $T_{act} = 50$ ms: a single drop is produced. (IV) The valve is open periodically over a time $T_{act} = 50$ ms: a monodisperse emulsion is produced. Figure adapted from [224].

valve to the inlet of the microfluidic systems through the tubings (see figure 2.11). We can place up to four valves in one glass slide. The externalized valve may be connected to any microfluidic droplet generators, such as T-junction, flow focusing etc, as shown in the figure. A Labview program is developed which allows the monitoring of up to three independent valves simultaneously in my study.

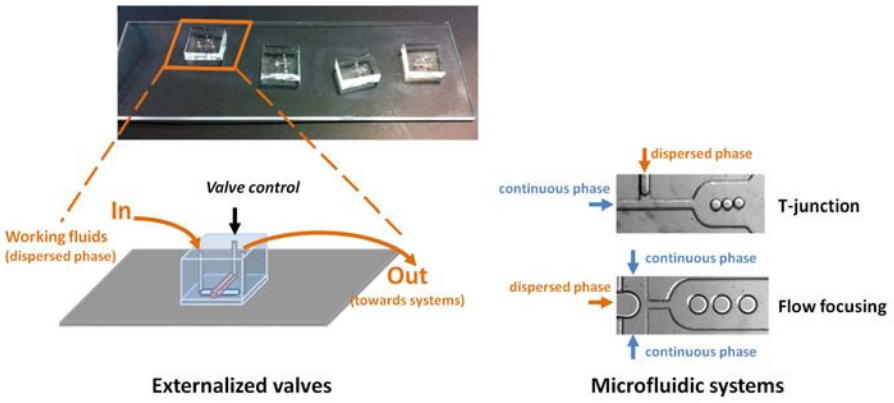

Figure 2.11: Photograph of four two-layer externalized valves on a glass slide. The working mechanism is shown in the illustration. The working fluid (dispersed phase) is flowing into the fluidic channel of the valve and flowing out into dispersed phase inlet of droplet generator (T-junction or flow focusing on the right as examples). The fluidic channel can be closed when control channel located on the top is under pressure.

The figure 2.12 below shows examples of the control over the production of droplets. In each actuation circle, a precise control is achieved in term of droplet size, spacing and number. In the examples shown in the figure, drops of fluorinated oil are produced in water with SDS as surfactant. The typical pressure of dispersed phase and continuous phase is in the order of tens mbar, and that of the control channle pressure is 1.5 bar. The opening time of valves is in the range between 10ms to 100ms.

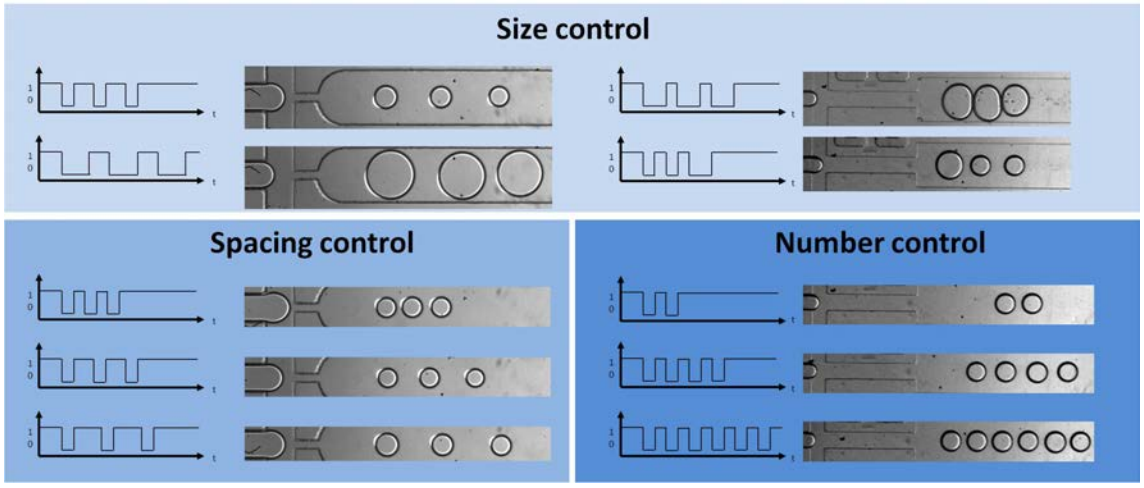

Figure 2.12: Pictures showing externalized valve control. The connected microfluidic systems are flow focusing droplet generators, the geometries are various (with constriction on the left and without on the right). Using various actuation signals applied to the valve, a precise control over the droplet size, spacing and number is achieved.

2.6 Conclusion

In this chapter, we first present the past experiment observations concerning the cluster synthesis which motivates this Ph.D. study. Inspired with the results from the paper of Malloggi et al. [15], we would like to gain an overall control on the cluster synthesis using microfluidic techniques. In order to better understand and control the droplet clustering process, we develop strategies to generate periodically a small number of droplets by using both 'active' and 'passive' droplet generation methods. After recalling the basis of the microfabrication principle, we investigate and compare two 'discontinuous' droplet production methods using electrodes and valves. Despite the electrode sorter provides an effective way to produce periodically a small number of droplet, it has certain limitations, such as fluid dependent working principle, which makes it inadequate for the further study. Externalized pneumatic valves offer us a better control over the drop-on-demand production in terms of droplet size, spacing and number etc. The valves are used as a tool to study the dynamical interaction between a small number of droplet moving in Hele-Shaw in the next chapter.

Chapter 3

Dynamics of a small number of droplets moving in Hele-Shaw cells

We presented in the previous chapter that the use of the external valves could provide an efficient control over the droplets production. We carried out a quantitative study on the interaction of the droplets confined in the microfluidic channel by taking advantage of this technique. Droplets confined in micro Hele-Shaw cells present a rich dynamics. The motion of the droplets induces dipolar flow field. Our goal here is to investigate dynamical mechanism that allows to assemble droplet in pairs, trimers, quadrimers ... in large number.

3.1 Article: Dynamics of a small number of droplets in microfluidic Hele-Shaw cells

This section is mainly based on the article: Dynamics of a small number of droplets in microfluidic Hele-Shaw cells, by B. Shen, M. Leman, M. Reyssat, P. Tabeling, Experiments in Fluids, 55, 1728 (2014).

3.1.1 Abstract

We investigate the dynamics of a small number of droplets (N = 1, 2, 3) in microfluidic Hele-Shaw cells. We study the cases N = 1, 2 and 3 droplets and analyze the influence of the side walls. In the course of the study, we observe spontaneous alignment of droplet pairs, pair exchanges, droplet escape, multiple reflections between walls, i.e. a number of phenomena that have not been reported yet. As a whole, using pairwise far field dipolar interactions between droplets, along with treating the walls as mirrors allow to reproduce the observations, even though limitations in the predictability of the model are pointed out in a few cases. From a more practical prospective, the work shows that the behavior of elementary droplet assemblies can be put under acceptable experimental control in a wide variety of situations, a feature potentially interesting for self assembly, mixing or transport of particles in microfluidic environments.

3.1.2 Introduction

Recent studies have revealed the rich dynamics of systems of droplets and particles (cylindrical and spherical) confined in shallow microfluidic systems, i.e. in micro Hele-Shaw cells. Small amplitude longitudinal and transverse waves [225], along with shock waves

induced by localized jams [226] have been observed in droplet lines. Shocks, pattern formation, dislocations have been observed in 2D populations of droplets [227] [206][228]. In the presence of side walls, oscillatory and chaotic regimes have been calculated and observed [229]. Studies of small clusters have revealed the existence of stable and metastable configurations [229].

The underlying physics of these systems is the following : flattened droplets or particles, confined in Hele-Shaw cells, and subjected to a steady flow, are advected downstream. These droplets, being slowed down by the walls, move at speeds smaller than the upstream velocity. In such circumstances, each droplet generates, in its own frame of reference, multipolar interactions with its neighbors. These interactions give rise to the dynamics revealed in the above references [203][230][202][207][231][232].

Owing to the complexity of the problem, simplifications are currently made in the literature. Most often, the problem is viewed as two dimensional and the interactions treated as dipolar and pairwise [206]. The extent to which these approximations are acceptable for describing experimental situations can be questioned. Higher order interactions may come into play. Lubricating films, flows driven by gradients of curvature, boundary layers close to the walls and in the vicinity of the droplets boundaries may also play a role by conveying 3D perturbations. The goal of the present experiment is to carry out a quantitative analysis of the dynamics of populations including up to three droplets in micro Hele-Shaw cells, and compare the results to the current approximate theoretical modeling. As a whole, the present work shows that the behavior of elementary droplet assemblies is well described by assuming 2D pairwise dipolar far field interactions. Despite this approximation must be taken cautiously, we demonstrate that the behavior of small clusters is predictable within this model when droplets enclose, or even touch each other, at the expense of reasonable discrepancies. The present work suggests that developing strategies of self-assembly, mixing or transport in microfluidic devices, based on the controlled dynamics of a few interacting particles or droplets may be envisageable.

3.1.3 Experimental system

Soft lithography technique is used to fabricate the microfluidic devices. As sketched in Figure 3.1, the systems are composed of two T junctions connected to a long shallow channel defining our micro Hele-Shaw cell. To avoid the coupling between two parallelized T junctions studied earlier [233] and better monitor the production, the two T junctions are filled independently. Oil droplets are independently formed at the T junctions and are driven into the micro Hele-Shaw cell, at controlled times. Two additional inputs of water (the external phase) allow to improve the cross-stream homogeneity of the outer phase flow conditions. Should these inputs be absent, the droplets would systematically drift laterally and small initial separations between them would be impossible to obtain.

Oil and water are injected at the T-junctions under controlled pressure conditions, using an MFCS Fluigent controller. By using an integrated flowmeter, we measure the corresponding water flow-rates (Q_1 and Q'_1). The water entries that homogeneize the flow structure in the Hele-Shaw cell (see Figure 1), are controlled by two syringe pumps NEMESYS, providing Q_2 and Q'_2. The total flow-rate of the water in the Hele-Shaw is thus $Q_T = Q_1 + Q'_1 + Q_2 + Q'_2$. The corresponding speed at infinity U is obtained by dividing the total flow-rate Q_T by the micro Hele-Shaw cross-sectionnal area.

In practice, the Hele-Shaw heights h vary from 18 μm to 48 μm, the width of the T junctions is 200 μm, the widths of Hele-Shaw cells vary from 500 μm to 3000 μm and their lengths l range between 1 and 3 cm. In the micro Hele-Shaw cell, the aspect ratio

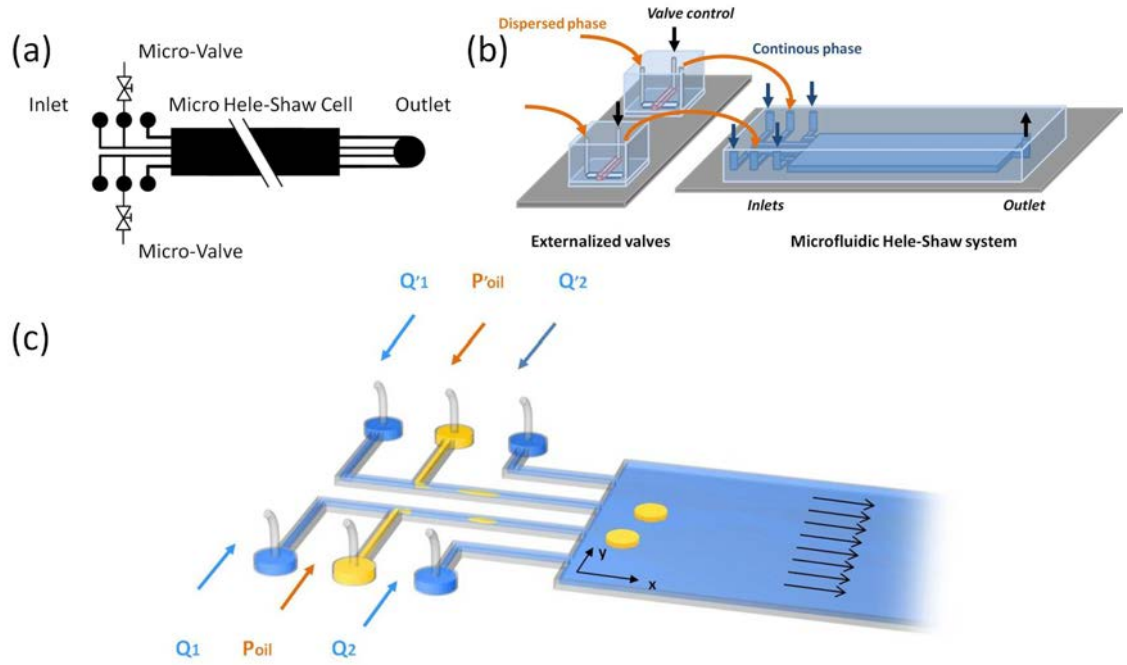

Figure 3.1: (a) Sketch of the microfluidic device. Two independent externalized valves are connected to the oil inlets to regulate the droplet production. (b) Sketch of the microfluidic device showing how it is connected with the two independant externalized valves. (c) Sketch of the experimental device showing how it operates: oil droplets (yellow) are formed at two T- junctions and injected into the micro Hele-Shaw cell. Two entries are added to the micro Hele-Shaw cell, in order to favor flow uniformity of the continuous phase (blue)

height-over-width therefore ranges from 0.006 to 0.1, a range acceptable for applying the lubrication approximation.

Concerning the microfabrication, we use PDMS (Dow Corning SYLGARD 184, 1/9 ratio of curing agent to bulk material) or NOA (Norland Optical Adhesive 81). The advantage of using NOA is to suppress any mechanical deformation in the micro Hele-Shaw cell that would affect the droplet trajectories. In the case of PDMS, standard soft lithography is used [94]. Thereafter, we close the system by binding thermally cured PDMS to a glass slide, after exposing the surfaces to oxygen plasma and bringing them into contact. In the case of NOA, we follow the protocol described by Bartolo et al. [234].

All the experiments employ fluorinated oil (FC 3283, viscosity $\mu = 1.4$ mPa.s) as the dispersed phase and DI water with 1%w/w sodium dodecyl sulfate (SDS) surfactant as the continuous phase (interfacial tension 18 mN.m^{-1}). The sizes of the droplets and the separation distances between two successive droplets in each T junctions are tuned by using externalized pneumatic valves, monitored by a Labview program, using a technique described previously [235] [224]. These externalized valves operate with a small dead volume ($\sim$ 10 nL), a small displaced volume (¡ 1 nL), and a fast response time ($\sim$ 10 ms). These characteristics guarantee a precise control over the droplet production. Droplets can thus be produced on demand, in an accurate manner. Typical droplet radii of the pancake-like droplets range between 100 μm and 200 μm.

Throughout the experiments, the water flow-rate varies from 2 μL.mn^{-1} to 30 μL.mn^{-1}. The capillary number Ca $= \mu U/\nu$ ranges between 2.5×10^{-6} and 3.7×10^{-5} and the Reynolds

number Re = $\rho UL/\mu$ varies between 2.2×10^{-3} and 3.4×10^{-2}.

The droplet motions are recorded with a fast camera (Photron) through an inverted microscope (×5, Zeiss). Image processing is used to extract the droplets characteristics such as their radius R, the distance between droplets r, the orientation angle θ with respect to the upstream flow direction and their longitudinal and transverse velocities U_x and U_y.

3.1.4 Theoretical modeling

In the case of a single droplet, the geometry of the system, along with the axes, are illustrated in figure 3.2 for the case of an isolated droplet.

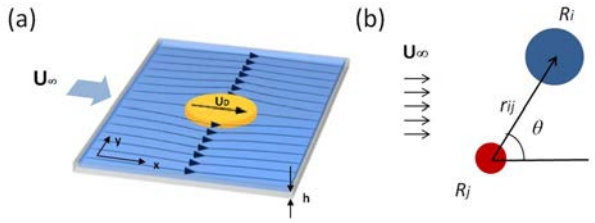

Figure 3.2: (a) Sketch of the streamlines around an isolated disc-like droplet confined between the channel "floor and ceiling", in a Hele-Shaw cell. (b) Sketch of the general case where the droplets are different.

An isolated droplet immersed in a uniform flow U_∞in a Hele-Shaw cell experiences a drag force that conveys it downstream (see figure 3.2(a)). The droplet motion U_D has an amplitude smaller than the upstream speed U_∞, owing to the friction exerted by the walls onto the droplet. In an infinite medium, we may assume the following relation: [206]

$$\mathbf{U}_D = \beta \mathbf{U}_\infty \tag{3.1}$$

where β is a parameter depending, in the small Reynolds number limit, for incompressible newtonian fluids and in an infinite medium, on three dimensionless numbers: the radius over the channel height, the viscosity ratio between the two fluids along with the Capillary number. To the best of our knowledge, although work has been done on related topics [232][236] , no systematic calculation of β is available in the literature. For the sake of simplicity, and in good consistency with the experimental literature [206], we will assume that β is independent of the flow conditions, an assumption that will be confirmed empirically in Section 3.1.5 within the range of experimental conditions we investigated. When several droplets move in the Hele-Shaw cell, the current approach consists in considering that the interactions are pairwise, dipolar and far field. Under these assumptions, the expression for the speed of droplet i, subjected to the mean flow and the action of the other droplets, reads [206][229]:

$$\mathbf{U}_i = \beta_i(\mathbf{U}_\infty + \sum_{j\neq i} \mathbf{V}^{(ij)}) \tag{3.2}$$

where $\mathbf{V}^(ij)$ is defined by

$$\mathbf{V}^{(ij)} = \frac{2\mathbf{r}_{ij}}{\mathbf{r}_{ij}^4}(r_{ij}\cdot\mathbf{p}_j) - \frac{\mathbf{p}_j}{r_{ij}^2} \tag{3.3}$$

in which one has

$$\mathbf{p}_j = R_j^2(\mathbf{U}_j - \mathbf{U}_{jext}) \tag{3.4}$$

$\mathbf{r}_{ij} = \mathbf{r}_i - \mathbf{r}_j$

in which $U_{jext} = U_j/\beta_j$ is the local upstream flow droplet j is subjected to. The differences in the droplet sizes are expressed through the radius R_j and the factor β_j, which may differ from one droplet to the other.

The system is linear in U_i. It must be solved to determine the droplet speed at each point. Thereafter the droplet position can be calculated. The process must be iterated to obtain the trajectories of all the droplets. Nonetheless, in the far field limit, the ratio of the typical radius over the typical intradroplet distance is small, and quadratic terms can be neglected. System 3.2 can be simplified into:

$$\mathbf{U}_i = \beta_i(\mathbf{U}_\infty + \sum_{j\neq i}(1-\beta_j)(\frac{R_j^2}{r_{ij}^2}\mathbf{U}_\infty - \frac{2R_j^2\mathbf{r}_{ij}}{r_{ij}^4}(\mathbf{r}_{ij}\cdot\mathbf{U}_\infty))) \tag{3.5}$$

Equation 3.5 can be brought to a more convenient form by working in a system of coordinates in which U_∞ lies along x (as shown in figure3.2) i.e.:

$$\mathbf{U}_\infty = U_\infty\hat{\mathbf{x}} \tag{3.6}$$

(in which $\hat{\mathbf{x}}$ is the unit vector along x). In such a system, one obtains the following equations:

$$U_{ix}^{(0)} = \frac{dx_i}{dt} = \beta U_\infty(1 + \sum_{j\neq i}(1-\beta_j)\frac{R_j^2(r_{ijy}^2 - r_{ijx}^2)}{r_{ij}^4}) \tag{3.7a}$$

$$U_{iy}^{(0)} = \frac{dy_i}{dt} = \beta U_\infty \sum_{j\neq i}\frac{-2(1-\beta_j)R_j^2 r_{ijx}r_{ijy}}{r_{ij}^4} \tag{3.7b}$$

in which

$$r_{ijx} = x_i - x_j \quad and \quad r_{ijy} = y_i - y_j \tag{3.8}$$

(7) defines a dynamical system that can be integrated by using standard MatLab routines. We used this formulation to compare theory to experiment.

3.1.5 Results and discussion

The case N=1 (isolated droplets)

We first investigate the case of a single droplet moving along the micro Hele-Shaw cell. In this case, the system contains a single T-junction along with the two diluting inlets; a single droplet penetrates the micro Hele-Shaw cell. In all cases, for a fixed channel geometry, we obtain a linear relation between the droplet speed U_D and the upstream flow velocity U_∞ (Fig. 3.3). Within the experimental error, the relation we obtain experimentally can thus be expressed in the form:

$$\mathbf{U}_D = \beta\mathbf{U}_\infty \tag{3.9}$$

in which β is the proportionality factor, independent of U_∞, in agreement with the theory 3.1.

Experiments at different R/h are carried out, varying both R (100 to 290 μm) and the height (18 to 48 μm). Widths vary from 1000 to 3000 μm, and we make sure that

the minimal distance to the wall is 3R to avoid confinement effects. Figure 3.3 shows that, within ±10%, the slope β does not depend on the ratio R/h. Its averaged value is 0.21 ± 0.02. Arguments shown later will confirm this conclusion, by indicating that the variations of β with the droplet size are on the order of 10^{-3}.

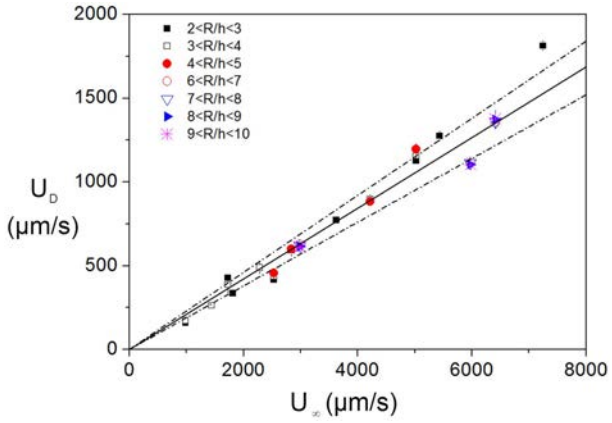

Figure 3.3: Measurements of the velocity of an isolated droplet U_D as a function of the velocity U_∞, regrouped by values of R/h. The solid line is a linear fit of the data, with a slope equal to 0.21. The error bars are the min and max values obtained, for each R/h, by varying the droplet radius and the channel height. Error bars are sometimes not visible, being smaller than the points. Within the error bar, β does not depend on R/h and its mean value is 0.21 ± 0.02 (solid line)

The case N=2 (pairs of droplets)

The case of identical droplets

We start here with the case where droplets have the same size. Figure 3.4(a) shows the evolution of a droplet pair aligned with the streamwise direction, for different separation distances. As shown in Fig. 3.4(a), the pair speed increases with the separation, up to a point when the droplets cease to interact and consequently move as isolated droplets.

An important observation is that, as shown in Fig. 3.4(a), the ratio of the pair speed U_x over U_D does not vary with the parameter R/h. In this plot, R/h has been varied between 2.5 and 10, and the data collapses onto a single curve, function of r/R. From dimensional grounds, within the small Reynolds numbers limit, one may conclude that the speed ratio depends on r/R only. The measurements agree well with the model, which yields to the following expressions: (see Appendix 1.(a).)

$$U_x = \beta U_\infty (1 - (1-\beta)\frac{R^2}{r^2} cos2\theta) \tag{3.10a}$$

$$U_y = -(1-\beta)\beta U_\infty \frac{R^2}{r^2} sin2\theta \tag{3.10b}$$

in which r is the initial pair separation and θ (mod. π) is the angle between the line joining the droplets centers and the Ox axis (see Fig. 3.2(b)). Eq. 3.15 shows that droplet pairs displace at an angle equal to 2θ with respect to the x axis. Droplet pairs normal to

the x axis move faster than isolated droplets. On the other hand, isolated droplets move faster than droplet pairs aligned along x (so-called 'peloton effect' [208]) .

The solutions 3.15 are represented as solid lines in Figure 3.4. It agrees well with the experiment down to r/R = 2, where deviations do not exceed 20%. This deviation is surprisingly low if we take into account that the far field approximation is no longer valid in this region.

Theory 3.15 and experiment agree well also in the case where the pair is oriented normally to the upstream velocity (see Fig. 3.4(c)). In this case, the doublet moves faster than an isolated droplet. This can be called an 'antipeloton' effect, because here the drag developed by the upstream flow appears larger than for isolated droplets. This can be explained by noting that the presence of the droplet pair deviates the incoming streamlines more importantly than in the isolated case. Thereby, larger local speeds and larger drags can be expected. More specifically, each droplet generates dipolar motions (Fig 3.4(b,d)) that exert drag forces on neighboring droplets. In the horizontal case, those forces are directed oppositely to the flow direction as pictured in Figure 3.4(b) while they are directed along the flow in the vertical case (Fig. 3.4(d)). As a consequence, dipolar interactions result respectively in a reduction/increase of the drag in the horizontal/vertical case; horizontal pairs are slowed down and vertical pairs fastened.

The acceptable agreement between theory and experiment is further confirmed by investigating the behavior of droplets pairs oriented by angle θ with respect to the upstream velocity. The pair speeds along the x and y directions, measured for different angles θ, are shown in Figure 3.5.

Here the droplets touch each other (r/R = 2). We obtain, as expected theoretically from formulas 3.15, that the pair speeds develop sine-like behaviors with respect to 2θ. The theory, represented by full lines, agrees well with the x speed component of the droplet pair, without any fitting parameter, and despite the long range hypothesis is not valid here. This agreement does not appear in the transverse component, that is overestimated by the theory by 30%. The transversal speed variation is only qualitatively predicted by the model.

The result of the behavior of non-touched droplets pairs (r/R ranges from 2 to 10) oriented by angle θ with respect to the upstream velocity is shown in the figure 3.6. The pair velocities develop sine-like behaviors as expected in the theory and their amplitudes are decreasing as the droplets get more spaced.

The case of droplets of different sizes initially aligned along the downstream direction

We consider here the case of droplets of different sizes initially aligned along the downstream direction. We monitor the distance between the droplet centers $\delta(t)$ = x2(t) - x1(t) in three different cases (Fig. 3.7): a small droplet moving behind a large one (a), a large droplet moving behind a small one (c) and, for the sake of comparison, two identical droplets placed one behind the other (b). Droplets initially lie parallel to the centerline of the micro Hele-Shaw cell ('horizontal' line). Their disalignement being at most of 10°, it can be neglected. The conclusion is suggested by the inspection of Figure 3.5, and supported by the evidence that there is no pair rotation (see Section 3.1.5 spontaneous pair alignment). In all these experiments, droplets cover a distance larger than 30 times their radius. For identical droplets, we recover the result, shown previously, that their separation does not change with time, within a 5% experimental uncertainty. As droplets are different, there is no more steady state: the separation diverges in case (a) while it contracts in case (c).

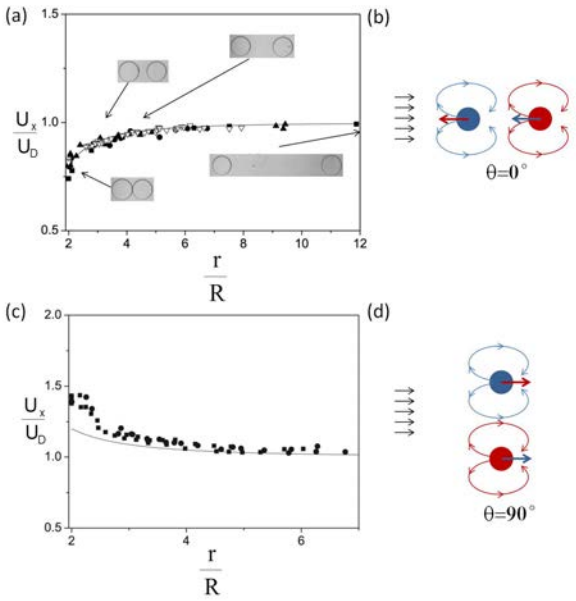

Figure 3.4: Velocity of droplet pairs, normalized by the velocity of an isolated droplet, as a function of their distances normalized by their radii. The velocity of isolated droplets was measured in situ. (a) Pairs of droplets oriented in the streamwise direction, $\theta = 0°$, (∇) PDMS system, h = 18 μm, w2 = 3000 μm, $U_D \approx 612$ μm.s^{-1}, (■) NOA system, h = 37 μm, w2 = 3000 μm, $U_D \approx 680$ μm.s^{-1}, (●) PDMS system, h = 48 μm, w2 = 3000 μm, $U_D \approx 1485$ μm.s^{-1}, (▲) PDMS system, h = 48 μm, w2 = 3000 μm, U_D ≈1700 μm.s^{-1}. (b) Representation of the recirculations generated by each droplet in the horizontal position. The blue droplet generates a force on the red droplet, represented by a blue arrow. Respectively, the force generated by the red arrow on the blue one is represented by a red arrow. (c) Pairs of droplets oriented perpendicularly to the direction of the flow, $\theta = 90°$, (■) NOA system, h = 37 μm, w2 = 3000 μm, $U_D \approx 322$ μm.s^{-1}, (●) NOA system, h = 37 μm, w2 = 3000 μm, U_D ≈462 μm.s^{-1}. Droplet radius vary between 100 and 200 microns. The solid lines show the theoretical results based on Eq. 3.15. (d) Representation of the recirculations generated by each droplet in the vertical position. Forces generated by each droplet are represented by arrows of the droplet color.

The long time behavior of the 'repelling' case (a) indicates that the factor β, introduced in Eq. 3.1, must slightly increase with the droplet size, in a way undetectable by measurements made on isolated droplets, owing to experimental uncertainty, as pictured in Section 3.1.5 the isolated droplets. We thus compared the observations with the theory by introducing a free parameter $\Delta\beta = \beta_2$ - β_1, which takes the variation of β with the droplet size into account. With this adjustable parameter, the theoretical predictions is given by the following equation : (see Appendix 1.(b).)

$$\frac{d\delta}{dt} = (\beta_2 - \beta_1)U_\infty + \frac{(1-\beta_2)\beta_1 R_2^2 - (1-\beta_1)\beta_2 R_1^2}{\delta^2} U_\infty \tag{3.11}$$

The solid lines, representing the above formula, agree well with the experiment.

From these experiments, we can provide an estimate for the variations of β with the droplet radius R, for a range of R/h varying between 2.5 and 5.

$$\frac{\Delta\beta}{\Delta R} \approx 1.6.10^{-4} \pm 0.5.10^{-4} \mu m^{-1}$$

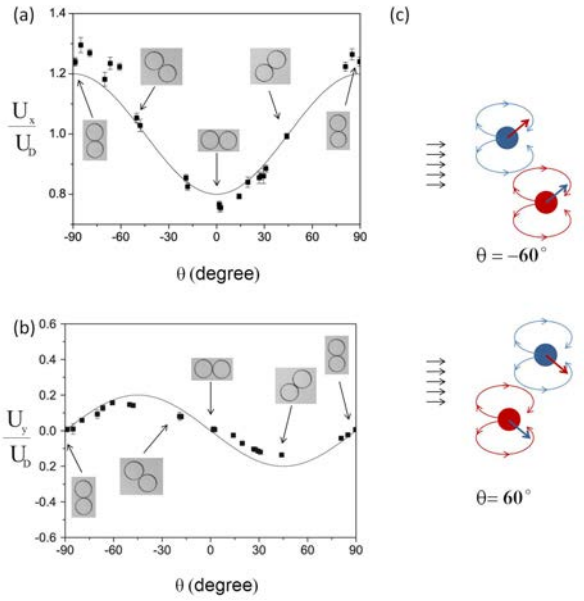

Figure 3.5: Velocity of contacting droplet pairs (r/R=2) normalized by the velocity of an isolated droplet, as a function of the angle of orientation θ. The isolated droplet velocity was $U_D \approx 1100\ \mu m.s^{-1}$. PDMS system, h = 46 μm, w2 = 3000 μm. (a) Measurements along x. Note that in this set of experiments, when the pair is vertical, the ratio U_x/U_D is smaller than on Fig 3.4(c). This variability is compatible with the standard type deviation we obtain experimentally over a set of experiments conduced in the same conditions (b) Measurements of the speed component along y. The solid lines show the theoretical results given by Eq. 3.15. (c) Representation of the recirculations generated by each droplet in the position with orientation of -60° (on the top) and 60° (at the bottom). Forces generated by each droplet are represented by arrows of the droplet color.

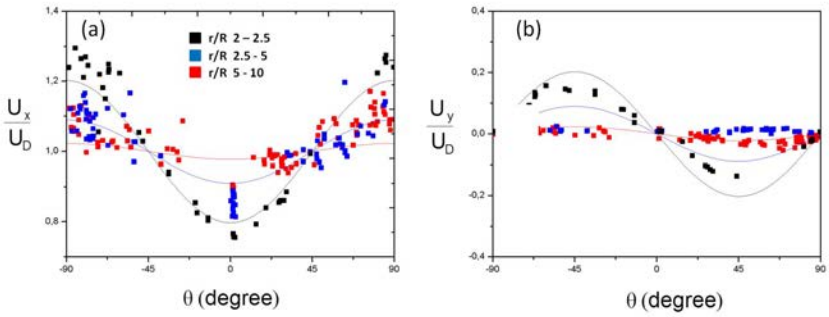

Figure 3.6: Velocity of contacting droplet pairs (r/R ranges from 2 to 10) normalized by the velocity of an isolated droplet in the same fluid condition, as a function of the angle of orientation θ. PDMS system, h = 46 μm, w2 = 3000 μm. (a) Measurements along x. (b) Measurements of the speed component along y. The solid lines show the theoretical results given by Eq. 3.15.

The very low value of the $\frac{\Delta\beta}{\Delta R}$ explains that those variations were not detectable for isolated droplets in Section 3.1.5 the isolated droplets part. It is remarkable that such small variations control the dynamics of droplet pairs, in the case where droplets are

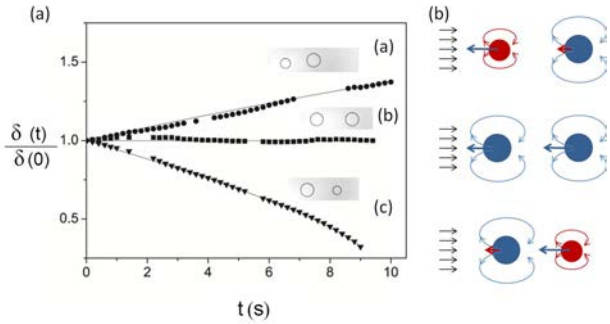

Figure 3.7: (a) Evolution of the distance between droplets as a function of time. Solid lines depict the theoretical model using an adjustment of the parameter $\Delta\beta = \beta 2 - \beta 1$. PDMS system, h = 48 μm, w2 = 3000 μm. (a): R2 = 209 μm, R1 = 155 μm, $\Delta\beta$ = 0.0055. (b): R2 = 206 μm, R1 = 201 μm. (c): R2 = 131 μm, R1 = 205 μm, $\Delta\beta$ = -0.0157. For identical droplets (case (b)), theory predicts that their separation remains constant (horizontal solid line).(b) Representation of the recirculations generated by each droplet in those three different cases. Forces generated by each droplet are represented by arrows of the droplet color.

unequal. This point must be taken seriously in studies attempting to model the dynamics of populations with droplets of different sizes.

Spontaneous pair alignment along the downstream direction

We observed an interesting phenomenon with unequal droplet pairs placed normally to the upstream direction. Their trajectory is shown in Figure 3.8(A). The pair rotates up to a point where it almost aligns with the downstream direction. In the meantime, the droplets approach each other and cluster. Eventually, the pair moves steadily downstream (not shown). The physical origin of the rotation comes from the fact that the large droplet develops vigorous recirculations that advect its small partner around it. The effect cancels out when the droplets are identical.

Figure 3.8(B) shows calculations based on Equations 3.7, without fitting parameter. The approximate theory reproduces well the internal evolution of the pair (rotation and mutual approach), prior to the collision. Beyond the collision time, the calculation indicates that the droplets interpenetrate, which is nonphysical. We thus stopped the calculation after the droplets come into contact.

The case N = 3: Pair exchange

For the case N = 3, we analyzed a number of different situations and figured out typical behaviors. We found a phenomenon that is well known in vortex dynamics, called "pair exchange" (a similar effect is known in the field of sedimentation (Guazzelli and Morris 2012)). The phenomenon is shown in Figure 3.9, for two different initial conditions. In Figure 3.9(A), the three droplets initially lie along the streamwise direction, one pair standing ahead of their third partner. Since the isolated droplet moves faster than the pair, it will approach the pair. Eventually, the droplet located at the front detaches, and gradually escapes the new pair formed by two other droplets. We thus obtain a horizontal "exchange". This horizontal exchange is the three-body version of the shockwave phenomenon discussed in previous work [208][226].

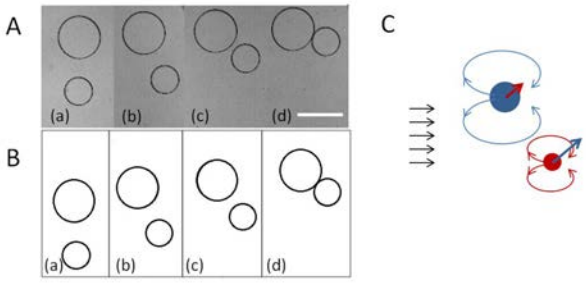

Figure 3.8: (A) Evolution of a pair of droplets with different size (R = 250 μm and 167 μm respectively) oriented normally to the upstream velocity U_∞ ≈6105 $.s^{-1}$. PDMS system, h = 48 μm, w2 = 3000 μm. (a) t = 0 s; (b) t = 1.6 s; (c) t = 3.2 s; (d) t = 4 s. The external phase flows from left to right. (B) The same situation calculated by using Equations 3.7 with the parameters of Figure 3.8(A) (U_∞ radii, initial positions, $\beta = 0.2$) (a) t = 0 s; (b) t = 2.97 s; (c) t = 4.06 s; (d) t = 5 s. A vertical drift on the order of 50 $.s^{-1}$ is found in the simulation, which is higher than the experimental drift. The scale bar corresponds to 500 μm. (C) Representation of the recirculations generated by each droplet in the position A-(b). Forces generated by each droplet are represented by arrows of the droplet color.

In another situation (Figure 3.9(C)), a "vertical" pair (i.e. normal to the streamwise direction) stands behind an isolated droplet. In this case, the pair moves faster, and thus will come closer to the isolated droplet. We observe that, as the pair approaches their partner, a droplet detaches from the triplet newly formed; eventually, the droplet is left behind while the new vertical pair formed with its former partner moves downstream at larger speed and consequently escapes away from it.

The two phenomena are correctly reproduced by Equations 3.7. This is especially true for the horizontal exchange (Figure 3.9(B)), where a semi-quantitative agreement is obtained, again without fitting parameter. Figure 3.9(D) shows a more complicated situation: the approach of the vertical pair is well reproduced by Eq. 3.7 , as is the outcome of the exchange, but there is a discrepancy between the experiment and the theory concerning the duration of the exchange process. In the experiment, full exchange is observed at 4.8 s while in the simulation, we need larger times (beyond 10 s) to reach a state where the exchange can be considered as completed. The reason for this discrepancy is due to the fact that, as the droplets get close to each other (See Figure 3.9(A)(d) and 3.9(C)(d)), Equations 3.7 become inaccurate. The inaccuracies propagate at later times, reaching substantial levels. Calculations nonetheless show that Eq. 3.7 still represents qualitatively well the evolution of the system at late times in this particular case.

Interactions with the walls

A single droplet moving along a wall

In these series of experiments, we drive a single droplet along a wall, and measure its speed as a function of its distance to the wall r_w (see Figure 3.10). The other wall is located at a distance at least about 800 μm (around 6R) so that its influence may be neglected. We observe that the speed of a droplet increases as its distance to the wall decreases. This is consistent with the idea that the lateral wall acts as a mirror and consequently develops an image that forms a pair with the droplet, oriented normally with

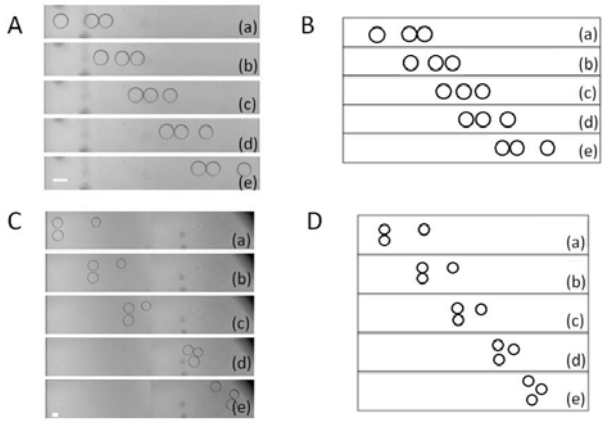

Figure 3.9: Image sequences of triplets of droplets moving from left to right in a Hele-Shaw cell. (A) An isolated droplet catches up with a "horizontal" pair, then the droplet ahead is released (R = 99 μm, 94 μm and 94 μm respectively). PDMS system, h = 48 μm, w2 = 1300 μm; flow velocity is $U_\infty \approx 2352 \mu m.s^{-1}$. (a) t = 0 s; (b) t = 1.2 s; (c) t = 2.4 s; (d) t = 3.6 s; (e) t = 4.8 s. (B) Numerical simulation with the parameters of Figure 3.9(A): U_∞, initial positions, $\beta = 0.2$. Here, the droplets radii are assumed to be identical and equal to the mean radius (R = 96 μm). (a) t = 0 s; (b) t = 1.56 s; (c) t = 2.5 s; (d) t = 3.75 s; (e) t = 5.93 s. (C) A "vertical" pair catches up with an isolated droplet, then moves downstream, abandoning its former partner (R = 165 μm, 172 μm and 150 μm respectively). PDMS system, h = 48 μm, w2 = 1300 μm; flow velocity is $U_\infty \approx 3450 \mu m.s^{-1}$. (a) t = 0 s; (b) t = 1.2 s; (c) t = 2.4 s; (d) t = 3.6 s; (e) t = 4.8 s. (D) Numerical simulation with the parameters of Figure 3.9(C): U_∞, initial positions, $\beta = 0.2$. Here, the droplets radii are assumed to be identical and equal to the mean radius (R = 162 μm).(a) t = 0 s; (b) t = 1.4 s; (c) t = 2.66 s; (d) t = 7.03 s; (e) t = 10 s. The scale bars correspond to 200 μm.

respect to the streamwise direction. The "vertical" pair (formed by the droplet and its image) moves therefore faster than the isolated droplet.

At a quantitative level, we compared the droplet speed with the theory (solid line), again without fitting parameter, taking the wall as a mirror and the droplet as pointwise. The distance to the wall is r_w, so that the distance to the droplet image is r = 2 r_w. We found good agreement between the theory and the experiment for r_w/R > 1.8. For short distances (rw/R < 1.8), the evolution seems more complicated: the measured speed is substantially higher than expected close in a range of r_w/R lying between 1.25 and 1.8. Surprisingly, the discrepancy decreases as the droplet approaches the wall further. The discrepancy observed between 1.25 and 1.8 is probably due to the fact that the far field assumption becomes inaccurate. Regarding the decrease of the droplet speed as the wall is approached further, a possible explanation bears on the idea that the width of the boundary layer located at the wall is around 50μm [198]. Therefore, for r_w/R $\sim$ 1, the droplet stands partially in the boundary layer and consequently, its speed is slowed down. The fact that the model reproduces the experiment in this case is thus fortuitous.

Droplet pair reflecting against a wall

The stream lines in a Hele-Shaw cell move parallel to the flow. It is thus impossible to study the reflection phenomena with a single droplet, as it moves parallel to the wall. We

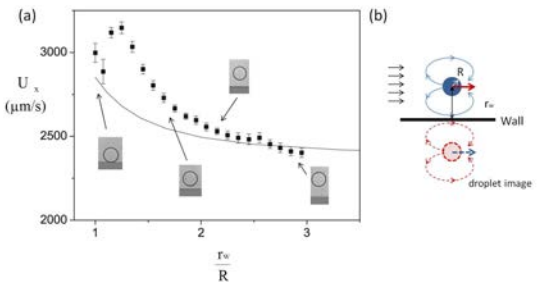

Figure 3.10: (a) Speed of a single droplet moving along a wall plotted versus the distance between the droplet center and the wall rw over the droplet radius R. The system is made in PDMS (h = 46 μm, w2= 1300 μm.). The radius of the droplet is R = 140 μm. The speed of the continuous phase U_∞ is 10800 $\mu m.s^{-1}$. It is measured in situ by seeding the flow with micrometric particles. The side wall is shown in dark grey. In the single image approach, the droplet and its image form a 'vertical' pair whose speed can be calculated by using Eq. 3.15. (b) Representation of the recirculations generated by the real droplet (blue) and its image (red). Forces generated by each droplet are represented by arrows of the droplet color.

used the dipolar interaction discussed earlier to send droplet pairs towards the wall and study reflection laws. We observed different situations. The first one is shown in Figure 3.11(A). In this situation, the pair moves towards the wall at a small incident angle (21°, measured with respect to the wall), deviates, avoids it, and eventually moves away from the wall. The pair keeps its integrity and the reflection angle is equal to the incident angle. We thus have pure symmetric reflection.

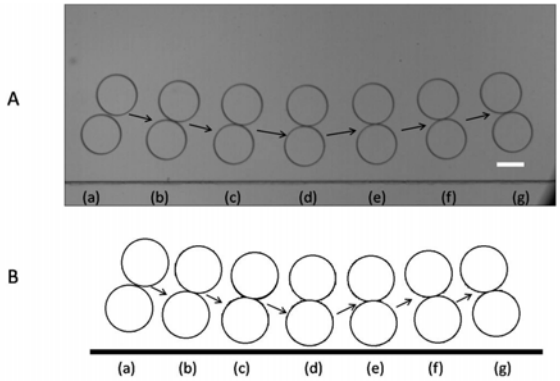

Figure 3.11: (A) Evolution of a pair of droplets approaching the side wall (R = 146 μm and 142 μm respectively) at an incident angle equal to 21°. The external phase flows from left to right. PDMS system, h = 48 μm, w2 = 1300 μm, flow velocity U_∞ = 4098 $\mu m.s^{-1}$. (a) t = 0 s; (b) t = 0.4 s; (c) t = 0.8 s; (d) t = 1.2 s; (e) t = 1.6 s ; (f) t = 2 s; (g) t = 2.4 s.The scale bar corresponds to 200μm. (B) Numerical simulation with the parameters of Figure 3.11(A) (U_∞, R = 144 μm, initial positions provided by the experiment, β = 0.2). (a) t = 0 s; (b) t = 0.38 s; (c) t = 0.75 s; (d) t = 1.13 s; (e) t = 1.5 s ; (f) t = 2.25 s; (g) t = 2.38 s.

A second case is shown in Fig. 3.12(A). Here, the incidence angle is larger (61°). The two droplets first come into (apparent) contact with the wall. Later, the droplet ahead of the pair moves along the wall, while its partner separates from the wall. The droplet

located ahead moves faster so that as time grows, the distance between them increases. Eventually, the droplets are far apart and the pair is destroyed.

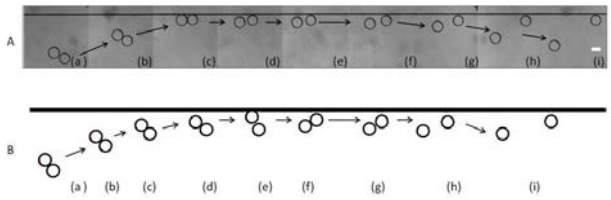

Figure 3.12: (A) Evolution of a pair of droplets approaching the side wall (R = 120 μm and 113 μm respectively). The flow is from left to right. The flow velocity $U_\infty = 3465$ $\mu m.s^{-1}$. PDMS system with h = 48 μm, w2 = 3000 μm. (a) t = 0 s; (b) t = 2 s; (c) t = 4 s; (d) t = 12 s; (e) t = 14 s ; (f) t = 16 s; (g) t = 18 s; (h) t = 20 s; (i) t = 22 s. The scale bar corresponds to 200 μm. (B) Numerical simulation with parameters close to those of Figure 11(A): $U_\infty = 3465 \mu m.s^{-1}$ and R = 116 μm. The initial angle had to be slightly changed to reproduce this escape phenomenon. (a) t = 0 s; (b) t = 1.28 s ; (c) t = 2.07 s; (d) t = 2.25 s; (e) t = 2.31 s ; (f) t = 2.34 s; (g) t = 2.41 s; (h) t = 2.84 s; (i) t = 3.55 s.

A third case is shown in Figure 3.13(A). In this case, the pair moves in a strongly confined space - the distance between the walls is twice the droplet diameter. The pair undergoes a sequence of events, including contact with the wall, rotation and drift towards the opposite wall. The process repeats periodically. We have observed up to five cycles in a long narrow channel.

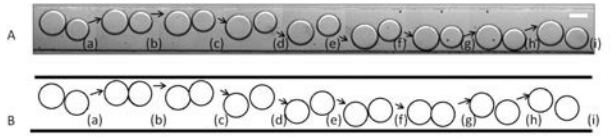

Figure 3.13: (A) Bouncing of a pair of droplets in confined conditions (R = 133 μm and 120 μm respectively). PDMS system, h = 41 μm, w2 = 500 μm. The external phase flows from left to right. (a) t = 0 s; (b) t = 0.1 s; (c) t = 0.2 s; (d) t = 0.3 s; (e) t = 0.4 s ; (f) t = 0.5 s; (g) t = 0.6 s; (h) t = 0.7 s; (i) t = 0.8 s. The scale bar corresponds to 200 μm. (B) Numerical simulation showing (qualitatively) the same phenomenon, using the same conditions as the experiment. (a) t = 0 s; (b) t = 1.17 s; (c) t = 2.28 s; (d) t = 3.36 s; (e) t = 4.47 s ; (f) t = 5.55 s; (g) t = 6.66 s; (h) t = 7.73 s; (i) t = 8.66 s.

Equations 3.7 quantitatively reproduce the experimental behavior observed in the case of pair reflection against the wall (see Fig. 3.11(B)). The good agreement may originate from the fact that at all times, the pair remains substantially distant from the wall. This is an interesting outcome, which indicates that in practice, walls can be considered as mirrors, and higher order reflections can be neglected as long as pairs remain distant from the wall.

The quantitative agreement gets worse as pairs approach the wall. One example is the escape shown in Figure 3.12(B). Here the behavior observed experimentally is reproduced only qualitatively, and only after adjusting the initial angle between the droplet. Numerically, there is a sensitivity to the initial conditions, while experimentally the escape regime appears robust with respect to slight changes in the experimental conditions. The existence of various regimes (reflection, escape) that we found, both experimentally and

numerically, appears consistent with the analysis of Uspal and Doyle (2012) [229].

The last situation (Fig. 3.13) is well reproduced by the large friction-single image theory. The details of the rebound (contact with the wall, rotation and drift towards the opposite wall) are well obtained numerically. However, we observed a discrepancy regarding the times at which the reflection events occur (see Fig. 3.13(A)-(B)). This is mainly due to the fact that in the experiment, we operated at fixed pressure, and consequently the upstream velocity U_∞ is not imposed. In this particular set of experiment, U_∞ must be taken as a free parameter. When this remark is taken into account, agreement between the theory and experiment is found to be good (albeit at the expense of a free parameter).

3.1.6 Conclusion

In this paper, we investigated the behavior of droplets conveyed by a mean flow, and confined in micro Hele-Shaw cells. We analyzed the case N = 1, 2 and 3 in detail. For N = 3, we observe several phenomena (rebounds, pair exchange) that have not been reported yet. We moreover show that the side walls generate a rich dynamics (escape, simple and multiple reflections). As a whole, the dipolar interaction model (far field, limited to nearest neighbours) provides an accurate picture as long as the droplet boundaries are distant by more than one radius from its neighbor or from the wall. Below this critical distance, the far field approximation is no longer valid, but theory still describes well most of the observed phenomena (speed of a pair of droplets, pair exchange, pair rotation, speed of a droplet close to a wall, rebounds); the agreement is surprisingly good in purely longitudinal studies. Whatever the distance between particles and the number of droplets involved (N = 1, 2, 3), the dipolar interaction model gives good qualitative predictions, with easy to compute equations, and without fitting parameters. The capacity of predicting the movement of small assemblies of droplets opens the possibility of devising self-assembly strategies based on hydrodynamic interactions between particles or droplets. It more generally suggests that controlling small populations of particles in microchannels, to mix or transport entities, seems feasible.

3.1.7 Acknowledgments

We gratefully acknowledge Ministry of Research, ESPCI and CNRS for their support of this work. We benefited from discussions with P. Doyle, A. Leshansky, D. Bartolo, M. Nagel, E. Guazzelli, A. Huerre and M-C. Jullien. We thank F. Monti for his technical help.

3.1.8 Appendix

Complex variables

A compact form of 3.7 can be found by using complex variables:

$$z = x + \mathbf{i}y \quad and \quad z_{ij} = z_i - z_j \tag{3.12}$$

Using such variables, one gets:

$$\frac{dz_i}{dt} = \beta_i U_\infty (1 - \sum_{j \neq i} \frac{(1-\beta_j)R_j^2}{(\bar{Z}_I - \bar{Z}_J)^2}) \tag{3.13}$$

For the sake of comparison with the experiment, it is interesting to calculate exact solutions to Eq. 3.13. For N = 1, one gets , $U_{1x}^{(0)} = \beta U_\infty$; $U_{1y}^{(0)} = 0$, which again expresses the motion of an isolated droplet. For N = 2 , system 3.13 reads:

$$\frac{dz_1}{dt} = \beta_1 U_\infty (1 - \frac{(1-\beta_2)R_2^2}{(\bar{Z}_2 - \bar{Z}_1)^2}) \tag{3.14a}$$

$$\frac{dz_2}{dt} = \beta_2 U_\infty (1 - \frac{(1-\beta_1)R_1^2}{(\bar{Z}_2 - \bar{Z}_1)^2}) \tag{3.14b}$$

We have not found exact solutions to this system in the general case. In two cases however, exact solutions can be obtained: (i) when droplets are identical and (ii) when they lie initially along the x axis.

Appendix 1.(a). Identical droplets

For two identical droplets, Equations 3.14 show that the droplets move at constant speed $\mathbf{U}(U_x, U_y)$. It is convenient to express the exact solution in the following way:

$$U_x = \beta U_\infty (1 - (1-\beta)\frac{R^2}{r^2} cos2\theta) \tag{3.15a}$$

$$U_y = -(1-\beta)\beta U_\infty \frac{R^2}{r^2} sin2\theta \tag{3.15b}$$

in which r is the pair separation and θ (mod. π) is the angle between the line joining the droplets centers and the Ox axis. Droplet pairs normal to the x axis move faster than isolated droplets. On the other hand, isolated droplets move faster than droplet pairs aligned along x (so-called "peloton effect").

Appendix 1.(b). Droplets lying along the x axis

When the droplets initially lie along the x axis, they stay on the x axis at all times. One thus has the relation:

$$z_2 - z_1 = \delta(t) \tag{3.16}$$

where the separation $\delta(t)$ is real. $\delta(t)$ satisfies the following equation:

$$\frac{d\delta}{dt} = (\beta_2 - \beta_1)U_\infty + \frac{(1-\beta_2)\beta_1 R_2^2 - (1-\beta_1)\beta_2 R_1^2}{\delta^2} U_\infty \tag{3.17}$$

The evolution of $\delta(t)$ depends on the signs of the terms of the right hand side of Eq. 3.17. For the sake of simplicity, and anticipating the experimental findings, we will restrict ourselves to the case where β slightly increases with the droplet radius, so that $\Delta\beta = \beta_2 - \beta_1$ is much smaller than β_1 and positive if $R_2 \geq R_1$; this implies that the quantity $(1-\beta_2)\beta_1 R_2^2 - (1-\beta_1)\beta_2 R_1^2 \approx$ (1-β_1)$\beta_1(R_2^2 - R_1^2)$ is positive.

On solving 3.17 under these assumptions, we find that when R1 < R2, the separation grows linearly at large times, according to the formula

$$\delta(t) = \Delta\beta U_\infty t = (\beta_2 - \beta_1) U_\infty t \tag{3.18}$$

In the opposite case ($R_1 \geq R_2$), the droplets approach each other. At a finite time, defined by

$$t_c = \frac{1}{\Delta\beta U_\infty}(\delta_c Arctan(\frac{\delta(0)}{\delta_c}) - \delta(0)) \tag{3.19}$$

with

$$\delta_c = \sqrt{\frac{(1-\beta_2)\beta_1 R_2^2 - (1-\beta_1)\beta_2 R_1^2}{\Delta\beta}} \tag{3.20}$$

$$\delta_c \approx \sqrt{\frac{(1-\beta_1)\beta_1 R_2^2 - (1-\beta_1)\beta_2 R_1^2}{\Delta\beta}} \tag{3.21}$$

$$\delta_c \approx 0.4\sqrt{\frac{R_2^2 - R_1^2}{\Delta\beta}} \tag{3.22}$$

the two droplets touch each other. From that moment on, they start intepenetrating and the model no longer provides physical results.

Chapter 4

Clustering based on hydrodynamics self-assembly: basic observations

4.1 Introduction

We have demonstrated that by integration of independent externalized valves, we can produce periodically a precise small number of droplets in a reproducible manner. However, reducing the droplet size down to several microns remains a huge challenge. In addition, the way to aggregate discrete droplets together without coalescence is another problem to solve (in the previous chapter, we observe the pair exchange phenomenon which is not desirable for clustering process, i.e. in such condition, we could only obtain doublet instead of triplet). In this chapter, we will describe a novel method to generate large amounts of clusters entities with a good size, composition, surface properties and shape uniformity.

4.2 Experimental set-up

The geometry of the microfluidic system is illustrated in Figure 4.1. The device, made with standard PDMS-based soft photolithography, consists of a two-layer structure with different heights. The first layer includes a T-junction and is followed by a shallow terrace. The depth (h_1) varies from 1μm to 10μm and the width of the T-junction channel (W) ranges from 10μm to 100μm. The second layer is composed of a microfluidic reservoir, with the depth (h_2) varying between 22μm to 163μm. The dispersed phase is injected from Inlet 1 and continuous phase from Inlet 2. More external continuous phase is injected through two additional inputs connected with Inlet 3 which allows us to modulate the flow field in the reservoir.

Depending on the liquids we use, water-in-oil or oil-in-water emulsions are formed. In the first part, as a model system, we adopt Fluorinated oil (FC-3283) as the dispersed phase and water with 2 % surfactant Sodium dodecyl sulfate (SDS) as the continuous phase. We use either pressure sources (MFCS Fluigent) or syringe pumps (NEMESYS) to drive the fluids. By using an integrated flow meter, we could also measure the corresponding flow-rates in the case of pressure control. The droplet motions are recorded with a fast camera (Photron) through an inverted microscope (Zeiss). Image processing is used to determine the droplets characteristics such as the size, velocity, emission frequency etc. The main

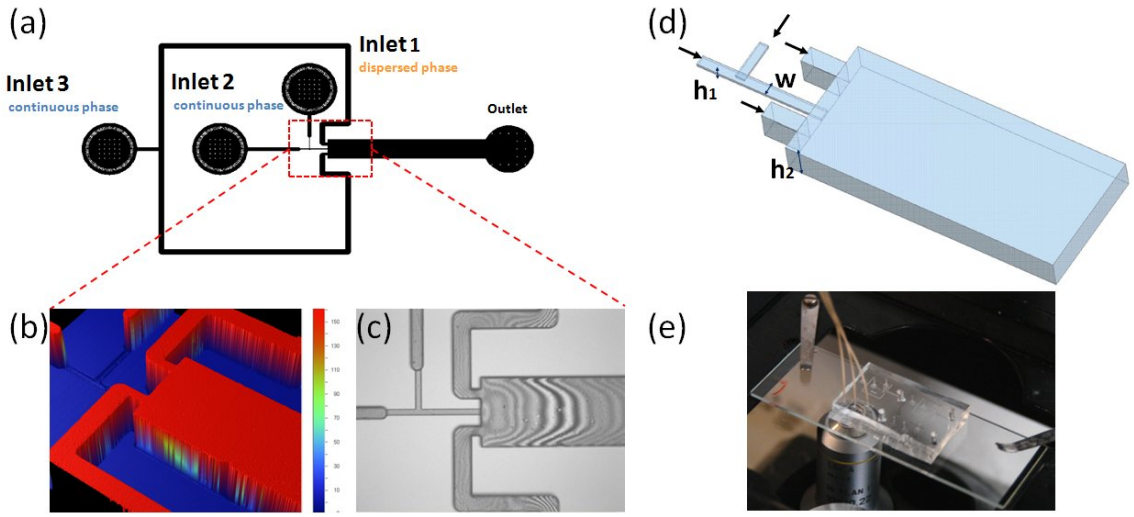

Figure 4.1: (a) Sketch of the design of microfluidic device. There are three inlets: dispersed phase (Inlet1), continuous phase (Inlet2) and dilution continuous phase (Inlet3). A circular filter is integrated inside of each inlet. (b) 3D surface profile plot of the center part of the microfluidic system. (c) Optical micrographs of the center part of the microfluidic device.(d) Illustration of the center part of the two-layers device: T-junction in a shallow channel (with the height h_1) followed by a deep reservoir channel and two additional entries (with the height h_2). (e) Photograph of an integrated chip mounted on microscope.

Geometry	W(μm)	h_1(μm)	h_2(μm)	W/h_1
A1	10	1	22	10
A2	20	1	22	20
B1	50	6.3	95	4.8
B2	100	6.3	95	5.4
C1	50	10	163	5
C2	100	10	163	10

Table 4.1: The typical dimensions of the geometrical parameters for the microfluidic devices.

characteristics of the typical microfluidic device geometry are summarized in Table 4.1. The width of the reservoir channel is 600μm and the length is 5000μm for all systems.

4.3 Regime decomposition

We can distinguish two stages during the hydrodynamics self-assembly: **Cluster Production** and **Cluster Transport**. Those two stages are illustrated in figure 4.2.

The **Cluster Production** takes place at the T-junction and at the 3D step. At the T-junction, the dispersed phase and continuous fluids flow through two orthogonal channels and form drop plug when they meet. The droplet plug then flows further under the pressure gradient in the Hele-Shaw channel towards 3D step where it could generate several smaller spherical droplets by step emulsification.

The stage of **Cluster Transport** is the process in which once the droplets enter the

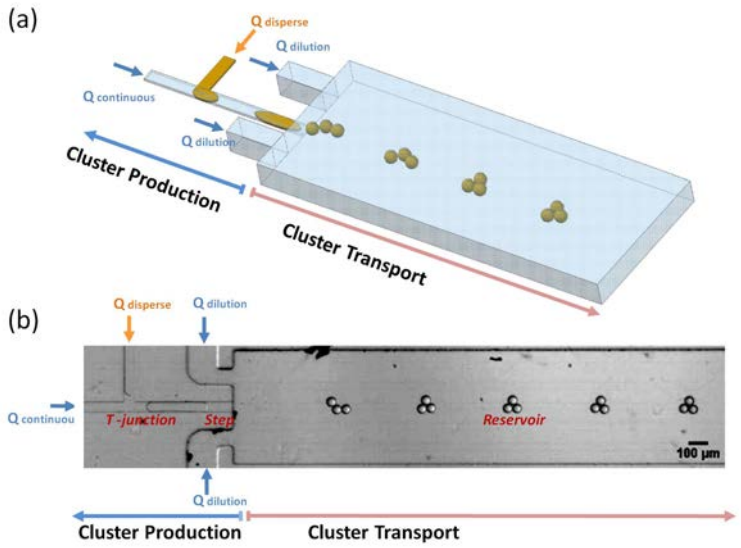

Figure 4.2: (a)Schematic drawing of the microfluidic device showing the dispersed (yellow) and continuous phase (blue) forming a droplet plug at the T-junction in the shallow layer and then breaking further into smaller spherical droplets in the 3D step. We distinguish the droplets generation part and droplets transport part in the device. (b) Optical micrograph of the microfluidic PDMS system with W = $50\mu m$, $h_1 = 10\mu m$ and $h_2 = 163\mu m$. A long plug can be seen in the shallow T-junction channel, it breaks into three droplets of equal size at the step. Scale bar is 100 μm.

3D reservoir, they will aggregate together and organize themselves to adopt some configurations according to the experimental conditions and to be conveyed downstream. In this stage, for the convenience description, we define two different regions in the microfluidic reservoir:

– region I - Close to the entry;
– region II - Away from the entry.

We will discuss the flow characteristics of those two regions in detail later in the **Cluster Transport** part.

4.3.1 Cluster production

Hele-Shaw T-junction production

The dynamics of break-up in the T-junction has been studied extensively and a great deal of progress has been made in understanding the physical mechanisms involved [126] [127] [128] [129]. Over a wide range of flow rates, uniform droplet production can be obtained.

In the chapter 1, we have briefly introduced the microfluidic T-junction. Previous experimental studies of droplet breakup at T-junctions have focused on two distinct breakup regimes [110] [112] [237] [238]. One is the **dripping regime**: the droplets generated are smaller than the channel width and it is observed that the droplets size depends predominantly on the capillary number Ca and not on the flow rate ratio $Q_{disperse}/Q_{continuous}$. Scaling models developed to describe these experiments assume that the viscous shear stress is the dominant force. Another breakup mechanism is the **squeezing regime** in which the droplet obstructs the channel as it grows and forms a plug-like shapes. The

droplet size depends predominantly on the flow rate ratio $Q_{disperse}/Q_{continuous}$ and not on the capillary number Ca. Scaling arguments developed to describe theses experiments neglect the influence of the viscous shear stress and assume that the dominant force is the squeezing pressure.

In our study, the dispersed phase channel width and the continuous phase channel width are the same, i.e. $W_{disperse}/W_{continuous}$ =1; however the ratio of the channel width to the channel height is quite large (W/h_1 ranges from 4.8 to 20, see Table 4.1), thus the formation of droplets takes place in a microfluidic Hele-Shaw T-junction. We use syringe pumps to inject fluids into microfluidic channels for most of the T-junction study, however, for the system with smallest dimensions (i.e. h_1=1μm), we take pressure controller (MFCS Fluident) for faster reponse time. We present a comprehensive experimental study in which we systematically vary the flow rate ratio $Q_{disperse}/Q_{continuous}$ and the capillary number for different channel geometries. As this analysis is only focused on the T-junction, we fix the flow rate of the dilution phase $Q_{dilution}$ = 15μL/min for all studies and vary only the flow rate from 30 nL/min to 500nL/min for the disperse phase and from 40nL/min to 4000nL/min for the continuous phase.

Interestingly, we observe that in our experiments, even if the conditions that the ratio $W_{disperse}/W_{continuous}$ of order 1 and the Ca is low enough (typical value between 0.001 to 0.008) are satisfied, the droplets don't obstruct completely the channel during the whole pinch-off process as they do in the squeezing regime: a gap exists through which the continuous phase can flow between the water-oil interface and the channel walls.

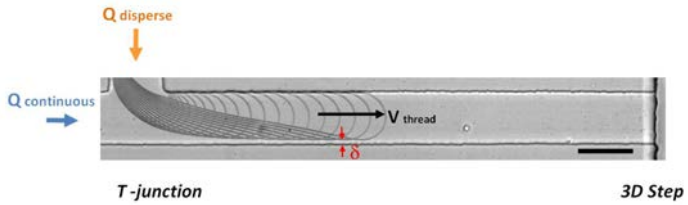

Figure 4.3: Chronograph of the droplet growth and pinch off process at the T-junction. 1ms separate two successive positions. System with $W = 50\mu m, h_1 = 6.3\mu$m, $Q_{disperse}$ =25nL/min,$Q_{continuous}$ =400nL/min and $Q_{dilution}$ =15μL/min.The scale bar is 50μm.

In figure 4.4, we plot the fully developped gap width as a function of flow rate ratio $Q_{disperse}/Q_{continuous}$ in figure (a), (b) and as a function of Ca for several fixed flow rate ratio ($Q_{disperse}/Q_{continuous}$ ranges from 0.052 to 0.207) in figure (c).

We observe that the gap width decreases when the droplet is growing as the droplet grows, then it reachs a constant value for a fixed flow rate ratio (see figure 4.3 and figure 4.4). The plug interface advance velocity during the pinch off is also constant. This breakup process in the Hele-Shaw T-junction is quasi-statics. This regime cannot be totally explained by the squeezing, we assume that the breakup mechanism depends on the flow rate ratio $Q_{disperse}/Q_{continuous}$ as well as the capillary number. This droplet breakup mechanism in Hele-Shaw channel deserves some more theoretical studies which, however, is out of the scope of this thesis.

The volume of the droplets can be adjusted by changing the flow rates of the dispersed phase and continuous phase. Figure 4.5(a) shows the dimensionless droplet volume (droplet volume V normalized by W^2h_1) as function of flow rate ratio $Q_{disperse}/Q_{continuous}$ for different systems. The dependence on capillary number is also shown in figure 4.5(b). Over the range of flow conditions that we apply, we observe that the droplet volume increases as the flow rate ratio increases and the droplet volume decreases as the capillary

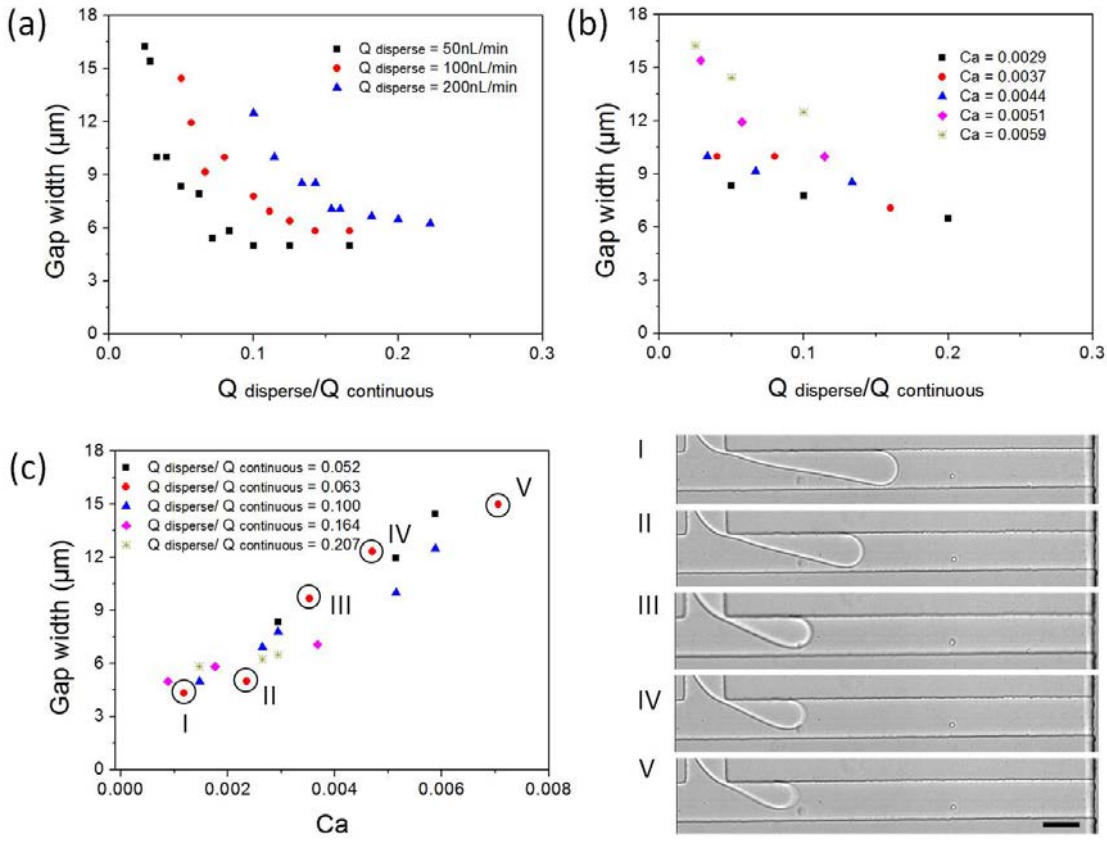

Figure 4.4: Dependence of the gap width between the droplet interface and the wall of the Hele-shaw channel ($W = 50\mu m, h_1 = 6.3\mu m$) on the dispersed and continuous phases flow rate ratio $Q_{disperse}/Q_{continuous}$ as well as the Capillary number. (a) Gap width as a function of flow rate ratio $Q_{disperse}/Q_{continuous}$, three series of data for constant value of $Q_{disperse}$=50nL/min, 100nL/min and 200nL/min respectively. (b) Gap width as a function of flow rate ratio $Q_{disperse}/Q_{continuous}$ for capillary number between 0.0029 to 0.0059. (c) Gap width as a function of capillary number for flow rate ratio $Q_{disperse}/Q_{continuous}$ varying form 0.052 to 0.207. The Roman numerals correspond to the optical micrographs shown below the figures, taken at $Q_{disperse}$ =25nL/min and $Q_{continuous}$ =400nL/min for I, 50nL/min and 800nL/min for II, 75nL/min and 1200nL/min for III, 100nL/min and 1600nL/min for IV and 150nL/min and 2400nL/min for V respectively. The scale bar is 50μm.

number increase, as shown in figure 4.5. This trend is consistent with many other studies [110] [112] [126] [127] [128] [129] .

For other microfluidic systems with different geometrical parameters (systems with W=50μm, h_1=6.3μm; W=50μm, h_1=10μm and W=100μm, h_1=10μm), the dimensionless droplet volume (droplet volume V normalized by W^2h_1) and the dimensionless droplet length (droplet length L normalized by W) present the same trends. The results obtained from four different microfluidic systems are shown in the figure 4.6.

All these experimental results above are performed by fixing $Q_{dilute}(P_{dilute})$, and by varing only continuous phase and dispersed phase. We carried out also another series

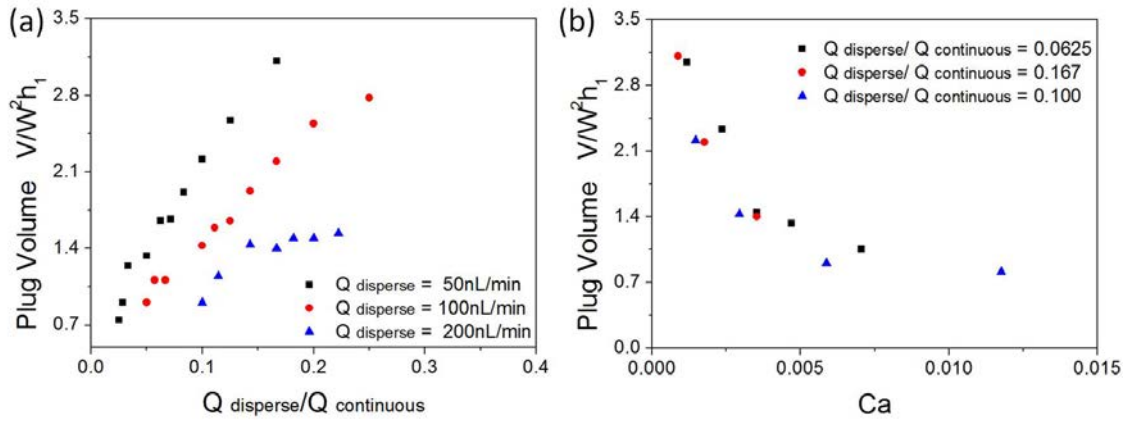

Figure 4.5: Dimensionless plug volume as a function of $Q_{disperse}/Q_{continuous}$ and capillary number. The microchannel geometry is given by W=50 μm, h_1 =6.3μm. (a) Dimensionless volume of the droplets (V/W^2h_1) plotted as a function of the flow rate ratio of the dispersed and continuous fluids for the geometry (W=50μm and h_1=6.3μm). There are three series of data for constant value of $Q_{disperse}$=50nL/min, 100nL/min and 200nL/min respectively. (b) Dimensionless volume of the droplets (V/W^2h_1) plotted as a function of capillary number for $Q_{disperse}/Q_{continuous}$ varying from 0.0625 to 0.100.

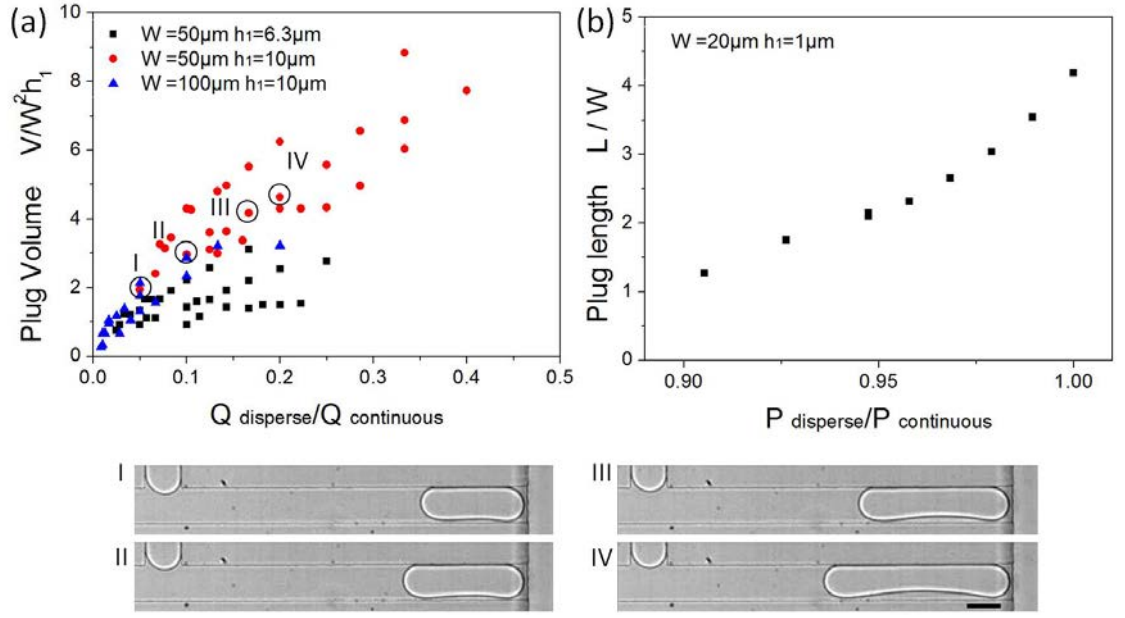

Figure 4.6: (a)Dimensionless plug volume as a function of $Q_{disperse}/Q_{continuous}$ for microfluidic systems (W=50μm, h_1=6.3μm; W=50μm, h_1=10μm; W=100μm, h_1=10μm). The Roman numerals correspond to the optical micrographs shown below the figures, taken at $Q_{disperse}$ =100nL/min and $Q_{continuous}$ =2000, 1000, 600 and 500nL/min for I, II, III and IV respectively. The scale bar is 50μm. (b) Dimensionless plug length as a function of $Q_{disperse}/Q_{continuous}$ for small system (W=20μm and h_1=1μm).

of experiments by fixing the $Q_{continuous}$ (or $P_{continuous}$) and $Q_{disperse}$ (or $P_{disperse}$) while changing the flow condition of the dilution phase Q_{dilute} (or P_{dilute}). We observed that the plug-like droplet production at the Hele-Shaw T-junction is less dependent on the dilution

phase flow rate (or pressure). With the microfluidic systems that we tested in table 4.1, we find that the plug droplet volume and the production frequency is slightly changed and the smaller the dimensions are, the less influence is observed on the droplet production.

We suggest that the hydraulic resistance in the shallow Hele-Shaw layer, is much higher compared with that in the reservoir channel, thus the real-time pressure difference changes (which is induced by the Q_{dilute} (or P_{dilute})) located in the reservoir have little influences on the plug droplet production process. Figure 4.7 shows that, with the system W=20μm, h_1=1μm, h_2=22μm, if we fix $Q_{disperse}$= 10nL/min , $Q_{continuous}$ = 50nL/min, and $Q_{dilution}$ varies from 50 nL/min to 1600 nL/min, the plug volume and plug production frequency are nearly unchanged over the whole range.

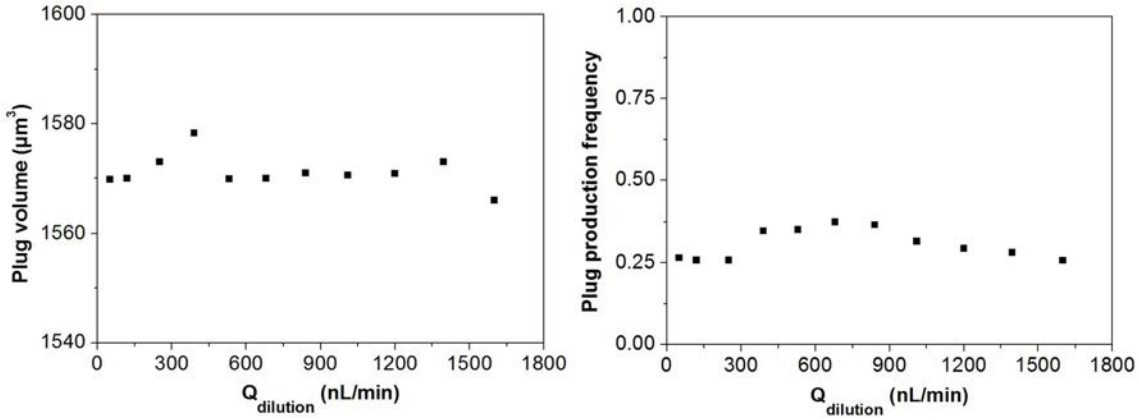

Figure 4.7: The plug-like droplets produced at T-junction is less dependent on the flow rate (pressure) of the dilution inlet. Data obtained from microfluidic system with W=20μm and h_1=1μm. $Q_{disperse}$= 10nL/min , $Q_{continuous}$ = 50nL/min, and $Q_{dilution}$=50-1600 nL/min. (a) Plug volume dependency. (b) Plug production frequency dependency.

By taking advantage of this effect, we could change the flow conditions in the reservoir channel without evoking droplet production disorder, which provides us a good tuning range over the droplets self-assembly behaviors. These additional dilute flows contribute to transport the droplet aggregates along with to space the clusters, i.e. increase the distance between two successive clusters. The effect of the dilution flow is further discussed in Cluster Transport part concerning cluster spacing control.

3D Step emulsification

Step emulsification method is widely applicable and robust to produce monodisperse droplets over a wide range of sizes [15] [121]. In this method, the dispersed phase fluid is pushed into a microchannel that leads to a step change in height. Monodisperse droplets are produced at the 3D step and then are transported by the flow of the carrier fluid in the reservoir channel. Several research groups have taken advantage of the steps in order to produce droplets of a well calibrated size, usually combining them with the classical T-junction or flow focusing junction [126]. Figure 4.8 shows dripping and jetting, two droplets generation regimes at 3D step.

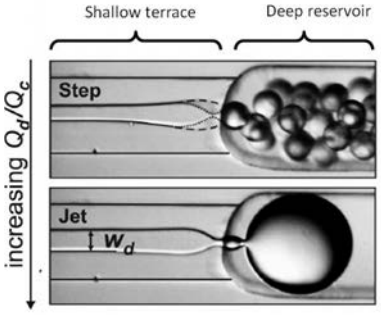

Figure 4.8: Optical micrographs of drop detachment *via* step and jet breakup mechanisms. Step break-up occurs precisely at the step. Jet breakup occurs downstream. Figure adapted from [121].

All these studies concerning step emulsification are focused on the stationary emission process (i.e. the dispersed and continuous phase flowing side by side with a tongue shape). While in our study, we explore a mixed breakup mechanism in which the T-junction production in the upstream and the 3D step generation are coupled: plug-like droplets are driven towards the step instead of a continuous flow. The droplet breakup at the step takes place in a discontinuous manner. According to our knowledge, this combination has not been reported yet. Figure 4.9 shows how plugs of different volumes break into small droplets at the 3D step.

As it has been discussed in the T-junction production, the volume of plug-like droplet is increasing with the flow rate ratio $Q_{disperse}/Q_{continuous}$ (see figure 4.9(a)). The plug breaks into several droplets according to its volume. We notice that although the number of droplets generated from the plug can be variable, the radius of the first droplet coming from the step increases at low $Q_{disperse}/Q_{continuous}$ and it reachs a constant value as $Q_{disperse}/Q_{continuous}$ increases. For the system with W=50μm, h_1=6.3μm, the droplet size is stabilized around 16μm (R $\approx$ 2.5 h_1). For other geometries (W=100μm, h_1=10μm), the trend is the same (see figure 4.10) and the droplet size is stabilized around 27μm (R $\approx$ 2.7 h_1).

The experimental results suggest that for a fixed geometry, it exists a corresponding critical volume (V*), below which there is no breakup, the narrowing process cannot be completed, i.e. the tongue's width couldn't reach the critical width to have the fast pinch-off, induced by Plateau -Rayleigh instability. Above this volume, the droplet can further break up into several smaller droplets at the 3D step according to the initial plug volume. As a result, we can have one droplet with a satellite, two droplets, two droplets with a satellite etc. In the mean time, if we plot the number of droplets generated at step as a function of the plug volume, the devil's staircase is observed when the number of the

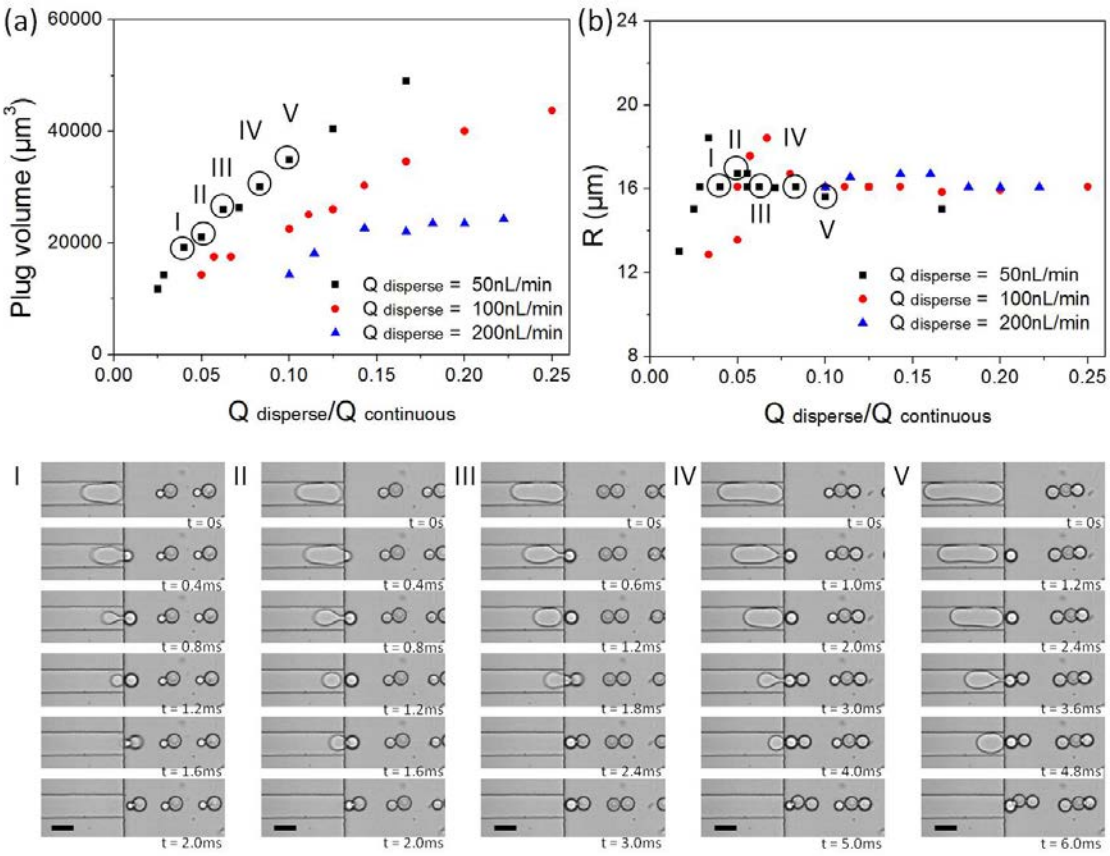

Figure 4.9: (a) Plug volume as a function of $Q_{disperse}/Q_{continuous}$ for microfluidic systems (W=50μm, h_1=6.3μm). The Roman numerals correspond to the optical micrographs shown below the figures, taken at $Q_{disperse}$ =50nL/min and $Q_{continuous}$ =1250, 1000, 800, 600 and 500nL/min for I, II, III, IV and V respectively. The scale bar is 50μm. (b) The radius of the first produced droplet as a function of $Q_{disperse}/Q_{continuous}$. There are three series of data for constant value of $Q_{disperse}$ = 50nL/min, 100nL/min, 200nL/min respectively.

droplets is an integer (N = 1, 2, 3 etc.). The devil's staircase in mathematical analysis refers to any singular function in general. This 3D step emulsification presents a behavior similar to the frequency locking phenomenon which gives rise to the devil's staircase. As a matter of fact, when the droplet plug volume is close to 2 times of the critical volume, for instance 1.95V* or 2.05V*, in both cases it tends to break into 2 equal sized droplets instead of one droplet and one big satellite droplet (1.95V*) or two droplets and one tiny droplet (2.05V*). Similar reasoning works for other integer N = 3, 4, 5 etc.

The dependence of R on W and h_1 are shown in the figure 4.12. We found empirically that corresponding critical radius R is around 2.5 times the height of the first layer h_1, this founding is confirmed by other studies [15] [121] [125]. This critical radius R is mainly dictated by the height h_1. The width W and the flow rate seem to have little influence.

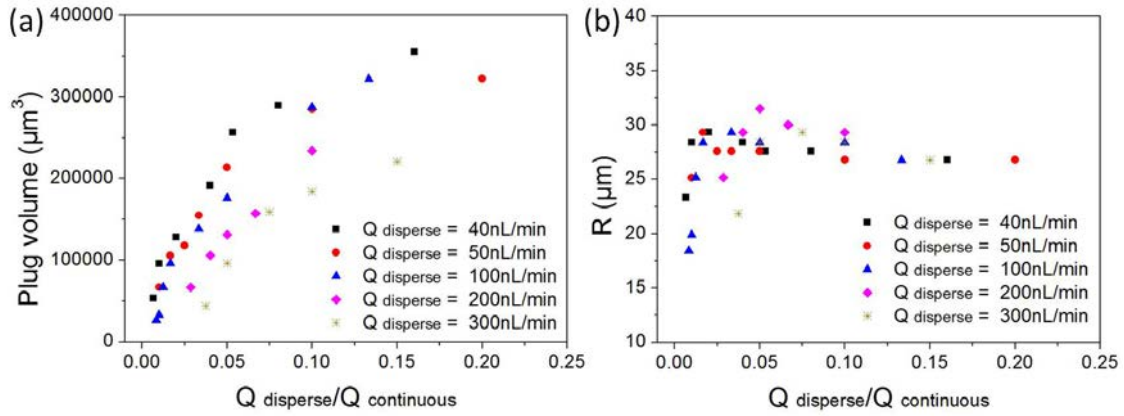

Figure 4.10: (a) Plug volume as a function of $Q_{disperse}/Q_{continuous}$ for microfluidic systems (W=50μm, h_1=10μm). (b) The radius of the first produced droplet as a function of $Q_{disperse}/Q_{continuous}$. There are three series of data for constant value of $Q_{disperse}$ = 40nL/min, 50nL/min, 100nL/min, 200nL/min, 300nL/min respectively.

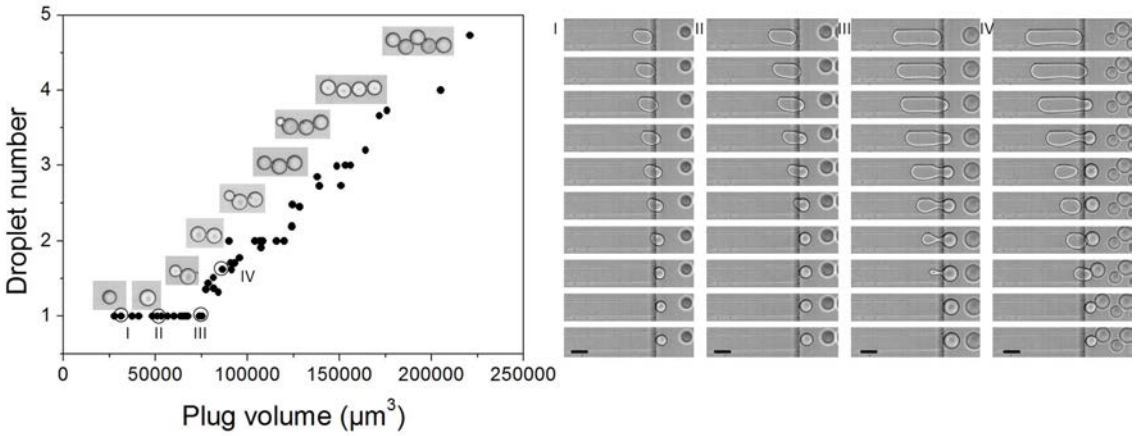

Figure 4.11: Droplets number as a function of the plug volume for a microfluidic system (W=50μm, h_1=10μm). Successive images of the droplet generation are shown on the right of the figure. The Roman numerals correspond to the optical micrographs taken at $Q_{disperse}$ =100nL/min and $Q_{continuous}$ =5000, 3000, 1000 and 750nL/min for I, II, III and IV respectively. The scale bar is 50μm. The corresponding time intervals are 0.1ms (I), 0.25ms (II), 0.6ms (III) and 1.1ms (IV).

Phase diagram

To conclude on the Cluster production part, figure 4.13 shows a typical phase diagram that describes the regimes for our microfluidic two-layers system. The regime of jetting is not shown in this diagram because it is located far away (at higher $Q_{disperse}$ value).

There are three main regimes:

– I: Dripping/Squeezing at T junction
– II: Transition
– III: Step Emulsification

With different geometrical parameters of the microfluidic devices (W, h_1, h_2), the regimes may shift but the general tendency will remain the same. As we may notice, the operation regime is located in the low $Q_{dispersed}$ and low $Q_{continuous}$ area.

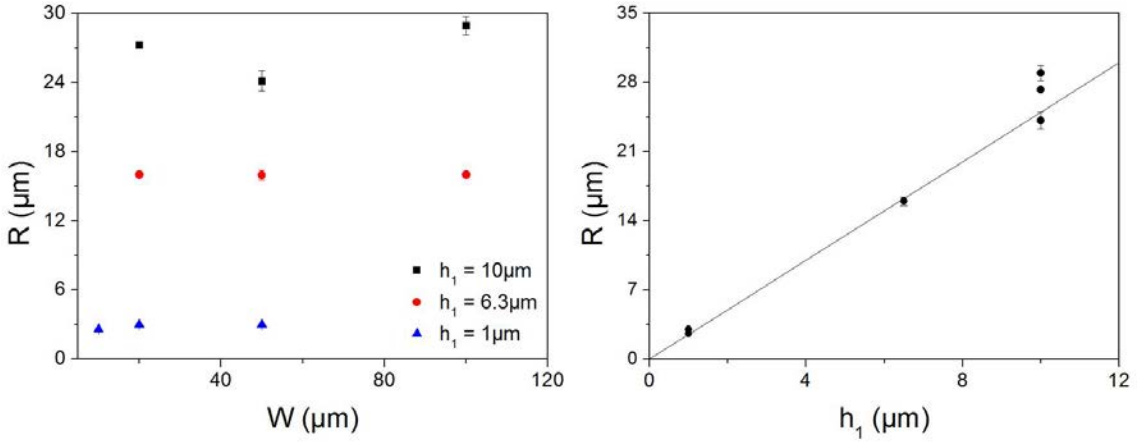

Figure 4.12: Dependence of the fully developed droplet radius R produced at the step, on the width of the T-junction W and the height of the first layer h_1, the flow ratios $Q_{disperse}/Q_{continuous}$ varies from 0.01 to 0.3 and the capillary number from 0.002 to 0.008 among all experimental data. In our experimental range, the radius is mainly dominated by h_1.

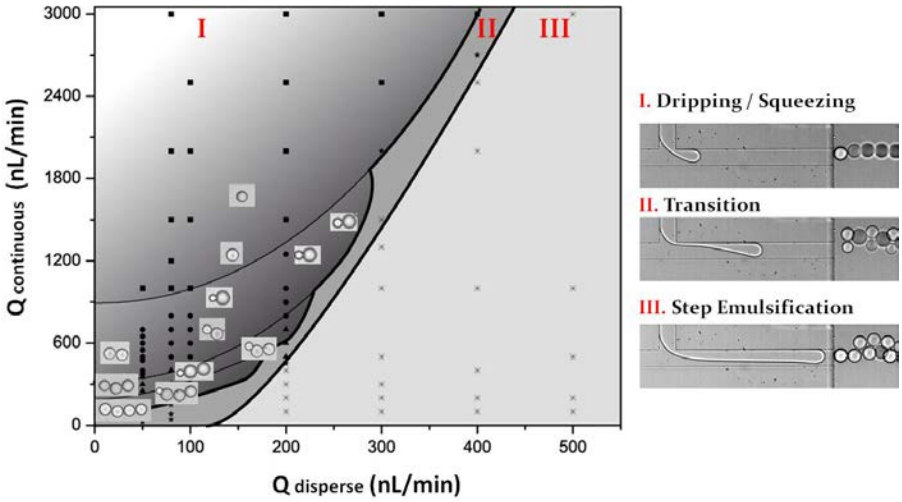

Figure 4.13: Phase diagramme showing the three main regimes. The most important for our study is the regime of dripping/squeezing at the T-junction. It is in this regime that different clusters can be obtained.

4.3.2 Cluster transport

After the droplets enter into the 3D reservoir channel, they are subjected to the flow field. We investigate the behavior of the droplet transport. Interestingly, the rearrangement of droplet aggregates is observed which may end with certain stable structures according to the flow conditions (for the adhesive formulation). In the transport part, we first introduce the way we control the spacing and measure the droplet position in z direction to have a full image of the droplet's motion in the reservoir channel. Afterward we describe the experimental cluster formation observations, followed by a numerical analysis of the flow field conditions in the absence of droplets in the reservoir channel. The hydrodynamic assisted clustering process will be further discussed in our preprint paper: Self-assembly driven by hydrodynamic dipolar interactions.

Cluster spacing control

As we have shown in the cluster production part (see figure 4.11), the number of droplets inside a cluster could be easily predicted by controlling the plug volume produced with the upstream T-junction. Once those droplets enter the microfluidic reservoir, they are immediately subjected to the flow field and be conveyed downstream. Lots of morphologies are discovered with our approach, as shown in figure 4.14.

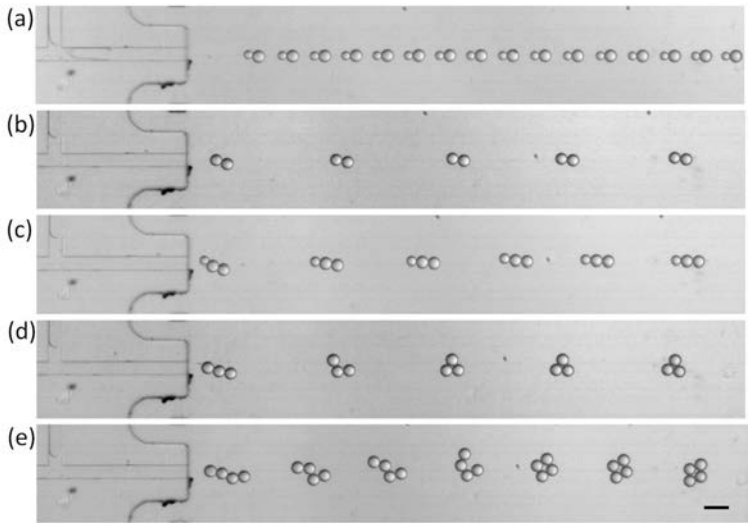

Figure 4.14: Optical micrographs of different morphologies obtained through our system. System with $h_1 = 50\mu m, h_2 = 160\mu m$. n=1.5, 2, 2.5, 3, 4. Scale bar is 100 μm.

The spacing of the clusters is one of the key parameters to control the clustering process. The spacing of the cluster depends on two values: the droplet **production frequency** and the **velocity field** in the reservoir which is mainly dominated by the dilution phase. The faster the droplets are generated and the more slowly they are conveyed, the higher the risks for the droplets to accumulate at the entrance of the reservoir channel and to lose their identities immediately. Fortunately, the droplet production is not much influenced by the dilution phase (see figure 4.7) which means that there is only a weak dependence between the systems. This makes it easy for us to finely tune the cluster spacing.

We show results of the clusters with different spacing for comparison. In figure 4.15, we keep the $P_{dilution}$ fixed and change slightly $P_{disperse}$ and $P_{continuous}$ simultaneously. This fine tuning of pressures allows us to have more or less the same length of plug and the cluster transport speed while the droplets production frequency at T-junction is modified. In figure 4.15 (a), droplet generation frequency (f = 1.64 Hz) is higher than that in figure 4.15 (b) (f = 0.31 Hz) and the cluster transport velocity is the same.

Figure 4.16 shows another example in which we control the spacing of triplet clusters by fixing the pressure of the dispersed $P_{disperse}$ and of the continuous phase $P_{continuous}$ while changing the pressure of the dilution phase $P_{dilution}$. In those experimental conditions, as $P_{disperse}$ and $P_{continuous}$ are fixed, the plug size and generation frequency is nearly the same (f $\approx$ 1.25 Hz). We increase $P_{disperse}$ and we observe that it is the transport speed of clusters that control the spacing between cluster entities: In figure 4.15 (a), $P_{dilution}$ is 5 mbar, it is increased to 10 mbar in (b) and 20 mbar in (c). The spacing distances between the clusters are 100μm, 400μm and 1100μm respectively in those three cases. Similar results can be easily obtained for other microfluidic systems with smaller geometrical dimensions (see figure 4.17; system with W=20μm, h_1=10μm, h_2=22μm).

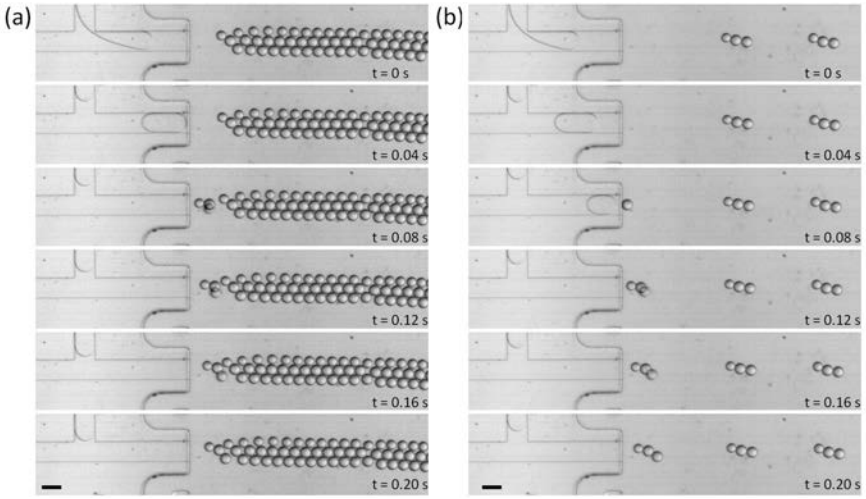

Figure 4.15: Spacing control of the cluster entities by changing $P_{disperse}$ and $P_{continuous}$. System with W=100μm, h_1=10μm, h_2=160μm. (a) $P_{disperse}$=33mbar, $P_{continuous}$=10 mbar, $P_{dilution}$= 20 mbar.(b) $P_{disperse}$=35mbar, $P_{continuous}$=10 mbar, $P_{dilution}$= 20 mbar. Scale bar is 100 μm.

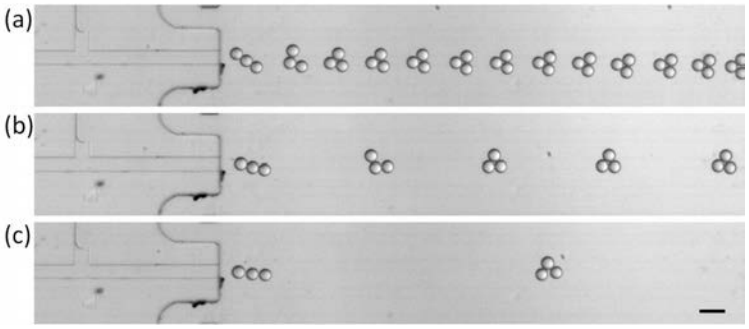

Figure 4.16: Spacing control of the cluster entities by changing $P_{dilution}$. System with W=50μm, h_1=10μm, h_2=160μm. (a) $P_{disperse}$=38mbar, $P_{continuous}$=11mbar, $P_{dilution}$= 20mbar. The distance between clusters is 100μm.(b) $P_{disperse}$=38mbar, $P_{continuous}$=11mbar, $P_{dilution}$= 80mbar. The distance between clusters is 400μm.(c) $P_{disperse}$=38mbar, $P_{continuous}$=11mbar, $P_{dilution}$= 120mbar. The distance between clusters is 1100μm. The scale bar is 100μm.

Droplet z position measurement

Adaptive focus control

We are interested in recognizing the real time z position of the droplets in the reservoir as a function of time to better understand their flow environment. By using the fully automated Leica microscope system with Adaptive Focus Control (AFC), the measurement of the z position of droplets could be realized. We carry out the z position measurement on the smallest microfluidic system which has W = 20μm, h_1 = 1μm and h_2 = 22μm.

The fully automated AFC is a powerful tool for recordings in combination with multi-positioning, z-stacking and multifluorescence experiments. After setting the focus position of the substrate of our PDMS devise as reference position z = 0 μm, we regulate the focus position progressively to screen throughout the whole height of the microfluidic reservoir channel (h_2 = 22μm). As the clustering process is reproducible and stationary, we could

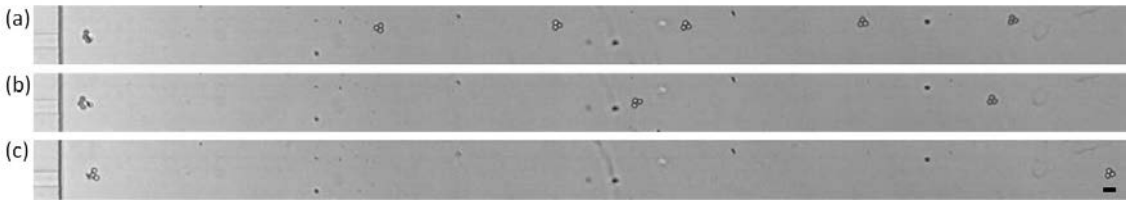

Figure 4.17: Spacing control of the cluster entities by changing $P_{dilution}$. System with W=20μm, h_1=10μm, h_2=22μm. (a) $P_{disperse}$=1000 mbar, $P_{continuous}$=1000 mbar, $P_{dilution}$= 5 mbar. The distance between clusters is 300 μm.(b) $P_{disperse}$=1000 mbar, $P_{continuous}$=1000 mbar, $P_{dilution}$= 10 mbar. The distance between clusters is 600 μm.(c) $P_{disperse}$=1000 mbar, $P_{continuous}$=1000 mbar, $P_{dilution}$= 20mbar. The distance between clusters is 1600 μm. The scale bar is 20μm.

register the videos of the cluster transport at different z positions and follow the z position evolution of the droplets during the transport process in the reservoir channel. Figure 4.18 shows an example of the clusters images taken at a fix distance to the step x $\approx$ 40μm, with different z position focus from 0μm to 22μm. We can identify the z position of the droplet with the sharpest image, which is in between z =11 μm and 15 μm.

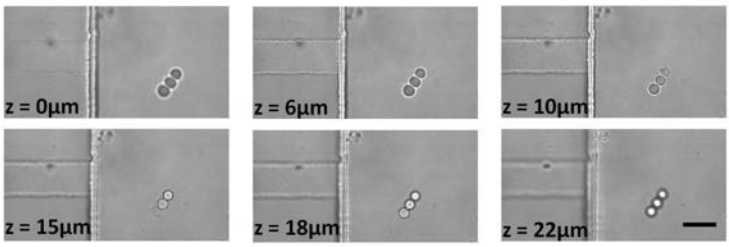

Figure 4.18: Optical micrographs of a triplet of droplets located at 40μm away from the step, with different z focus position from the bottom of the microfluidic channel z = 0 μm to the top z = 22μm. When the focus is away from the droplets, the cluster's contour is blurred and it turns clearer if the focus is on its location. The scale bar is 20 μm.

With this method, we carried out the measurements of the droplet position under different flow conditions. Results are reported in graph 4.19. A fast evolution towards the middle height z = 11 μm is observed within a few tens of micron.

Microscope confocale imaging

Confocal imaging was also carried out to invetigate the droplet z position. This was performed at le Commissariat à l'énergie atomique et aux énergies alternatives (CEA), Saclay in France. We produced a stationary train of clusters made of aqueous droplets flowing in the mineral oil. To help visualization, the dispersed phase was mixed with fluorescein isothiocyanate dextran. Rhodamine B red dye (6×10^{-3}% in aqueous solution), was infused into the channels and washed before the experiments to help visulizing the wall of channels. This dye has affinity to the PDMS and permeates the porous polymer matrix. Fluids were pumped into the devices through PEEK tubing using a pressure controller (MFCS Fluident). We performed the experiments with different flow conditions, the $P_{dillution}$ varies from 250 mbar to 700 mbar.

The trajectory of the stationary clusters train appears as a florescent tube due to the long imaging exposure time and the acquisition frequency. Figure 4.20 is the reconstruction of superimposed images with Olympus FLUOVIEW software. Throughout the

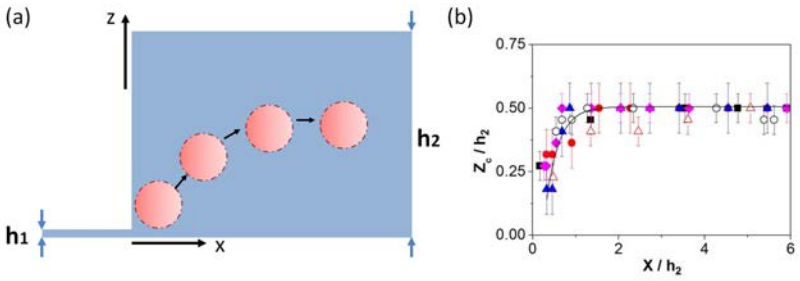

Figure 4.19: The droplet position in the reservoir channel. (a) Schematic drawing of the xz plan showing the droplet generated at the 3D step is flowing in both x and y directions. (b) The droplet position in z normalized by the reservoir channel height h_2 as a function of the distance to the step x. (■) N=4,$P_{dilution}$=0 mbar, (●) N=4,$P_{dilution}$=10 mbar, (▲) N=4,$P_{dilution}$=50 mbar, (◆)N=4,$P_{dilution}$=100 mbar, (❍)N=5,$P_{dilution}$=20 mbar, (△)N=6,$P_{dilution}$=20 mbar.

experiences, we observed a fast evolution of clusters towards the middle of the reservoir channel. In this reconstructed image, we put the entries in the up side to better visualize the coming flow.

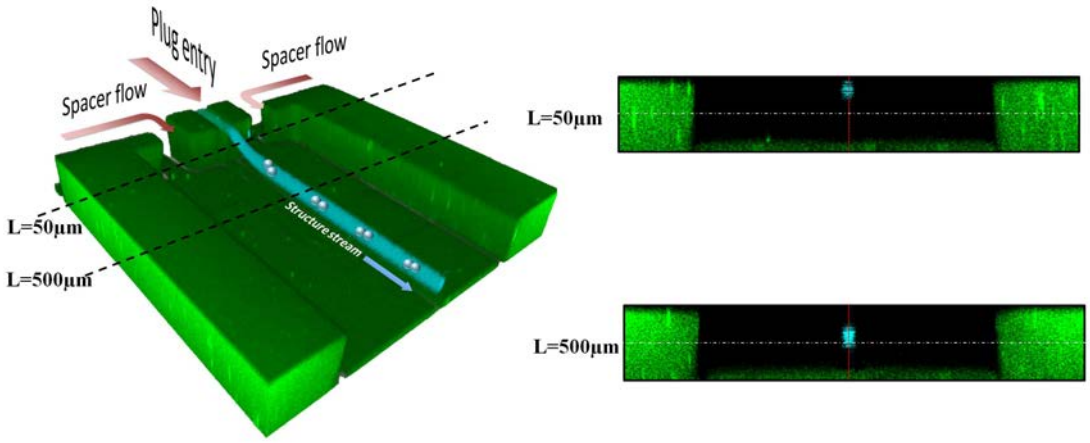

Figure 4.20: A three-dimensional confocal microscopy image of the collective trajectories of doublet clusters shows how the position of the cluster evolute after the step production. The surface of the channel is labeled for a more vivid observation. We add artificially the doublet clusters in the envelop of their trajectories. Two cross-sections of yz plan are shown in the right: close to the entries at L= 50μm and away from the entries at L= 500μm. A fast evolution towards the mid-plan is observed. PDMS system with W = 50μm, h_1 = 10μm and h_2 = 163μm. The stable doublet clusters production is obtained with $P_{disperse}$=80 mbar, $P_{continuous}$=90 mbar, $P_{dilution}$= 320 mbar.

4.4 Morphologies transition observations

4.4.1 (I): Stable morphologies

The morphologies of cluster aggregates increase dramatically with the number of constituent droplets. The complexity of possible organization is directly related to the droplet's number and size. The enumeration of clusters determines the set of minimally structures that can be formed by self-assembly.

Arkus et al.[239] have conducted an analysis which combines graph theory with geometry to analytically solve the problem for clusters satisfying minimal rigidity constraints($\geq$3 contacts per particle, $\geq$3N-6 total contacts). They have shown that up to N = 9, every packing has exactly **3N-6** contacts, so that all packing have the same potential energy. However, for n$\geq$9 the ground stated degeneracy increases exponentially. If we expand the graph theory to lower dimensions, the finite close packing is **2N-3** for 2D structures, and **N-1** as for 1D structures.

To begin with, we limit ourselves with clusters of identical constituent droplets (i.e. no satellite droplet is presented in the cluster). In the case of N = 2, only doublet can be obtained. For N = 3, stable triangle or chain structures are both possible to be produced with our experiments. For larger number of spheres, i.e. N $\geq$4, three dimensional structures are the finite close packings. The Figure 4.21(a) shows the three dimensional, two dimensional and one dimensional close packing structures of droplets having equal size from N = 2 to N = 6. All the corresponding clusters have been observed under different experimental conditions, results are shown in figure 4.21(b). When N $\geq$6, the clusters develop degeneracy in both 2D and 3D structures with different probabilities, we confirm this result with our experimental observations.

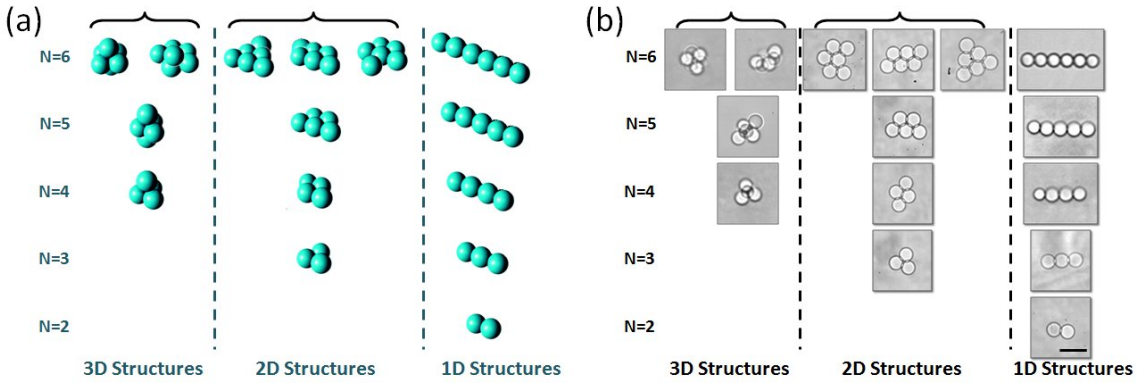

Figure 4.21: (a) The possible closing packing structures of clusters from N = 2 to N = 6.(b) The closing packing structures of clusters obtained from experiments with Fluorinated oil-in-water emulsion. The number varies from N = 2 to N = 6. When N=6, the degeneracy appears: 2 ground states for 3D structures and 3 ground states for 2D structures. The scale bar is 10 μm.

Besides those conventional packings, we also observe some unusual structures such as stable symmetrical T-shaped clusters which can also have long-life state. We have discovered many other packings that are hypostatic, namely they have fewer than the 2N-3 contacts required to be linearly rigid in 2D structures. Those morphologies are unfavorable in the terms of the minimization of potential energy, nevertheless, under hydrodynamic conditions, those clusters could be very stable (see figure 4.22(a)). In the presence of satellite droplets, more complex structures are also available. Figure 4.22(b) shows two

trains of clusters with satellites droplets.

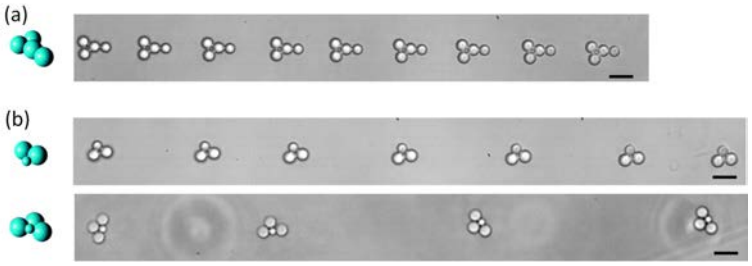

Figure 4.22: (a) Optical micrograph of a train of stable T-shaped clusters. (b) Optical micrographs of clusters that consist of non-identical droplets (two droplets and a satellite droplet/ three droplets with a satellite droplet). The scale bar is 10 μm.

The rearrangement of droplets configurations takes place immediately after they are produced at the step. The evolution towards stable clusters are shown in the figure 4.23. Figure(a), (b) are triplets and quadruplets of droplets with diameter 50μm and (c), (d) with diameter 5μm.

Similar fast evolutions towards stable morphologies are observed using numerical simulation(see figure 2, self-assembly kinetics in preprint). We reproduce well the rearrangement using dipolar interaction and adhesion interaction which suggests that it is the interplay between the hydrodynamic and physico-chemical forces that mediates the evolution of constituent droplets positions in the cluster. Here we mainly present the observations and the discussion of the physics will be addressed in the paper.

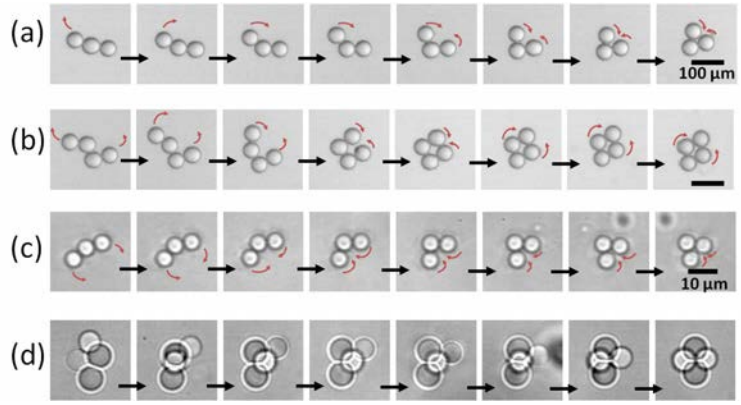

Figure 4.23: (a) Snapshot showing the evolution towards clusters to triangle-like stable triplet clusters. (b) The evolution towards clusters to rhombus-like stable quadruplet clusters. (a), (b) Stable clusters obtained with PDMS system with W=50μm, h_1=10μm, h_2=163μm. Scale bar, 100 μm. (c) Snapshot showing the evolution towards clusters to triangle-like stable triplet clusters. (d) The evolution towards clusters to tetrahedron stable quadruplet clusters. (c), (d) Stable clusters obtained with PDMS system with W=20μm, h_1=1μm, h_2=22μm. Scale bar, 100 μm. Scale bar, 10 μm. The formulation used is fluorinated oil droplets in water with 2% SDS.

We characterized the polydispersity of stable clusters obtained. As for the anisotropic objects, we use Feret's diameter to analyse cluster distribution. Feret's diameter is deducted from the projected area of the particles using a slide gauge. It is defined as the distance between two parallel tangents of the particle at an arbitrary angle. We plot the

histogram of the ratio of the Maximum Feret's diameter D_{fmax}, and Minimum Feret's diameter D_{fmin} of each clusters flowing in the reservoir. Figure 4.24 shows results of the doublets, triplets and quadruplets of droplets with diameter 50μm and figure (c) the pentamers of droplets with diameter 5μm. The clusters produced with our approach are highly monodispersed, with CV$\leq$5 %.

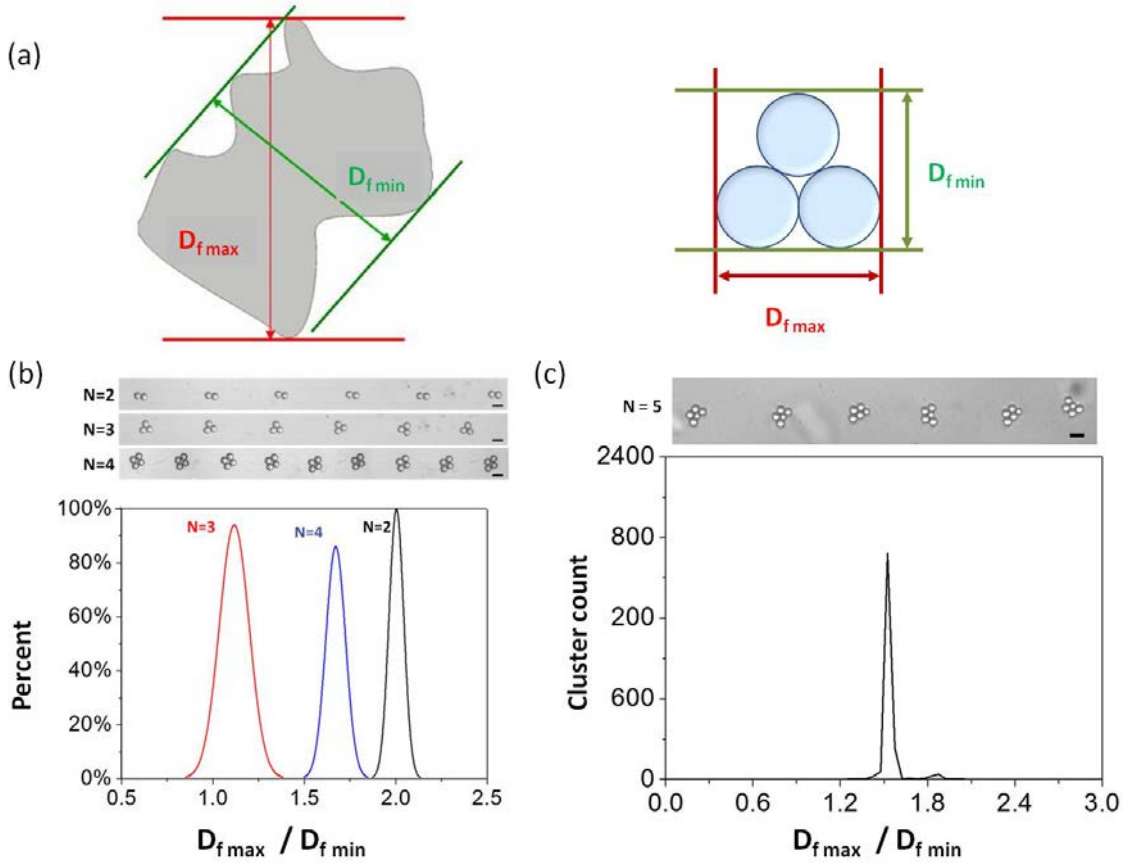

Figure 4.24: (a) Definition of Feret's diameters, the maximun diameter is illustrated in red and minimun in green. (b) Size distribution of a population of 152 doublets, 382 triplets and 217 quadruplets with d= 50 μm in diameter, showing a coefficient of variation CV (i.e., the quantity 100 σ/ (D_{fmax}/D_{fmin})) below 5%, where σ is the standard deviation and D_{fmax}/D_{fmin} is the ratio between the Feret's maxium diameter and the Feret's minimum of clusters obtained with image processing. Scale bar, 100μm. (c) Size distribution of a population of 2134 pentamers, with d= 5 μm in diameter. Scale bar, 10μm.

4.4.2 (II): Oscillatory morphologies

So far we have presented the stable morphologies. We observe that the clusters could develop permanent 2D configurational chaotic oscillations too, a phenomenon never reported in the literature. In the following part, we will present qualitatively this dynamical oscillation behavior.

The chaotic oscillations are observed as the velocity field increases and the adhesion between the droplets decreases. Those clusters develop 2D configurational chaotic oscillations. Figure 4.25 shows time sequences of oscillation events. Clusters composed of 3, 4, 5 droplets show similar oscillatory behaviors. Droplet may glide and rotate from one

position to another without detaching from the each other.

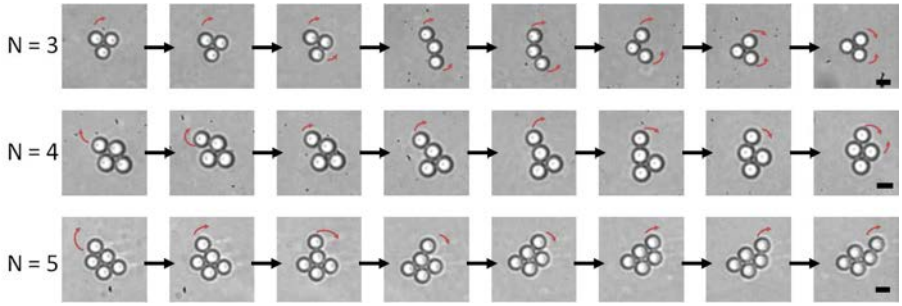

Figure 4.25: Snapshot showing the oscillation of clusters (N = 3, 4, 5). Clusters are flowing from left to right. The scale bar is 5μm. Fluorinated oil droplets in water with 0.4% SDS.

With the image treatment, we measure the average of droplet distances inside a cluster:

$$\overline{r} = \frac{\sum_{i,j}^{N} r_{ij}}{C_N^2}$$

We plot the average of droplet distances $\overline{r}$ normalized by the droplet radius R as a function of the time (see figure 4.26). In the finite close packing state, the dimensionless value $\overline{r}/R$ is the lowest value corresponding to the most compact form. When the cluster undergoes oscillations, this dimensionless value will fluctuate according to the conformations. The oscillatory time scale under this experiment condition is in the order of seconds.

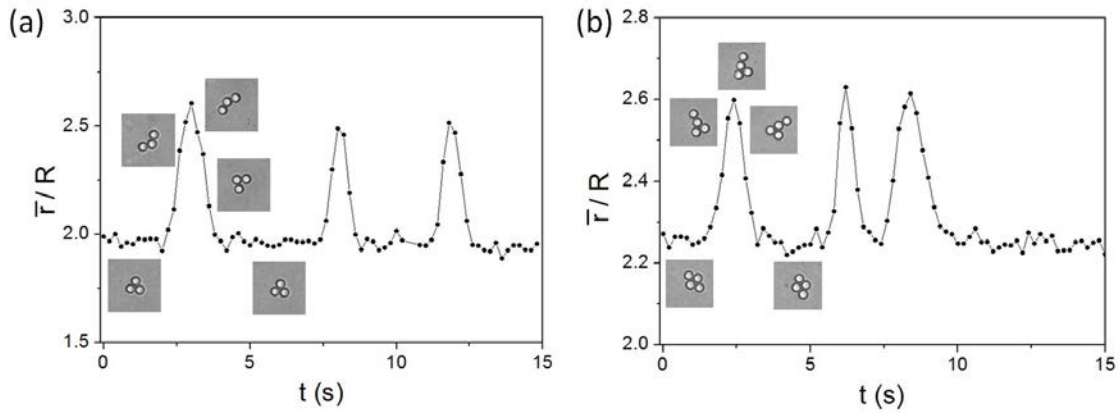

Figure 4.26: Average of droplet distances $\overline{r}$ normalized by the droplet radius R as a function of the time. (a) Oscillatory cluster composed of three droplets. (b) Oscillatory cluster composed of four droplets.

4.4.3 Adhesion force effect

For a given number of droplets, the cluster aggregates can adopt stable configurations or show dynamical oscillatory states. Whether the morphologies of clusters adopt stable or oscillatory states strongly depends on the experimental conditions. We identify that the adhesive interactions between droplets play an essential role in the clustering process.

If we reduce the adhesion between the droplets, the clusters tends to move from stable state to oscillatory state (which is the case that in figure4.23 (with 2% SDS) and figure 4.25 (with 0.4% SDS)). If the adhesion is weak enough, the clusters cannot be obtained whatever the flow condition is; the droplets don't aggregate to be transported as an entity but as individual objects. In the figure 4.27, we show one example of such non-adhesion behaviors (with 0.2% SDS). The analysis concerning adhesion interactions will be discussed in details later in Chapter 5.

The figure 4.27 shows the experimental result of fluorinated oil in water stabilized with 0.2% (1 CMC) SDS. Three droplets are produced successively from one plug-like droplet. Then they get dispersed following the streamlines separately once entering into the reservoir.

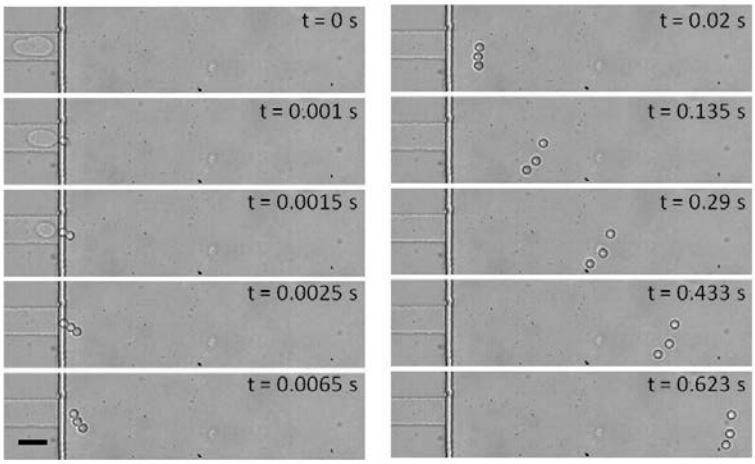

Figure 4.27: Snapshot showing the separation of non-adhesive droplets in the reservoir channel, the clustering process cannot be achieved using Fluorinated oil droplets in water with 0.2% SDS. The scale bar is 20μm

We compare behaviors of 'adhesive' and 'non adhesive' droplets in different flow conditions, the experimental observations are shown in figure 4.28.

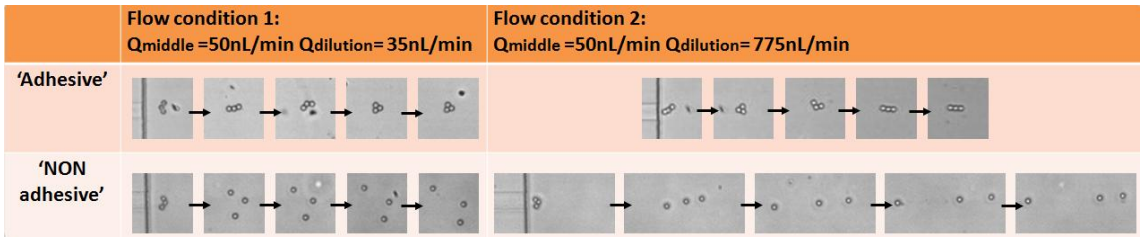

Figure 4.28: Comparison behaviors of 'adhesive' and 'non adhesive' droplets in different flow conditions. 'Adhesive' emulsion is Fluorinated oil in water with 2% (10 CMC) SDS and 'non-adhesive' emulsion is with 0.33% (10 CMC) copolymer Pluronic F-68.

4.4.4 Flow condition effect

With the same formulation of emulsion (dispersed and continuous phases, surfactant etc.) and experimental conditions (droplet size, temperature etc.), we observe that the flow field can dramatically alter cluster morphologies too. In order to screen the controlling factors which govern the behaviors of the cluster self-assembly, we adopt the emulsion

formulation with fluorinated oil droplets in an aqueous continuous phase with 2 % SDS. We are limited to produce clusters made of three equal-sized droplets N = 3. Using triplet clusters allows us to study the clustering process without provoking too much complexity. Figure 4.29 shows the experimental observations for the system $h_1 = 10\mu m$, $h_2 = 163\mu m$. We set the dispersed and continuous phase pressures fixed and increase the dilution phase pressure. Under low dilution pressure, the three droplets adopt the triangle-like close packing structure (at $P_{dilution}$= 20mbar). As the pressure increases, the droplets configuration evolves to linear chain-like shape (at $P_{dilution}$= 160mbar) and eventually separate at higher pressure (at $P_{dilution}$= 180mbar).

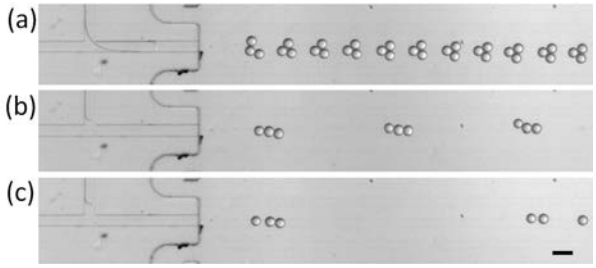

Figure 4.29: Cluster structures transition. PDMS system, W=50μm, h_1=10μm, h_2=163μm. (a)$P_{disperse}$=38mbar, $P_{continuous}$=11mbar, $P_{dilution}$= 20mbar. (b)$P_{disperse}$=38mbar, $P_{continuous}$=11mbar, $P_{dilution}$= 160mbar. (c)$P_{disperse}$=38mbar, $P_{continuous}$=11mbar, $P_{dilution}$= 180mbar. Scale bar is 100μm.

A more quantified work is carried out for a small system (W=20μm, $h_1 = 1\mu m$, $h_2 = 22\mu m$), the size of the droplet decreases by one order of magnitude with R around 2.5μm. Throughout the experiments, we span a range of flow rates and the typical flow velocity ranges from 70 μm/s to 2000 μm/s in the reservoir channel which allows us to estimate the Reynolds number and the Capillary number in our device (the width of the reservoir channel is $600\mu m$). The corresponding Reynolds number Re = ρUL/μ varies between 3×10^{-6} and 9×10^{-5} and the capillary number Ca = μU/ν range between 4×10^{-6} and 10^{-4}. The transition of morphologies is observed (see figure 4.30).

We conclude that the close packing structures are favored under high adhesion and low flow field conditions. In order to better understand the flow field influence on the clustering process, we conduct a numerical simulation in the absence of droplets to investigate the flow field in the reservoir channel under different experimental conditions.

4.5 Numerical simulation

In collaboration with Florent Malloggi (CEA Saclay), we carry out this numerical simulation study. Three-dimensional flow simulations are used to compute the streamslines and flow conditions in the microfluidic reservoir in the absence of clusters. The simulations are set in COMSOL Multiphysics which is a commercial software widely used in industries as well as in research laboratories. Its graphical user interface (GUI) and a set of predefined user interfaces with associated modeling tools provide an easy preparation of the simulation and offers clarity in the choice of the governing flow equation without requirement to write them in variational form. We use the 3D Stokes flow module as the experimental Reynolds number throughout our experiments remains below 10^{-2}. The flow geometry mainly consists a rectangular cross-section with three entries: one in the middle for which the flow rate contribution comes from inlet 2 (continuous phase to produce droplets at

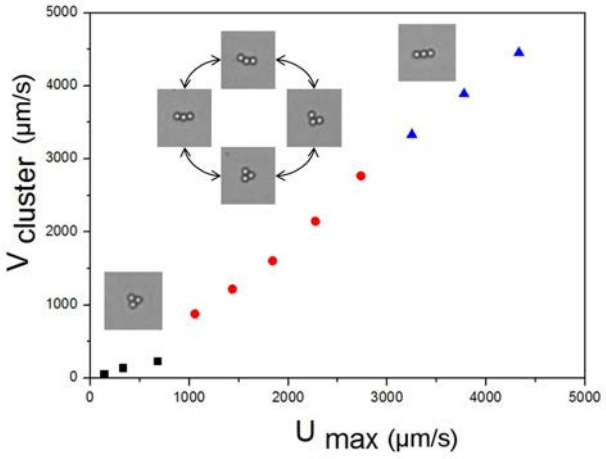

Figure 4.30: Clusters morphologies transition. We present here the cluster aggregate velocity as a function of the maximum flow velocity (poiseuille flow in z direction) in the reservoir channel. Triangle structures (black) are obtained under low U_{max}, chain structures (blue) at high U_{max} and in between is the oscillatory states (red).

T-junction) and two entries symmetrically located at both sides which represent the inlet 3 (dilution phase).

We simulate the system with the smallest dimensions. The height of the channel is constant and its value is h_2=22μm except in the mid inlet channel where the height is h_1 1μm. Figure 4.31 shows a perspective view of the design along with the meshed channel. The domain is meshed with a density of 4 nodes on the channel height edges, 80 on the width and 200 on the length edges (tetrahedral elements).

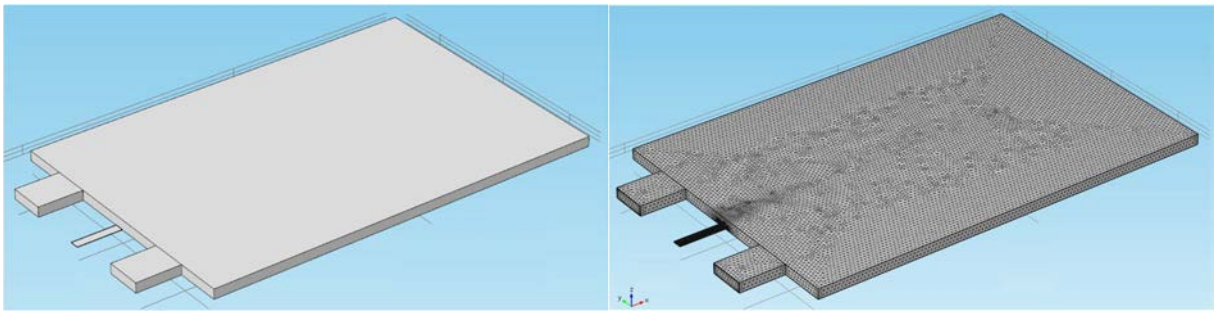

(a) (b)

Figure 4.31: Design of the system for the 3D-simulation of the flow.(a) geometrical design for the fluid domain. (b) the mesh obtained with Comsol.

For convenience description we define two different regions in our device (see figure 4.32). Region I is the reservoir area near the step and close to the entries where we expected to have an elongation flow. Region II represents the area where the entry effect can be neglected, a stationary flow is expected, a plug flow in xy plan and a poiseuille flow in z. The fluid flows from left to right. It flows through 3 inlets (W_{mid}=20μm, h_1=1μm and W_{side}=80μm, h_2=22μm) and enters a larger reservoir channel (W=600μm, h_2=22μm).

We simulate the flow with the following parameters:

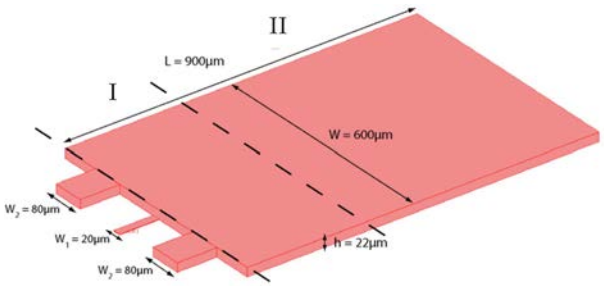

Figure 4.32: Two different regions of the fluid domain.

Flow condition	Q middle(nl/min)	Q side(nl/min)	Experimental clustering observation
NO 1	50	35	close packing
NO 2	50	240	oscillation
NO 3	50	775	chain-like packing

Table 4.2: three flow conditions for simulation

Inlet: We simulate the flow by imposing the flow rates Q_{middle} and Q_{side}. To compare with the experimental results, we set Q_{middle} =50nl/min, varying the Q_{side} progressively from 0 nl/min to 775 nl/min.

Outlet: Outlet is connected to a channel of 1mm length. This channel is left open to ambient pressure $P_{outlet} = 0$ mbar.

We consider the fluid as Newtonian (constant viscosity η=$10^{-3} Pa.s^{-1}$) and the flow in a stationary state (no temporal dependence).

We should first recall the experimental results, three behaviors of the clustering are observed according to the flow conditions: when the flow rate of dilution phase is low compared with the one of the middle phase, the clusters adopt close packing morphology; when the flow rate of dilution phase is high, the clusters form a chain-like structure and in between the two, we observe oscillations of the two configurations. The corresponding flow conditions are shown in the table 4.2. We present numerical simulations of the corresponding three cases to provide comparison with the experimental data and explore the dependence of the flow conditions and morphology of the clusters.

We present in the figure 4.33 the maps of velocity field as well as the streamlines in the middle height of the channel (h=11μm) for the three flow conditions indicated in the table 4.2. It is a projection along the xy plane.

As expected, the velocity decreases when entering in the main chamber. Indeed for a given flow rate the mass conservation gives $Q_0 S_0 = Q_1 S_1$ with Q the flow rate and S the channel cross section. From the entries to the reservoir, the cross section increases thus Q decreases due to mass conservation. The reservoir channel is a Hele-Shaw cell (with aspect ratio W/h=27), we obtain a creeping flow quickly after a small entry region as expected for all cases.

We use the following notation for the velocity vector:

$$v = \begin{pmatrix} u(x,y,z) \\ v(x,y,z) \\ w(x,y,z) \end{pmatrix}$$

In the region I, the flow is complex u≠0, v≠0 and w≠0. However we proceed at the following simplification. From the streamlines of figure 4.34 (a) for the flow condition

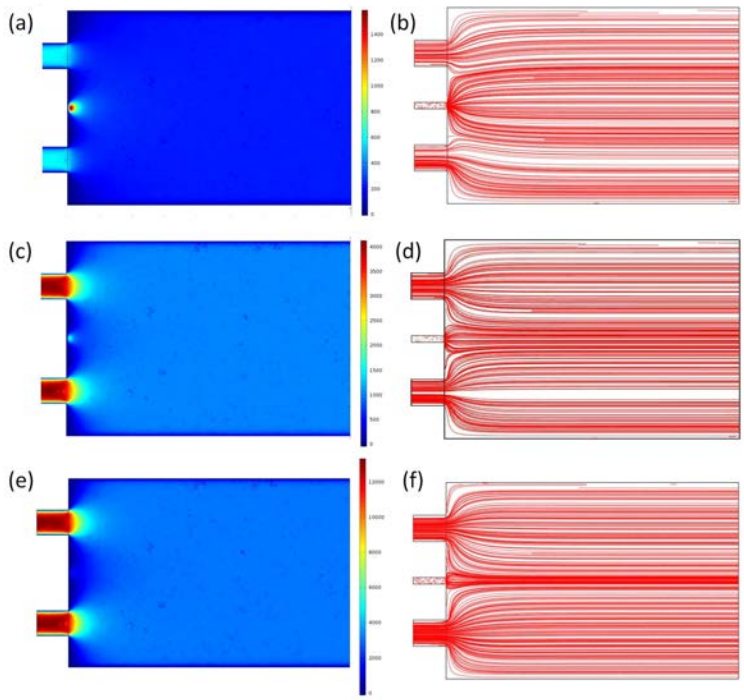

Figure 4.33: The velocity field (a) and the streamlines (b) for flow condition NO 1; (c), (d) for flow condition NO 2 and (e), (f) for flow condition NO 3.

NO 3, we clearly see that the z-component of the velocity field vanishes after few tens of microns (30μm), i.e. w is almost 0 after this distance. The similar range is confirmed for other flow conditions by the simulation. This result is consistent with the measurements of droplet z position with Adaptive Focus Control and with Microscope Confocal Imaging.

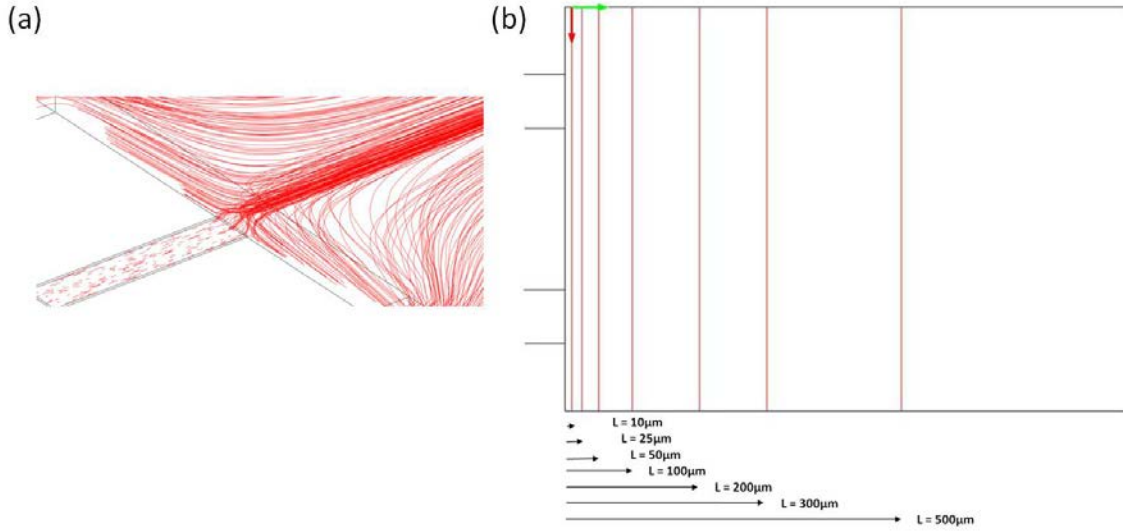

Figure 4.34: (a) Zoom of streamlines near the middle inlet. (b) Transversal cut at different positions: x=L=10μm - 25μm -50μm -100μm -200μm -300μm- 500μm.

Moreover since the main contribution to the velocity field comes from side channels this approximation seems correct. Hence the velocity profile can write:

$$v = \begin{pmatrix} u(x,y,z) \\ v(x,y,z) \\ 0 \end{pmatrix}$$

We made several transversal cut velocity profiles at different positions(see figure4.34 (b) for the cut and figure4.35 for the velocities): x=L=10μm - 25μm -50μm -100μm -200μm -300μm- 500μm and for z=h/2=11μm (x=0 is for the beginning of region I).

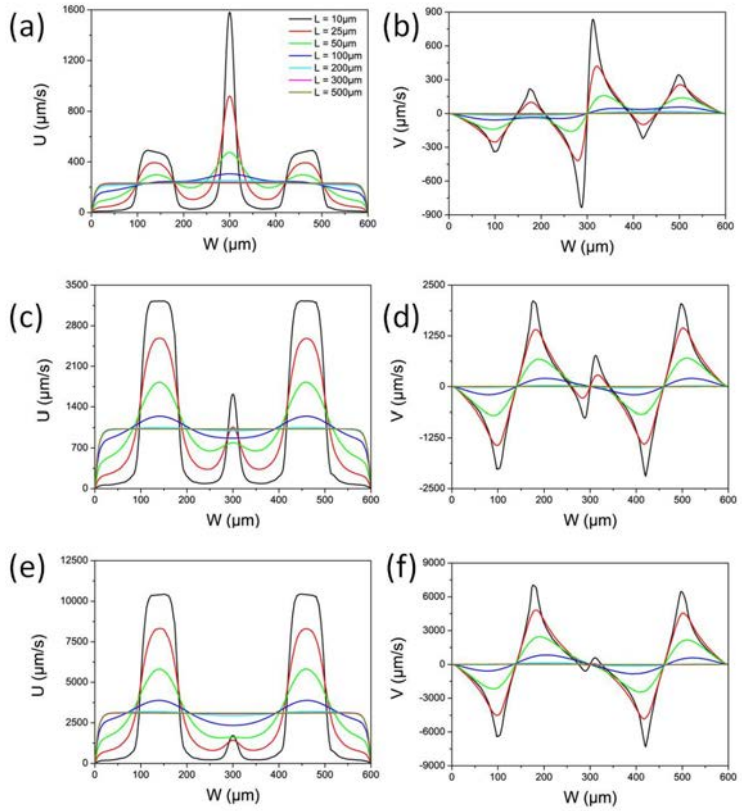

Figure 4.35: Transversal cuts of the velocity field (z=h/2=11μm). Velocity vector U (a) (x componet) and V(b) (y componet) for flow condition NO 1, (c) and (d) for flow condition NO 2 and (e) and (f) for flow condition NO 3.

After L=300μm the flow adopts a plug like profile, i.e. v is almost 0 and u is almost uniform, as shown in figure 4.35. In the region II, the velocity profile writes:

$$v = \begin{pmatrix} u(x,y,z) \\ 0 \\ 0 \end{pmatrix}$$

Since the clustering formations take place in the mid-plan of the reservoir channel in the region II, where the flow field is plug flow in xy and poiseuille flow in z, the shear stress can be neglected. We suggest that the dipolar interation is responsible for the dynamical evolution of the droplets towards cluster. This study will be discussed in the preprint paper in chapter 5.

4.6 Conclusion

Through the use of dedicated two-layer microfluidic devices and by coupling T-junction and step emulsification droplet production, we demonstrated the direct assembling of droplets into clusters (of adhesive formulation) within this device. We discussed two regimes: the cluster production and the cluster transport. Various morphologies of clusters were observed and the corresponding experimental conditions were well precised. This mechanism produced high yield monodisperse clusters in a robust way. We proposed some explanations for the droplets generation mechanism and the cluster transport behavior in the microfluidic reservoirs, with support from numerical and modeling work. We mainly focused ourselves on the flow field effect in this chapter. A further investigation on the clustering process by scanning other parameters such as the surfactants, electrolytes will be provided in the next chapter. A theoretical analysis on dipolar interaction will be provided in the preprint in chapter 5.

Chapter 5

Clustering based on hydrodynamics self-assembly: towards more complex clusters

5.1 Introduction

In the previous chapter, we discussed simple cluster formation whereas in this chapter, we further carry out a serie of experiments with different formulations to investigate the influence of physical chemistry to the hydrodynamics assembly process. The goal is to use the broaden fluids is attempting to produce more complex clusters. We start with adhesion study, trying to understand the adhesion origin between the droplet interfaces in order to better reinforce their interaction. This study will give us an insight of how resistant those clusters are when they are submitted to hydrodynamic forces as well as the morphology preferences they adopt under different conditions (2D and 3D structures). Then we focus on the hybrid cluster and magnetic clusters synthesis which is potentially interesting to develop directional interactions between the building blocs for complex assembly. We also investigate the solidification of the clusters which is important for material applications. A proof of concept and some perspectives are provided in this chapter for the future studies.

5.2 Sticky clusters

5.2.1 Introduction

The interaction energy of emulsion droplets is the result of the effect of different factors (drop radius, interfacial tension, Hamaker constant, electrolyte, micellar concentrations, etc.) Although a strong, steep repulsion at short range is necessary to stabilize the droplets against coalescence, emulsion droplets can exhibit adhesion when they experience pronounced attraction and form aggregates[105].

The aggregation may be weak and reversible or strong and irreversible. This is entirely determined by the nature of the interactions between the droplets. The possible interactions can be classified by the nature of attractive or repulsive forces. Attractive forces include van der Waals interaction, depletion forces and hydrophobic interactions etc.. The repulsive forces include electrostatic interaction and steric interactions and so on.

The attractive interaction may arise from a variety of different forces. For example, emulsions stabilized by ionic surfactants become adhesive at high electrolyte concentra-

tions due to the considerable screening of electrostatic repulsions by electrolytes, as described by the Derjaguin-Landau-Verbey-Overbeek (DLVO) theory[240][241][242].

The DLVO interaction combines the effects of the van der Waals attraction and the electrostatic repulsion in its conventional form. In the case of deformable droplets the surface extension energy should be also taken into account[243]. Van der Walls energy diverges as 1/r at small separations and decays as $1/r^6$ at large distance. The electrostatic repulsion is finite at small distances and decays exponentially. The overall interaction energy is dominated at small and large separations by the attractive term, whereas the intermediate region could be repulsive due to the electrostatic contribution. Figure 5.1 shows the schematic plot of the DLVO interaction potential energy E of model particles[244]. A strong long-range repulsion with a high energy barrier is present for highly charged surfaces in dilute electrolyte (i.e. long Debye length). When the surface charges are reduced or the concentration of the electrolyte solution are increased, a small secondary minimum in the potential curve appears. The particles may undergo a reversible flocculation due to the secondary minimum because of its weak energy barrier, resulting in slow particle aggregation. Below a certain surface charge or above a certain electrolyte concentration (known as the critical coagulation concentration), the energy barrier falls below the zero axis and particles then coagulate rapidly.

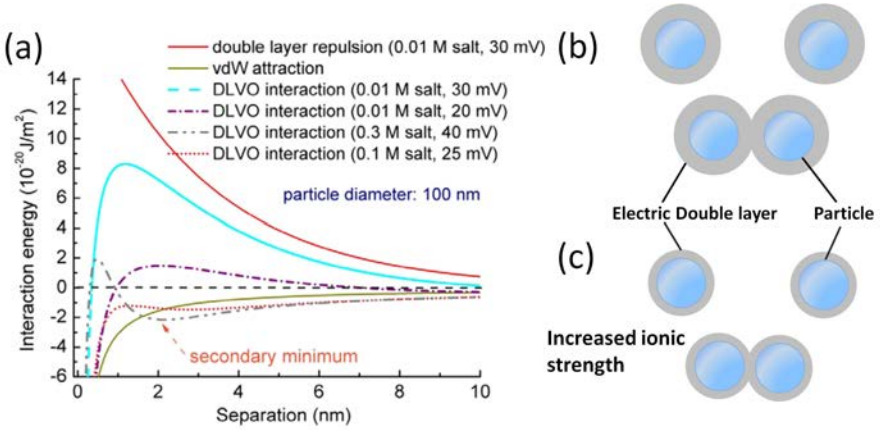

Figure 5.1: (a) Schematic plots of the DLVO interaction potential energy E (the Hamaker constant A is 1.5 $\times$ 10^{-20}J)[244].(b) Illustration of the situation where, as particles approach each other, the electric double layers overlap and cause repulsion.(c) In the case of an increased ionic strength, the electric double layers shrink which allows the particles to get closer without being repelled.

Emulsions stabilized by non-ionic surfactant can be adhesive even without electrolyte because of the absence of long range repulsion forces such as electrostatic interactions, for example, dodecane in water emulsion stabilized by the non-ionic surfactant n-decyl-β-D-gluocoside (C_{10}) shows strong adhesion between the droplets[245].

Another interaction force which leads the emulsion adhesive is the attractive depletion forces [246] [247] [49] [248] [249]. The depletion phenomenon occurs when two species of different sizes are suspended in a liquid in the right proportion. The larger droplets experience an induced 'depletion' attraction due to an unbalanced osmotic pressure arising from the exclusion of the depletants (the smaller non-adsorbing particles, polymers, micelles of surfactant etc.) from the region between the larger ones. The attractive interaction is expected when the separation between the surfaces of droplets is small enough to sense the structure the solvent, that is, the diameter of the smaller depletants. An illustration

is shown in the figure 5.2, representing how an attractive entropic force results from the exclusion of depetants between the inter-particle region.

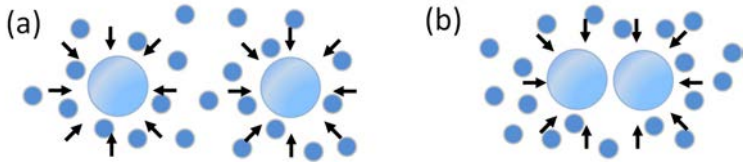

Figure 5.2: Depletion attractions.(a) When the separation between the large particles/droplets exceeds the diameter of depletant, depletants may enter the interstitial region with only minor modifications of their distribution. Thus the internal and external osmotic pressures balance each other and there is no force induced by the depletants. (b) When the separation is smaller than a depletant's diameter, the depletants are excluded from the interstitial region. The external osmotic pressure is not balanced and there is a net attractive force between the bigger particles/droplets.

Some works show that emulsions with droplets larger than 1μm are particularly sensitive to small changes in surfactant concentration and the adhesion boundary corresponds to the equilibrium between the osmotic pressure $\Pi_m = C_m RT$ and the capillary pressure $P_c = 2\gamma/r$ where C_m is the concentration of micelles in the continuous phase, γ is the interfacial tension and r the droplet radius [250]. Emulsion is adhesive if the osmotic pressure exceeds the capillary pressure. We should note that at higher concentrations of micelles, the depletion interaction develops into the oscillatory structural forces [1], which are characterized by alternate zones of attraction and repulsion.

This attractive interaction may also reasoned from the insolubility of the surfactant and the surrounding continuous phase. For instance, steric forces, although it's a repulsive force, may lead emulsion attractive if the surfactant chains are not placed in a good solvent[251][252]. Poulin et al. have been demonstrated experimentally by using binary mixtures of oils, one in which the surfactant is soluble and another one in which the surfactant is insoluble, that the adhesion is favored when the surfactant becomes less soluble in the continuous phase. For example, water droplets can be stabilized by Span 80 in a silicone oil/dodecane mixture. The surfactant Span 80 is soluble in dodecane whereas it is not in silicone oil. As shown in figure 5.3, the energy of adhesion between water droplets varies strongly as the composition of the mixture is changed. A sharp rise can be seen as the surfactant becomes insoluble in the solvent owing to the large content of silicone oil. Similar behavior was observed for inverted emulsion stabilized by phospholipids.

5.2.2 Experimental method

Physicochemical conditions

– **Different phases**

In the previous study, we have shown that in the direct emulsion, fluorinated oil in water with 2%wt SDS as surfactant presents an adhesive behavior. This formulation allows to produce easily clusters with our dedicated devices. We would like to expand our study of the hydrodynamic assisted clustering to the inverted emulsions, i.e. the

1. In the presence of larger amount of micelles, the total force between surfaces may oscillate due to occurrence of oscillatory forces. Structural forces are a consequence of variation in the density of packing of small particles around a surface on the approach of a second one(stratification) [105].

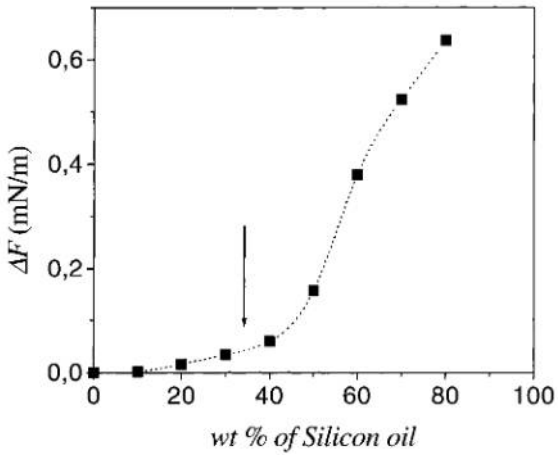

Figure 5.3: Energy of adhesion between Span 80 monolayers in a silicone oil/dodecane mixture. The arrow indicates the insolubility threshold of the amphiphile[252].

water-in-oil systems. However, the swelling of untreated PDMS in the presence of certain solvents/oils require particular attentions, especially for the shallow channels [253]. In our study, we restricted our work to the use of mineral oil and fluorinated oil to ensure that no undesirable swelling effect occurs. Nevertheless, the swelling of the device could be avoided by various treatments of PDMS surface or by the use of other materials such as glass and microfluidic sticker etc. Therefore various organic solvents are potentially applicable, but this part is out of the scope of the present work.

– **Surfactants**

Two kinds of surfactant are used for the oil-in-water emulsion: anionic surfactant SDS and non-ionic polymeric surfactant Pluronic F-68. Sodium dodecyl sulfate (SDS) is a low-molecular mass organic compound with the formula $CH_3(CH_2)_{11}OSO_3Na$. It is the most widely used of the anionic alkyl sulfate surfactants. This surfactant is of an organosulfate consisting of a 12-carbon tail attached to a sulfate group, giving the material the amphiphilic properties. The class of Pluronic block is a widely used non-ionic surfactant which is a copolymer of hydrophilic ethylene oxide (EO) and hydrophobic propylene oxide (PO) arranged in A-B-A tri-block structure, the Pluronic F-68 has an average formula of $(EO)_{75} - (PO)_{30} - (EO)_{75}$.

For water-in-oil emulsions, we use the non-ionic surfactant sorbitan monooleate (Span 80) to stabilize water in mineral oil. With the formula $C_{24}H_{44}O_6$, the value of hydrophilic-lypohilic balance (HLB) [2] is 4.3, rendering it more soluble in oil phase than in the aqueous phase. In order to stabilize the system of water-in-fluorinated oil, we use PEG di-Krytox, a copolymers of the A-B-A type with a $(PO)_2 - (EO)_{18} - (PO)_2$ hydrophilic part in between the two perfluorinated chains.

The chemical structures of the four molecules are shown in the figure 5.4 and the details of physicochemical characteristics are listed in the table 5.1:

– **Electrolyte solutions**

Solutions of various concentrations of sodium chloride (NaCl) and potassium chloride

2. Hydrophile-Lipophile Balance is an empirical expression for the relationship of the hydrophilic and hydrophobic groups of a surfactant. The higher the HLB value, the more water-soluble the surfactant [254][255].

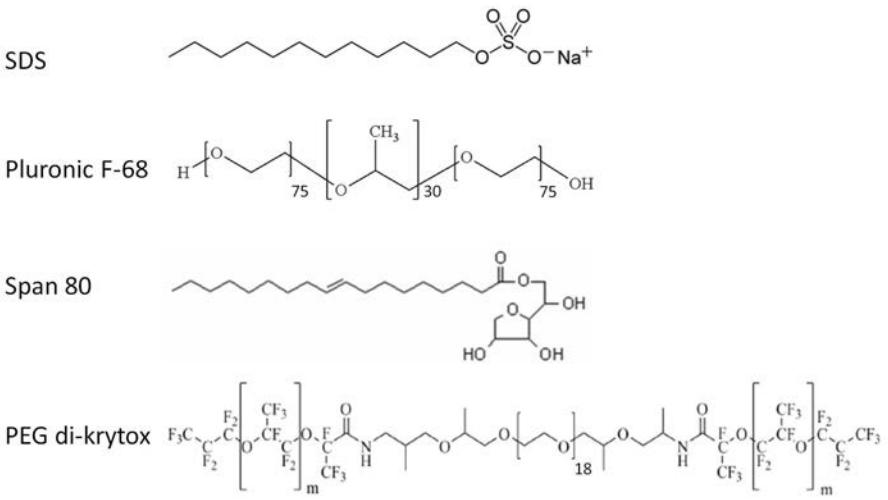

Figure 5.4: Chemical structures of the surfactants used.

Surfactant	Type	$M_w(g/mol)$	HLB	Emulsifier type	CMC
SDS	anionic	288.38	40	O/W	8.2mM(w/w)
Pluronic F-68	nonionic	8400	29	O/W	0.04mM
Span 80	non-ionic	428.60	4.3	W/O	0.025%
PEG di-krytox	nonionic	14000	1.45	W/O	0.033%(w/w)

Table 5.1: Properties of surfactants used.

(KCl) are prepared. The presence of salt above certain quantity may induce the precipitation of anionic surfactant SDS at room temperature. As a matter of fact, it is well recognized that SDS is very sensitive to the polarity of the medium. The solubility of the surfactants with sulfate group increases from the low hydrated large counterion towards the strong hydrated small counterions: $K^+ < Na^+ < Li^+$. The order of this series is inverse for the carboxylate polar group[256][257] [258]. As for the non-ionic surfactant Pluronic F-68, the precipitation concentration value in the presence of salt is much higher due to the lack of charge.

Experiments

It is not obvious to characterize the aggregation process and the adhesion energy of the clusters obtained in our system. For example, we have thought to use the Dynamic Light Scattering (DLS) technique to probe the behavior of the emulsions. However, the smallest size of droplets is a few microns in diameter which reaches the limit of the light scattering technique. Furthermore, the fluorinated oil use is relatively heavy (ρ=1820 kg/m^2) so that the sedimentation of droplets is not negligible.

We thus investigate the adhesion behavior of droplets directly within the microfluidic device. A qualitative analysis is given by the observation of the cluster formation in the microfluidic reservoir near the 3D step.

We use pressure control to generate the droplets with typical dilution phase pressure below 10 mbar. Working at low pressure is to ensure the droplets production under slow flow field so that we could better screen whether the adhesion takes place or not.

For the study of the surfactant effect, we use **normal injection method** in which

the continuous phase and dilution phase are exactly the same fluids, thus there is no concentration gradient across the channel. Regarding the study of the electrolyte effect, we use another method: the salt solution is injected only into the dilution channels. The continuous phase with surfactants as well as the dispersed oil phase are coming from the middle inlet as usual. With this **coflow diffusion strategy**, we are able to study systematically the effect of salt concentrations and salt types on the aggregation process. The sketch of the two methods is shown in the figure 5.5. Finally, to produce the direct emulsion oil-in-water, we prepare hydrohylic PDMS system, and hydrophobic PDMS system for inverted emulsion water-in-oil.

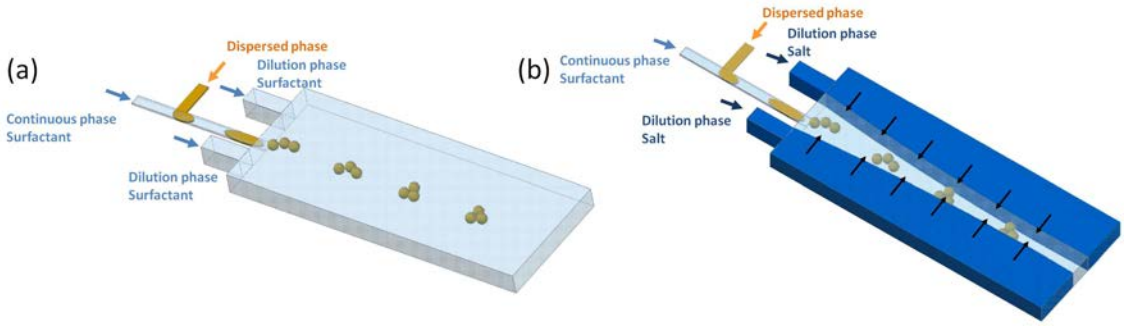

Figure 5.5: Schematic drawing of two injection strategies. (a) the normal injection. (b) the coflow diffusion injection.

5.2.3 Results

Influence of surfactant: type and concentration

We vary systematically the surfactant concentration, from 1 CMC up to 10 CMC for SDS and 1 CMC to 60 CMC for Pluronic F-68. Critical micelle concentration (CMC) is defined as the concentration of surfactants above which micelles form and all additional surfactants added to the system go to micelles.

Emulsions stabilized by 1 CMC SDS do not exhibit evident adhesion. Weak adhesion between droplets begins to appear at 2 CMC, however, with a tiny perturbation at the microfluidic reservoir, the droplets rapidly disperse, (it is in this regime, that we are able to observe oscillatory movement of the clusters, ref chapter 4, morphologies transition observations part). The adhesion is very remarkable at 5 CMC in which case they can resist higher shear stress. Beyond this concentration, we could produce stable clusters by tuning the flow condition as mentioned in the previous chapter. Figure 5.6 shows comparison of the behaviors of cluster transported near the step for formulation with 1 CMC and 10 CMC SDS under similar flow condition. With 1 CMC SDS, three droplets and a satellite droplets are produced at the step, they are separated as they are convected over a short distance $\sim$ 250 μm (figure 5.6 (a)). Whereas at 10 CMC, the droplets produced are sticked together, forming a cluster entity (figure 5.6 (b)).

The observations of the cluster formation near the step under low shear environment are listed in the table below 5.2 :

According to the experimental results, we suggest that, for emulsion stabilized by SDS, the adhesion mainly comes from the contribution of the depletion force [259][260]. Above 1 CMC, micelles of surfactant SDS begin to be present in the surrounding fluid. At 10 CMC SDS, even though well above the CMC, the solution is still within the spherical micellar region of the phase diagram [261], so that the oscillatory structural force has not

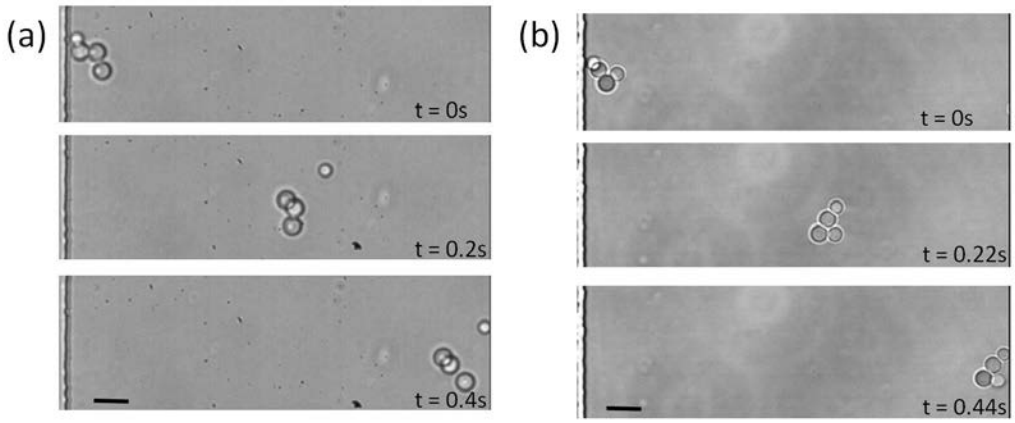

Figure 5.6: Comparison of droplets transport behaviors with 1 CMC SDS and with 10 CMC SDS. (a) Snapshots of droplets transport at various time with 1CMC SDS as surfactant in the continuous phase. Three droplets and a satellite droplet are produced at the step then they separate rapidly.(b)Snapshots of droplets transport at various time with 10 CMC SDS. The droplets are aggregated together. The black vertical line on the left of each images represents the 3D step; the scale is 10μm.

.

Concentration of SDS	Observation
0.5CMC	No visible adhesion, no cluster can be formed
1CMC	No visible adhesion, no cluster can be formed
2CMC	Weak adhesion, oscillatory cluster can be formed
3CMC	Weak adhesion, oscillatory cluster can be formed
5CMC	Strong adhesion, stable cluster can be formed
10CMC	Strong adhesion, stable cluster can be formed

Table 5.2: Observation of droplets adhesion with different concentrations of SDS.

been developed to play a role. By taking advantage of the spontaneous pinch off at 3D step, this droplets generation mechanism ensures that the separation distance between droplets after step is small, thus the droplets are close enough to be under the depletion attraction once entering in the microfluidic reservoir.

We repeat similar experiences with the non-ionic polymer surfactant Pluronic F-68 and we observe that, however, over the range from 1 CMC to 60 CMC, no adhesion is observed even under extremely low shear environment. The image sequences of the droplets separation near the step with 10 CMC pluronic F-68 are shown in figure 5.7.

Concentration of Pluronic F-68	Observation
0.5CMC	
1CMC	
5CMC	No visible adhesion, no cluster can be formed
10CMC	
60CMC	

Table 5.3: Observation of droplets adhesion with different concentrations of Pluronic F-68.

A possible explanation of these two different behaviors is that the surfactant-induced

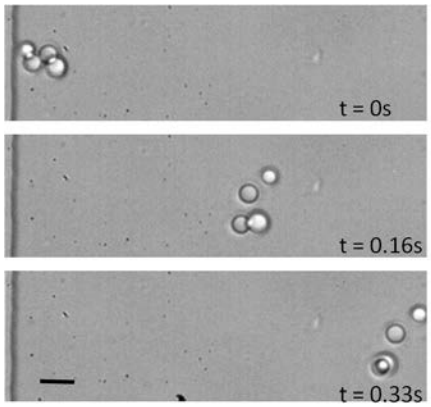

Figure 5.7: Snapshots of droplets transport at various time with 10 CMC Pluronic F-68 as surfactant in the continuous phase. Three droplets and a satellite droplet are produced at the step and then separate rapidly. The black vertical line on the left of each images represents the 3D step; the scale is 10μm.

flocculation, originated from the exclusion of micelles between approaching droplets, depends on the concentration of the depletion agents and the overlap volume of the depletion zone [49]. Based on osmotic force approach [51], the osmotic pressure, arising from excluded micelles, is related to the concentration of micelles by the approximation [250]:

$$\Pi_m = (CRT/M)(1 + 2C/\rho) \tag{5.1}$$

where C is the total micelle concentration in g/cm^3, M is the micelle molecular weight, and ρ is the micelle density. As Pluronic F 68 (M_w = 8400g/mol) could form bigger micelles compared to SDS (M_w = 288.38 g/mol) at the same concentration, the osmotic pressure is lower, thus the attractive force is weaker.

Influence of electrolyte: type and concentration

Time-dependent coflow diffusion

Special attention is given to the coflow diffusion method. As we see in the figure 5.5 (b), the diffusion takes place along the channel; the diffusion depends on the flow field conditions. We would like to know at which time scale and length scale under our typical experimental condition, the salt concentration reaches the cluster position and eventually effects the adhesion between the droplets. However, this is a dynamical process which depends on various parameters. In the first time, we will give some dimensional analysis about this time-dependent phenomenon.

If we consider the diffusion of a single solute with absence of convection, the diffusion equation writes:

$$\partial_t c = D\nabla^2 c \tag{5.2}$$

Where c is the concentration of the solute, D is the diffusion constant.

Simple dimensional analysis can already give an idea of this diffusion process within the micro-channel, T_0 and L_0 denotes the characteristic time- and length- scale over which the concentration varies, we have:

$$L_0 = \sqrt{DT_0} \quad or \quad T_0 = \frac{L_0^2}{D} \tag{5.3}$$

The typical value of D of small ions in water is around $2{\times}10^{-9}m^2/s$, which yields the characteristic time T_0 for diffusion across the typical microfluidic distance $L_0 = 100\mu$m: T_0 =5s; this time scale is well compatible with our experimental scales.

We now need to describe in detail the geometry of our device:

The middle inlet connected to the reservoir has a flow rate Q_{middle}, and the two dilution inlets have Q_{side} each. Due to the mass conservation, we assume that the region has repartition of flow in the reservoir width as shown in the figure 5.8.

$$W_{middle} = \frac{Q_{middle}}{Q_{total}} W \quad and \quad W_{side} = \frac{Q_{side}}{Q_{total}} W \tag{5.4}$$

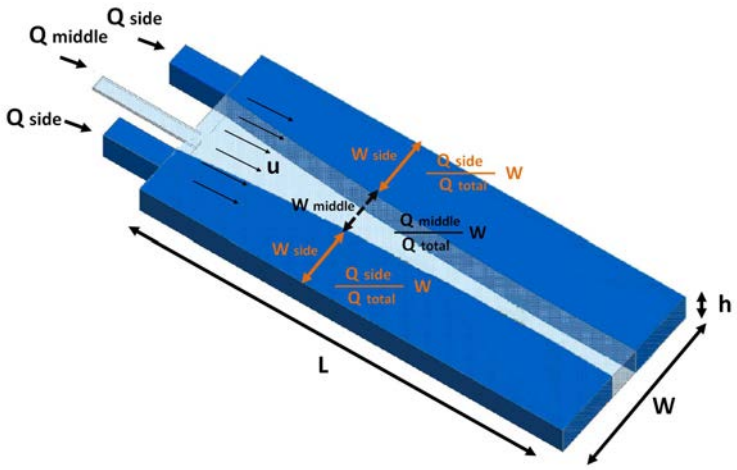

Figure 5.8: Schematic drawing of the diffusion process in the coflow condition. The dispersed phase and continuous phase with surfactant are injected in the middle channel with Q_{middle}; more continuous phase and salt is injected in the side channel with Q_{side}. The mean flow velocity in the reservoir channel is u and the repartition of width occupied with each phase is indicated in the sketch.

According to the diffusion results from Comsol, we confirm that this assumption is reasonable. The results of the flow diffusion study and the streamline maps of three different cases are shown in the figure 5.9.

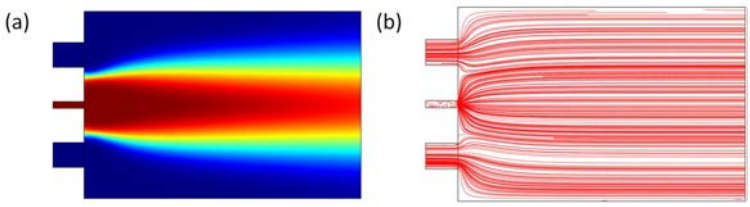

Figure 5.9: The diffusion map and the streamlines in the reservoir channel at middle plan Z=11μm from COMSOL simulations. Q_{middle}=50nl/min, Q_{side}=35nl/min. (a)Diffusion map. The repartition of the width of phase in the reservoir channel near the step: $W_{middle}/W = 0.34$ which is close to the ratio value of $Q_{middle}/Q_{total} = 0.42$ (b) Stream lines map in this flow condition.

The mean velocity is defined as the total flow rate ($Q_{total} = Q_{middle} + 2Q_{side}$) divided by the cross section of the reservoir channel S.

$$u = \frac{Q_{total}}{S} = \frac{Q_{middle} + 2Q_{side}}{Wh} \tag{5.5}$$

Regarding the behavior of solute (salt in our case) with diffusion constant D in water, two time scales become relevant, the time τ_{conv} , the time which it takes to be convected down stream to the outlet of the reservoir channel, and the time τ_{diff} which is the time needed for the salt to diffuse across the interface to the middle line of the channel:

$$\tau_{conv} = \frac{L}{u} \tag{5.6}$$

$$\tau_{diff} = \frac{(\frac{1}{2}\frac{Q_{middle}}{(Q_{middle}+2Q_{side})}W)^2}{D} \tag{5.7}$$

By requiring $\tau_{conv} = \tau_{diff}$, we could infer the distance from the step L^* where effective mixing has been taken place.

$$L^* = \frac{W^2}{4D}(\frac{Q_{middle}}{Q_{middle} + 2Q_{side}})^2 u = \frac{W}{4Dh}\frac{(Q_{middle})^2}{Q_{middle} + 2Q_{side}} \tag{5.8}$$

As studied in chapter 4, we take an example of the small system with $h_1 = 1\mu m$, $h_2 = 22\mu m$. The typical flow rate to favor the close packing cluster formation is relatively low, below few hundreds of nanoliters per second (ref table 4.2 in chapter 4) and the corresponding mean flow velocity ranges from 50μm/s to 350μm/s. The ratio of flow rates Q_{middle}/Q_{total} is around a third. With W=600 μm and D$\approx 2\times10^{-9}m^2/s$, we found that L^* is in the order of few millimeters (from 250 μm to 1750μm). Similar result of the typical length scale is obtained for bigger system with $h_1 = 10\mu m$, $h_2 = 160\mu m$. This value of diffusion length scale is in agreement with our experimental observations where an adhesion change begins to be observed after the droplets have been transported by several millimeters away from the 3D step.

Observations

With 5% NaCl solution, the emulsion of oil-in-water stabilized with 0.004M (about 0.1%, 0.5 CMC) SDS becomes adhesive, the transition of non-adhesive to adhesive is quite remarkable. The figure 5.10 shows some morphologies of clusters under such conditions.

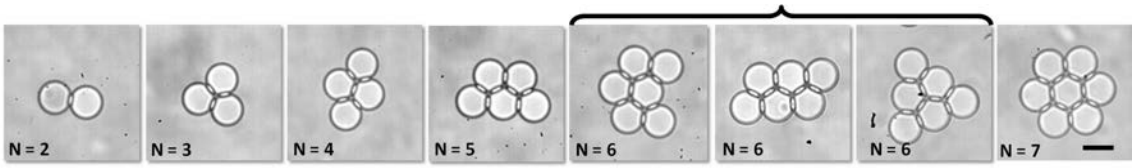

Figure 5.10: Optical micrographs of 2D clusters made of fluorinated oil in water with 0.5 CMC SDS in the presence of NaCl salt after stopping the flow. We could obtain close packing structure of N=2, 3, 4, 5, 6, 7. The droplets develop contact patch between their interface, however, the droplets are weakly deformed. Scale bar is 5μm.

The effect of salt on the emulsion stabilized by Pluronic F-68 shows similar results. With 5% NaCl, the emulsion of oil-in-water with 2% Pluronic becomes adhesive. The comparison of the formulation with and without salt is shown in the figure 5.11. Without

salt, the droplets separate rapidly after being transported by a short distance away from the step (see figure 5.11 (a)). By contrast under similar flow condition, the droplets remain adhere together in the presence of salt in figure 5.11(b). However, we observe that the adhesion is not strong enough, the smallest satellite droplets may detach from the clusters under some perturbations in the downstream of the reservoir channel (see figure 5.11 (c),(d)).

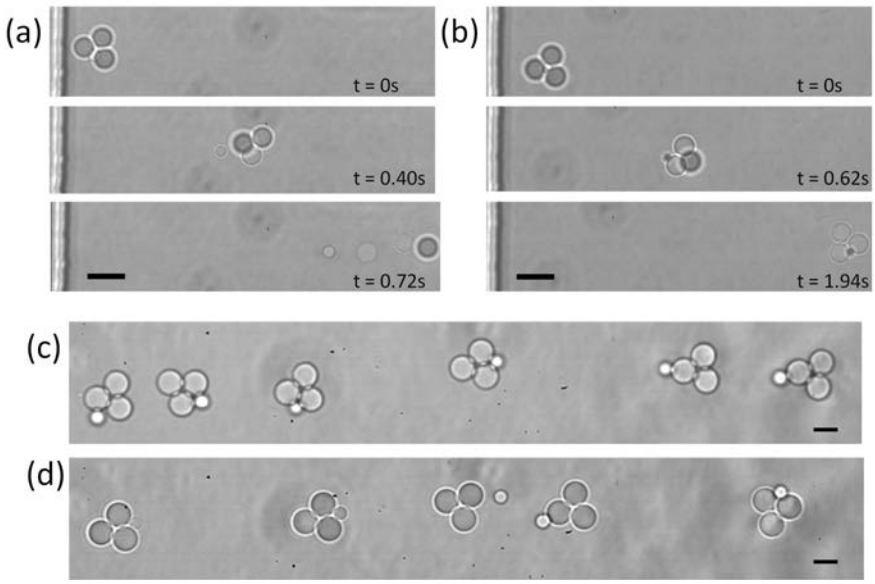

Figure 5.11: Comparison of droplets transport behaviors stabilized with 60 CMC Pluronic with and without salt. (a) Snapshots of droplets transport at various times without NaCl in the dilution continuous phase. Three droplets and a satellite droplet are produced at the step then they separate rapidly.(b) Snapshots of droplets transport at various times with 5% NaCl in the dilution continuous phase.The droplets are aggregated together after the production. The black line on the left of each images represents the 3D step; the scale bar is 10μm. (c) Optical micrograph of the clusters (in the presence of 5% NaCl) in the reservoir channel away from the 3D step, the distance to the step is about 800 μm. A train of clusters is convected downstream, the positions of satellite droplets may vary from one entities to another. (d) One example showing that the small satellite droplet could get detached from the clusters. Optical micrograph taken at the location where the distance to the step equals to 1000 μm. The scale bar is 5 μm.

The adhesion of the cluster is further reinforced in the presence of higher concentration of salts. With 30% NaCl, a concentration close to saturation of the solubility of NaCl in water, we observe that the aggregates of droplets become so adhesive that they only form close-packing structures (see figure 5.12).

The angle of contact between droplets is an indication of adhesion energy [262] [251]. The relation between the adhesive energy ϵ and the the resultant contact angle is known as the Young Dupré equation: $\epsilon = 2\gamma$ [1-cos(θ)] where γ is the interfacial tension in the presence of surfactant and θ the contact angle. Over a large range of different concentrations of NaCl in our study, the contact angles are all very small ($\theta \leq 20°$, the adhesion energy is below 2.5 mN/m in our experiment condition. We are not able to measure accurately the contact angle for each concentration. However, at room temperature, in the presence of KCl, the increase of contact angle between droplets is much more evident ($\theta \sim 45°$, the adhesion energy is about 10 mN/m. The contact angle of a pair of droplets in the

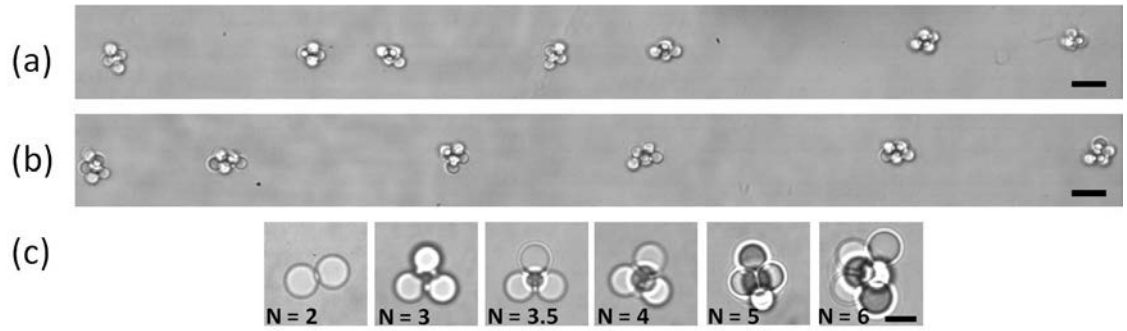

Figure 5.12: Droplets transport behavior stabilized with 60 CMC Pluronic and 30% NaCl in the dilute continuous phase.(a)A train of clusters (N=5) is convected downstream.(b) A train of clusters (N=6) is convected downstream. The scale bar is 10 μm. (c) Optical micrographs of clusters obtained. We could produce close packing structures of N= 2, 3, 3.5, 4, 5, 6.

presence of NaCl and KCl is shown in the figure 5.13.

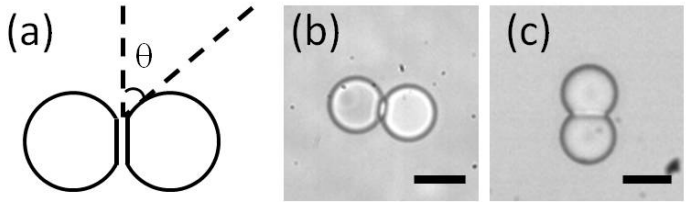

Figure 5.13: (a) Sketch showing the determination of the angle of contact between two droplets. (b) Optical micrographs of the contact angle of a pair of fluorinated oil FC 3283 droplets in water at room temperature in the presence of NaCl. Scale bar is 5 μm (b) and (c) in the presence of KCl. Scale bar is 50 μm.

We carry out the salinity study of KCl on bigger droplets produced with systems of $h_1 = 10\mu m$, $h_2 = 163\mu m$. The solution with 1% KCl is introduced by the two side dilution channels and stronger adhesive behavior is observed as the droplets are transported downstream where the salt concentration reaches a certain value after the diffusion. The figure 5.14 shows that the contact angles between the droplets increase as the droplets are driven to the diffusion area in the reservoir channel, which indicates that the adhesion energy is dramatically increased.

A closer look of the production of doublet and triplet is given in figure 5.15 (a) and (b), the flow is from left to right, a salt concentration gradient is present in this direction. Some more morphologies can be found in figure 5.15 (c).

Another interesting phenomenon is also discovered in this study: we observed systematically that the strong adhesive doublets rotate from 0° to 90° with respect to the flow direction (see figure 5.16). This original observation deserves a complementary hydrodynamic study which is out of the scope of the thesis here. We suggest that this rearrangement in the orientation of anisotropic objects may be explained by the secondary flow induced by the salt diffusion over the width of the channel.

The diffusion speed as well as the real salt concentration in a precise location depends on many parameters, i.e. the flow velocity, the temperature, the nature and the concentration of salts etc. The quantification is quite challenging. Nevertheless, some phenomena can be identified and should be underlined (see figure 5.17):

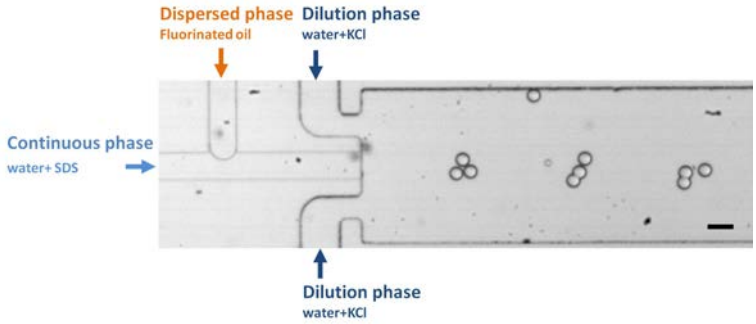

Figure 5.14: Optical micrograph of the triplets production in the microfluidic system. Dilution solution with 1% KCl is introduced in the two side channels. PDMS systems with W=100μm, $h_1 = 10\mu m$, $h_2 = 163\mu m$. As the droplets are driven downstream in the reservoir channel, a patch between their interfaces begins to appear and the contact angle increases. The scale bar is 100 μm.

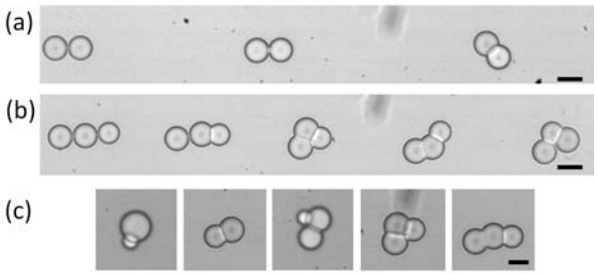

Figure 5.15: Droplets transport behavior stabilized with 0.5 CMC SDS and 1% KCl in the dilute phase. The geometry is the same as the one in Figure 5.14. The concentration of salt in the carrier fluid increases with the flow direction (from left to right) in this figure. (a) A train of doublets is convected downstream. We observe the evolution of the contact angles along the channel. (b) A train of triplets is convected downstream. We observe the evolution of the contact angles along the channel. (c) Optical micrographs of clusters obtained. We could get structures of N =1.5, 2, 2.5, 3. The scale is 50 μm.

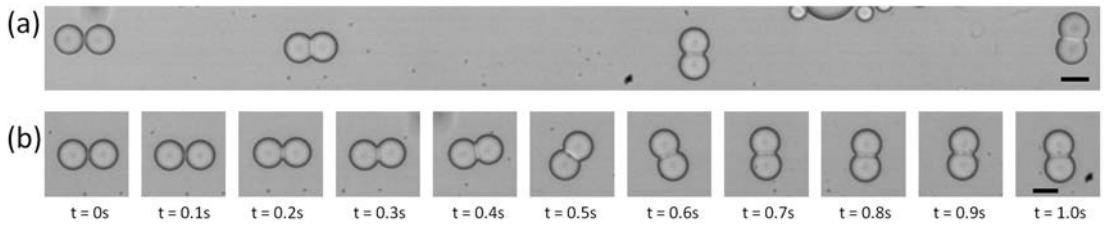

Figure 5.16: Self-rotation of an adhesive doublets under flow field in the reservoir channel. The droplets are produced with 0.5 CMC SDS and 1% KCl in the dilute phase. The fluid flows from left to right. (a) A train of doublets is driven downstream. When the pair of droplets has not developed strong adhesion, their orientation is along with the flow direction. While the pair manifests stronger adhesion due to the salt diffusion, they rotate gradually until perpendicular orientation with respect to the flow direction. (b) Snapshots of the evolution made by following the self-rotation of one doublet at various time. The scale bar is 50 μm.

1. We observe the adsorption of the droplets on the walls of the microfluidic channel close to the outlets in the presence of salts. The adhesion increases not only between the droplets but unfortunately also between the droplets and the walls.
2. We identify spontaneous coalescence between the droplets at high concentration of salts.
3. We observe the precipitation of surfactants evoked in the microfluidic channel.

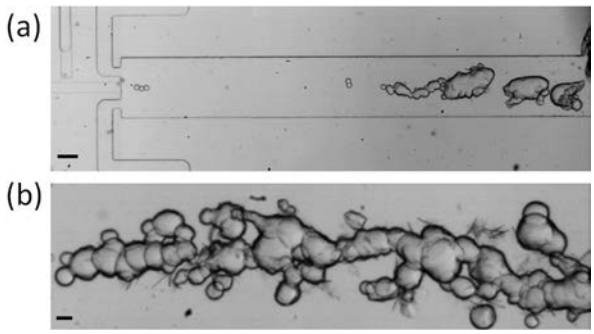

Figure 5.17: Some observations in the presence of salt (with 1 CMC SDS and 1% KCl). (a) The droplets may be adsorbed on the channel walls near outlet. (b) The new arrived droplets get sticked to the gel-like aggregates of previous droplets and spontaneous coalescence could happen. On the surface of the adhered droplets, the precipitation of surfactant is observed.

A further profound study could be dedicated to the electrolyte part attempting to reinforce the droplets adhesion without provoking side effects. To conclude on the work done so far, the addition of salts, in the case of ionic surfactants, screens electrostatic repulsions between the hydrophilic polar heads. For the non ionic polymeric surfactant, the increased salt concentration makes water a poorer solvent for the hydrophilic part of surfactant. The mean spontaneous curvature is decreased by the collapse of the polyethylenen oxide head units resulting from dehydration. Both behaviors could contribute to the further approach of the droplets interfaces. As a result, more sticky droplets are able to be produced.

According to the experimental results, it is evident that the salt can dramatically change the adhesion behavior of the emulsion stabilized by SDS or Pluronic. This offers a very promising way to control the adhesion of droplets and the clustering process.

Adhesion for inverted W/O emulsion

To realize the full potential of this new self-assembly mecanism, it is important to demonstrate that this approach could elaborate clusters using the wide variety of fluids. The water-in-mineral oil emulsion stabilized by non-ionic surfactant Span 80 is stable with respect to coalescence. We discover that the cluster formation occurs not only with the oil-in-water emulsion but also water-in-oil emulsion, i.e. this assembly mecanism is proven to be fluids independent. The droplets form spontaneously clusters near the step.

Table 5.4 shows the phases and surfactant used in the direct and inverted emulsions. Although the properties of fluids (surface tension, viscosity etc.) are different, stable clusters are formed in both cases.

Some clusters made of water droplets in mineral oil with different morphologies are listed in figure 5.18.

Emulsion	Dispersed system	Continuous	Surfactant	Viscosity (cP)	Density (g/mL)	Interfacial tension (mN/m)
Oil / Water	Fluorinated oil	Water	2 %wt SDS	Oil:1.4 Water: 1	Oil:1.82 Water:1	18
Water / Oil	Water	Mineral oil	2 %wt Span 80	Oil:15.3	Oil: 0.84	11

Table 5.4: Direct and inverted emulsion formulations and their characteristics

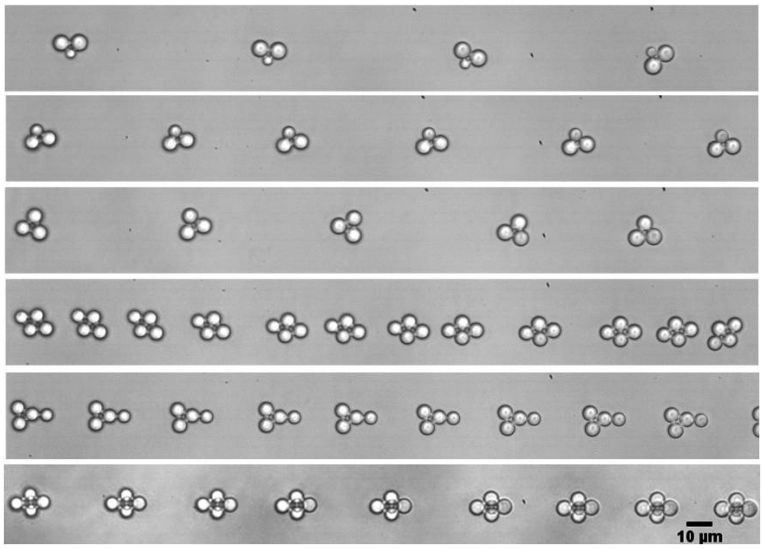

Figure 5.18: Optical micrographs of water-in- mineral oil clusters (stabilised with 2% Span 80) with N=2.5, 3, 4, 5. The scale bar is 10μm.

The mechanism of the pinch off of water droplet in oil at the 3D step is the same as the one of oil droplet in water emulsion. Again, we verify that the empirical law is still valid: the diameter of the droplet is around 5 times the channel height h_1 even if the properties of fluids (surface tension, viscosity etc.) are changed (see figure 5.19).

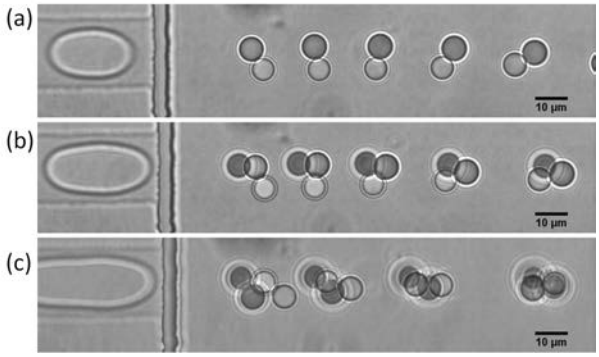

Figure 5.19: Cluters production: water droplet in mineral oil with 2% Span 80. System with w_1=20μm, h_1=1μm and h_2=22μm. Formation of clusters of N droplets with N=2, 3, 4. The scale bar is 10μm.

Micellisation of surfactants could also take place in organic solvent systems, but this process of surfactant aggregation in non-aqueous solvents differs considerably from those of

water-based systems [263] [264]. Surfactants in non-aqueous and non-polar solution form reverse micelles with hydrophilic core [265]. The so-called 'hydrophilic effect' lowers the unfavorable interactions between the hydrophilic part of the surfactants and the non-polar solvent molecules and concomitantly increases the interactions between the hydrophilic groups. This is the primary driving force for the formation of micelles in non-polar solvents. Span 80 has a long hydrophobic tail so that reverse micellisations of Span 80 are favored in non-polar solvent. The micellisation is reported in several previous studies [266] [267]. The CMC of Span 80 in mineral oil at 25° is 0.025% w/v [268], that is around 0.03% w/w. In our inverted emulsion study, we add 2 %w/w Span 80 in mineral to stabilize water droplets. The micelles of Span 80 are expected to form spontaneously and to induce the depletion force making the droplets adhesive. Moreover, the presence of trace amounts of polar substances like water can help to induce the hydrophilic effect [269]. We use the mineral oil purchased from Sigma-Aldrich (reference M 5904) as received without any anhydrous treatment what makes it highly probable to have trace of water due to the stock and usage condition. We infer that it is mainly the depletion interaction that rendering the water-in oil emulsion adhesive.

We have observed, under some experimental conditions, the dissolution of the water droplets in mineral oil in microfluidic channel, a phenomenon that have never been observed in the formulation of fluorinated oil droplet in water. This phenomenon occurs in very dilute regime (few droplets in the reservoir) and after a relative long period of stay in the channel (at rest flow for example as the example shown in the figure below). It can probably be explained by a competition between the cluster transport speed and dissolution rate. Figure 5.20 shows the process of dissolution of water droplets (droplet diameter = 5μm) at stop flow condition.

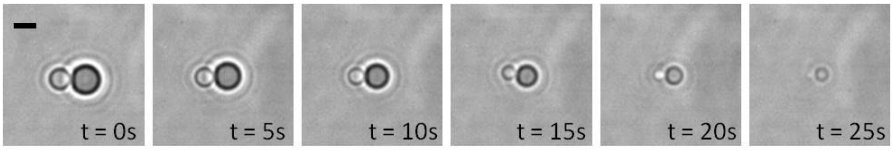

Figure 5.20: Snapshots of dissolution process of the water droplets in mineral oil at various time. The scale bar is 5 μm.

The emulsion of water droplets in fluorinated oil FC 3283 displays the same problem with a dissolution rate much faster. This formulation shows modest adhesion (see figure 5.21).

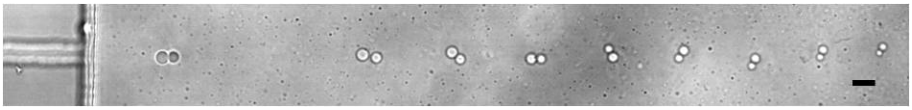

Figure 5.21: Dissolution process of the water droplets in Fluorinated oil FC 3283 in the microfluidic reservoir channel. The scale bar is 10 μm.

In general, oils dissolve some water. However, each oil has its specific water-saturation point. The solubility depends strongly on the oil composition, pure base oils have very limited solubility, which is related to the ratios of paraffin, naphthenic, and aromatic compounds [270]. The saturation point at 20° varies from approximately 30 parts per million (ppm) of paraffin oils to over 200 ppm of fully aromatic liquids, but it is typically between 40 to 80 ppm. Solubility may increase significantly with the use of additives. The typical value for new lubrication oil is < 500 ppm. Oxidation products also increase

solving efficiency. Mineral-based transformer oils typically have very little additives and therefore have relatively low solubility like base oil, whereas lubrication oils with greater amounts of additives generally have much higher solubility (see figure 5.22).

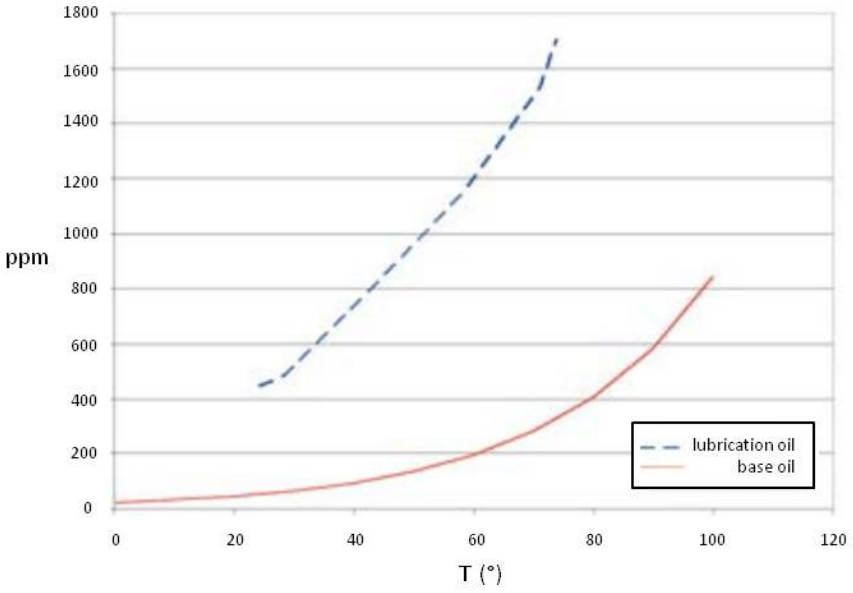

Figure 5.22: Average water solubility of mineral base oil and one lube oil as function of temperature[270].

This argument is in agreement with our experimental observations. The FC 3283 is a commercially used lubrication oil which has stronger solubility of water compared to mineral oil. In normal volume fraction of water, this low solubility of water in oil is not a big issue, while in our condition, the volume fraction is very small. In addition, the solubility of a droplet increases sharply as its radius tends to zero because of the Laplace pressure.

We could make the following estimation: along $L = 5000$ μm reservoir channel with the height $h_2 = 22$ μm and width $W = 600$ μm, we have produced 100 pairs of doublets with 50μm spacing and the radius of droplet being R =2.5 μm.

The volume fraction ϕ writes:

$$\phi = 2N\frac{\frac{4}{3}\pi r^3}{WhL}$$

ϕ is in the order of a few hundreds ppm ($\leq$ 200 ppm) which is in the order of stabilization value. There is a method that may be tried to solve this problem: adding a small amount of solutes (e.g. sugars or salts such as $MgSO_4$) should allow the water droplets to become more stable in terms of solubilization due to osmotic pressure.

5.3 Hybrid clusters, magnetic and non magnetic clusters

5.3.1 Introduction

As we have mentioned before, the ability to design and assemble three-dimensional structures from colloidal particles is limited by the absence of specific directional bonds. Complex or low-coordination structures, common in atomic and molecular systems, are rare in the colloidal domain[78]. In order to synthesize new complex networks, several pathways could be further explored. For instance, the idea which consists in using preformed hybrid 'colloidal molecules' with a controlled morphology and bearing surface functions susceptible to react together as reactants to create more sophisticated clusters has not been explored yet [38] (see figure 5.23).

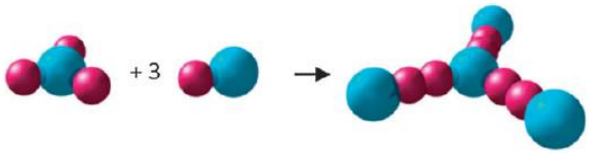

Figure 5.23: Schematic representation of the 'colloidal chemistry' concept. Figure from [38].

We aim at bringing anisotropy to the clusters with our approach. By integrating additional functionalities to our microfluidic chips, we successfully generate clusters containing droplets of different chemical compositions which can potentially develop directional reaction.

5.3.2 Experiment

To demonstrate this possibility, we made several new designs based on the two layers system. One more T-junction is added joining the main channel in the first layer, so that two types of droplets are able to be produced alternatively by the two independent T-junctions. Figure 5.24 shows a typical geometry design. We also design some systems with one T-junctions shifted at a certain distance with repect to another in order to play with the alternative production frequency (design shown in figure 5.27).

The dispersed phase 1 (yellow), the dispersed fluid 1'(violet) and the continuous phase are respectively injected by pressure controller MFCS into inlets 1, 1', 2 ,3. The mechanism of plug break-up and droplets assembly are the same as we described in chapter 4 on the cluster production part.

We examine the hybrid cluster production and assembly in a qualitative way. Two kinds of formulations have been used. To begin with, a dye is added at high concentration in the dispersed phase. Methylene blue, a blue ionic dye, is chosen. Methylene blue is a heterocyclic aromatic chemical compound with the molecular formula $C_{16}H_{18}N_3SCl$. It appears as a solid, odorless, dark green powder, that yields a blue solution when dissolved in water at room temperature. The surface tension $\gamma_{water/air}$ is lowered from 72 mN/m to 60 mN/m at high concentration of methylene blue. This decrease in surface tension indicates an increase in the degree of partition of the dye at the interface [271]. Mineral oil with 2% surfactant Span 80 is used as carrier fluid. The anisotropy in color will bring evidences on heterogeneous cluster production but it does not allow to develop directional assembly.

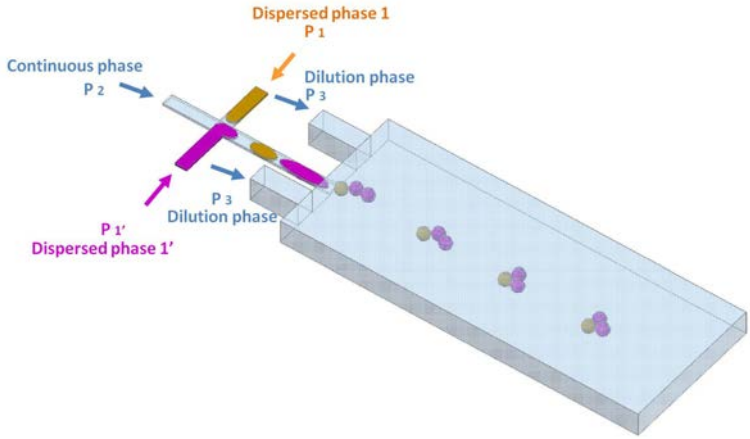

Figure 5.24: Schematic drawing of the the generation of hybrid clusters with microfluidic system.

We thus consider another formulation using magnetic particles instead of dyes to investigate the potential directional reactivity of the hybrid clusters. With microfluidic, we can generate droplets containing magnetic materials. In the presence of magnetic field, we are able to induce response behaviors of such droplets. Magnetic droplets have been studied extensively within lab-on-chip devices, especially for bioassay [272]. The magnetic manipulation of droplets could be advantageous as magnets can be positioned externally. Furthermore, magnetic forces are generally independent of pH and ionic strength[273].

According to the surface chemistry of the magnetic beads, they can be either stabilized in water or in oil. We use two different kinds of superparamagnetic particles. The first consists of aqueous dispersion of micro-spheres (magnetic core (maghemit $Y - Fe_2O_3$) and silica matrix), with thiol group grafted to their surfaces (purchased from Chemicell GmbH). The size of particles is around 500nm. The second type of colloidal particles consists of magnetite Fe_3O_4 nanoparticles of 40nm which is dispersed already in octane (80%) (purchased from ademtech) and which we can further dilute with mineral oil. We use mineral oil with 2% Span 80 as carrier fluids for the water-in-oil emulsions and water with 2% SDS for oil-in-water emulsions.

We apply both inhomogeneous and homogeneous magnetic field. For the inhomogeneous field, a permanent magnet is positioned at an adjacent reservoir channel ($\sim$ 3mm to the side wall), so that it generated a magnetic field perpendicular to the channel. The magnetic field pulls the droplets towards one side through the magnetic forces acting in the particles inside. We also create a homogeneous magnetic field where the lines of force are parallel and the magnetic field is equally strong in all places.To do so, we place two magnets at each side of reservoir channel. There is a reasonably homogeneous field in the gap between the magnets.

5.3.3 Results

As the size of the droplet is mainly determined by the height of the first layer h_1 (see figure 4.12 in chapter 4), we could have some specific combinations by tuning the volumes of the two successive droplets of different fluids. Figure 5.25 shows the formation of hybrid clusters. Alternating transparent and blue plug-like droplets are formed at each T-junctions. In figure 5.25 (a), the volume of transparent plug droplet is sufficient to break into two spherical droplets at step while the blue one is not, thus clusters made of two

transparent and one blue are obtained. Figure 5.25 (b) demonstrated that we can control the inner structures, clusters of two transparent/one blue or of one transparent/two blue, simply by altering the pressure control of the inlet 1 and 1'.

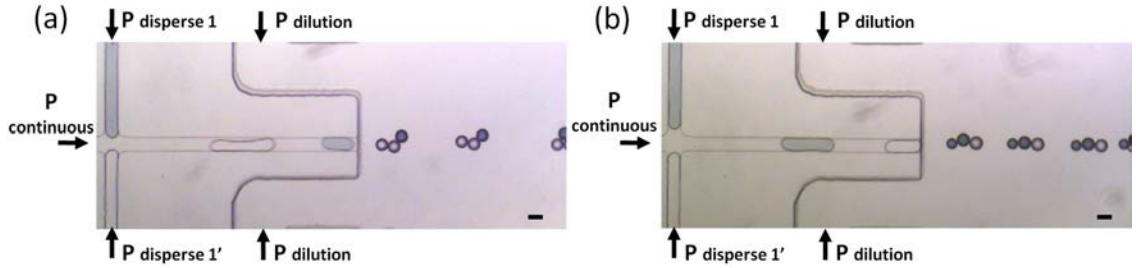

Figure 5.25: Formation of hybrid clusters. PDMS system with W = 50μm, h_1 = 10μm and h_2 = 163μm.(a) Alternating bigger transparent and smaller blue plug droplets are formed at T-junctions. The transparent droplet breaks into two spherical droplets which attach to the spherical blue droplet coming from the previous blue plug. (b) Alternating smaller transparent and bigger blue plug droplets are formed at T-junctions. The blue plug droplet breaks into two spherical droplets which attach to the transparent droplet coming from the previous plug. Scale bar, 100μm.

Nevertheless, the tuning of the simultaneously droplet production hasn't been optimized yet. This challenge arises from two main aspects: one is the coupling of the droplets production. Barbier et al. has studies the dynamics of two microfluidic droplets emitters placed in parallel. Complex dynamical behavior, including synchronization, quasi periodicity, and chaos were observed [233]. We need to find the synchronized regimes to generate well-controlled mono-dispersed droplets of two populations. Another aspect is the good control over the distance between two heterogeneous plug-like droplets: the distance of the two successive plug-like droplets generated from two fluids should be close enough to form a single cluster entity. If the distance is too far away, two populations of clusters made of transparent droplets and blue droplets will be produced separately as shown in figure 5.26.

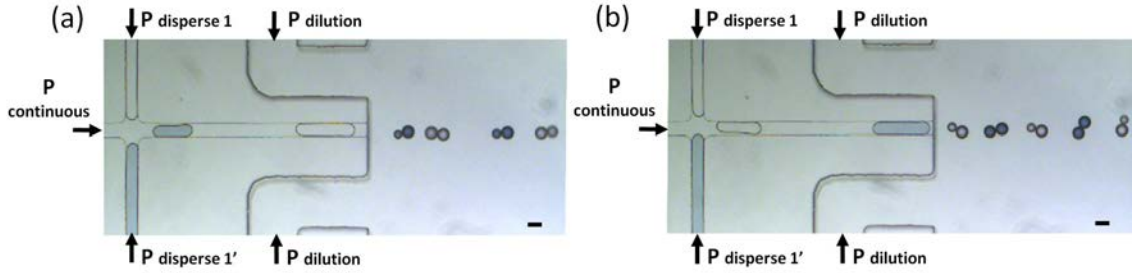

Figure 5.26: Spacing between the transparent and blue plugs is not well adjusted to form hybrid clusters. PDMS system with W = 50μm, h_1 = 10μm and h_2 = 163μm.(a) Alternating bigger transparent and smaller blue plug droplets are formed at T-junctions. The transparent droplet breaks into two spherical droplets and the blue one breaks into one and a satellite droplet. A train of transparent doublets and blue dumbbells is transported in the reservoir. (b) A train of blue doublets and transparent dumbbells is transported in the reservoir. Scale bar, 100μm.

By shifting a certain distance from one T-junction to another, we gain some ranges over

the spacing control (see the figure 5.27 showing T-junctions production of water droplets with or without magnetic particles). A regular train of doublets is produced steadily.

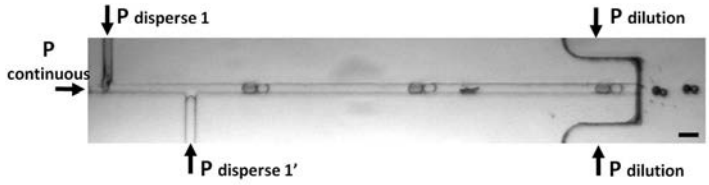

Figure 5.27: The magnetic (black) and non-magnetic (transparent) plugs are produced alternatively from two T-junctions located with 200 μm apart. PDMS system with W = 20μm, $h_1 = 10\mu$m and $h_2 = 163\mu$m. Scale bar, 40μm.

We have produced various hybrid clusters (with dye and with magnetic particles), their morphologies are listed in the figure 5.28.

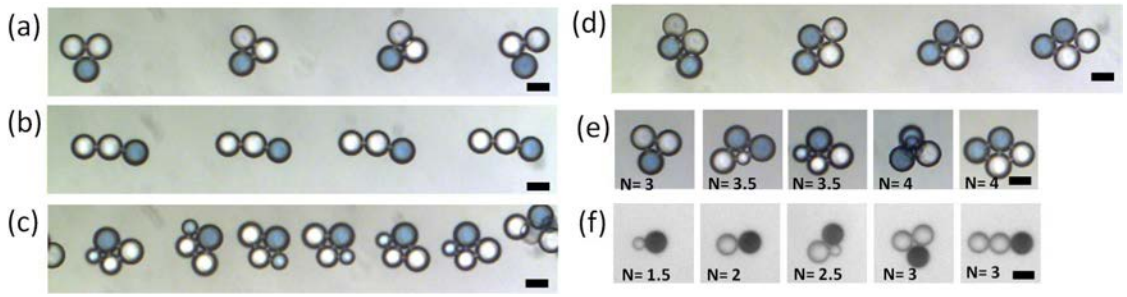

Figure 5.28: Optical micrographs of hybrid clusters with different morphologies. (a)-(d) Trains of anisotropic clusters with blue dye: (a) N=3, triangle shape; (b) N=3, chain-like shape; (c) N=3.5, derived lozenge shape; (d) N=4, lozenge shape. (e) Some examples of the anisotropic clusters with blue dye. N = 3, 3.5, 4. (f) Some examples of the anisotropic clusters with magnetic particles. N = 1.5, 2, 2.5, 3. The scale bar is 50μm.

The concentration of magnetic particles inside a droplet plays an important role on the magnetic manipulation. Figure 5.29 shows the behaviors of simple droplets containing magnetic particles of three different concentrations in an inhomogeneous field under the same experimental conditions. Naturally, when the magnetic particle concentration is low, superparamagnetic droplets still flow in the streamline direction since the magnetic force is too weak to drag them downward. However, they are strongly deflected when the magnetic particle concentration is high enough. The obervations are shown in figure 5.29.

The deflection phenomenon is equally observed with clusters as well as a single droplet. We produce small aggregates of magnetic droplets with the two-layer systems. In the absence of magnetic field, the triplet clusters are flowing without deflection (figure 5.30(a)) and they are dragged to the bottom when an inhomogeneous field is applied (figure 5.30(b)). Within our experimental condition, the adhesion between the magnetic droplet does not visually affected by the magnetic force, the individual droplets remain together in the cluster as an entity without detaching from each other.

We are more interested with the behaviors of clusters in a homogenous field. When a magnetic field is applied, spontaneous alignment of magnetic droplets will take place, and as the magnetic forces in y-direction are canceled out, they will move only horizontally in the flow direction along the reservoir channel which is easier for us to study their movements and interactions. Figure 5.30(c) shows that a train of magnetic doublet droplets

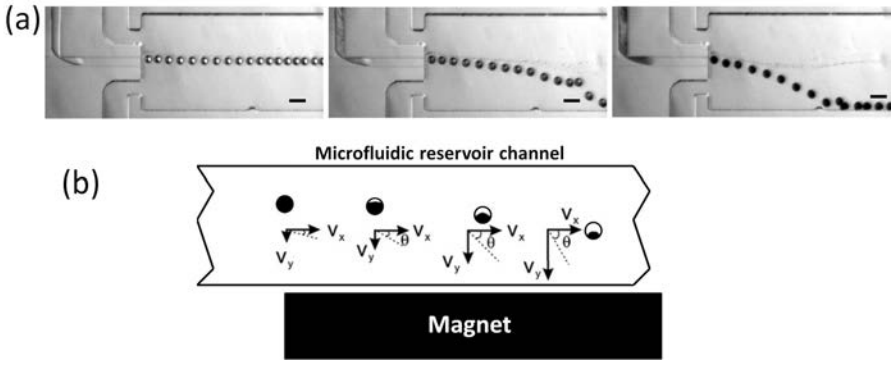

Figure 5.29: (a) Optical micrographs of droplets with three different concentrations of magnetic particles in an inhomogeneous magnetic field. PDMS system, W=50μm, h_1 = 10μm, h_2 = 163μm. Left: a train of droplets which contains little magnetic particles (the color is close to transparent). No deflection is observed. Middle: a train of droplets containing modest magnetic particles. A deflection is observed. Right: a train of droplets containing high concentration of magnetic particles. A faster deflection is observed. The scale bar is 100μm. (b)Schematic diagram of the droplet velocity component. V_x and V_y are the droplet velocity component in the x-direction and y-direction respectively. Although V_x is constant in experiments depending only on laminar flow velocity, V_y gradually increases due to the magnetic force. Therefore superparamagnetic droplets are dragged towards the bottom. The schematic is adapted and modified from [274].

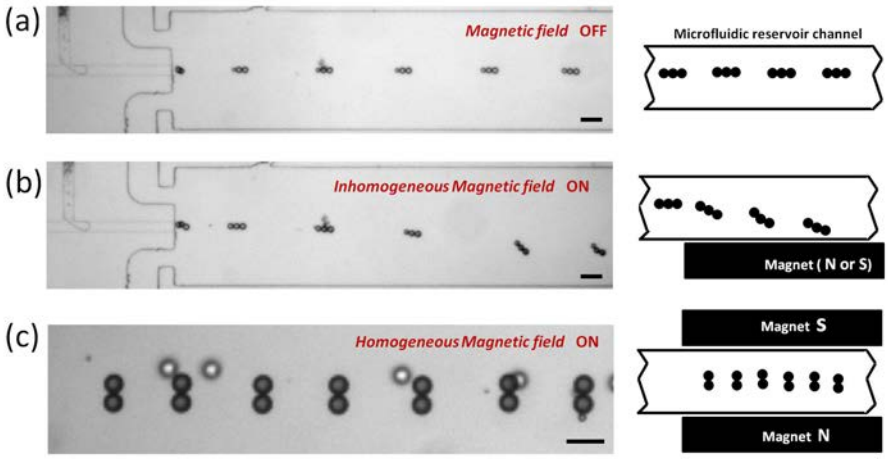

Figure 5.30: (a) Optical micrographs of triplets of droplets flowing in the absence of magnetic field (the flow direction is from left to right). PDMS system, W=100μm, h_1 = 10μm, h_2 = 163μm. (b) Triplets of droplets deflected in the presence of a inhomogeneous magnetic field. The magnet is placed at the bottom side of the reservoir channel. (c) Doublets of droplets oriented verticaly flowing in the presence of a homogeneous magnetic field. The magnets are placed at each side of the reservoir channel. The scale bar is 200μm.

are flowing steadily from left to right and each doublet is oriented vertically in the applied magnetic field.

As we have discussed before in Chapter 4 on the cluster spacing control part, the spacing between the clusters can be controlled easily experimentally. Figure 5.31(a) shows

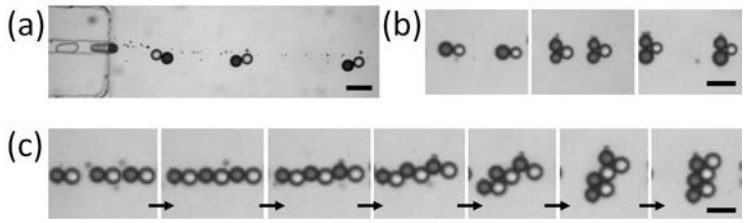

Figure 5.31: Optical micrographs of magetic anisotropic clusters. (a) The production of cluters of doublets. (b) The clusters of doublets (on the left) and the clusters of triplets (in the middle and on the right) are well spaced, no interaction takes place. (c) Three doublets interacting with each other in the presece of homogeneous magnetic field. The magnets are placed in each side of the reservoir channel. The scale bar is 40μm.

the production of hybrid doublets where their spacing is at least 15 times the radius of the droplets. When the hybrid clusters keep distant away from its neighbours, like in the figure 5.31(b), they do not interact with each other just like isotropic clusters do, only the alignment of magnetic droplets inside a cluster is observed. When the clusters are close enough to develop magnetic dipole between them, we found that the rearrangement is most likely to adopt an alternative magnetic and non-magnetic droplet patterns. Figure 5.31(c) shows the evolution of three doublets. They are initially oriented horizontally one after another. A zig-zag movement followed by an alignment of magnetic droplets take place after the droplets are getting into contact.

This planar alternative magnetic-non magnetic droplet patterns can extend to several layers before ending up with an evolution towards 3D spiral cylindrical structures (see figure 5.32).

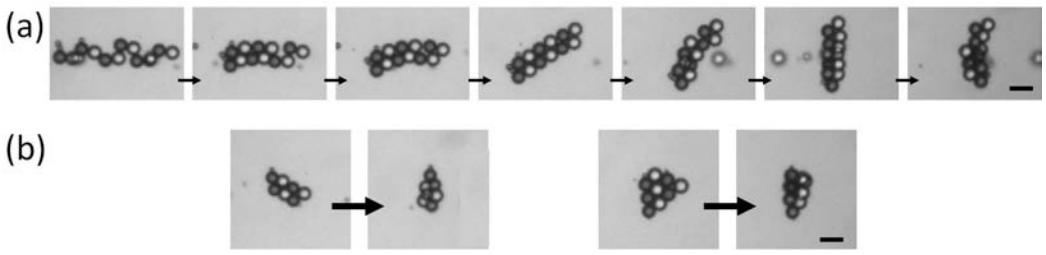

Figure 5.32: (a) Optical micrographs of six clusters of doublets interacting together. An alternative magnetic and non-magnetic intermediate structure is formed and the final stable structure is 3D cylindrical structures. (b) Several examples of evolutions from alternative patterns towards 3D spiral cylindrical structures. The scale bar is 40μm.

Our experimental observations are just preliminary results which yield future perspectives for manipulations with the magnetic-anisotropic clusters for assembly. The adhesion could resist the magnetic force as well as the shear stress to some degree. We can thus manipulate those hybrid clusters without provoking structure destruction and can conduct operations such as the translation and the rotation to bring the clusters to a precise location. We can imaging more precise and sophisticated operations to control the trajectory of the clusters by combining the flow velocity and the magnetically induced velocity. Magnetic tweezers (MT) [275] [276] as well as various magnetic micro-manipulators and arrays of manipulators are available [277][278], they could provide more technical supports for assembling our anisotropic building blocks.

5.4 Solidifying clusters

We explore there the possibility to synthesis particle clusters by introducing solidifiable liquid as the dispersed phase. As mentioned in the introduction, there are a number of synthetic methods for the solidification of drop precursor liquids. The more frequently used methods include free-radical polymerization (photo and thermally initiated), polycondensation reactions, ionic crosslinking, cooling, solvent extraction and self-assembly[129].

For the purpose of demonstration, we choose a liquid which may undergoes sol-gel polymerization [279]. The sol-gel transition is a process which occurs in liquid solution of organometallic precursors (TMOS, TEOS, Zr(IV)-Propoxide, Ti(IV)-Butoxide, etc.), which, by means of hydrolysis and condensation reactions, lead to the formation of a rigid non-fluid mass. This sol-gel solidification reaction is chosen because it is a simple, mild and convenient method [280][281] without any other requirement of additional functionality on the microfluidic chips. The reactions take place at room temperature in a wide range of pH/ionic strength conditions. In addition, we have shown in inverted W/O emulsion part, that the water droplets can form clusters and undergo a dissolution process in which water is progressively lost in the dilute regime within the microfluidic reservoir. Through adding the organometallic precursors in the water droplet, we can solidify the droplets into gel particles by taking advantage of water elimination which favors the condensation reaction.

We prepare aqueous solution of tetraethylorthosilicate (TEOS) under hydrolytic condition using base catalysis to form silica gels. The chemical steps in sol-gel polymerization, including hydrolysis and condensation, result in formation of a network of Si-O-Si chemical linkages from the alkoxysilane. The key steps of the TEOS sol-gel reaction are shown in the figure 5.33.

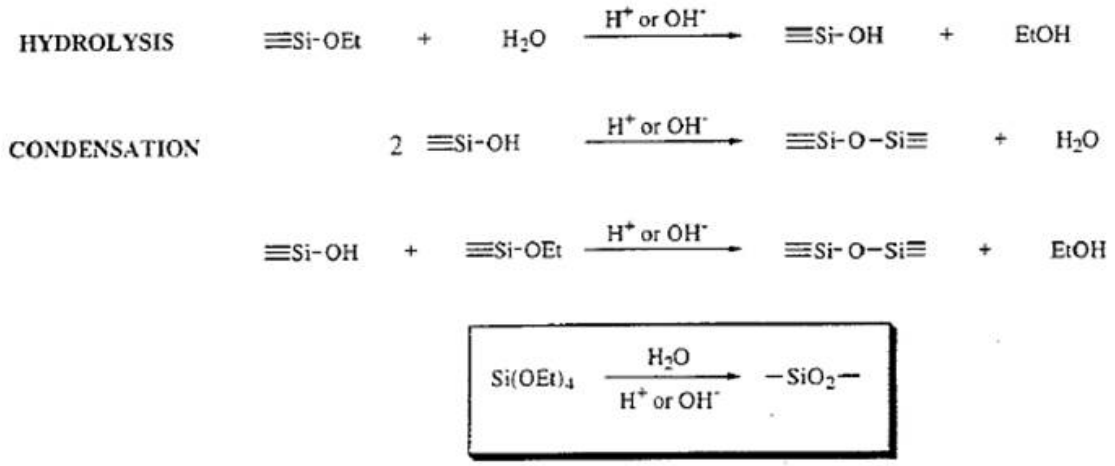

Figure 5.33: Summary of the key steps in sol-gel polymerization of ethoxysilanes: hydrolysis and condensation of alkoxysilanes (water condensation and alcohol condensation).

Silica sol solution is achieved by mixing 2 ml tetraethyl orthosilicate (TEOS, 99.0%, Fluka) and 0.2ml triethyl amine (TEA, 99.5%, Fluka) with 10 ml water under stiring at room temperature until one single homogeneous phase appeared ($\sim$ 8h).

The experimental setup and method are the same as that described previously. We use PDMS system with W=20μm, $h_1 = 1\mu$m, $h_2 = 22\mu$m. The precursor aqueous solution is used as dispersed phase and mineral oil with 2% surfactant Span 80 as the continuous and dilution phase.

We adjust the inlet pressures to produce a train of triplet clusters, then we stop

abruptly the pressures to 0 mbar. Embedded in the fluid at rest, the triangle clusters made of silica xeroglels are formed in few seconds as shown in figure 5.34. The sol droplets experience consecutive stages of shrinkage, condensation and solidification. During the whole process of 'drying', the silica particles stay connected one another forming clusters with a thin film of surfactants between the particle interfaces.

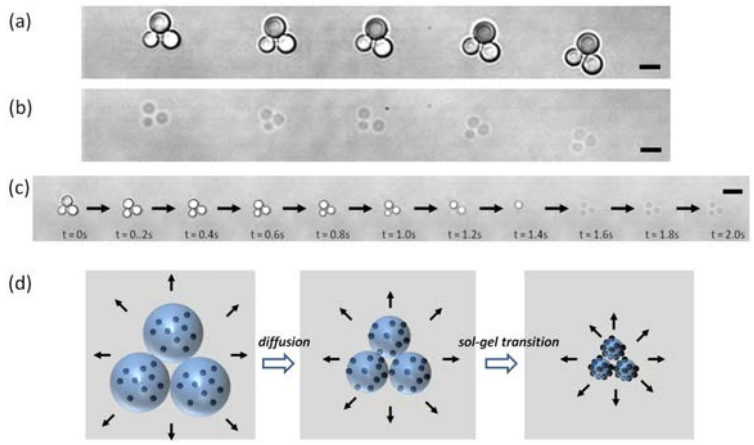

Figure 5.34: Optical micrograph of the formation of the sol-gel transition in the microfluidic reservoir channel containing mineral oil as continuous phase. (a) A train of liquid triplets. Water droplets containing TEOS and TEA. Scale bar, 5 μm. (b) Optical micrograph of a train of solid triplets which is formed as the water diffuses after several seconds. The optical indice of the dispersed phase changes with the water content. Scale bar, 5 μm. (c) Snapshots showing the silica sol-gel transition following one individual cluster. The scale bar is 10μm. (d) Schematic of the solidification process. Black arrows show water diffusion. Silica gel germs (black grains) grow and get contected inside the droplet as the water diffuses in the oil.

The adhesion of those solidified clusters remain to be reinforced. We observe that the detachment of the silica particle may appear in some clusters when the reservoir channel is flushed afterwards. The solidification is a delicate process. We also notice during the experience that the diffusion process requires a profond study. For example, in order to accelerate the solidification time, we adopt the fluorinated oil in which the water diffuses faster. In that case, the pre-solidification takes place in the Hele-Shaw T-junction main channel and the plug-like droplet experiences the sol-gel transition so fast that it can no longer break. We obtain only the flat plug gels (see figure 5.35). This liquid risks to clog the channel in the later time.

Figure 5.35: Optical micrograph showing that the sol-gel transition can take place so fast that the plug-like droplet becomes solid and can not break into smaller droplets. The continuous phase here is fluorinated oil FC 3283. The scale bar is 20μm.

To conclude, solidifying the clusters remains to be improved to really obtain solid anisotropic colloidal molecules.

5.5 Article: Self-assembly driven by hydrodynamic dipolar interactions (preprint)

Self-assembly driven by hydrodynamic interactions in microfluidic devices.

B. Shen[1], J.Ricouvier[1], M. Reyssat[1], F. Malloggi[2], P. Tabeling[1]

Abstract

Recent progress in colloidal science has led to produce self-assembled structures whose complexity raises hopes for elaborating new materials. However, with the actual techniques, producing building blocks is a slow process, and, consequently, the throughputs are too small to envisage industrial applications.
We discovered a novel self assembly mechanism that may unlock this bottleneck. It is based on the hydrodynamic dipolar interactions that develop when droplets are slowed down by the microchannel walls along which they are transported. Using microfluidic devices, we fabricate, in a continuous flow process, under unprecedented control, a rich ensemble of planar and tridimensionnal micrometric clusters possessing geometrical, chemical, and/or magnetic anisotropies. A dynamical model reproduces the observations extremely well. Thousands of highly monodispersed self-assembled structures are formed in a few minutes, with almost one hundred percent yields. Continuous productions of millions of building blocks per second for elaborating new functional materials can be envisioned.

1 MMN, ESPCI, UMR Gulliver,10 rue Vauquelin, 75005 Paris , France
2 UMR 3299 CEA/CNRS NIMBE-LIONS, CEA Saclay, F-91191 Gif-sur Yvette, France

The field of colloidal self assembly has made considerable progress over the last few years by synthesizing building blocks, most often particle clusters, whose structural complexity enables the elaboration of materials possessing new, interesting properties[1,2,3,4,5,6,7,8], such as complete three dimensional photonic band gaps in the visible spectrum, which frequently appears as the « Graal » of the field[2,5]. However, the evolution towards complexity has been made at the expense of the speed, and, with the approaches undertaken in the field at the moment, it is unclear whether it will be possible, in a near future, to satisfy the high throughput conditions requested for producing samples of sizes appropriate for developing industrial applications. This represents a major bottleneck. In the past, colloidal materials of millimeter sizes could be produced in hours by drying colloidal solutions, but these materials relied on the assembly of identical colloids and therefore could only give rise to phases of simple symmetry, such as cubic centred, hexagonal closed paked or body centred cubic, improper for developing interesting functionalities[6]. Now, the level of structural complexity of the building blocks has considerably raised but, in order to form colloidal molecules with rich structures, from which a new material can be elaborated, each individual colloidal « atom » must undergo a lengthy brownian search to find its right location on the colloidal "molecular" scaffold. This is too slow a process. By assuming micrometric particles and decamicrometric travel distances, one finds, consistently with Ref[8], that it needs tens of minutes to be complete,. These calculations imply that, with an irrealistic yield of 100%, and a thousandfold parallelized process, the production of a millimeter cube material incorporating billions of complex building blocks would take thirty years[9]. Because of the slowness of the brownian dynamics, the impossibility to accelerate it substantially, added to moderate or mediocre yields, due to the presence of local potential minima which trap the system in long live metastable sates, our ability to synthesize functional colloidal materials of industrial interest with the existing techniques can be questioned.

Bringing deterministically the particles at the right locations by using a flow would certainly accelerate the self assembly process by orders of magnitudes along with achieve 100% yields, but this represents a formidable challenge. The difficulty is to generate local eddies or local circulations on the scale of the colloidal particles, i.e micrometric, that would transport each entity in a way appropriate for synthesizing a desired structure. This raises an interesting challenge for microfluidic technology, whose goal is precisely to control flows at the micrometric scale. In fact, thus far, microfluidics has not significantly impacted the field of colloidal assembly[10,11,12,13]. Investigators have placed particles into droplets rather than in wells, in an attempt to raise the throughput but this has not been sufficient to convey significant progress. Rearranging particles with inertial forces has been demonstrated [14,15], but this approach, although developing extremely high throughputs, is not adapted for producing assemblies relevant for material science applications. Recently, it has been shown that it is possible, theoretically, to form arbitrary assemblies of particles in microfluidic chambers by imposing specific sequences of pressures steps at multiple fluid entries[16,17]. This concept is awaiting experimental support. In the present work, we propose a new pathway, that bears on the combined action of droplet-droplet attraction and dipolar hydrodynamic interactions, the latter being mediated by the microchannel walls along which droplets are transported at small Reynolds numbers. With it, we could produce, with a continuous flow process, aggregates with anisotropic structures (geometric, chemical, magnetic), with almost 100% yields, under high throughput conditions. This approach has the potential to generate large libraries of building blocks, that could eventually be assembled to synthesize functional materials of decent sizes in a realistic time frame. The goal of the paper is to report these findings.

Results

Device and flow organization. As sketched in Fig. 1a, the microfluidic device is based on a two-level lithography. It is based on a geometry published in Ref[18], in which droplets of submicrometric sizes were produced under excellent control. The geometry is thereby well adapted to operate with colloidal objects. The thinner channels of our microfluidic device (heigths between 1 and 10 µm), are located upstream. In this part, immiscible fluids meet at T-junctions, and, owing to a specific synchronization procedure (see Supp Mat 1), sequences of slugs, grouped by pairs, are generated. Driven by the flow, these pairs arrive at a step marking the separation between the thin channels in which they have been generated and a deeper microchannel, called « self assembly channel » (SA channel) in which they will be processed. At the step, owing to the formulation we take, the slugs break up into sticky droplets that aggregate (see Fig. 1a). As

these clusters are transported along the SA channel, they rearrange internally, adopting eventually stationary configurations.

Two additional flow entries, located at 200 µm from the vertical symmetry plane of the device, provide an additional control on the slugs break up process and the cluster dynamics in the SA channel. These additionnal flows contribute to confine the droplet aggregates in a narrow tunnel parallel to the mean flow in the SA channel along with dilute them, i.e increase the distance between two successive clusters. The effect of the control flow is illustrated in Supp Mat 2.

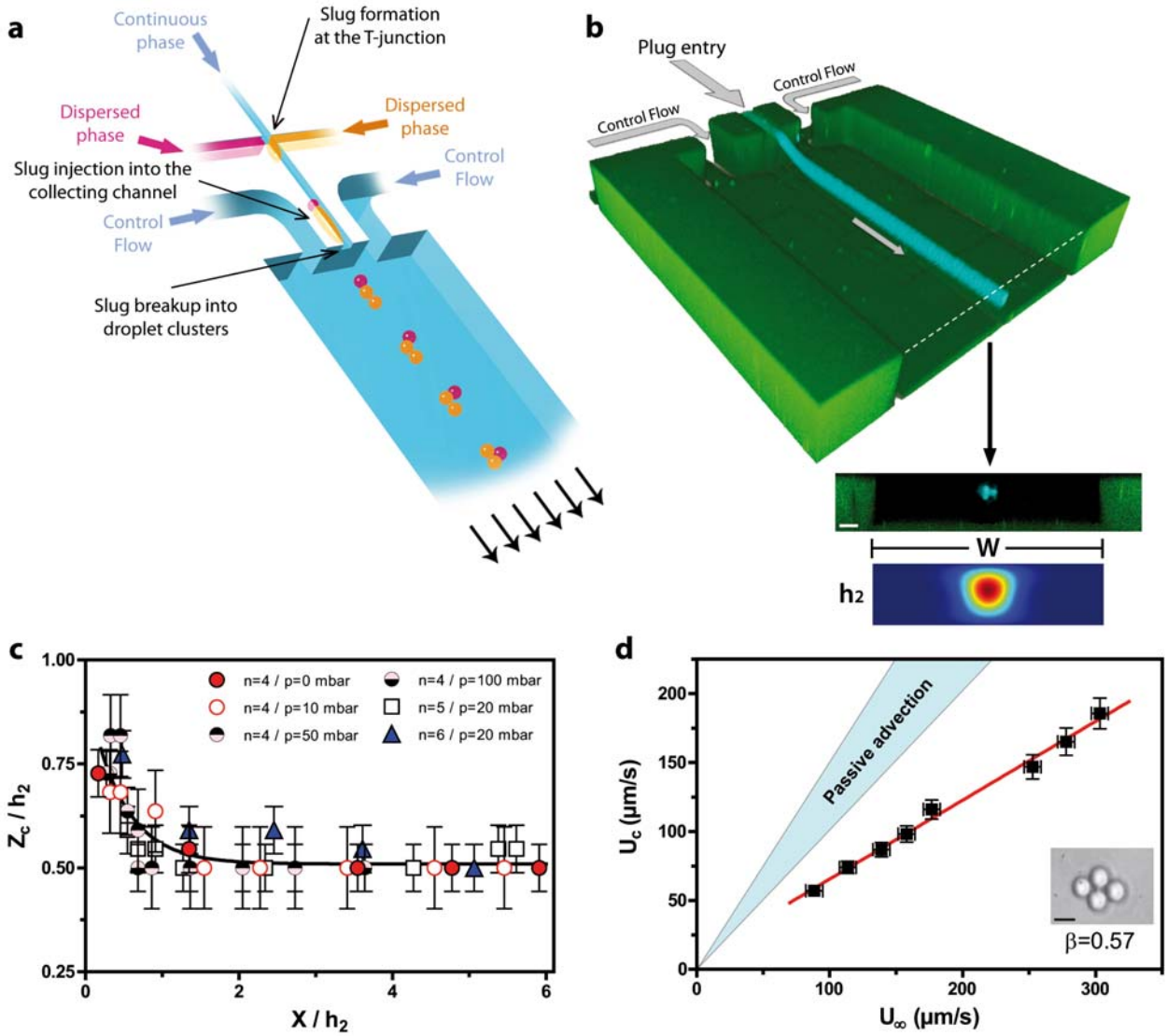

Figure 1 : Sketch of the device, flow structure and droplet positioning in the SA channel. (a) Sketch of the two-level microfluidic device. In the thinner part, located upstream, slug pairs (red and orange) are generated, and arrive at a step where they breakup into sticky droplets, forming clusters that are processed and conveyed downstream in the (deeper) SA channel. (b) Confocal image of the system, taken over long exposure times, that reveal that the clusters are confined in a tube whose center is located close to the mid plane of the SA channel and comparison with COMSOL simulations (see Supp Mat 3), that show that the flows emanating from the central inlet are confined in a tube, also located close to the SA channel symmetry axis. (c) Cluster position measurement using Adaptive Focus. Cluster position along the z axis, normal to the mean flow, normalized by the SA channel height h_2 as a function of the distance to the step x normalized in the same manner. The plot shows that, within the range of experimental conditions we considered, and after a short transient, that does not exceed two SA channel heights, the planar clusters self-center in the SA channel. All the experiments are performed in PDMS system, with h_1=1 µm, h_2=10 µm and d = 5 µm using fluorinated oil, water and 2 % SDS. (d) Dumbbell speed U_C as a function of the

mean flow speed U_∞. The full lines are, resp. the lower limits of passive advection, corresponding to $U_C = U_\infty$ (if the cluster obstructed the SA channel) and $U_C = \frac{4}{3}U_\infty$ (if the cluster was pointwise). The PDMS system dimensions are h_1=1 µm, h_2=22 µm, w= 20µm, using fluorinated oil in water, with 2% SDS. The pressures are respectively 903 mbar, 861 mbar and 1-8 mbar at the dispersed, continuous and control entries of the device of Fig 1a. Scale bar, 5µm.

Droplet formation at the step and cluster behavior in the SA channel: Depending on the flow conditions, slugs arriving at the step can break up into droplets of identical sizes or different sizes. There is in fact a devil staircase[19] that controls the droplet generation process, since two frequencies of emission interact, the first between associated to the slug production, the second to the slug breakup at the step. In practice, the droplet sizes along with the droplet number per cluster, are precisely controlled by adjusting the flow-rates. This part is detailed in Supp Mat 1.

The droplets generated at the step are initially localized close to the top wall of the SA channel (see Fig. 1a,b). As already mentioned, owing to the sticky formulation we use [20,21] (see Methods, Fluids and surfactants), the droplets aggregate together just after they are generated, without coalescing. We found useful to distinguish between two situations, depending on whether the droplet clusters tend to form a planar structure in the SA channel or whether they adopt 3D configurations therein. The former case occurs at « moderate » adhesion, i.e when the droplet stick onto each other without deforming substantially their interfaces at the contact points. 3D structures are obtained at « large adhesion », i.e when these interfaces are significantly flattened at the contact points. In both cases, the adhesion mechanism results from depletion forces developing in the presence of micelles. Large adhesion is obtained by adding salt and therefore lowering the electrostatic repulsive barrier.

The plots and images of Fig. 1 are obtained in the 2D case. Here, the aggregates tend to form planar structures that self-center in the SA channel as they travel downstream. This feature is shown by the confocal image of Fig. 1b which displays the time averaged trajectories of “dimers”, i.e clusters including two droplets. The long time exposed image shows that the dimers are confined in a tube. The tube is parallel to the channel walls and its center lies close to the horizontal symmetry plane of the SA channel (Fig 1b). The height of the tube does not exceed 50 µm in height, which implies that the two droplets, whose diameters are 50µm, must lie in the same horizontal plane. The structure of the cross section of the tube suggests that the two droplets move dowtream with an oblique orientation with respect to the main flow. The optical measurements of Fig. 1c obtained in a variety of flow conditions, with clusters of different shapes (triangles, losanges, trapezes,…), confirm the centering of the clusters in the SA channel. The COMSOL study of Fig. 1b brings interesting information on the self centering effect. It shows that the streamlines emanating from the central inlet channel are confined in a narrow tube located, approximately, at the same position as the droplet clusters tube. The coiencidence indicates that the self centering effect is kinematically-driven. Nonetheless, we found that cluster speeds are significantly below those they would adopt if they were passively advected by the flow (see Fig. 1d). This effect, described in the literature for the case of isolated droplets [22,23], is presumably due to cluster friction against the channel walls. We observe that in our case, the slowing down effect is significant (Fig. 1d). For a height over droplet diameter ratio of 1:3, cluster speeds are typically reduced by a factor of 2 as compared to the speed they would adopt if they were passively advected.

Self centering and slowing down are also observed for 3D structures. In this case, the center of mass of the cluster is located along the symmetry axis of the SA channel. We hypothesize that the fact that droplets do no move freely with respect to each other prevent them to adopt planar configurations.

Self assembly kinetics : As evoked precedently, the droplets form clusters that reconfigure spontaneously as they travel downstream in the SA channel. Here, we analyse this remarkable phenomenon in detail. In Fig. 2 b-d, obtained for moderate adhesion, we track clusters located initially at 300 µm (Fig. (b),(c)), 240 µm (Fig. (d)) and 20 µm (Fig. (e)) downstream from the step, i.e in the plateau region of Fig. 1c. The microscope objective being of high numerical aperture (NA = 1.3, with a depth of

field of 20 µm) and the droplet interfaces being well focused, we confirm that the structures are planar in those cases. In Fig. 2 b-d, the clusters have initiatlly the form of bent chains, owing to the fact that droplets are produced in a row, and, just after the step, the streamlines along which they are transported are curved. These 2D clusters undergo internal rearrangements and eventually adopt symmetric stationary configurations, i.e a horizontal equilateral trimer for N=3, a flat losange for N=4 and a flat isocele trapeze for N=5 (Fig. 2 b-d). The process takes a few seconds to be completed. During the conformationnal changes, droplets roll aside each other in the horizontal plane. Eventually the clusters adopt stationary configurations for which, compared to the initial conditions, the number of internal droplet-droplet contacts C is augmented and the level of symmetry of the structure is increased. This self assembly process produces structures that do not depend on the detail of the initial conditions. Similar comments can be done for the 3D case. This is shown in Fig. 2 e, obtained for large adhesion, where the formation of a compact tetrahedron is achieved at the term of a dynamical sequence which also takes a few seconds.

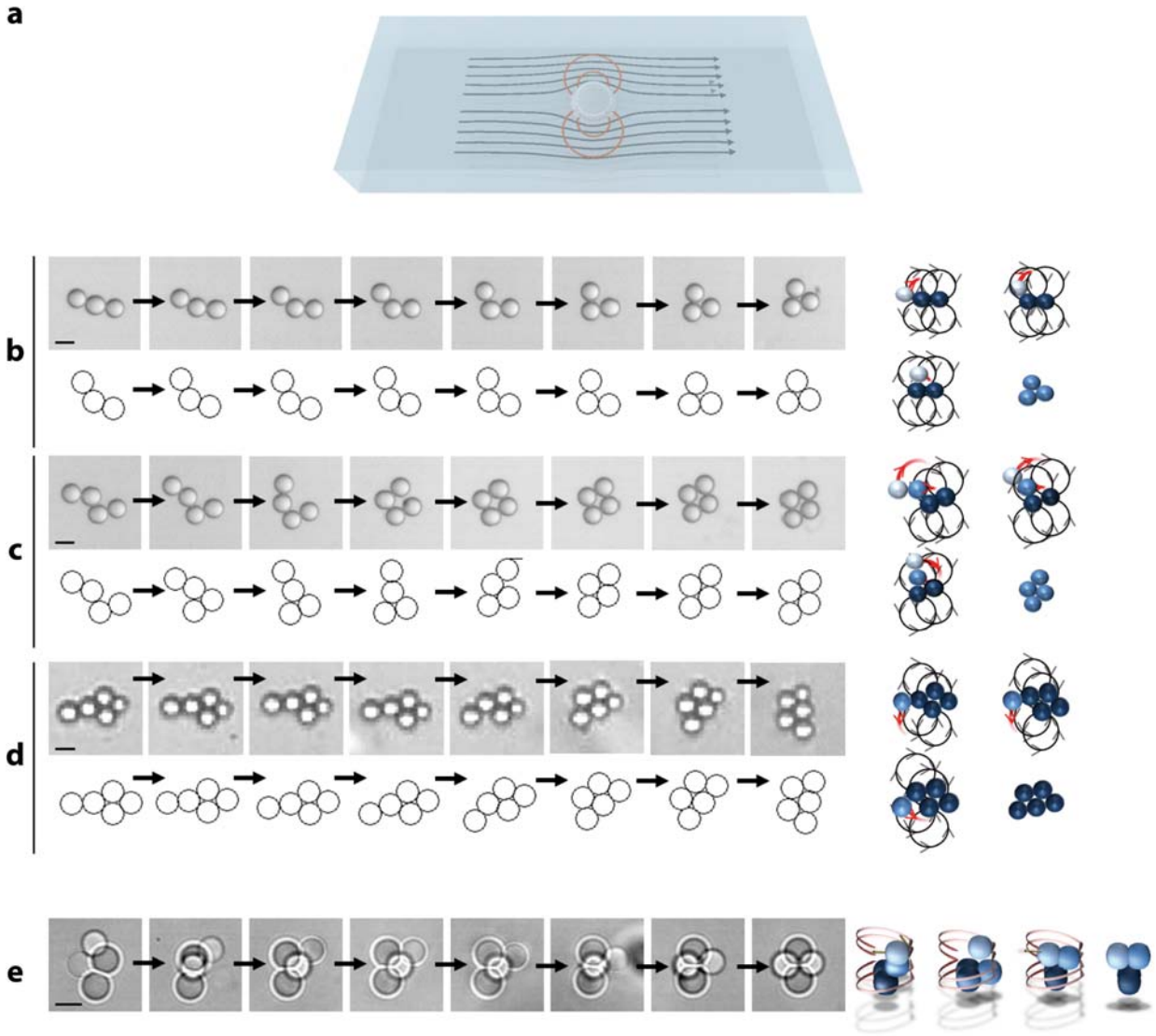

Figure 2. Self-assembly kinetics. (a) Schematic view of the flow field associated to an isolated droplet moving in a microchannel, for the case of moderate ratios height over diameter. (b) Dynamics of a cluster of three droplets evolving towards an equilateral triangular planar structure. *Up:* Experiment made with fluorinated oil in water, 2 % SDS, with droplets 50 µm in diameter. Between each snapshot, the time interval is 0.12s. Scale bar, 50µm. *Right*: Representation of the recirculations associated to each droplet within the cluster, that bring the left droplet towards the center of the central dumbbell. Eventually, after 0.84s, the cluster reaches a steady configuration in which the effect of the recirculations cancel out. *Down:* numerical simulation based on Eq (1), with Y=1.5 and time intervals of one characteristic times τ (see Supp Mat 4). (c) Same situation for N=4 (d=50 µm, time interval 0.4 s).

Scale bar, 50µm. Y=0.8, intervals of 6 τ and (d) N=5 (d=5 µm, time interval 1s). Scale bar, 5 µm. Y=0.8 and intervales of 15 τ. (e) *Left:* Kinetics of a tridimensionnal tetrahedron, in the case N=5. The fluids are fluorinated oil in water with 2 % SDS in presence of 5 % Nacl. Here, d=50 µm, and the time intervals are 0.04 s. Scale bar, 5µm. *Right:* Representation of the dipolar recirculatons leading to the formation of a compact tetrahedron.

The self assembly process shown in Fig. 2 b-e is not driven by brownian fluctuations : it would take days to develop the internal displacements of Fig. 2, while only a few seconds suffice in the experiments. In order to understand this spectacular self assembly mechanism, we focus on the two dimensionnal structures, which, owing to their simplicity, are more amenable to a thorough analysis. As demonstrated in Fig. 1 b-d, the planar clusters lie in a plane located close to the symmetry axis of the SA channel, i.e in a region where the shear is zero. The paradox is that they are advected by an approximately uniform steady flow and in the meantime, they develop a spectacular dynamics that leads to rapid internal rearrangements. We propose here that the physical origin of the phenomenon is linked to the presence of the top and bottom walls of the SA channel. We have checked, by increasing the height over droplet radius ratio, thus decreasing the confinement, that the self assembly process of Fig. 2 b-e is no longer in action. In this case, the droplets keep their initial configuration as they travel in the SA channel. This experiment indicates that the mechanism at work is mediated by the walls. The argument we propose here is thus based on the hypothesis that for moderate ratios of h_2/R, the microchannel walls slow down the clusters' speeds, in a way shown by Fig. 1d, i.e by approximately 50%. The kinematic consequence of this slowing down effect is that around the droplets, a dipolar hydrodynamical field develops, as sketched in Fig 2a. In fact, in a frame moving with the average speed of the external phase, the clusters move backward, and, owing to mass conservation, the fluid that it must displace to recede recirculates in the forward direction, which gives rise to the dipolar-like pattern sketched in Fig. 2a. In fact, this reasoning can be made for each droplet embedded in a cluster. In each aggregate, the horizontal recirculations developed by each droplet exert viscous drags onto their partners, displacing them with respect to each other, therefore provoking configurational changes. The type of droplet-droplet interaction we invoke here has been studied in the literature[24,25,26,27,28,29,30], but only for the case of non sticky droplets. To the best of our knowledge, the role of dipolar interactions in aggregates has never been analyzed theoretically and the demonstration that it can play an interesting role from a self assembly prospective has never been envisaged.

The dipolar interactions we discuss here explains well, at a qualitative level, the cluster dynamics in the SA channel (see Fig. 2). In the case of N=3, the droplet located at the rear of the aggregate is subjected to the recirculations generated by its partners, which work at bringing it closer to the center of the dumbell they form (see Fig. 2b). As the droplet arrives at its final destination, the action of the recirculations cancels out by symmetry, and the configuration becomes stationary. In the case of N=4 the two droplets located at the rear of the structure are subjected to a similar effect (Fig. 2c). In this case, the action of the recirculations is stronger for the farther droplet, which explains that it moves more rapidly than its partner. Here too, after the droplets have reached their final destinations, forming an isocelar losange, the dipolar hydrodynamic forces exerted onto each droplet cancel out by symmetry, and consequently, the morphology does not evolve anymore. Similar reasoning can be done for N=5. We suggest that the same mechanism is at work in the 3D case. Fig. 2e shows how the action of horizontal, dipolar-like recirculations work at transforming a three-dimensional featureless aggregate into a symmetric closed packed tetrahedron for N=4.

Modeling the self assembly dynamics in the case of planar structures : The mechanism discussed above can be modelled in some detail in the 2D case. Similarly as in Refs[24,29,30] we model the droplet-wall interactions by far-field pairwise dipolar interactions, noting that this approach remains acceptable at a semi-quantitative level when droplets touch each other[30]. We thus model the behaviors of our clusters by the following system of 2D dimensionless equations (derived in Supp Mat 4), placing ourselves in a frame of reference moving with U_∞, taking R (the droplet radius) as the reference scale and $\tau = R(1-\beta)/U_\infty$ (in which U_∞ is the speed at infinity) as the reference time:

$$\frac{d\tilde{\boldsymbol{r}}_{\boldsymbol{i}}}{d\tilde{t}} = \sum_{j\neq i}\left(\left(\frac{1}{\widetilde{r_{ij}}}\right)^2 \boldsymbol{e}_{\infty} - 2\left(\frac{1}{\widetilde{r_{ij}}}\right)^2 \boldsymbol{e}_{ij}\left(\boldsymbol{e}_{ij}.\boldsymbol{e}_{\infty}\right)\right) + Y\sum_{j\neq i}\left(\left(\frac{1}{\widetilde{r_{ij}}-2}\right)^2\right)\boldsymbol{e}_{ij} + \boldsymbol{G}_{ij}$$

in which $\frac{d\tilde{r}_i}{dt}$ is the dimensionless speed of droplet *i* (in which $\tilde{\boldsymbol{r}}_{\boldsymbol{i}}$ is its position, and $\tilde{t}$ the dimensionless time), $\boldsymbol{e}_{\infty}$ the unit vector projected onto the mean flow at infinity, ß the reduction factor of the cluster speed (due to friction against the wall, as discussed in the previous sections), $\widetilde{\boldsymbol{r}_{ij}}$ the separation vector between droplets *i* and *j*, $\boldsymbol{G}_{ij}$ a repulsive short range term that prevents droplet interpenetration (see Supp Mat 4), and *Y* is a dimensionless number given by the following expression:

$$Y = \frac{A}{72\pi\eta R^2 U_{\infty}(1-\beta)} \quad (2)$$

in which *A* is the Hamaker constant used in the attractive part of the droplet-droplet potential (Supp Mat 3), and η the external phase viscosity. In Equation (1), the first term of the RHS is the drift caused by the mean flow, the second the dipolar droplet-droplet interaction, the third the adhesive term and the last one a short range repulsive term that prevents coalescence. To the best of our knowledge, the dimensionless number *Y* is new. It represents the ratio of the adhesive droplet-droplet forces over the dipolar forces. Physically, at small *Y*, adhesion is small and droplets separate out while at large *Y*, droplets stick together permanently. Between the two regimes, there is a narrow range of Y within which a complicated dynamics develops ; its analysis stands beyond the scope of the paper.

Solutions to Eq (1), obtained with the initial conditions of Fig. 2, are shown in Fig. 2b-d. The agreement between theory and experiment is remarkable. The sequences of events calculated with Eq (1) coiencide almost perfectly with the experiment for the three cases we considered, i.e N=3, 4 and 5. The model demonstrates that a dipolar interaction, coupled to adhesion conditions, nurtures a novel self assembly mechanism, that leads to the formation of symmetric structures. The excellent agreement between the model and the experiment suggests that this mechanism is at work in our microfluidic experiments.

The model tells us that it takes a time $\tau = R(1-\beta)/U_{\infty}$ (3) to reach a stationary configuration. With the speeds and sizes at hand and a factor ß significantly smaller than unity, τ is on the order of a few seconds, which agrees well with the experiment. This estimate moreover shows that there is a potential to improve the speed of the self assembly process by increasing U_{∞} and downscaling.

Stationary structures : At late times, i.e. after a few seconds, steady configurations are obtained. The planar structures we observed are displayed in Fig. 3a. Typically, chains are obtained at large control flows, and more compact structures are produced at smaller values of this parameter. As shown in Fig. 3a, the structures have different shapes - T, crosses, losanges, trapezes, triangles,.. - . All are symmetric with respect to a mirror plane. The mirror symmetry was not preexisting in the initial clusters produced at the step. This confirms that the self assembly mechanism always works at driving the clusters from less to more symmetric states. This observation has a dynamical significance: symmetrisation is necessary for cancelling out the action of the dipolar recirculations generated by each droplet and consequently ensure configurational stationarity. Maintained by depletion forces the late time structures do not evolve anymore after they are formed. We have checked by stopping the flow that they survive for periods of time varying, depending on the droplet sizes, from hours to days, consistently with diffusive times R^2/D (where D is the diffusion constant of the droplet) we can estimate in each case. This remark has a practical interest from analysis and processing prospectives.

On Fig. 3a, the stationary planar structures are classified in function of the number *N* of droplets they include and the number *C* of droplet-droplet contacts they achieve. All the configurations are confined in a triangular-shaped domain: the lower boundary is the line $C = N-1$, corresponding to the structures achieving the smallest number of contacts, i.e the chain. The upper line $C = 2N-3$ corresponds to clusters

maximizing the number of contacts in 2D. Inside the triangle, the structures adopt various shapes, in form of T or crosses. Apart from three exceptions, we have succeeded, by varying the flow conditions, to fill the space, i.e achieve all possible contact numbers. As long as N is smaller than 6, the structures are unique for a fixed pair (N, C). However, similarly as in three dimensions, degeneracies are observed for N = 6. This is shown in Fig. 3a, in which three distinct morphologies are associated to the pair N=6, C=9 . All the configurations shown in the diagram – including the degenerate ones - are associated to well defined flow conditions and are therefore reproducible.

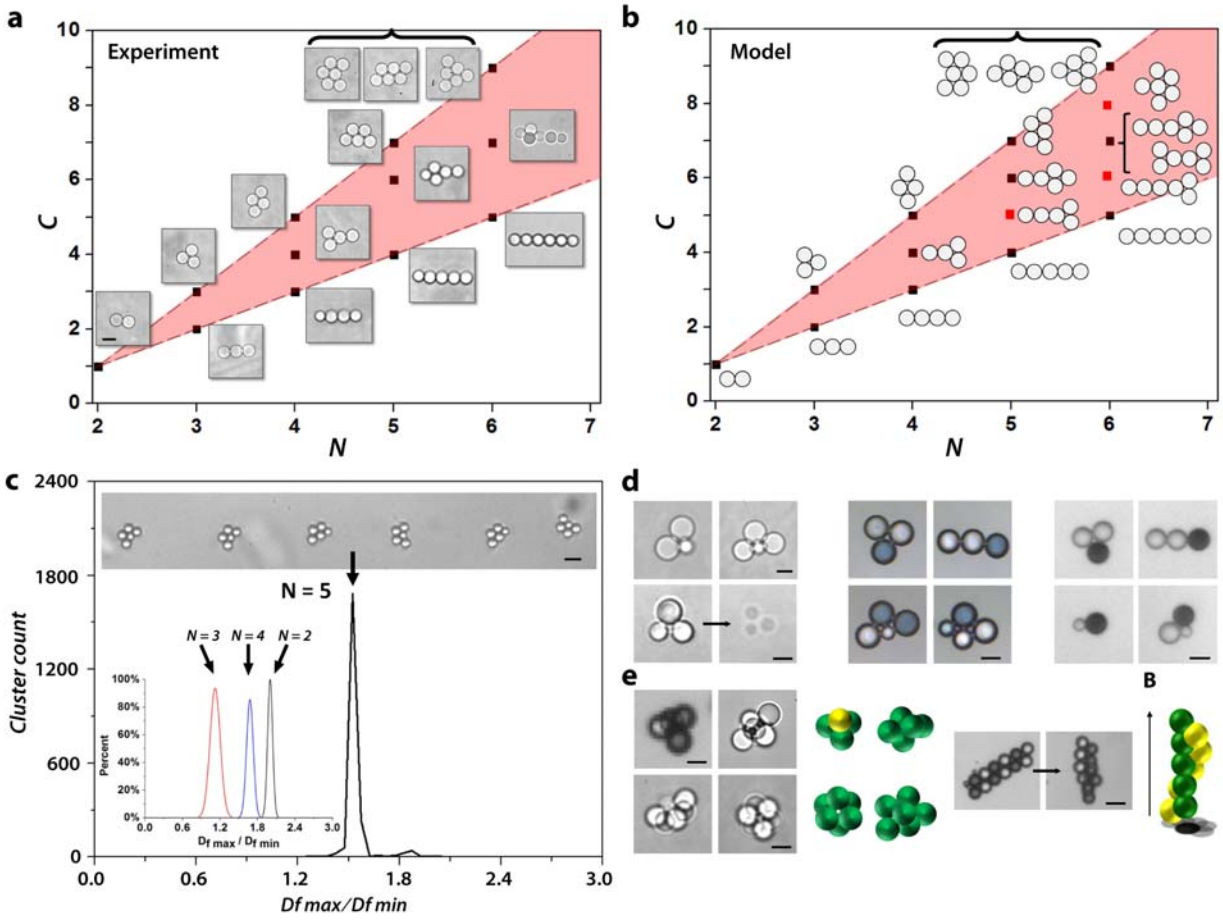

Figure 3 : **Stationary configurations** (a) Observed cluster morphologies at late times, i.e after a few seconds. Scale bar is 5µm. (b) Simulation of the stationary morphologies, based on Eq (1). (c) Histogram of pentamer clusters aspect ratio $\lambda = D_{max}/D_{min}$ for a population of 2134 clusters, inclusing 5 droplets, 5µm in diameter, in which D_{max} is the Feret maximum diameter and D_{min} the minimum one. The coefficient of variation (i.e., the quantity $100\ \sigma/\langle\lambda\rangle$) of the major cluster population is ~ 2%, where σ is the standard deviation and $\langle\lambda\rangle$ is the statistically averaged aspect ratio. On the picture, the scale bar is 10 µm. *Inset:* Distributions of the aspect ratios for populations of 152 dumbbells, 382 trimers and 217 quadrimers , all with droplet diameters of 50 µm. (d) A collection of clusters possessing anisotropic structures. *Left array:* shape anisotropies, (left) AB_2 type structure, (right) AB_3 trigonal pyramid; (Scale bar, 5µm), (bottom) Sol gel transition using water,TEOS,TEA,Minerail oil and 2 % Span 80 (scale bar , 5µm) *Central array:* chemical anisotropies for N=3 (compact AB_2 and linear AB_2 type structures) and combination of chemical and geometrical anisotropies (heterogeneous trigonal pyramids). Scale bar, 50 µm. *Right array*, obtained witt fuorinated oil in water, with 2 % SDS; Various structures with droplets incorporating ferromagnetic particles (AB2, linear AB2, dumbbell). On the lower figure, combination of magnetic and geometric anisotropies. Scale bar, 50 µm. (e) Three dimensional clusters. *Left array:* Polyhedron clusters with N = 4, 5, 6, and AB_3 tetrahedron structure, with a magnetic droplet (black) capable of developing a directional, localized magnetic bonding. Scale bar, 50 µm for tetrahedron structure and 5µm for the rest of clusters (with N = 5, 6). *Center left:* Representations of the 3D structures using yellow for the magnetic and green for the non magnetic droplets. *Right:* Evolution of a magnetic structure into an helix in the presence of homogeneous magnetic field whose

direction is signalled by the arrow (Scale bar, 40 μm). *Extreme right*: Representation of the 3D spiral structure, using yellow for the magnetic and green for the non magnetic droplets.

We used Equation (1) to calculate the ensemble of steady configurations generated by the system at late times. They are displayed in Fig. 3b. We found that all the steady structures observed experimentally are reproduced numerically. Nonetheless, Eq (1) identifies three stationary structures that the experiments has not revealed: one is in form of a T, the other is a H, and the third one has the form of a mushroom. As in the experiment, the structures are unique for a given couple *(N, C)* except for $N = 6$ where degeneracies appears. In this case, Eq (1) obtains three stationary states for $C = 9$ (as in the experiment) and two for $C = 7$ – only one was observed (Fig 3a) -. As a whole, experiments and theory agree extremely well, if we consider that, in the experiments, the space of initial conditions is more difficult to span thoroughly than in the model.

The notion of high throughput and close to 100% yield are demonstrated in Fig. 3c. The sharp peak appearing on the Figure represents the histogram of the aspect ratios of 2134 clusters produced in a continuous way, i.e with no interruption. 95% of them have exactly the same compact trapezoidal structure, with *N=5* and *C=7* (Fig 3c) -. Such structures have less than 2% geometrical dispersivity (estimated with the standard type distribution of Fig. 3c). The rest of the clusters, associated to *N=5, C=6*, are in form of crosses. No other shape is observed. Comparable performances have been obtained for *N= 2, 3 and 4* (see the histograms in Fig 3c). In those cases, 100 % yields are obtained.

The hydrodynamic self-assembly mechanism we discovered here is obviously not restricted to identical droplets. This remark is crucial from the prospective of material synthesis, since heterogeneities in the basic blocks, capable of driving directional interactions, must be present to obtain materials with interesting functionalities[4,5]. Fig. 3d shows that, with our approach, stationary structures including unlike droplets, with heterogeneous chemistries and shapes, and different magnetic properties, can be produced under full control. In fact, Fig. 3d illustrates well the classification of anisotropic structures proposed in Ref[6], based on shapes, geometry and chemistry. Structures with unlike droplets are obtained by working with slugs that break up into sequences of droplets of different sizes, according to the devil's staircase dynamics mentioned earlier[19] (see Supp Mat 1). Structures with different chemical compositions are obtained by exploiting the full capability of the devices, i.e driving slug pairs of different compositions into the SA channel (see Fig. 1a). Structures with magnetic droplets are obtained in the same way, with magnetic nanoparticles injected in one of the dispersed phases. With ferromagnetic droplets, we can explore a broader configurational space. Fig 3e shows a cluster assembling two rows of six droplets, one ferromagnetic, the other non. On applying a magnetic field, the structure undergoes a morphological change that give rises to a spiral. Also interesting from a material propective, is the fact that, on using a sol-gel transition, the clusters can be solidified.

Our approach also produces 3D clusters with high yields and large throughputs. Fig 3e displays a subset of the three dimensional structures we obtained. All are close packed polyhedrons. Despite the fact that self assembly is driven by hydrodynamic interactions *and not* by brownian fluctuations[31], the structures we obtain are unique up to *N=5* and degenerate for *N=6,* exactly as for the brownian case. This remark may suggest a different way to understand the problem of configurational selection, which is still open at the moment. Indeed, similarly as in 2D, the chemical compositions of the droplets forming these structures can be varied at will, as long as there is no interference with the surfactants. Fig. 3e shows a tetrahedron where the base is composed of ferromagnetic droplets, while the top includes a non magnetic one. The opposite situation (one ferromagnetic droplet, three non magnetic) has also been obtained (not shown). These structures have the capability to develop localized (magnetic) bonding, whose importance for material synthesis is repeatedly stressed in the literature (see, for instance, Ref [9]).

Discussion and conclusion : We have discovered a novel mechanism that assembles particles (droplets in our case), to produce an ensemble of elementary structures of great diversity. The clusters we produce can conceivably be incorporated into large assemblies to obtain a material, provided they can be stabilized and extracted from the microfluidic device. The mechanism we discovered is based on

hydrodynamic dipolar interactions, which, compared to brownian motion, accelerates the self assembly process by orders of magnitudes. With this mechanism, we succeeded to form, using a continuous flow process (by opposition to the batch process used in the field), a rich ensemble of micrometric structures with controled anisotropies (geometrical, chemical, magnetic) in 2D and 3D, as well as spirals, many of them having capabilities, from a structural standpoint, to develop directional interactions. The syntheses are achieved rapidly (a few seconds), under high throughput conditions, with almost one hundred percent yields, three critical conditions that, coupled with the complexity level that is accessible, opens a new pathway towards the elaboration of functional colloidal materials of sizes appropriate for industrial applications. In our case, producing 10^9 structures in a one thousandfold parallelized device would take 30 days instead of 30 years with the standard approach. This is still a long time but there is much room for considerably improving the situation. Higher flow speeds can be increased by increasing pressures as long as the flow remains in the step emulsification regime[32], smaller (submicrometric) droplets can be obtained by downscaling [19,33], and more massive parallelization can be realized. The prospectives for increasing production rates, given by Eq (3), by orders of magnitude, are thus excellent. Down the road, as we mentioned in the abstract, production rates of millions of clusters per second can be envisioned. Other issues that must be addressed for producing a material is the stabilisation of the cluster integrity, their extraction from the chip and their final assembly. Stabilisation should not raise any particular difficulty, owing to the considerable range of possibilities that are avaible in terms of surfactant chemistry, photocurable materials, polymerisation techniques … The solidified cluster shown in Fig. 1d indicates that solutions exist. The final assembly of the clusters can be done by drying, with or without electrical or magnetic field, adding a few hours to the overall process. The fact that, in principle, the droplet chemisty can be changed at will, along with their physical properties (refraction index, electrical conductivity, magnetic susceptibility,…) should greatly facilitate the realization of these steps and, in the meantime, enable the development of interesting functionalities.

Materials and Methods

Microfluidic devices. The microfluidic devices are made by standard soft photolithography and replica-molding techniques from polydimethylsiloxane (PDMS). The molds are prepared using photolighography of a UV-curable epoxy (SU8 20XX series, Microchem). Thet consist of two-layers structures with different heights. The first layer includes one or several T-junctions and is followed by a shallow terrace. The depths of the thin channels (h_1) vary between 1 to 10 um and their widths between 10 µm to 100 µm while those of the collecting channels, i.e. SA channel (h_2) vary between 22 µm and 163 µm, with a width of 600 µm.

Fluids and surfactants. We use different formulations: direct O/W emulsions and inverte W/O emulsions. To produce oil in water structures, we use Fluorinated oil (FC3283, 3M) as the dispersed phase and water with surfactant Sodium dodecyl sulfate (SDS) ([c] varie between 0.5 CMC and 10 CMC) as the continous phase. In another case, we use deionized water as the dispersed phase and mineral oil with Span80 (2%) as the continous phase. The formulations with surfactants above the CMC develop adhesive forces between droplets, thanks to depletion forces generated by the presence of micelles combined to (attractive) Van der Waals interactions. In the meantime droplet coalescence is prevented, owing to the presence of a stable film between the droplets. By adding salt in the O/W emulsion, the repulsive electrostatic barrier is lowerd and adhesion between droplets is enhanced.

Hybrid clusters chemical composition. Two kinds of formulations have been used to produce hybrid clusters. Methylene blue ($C_{16}H_{18}N_3SCl$), a blue ionic dye, is added at high concentration in the dispersed aqueuse phase. It yields a blue solution when dissolved in water at room temperature. The surface tension water/air is lowered from 72 dyn/cm to 60 dyn/cm at high concentration of methylene blue. This decrease in surface tension indicates an increase in the degree of partition of the dye at the interface. Mineraloil with 2% surfactant Span 80 is used as carrier fluid. As for the preparation of the magnetic clusters, we use two different kinds of superparamagnetic particles. The first kind consists of aqueous dispersion of micro-spheres (magnetic core (maghemit Y − Fe2O3) and silica matrix), with thiol group grafted to their surfaces (purchased from Chemicell GmbH). The size of particles is around 500nm. The second type of colloidal particles consists of magnetite Fe_3O_4 nanoparticles of 40nm which is dispersed already in octane (80%) (purchased from ademtech) and which we can further dilute with mineral oil to obtain 0.01 %v/v of ferrofluid in mineral oil. The solution is stabilized by 2% Span80 in the organic phase We use mineral oil with 2% Span 80 as carrier fluids in the previous aqueous dispersion and water with 2% SDS for the latter.

Solidifiable clusters. Silica sol solution is achieved by mixing 2 ml tetraethyl orthosilicate (TEOS, 99.0%, Fluka) and 0.2ml triethyl amine (TEA, 99.5%, Fluka) with 10 ml water under stiring at room temperature until one single homogeneous phase appeared (~ 8h). The precursor aqueous solution is used as dispersed phase and mineral oil with 2% surfactant Span 80 as the continuous and dilution phase. We use PDMS system with W=20μm, h_1 = 1μm, h_2 = 22μm to produce droplets of 5 μm diameter and develop a sol-gel transition leading to cluster solification in the fluid at rest.

Fluid driving and measurement equipement. To drive the fluids, we use pressure sources (MFCS Fluigent) or syringe pumps NEMESYS. By using an integrated flowmeter in the case of pressure sources, we could also measure the flow-rates of the external phase injected in the different entries. Throughout the experiments, we span a range of flow rates varying between 5 and 100μl/min. The droplet motions are recorded with a fast camera (Photron) through an inverted microscope (Zeiss). Image processing is used to determine the droplets characteristics.

Adaptive focus z position measurement. By using the fully automated Leica microscope system with Adaptive Focus Control (AFC), the measurement of the vertical position (z coordinate) of the clusters could be performed. These measurements were made on a microfluidic device with w = 20μm, h_1 = 1μm and h_2 = 22μm. After the detection of the lower wall z = 0 is performed, we span the height of the microfluidic SA channel (h_2 = 22μm), up to the upper wall, plot intensity profiles and localize the maximum to determine the cluster "altitude" z. The process being reproducible , averaging over many clusters was carried out.

Microscope confocale imaging. We produced a stationary train of clusters made of aqueous droplets in mineral oil. To improve the quality of visualization, the dispersed phase was mixed with fluorescein isothiocyanate dextran. Rhodamine B red dye (6×10−3% in aqueuous solution), was infused into the channels and washed before the experiments. This dye permeates the PDMS matrix. Fluids were pumped into the devices through PEEK tubing using a pressure controller (MFCS Fluident). The microfluidic system was characterized by w = 50μm, h_1 = 10μm and h_2 = 163μm. A series of experiments with different flow conditions was performed, with pressures at the control entries varying from 250 mbar to 700 mbar. Before of a slow exposure time, clusters could not be resolved at the individual level; their averaged trajectories form a florescent tube on Fig 1a.

Acknowledgements

we gratefully acknowledge Ministry of Research, ESPCI and CNRS for their support of this work. We thank B. Cabane, A. Leshansky, R.Dreyfus, D.Pines, S.Quade for enlightening discusions, F. Monti for technical help, A.Simon for help in the preparation of the manuscript, all the MMN for fruitful interactions.

[1] Van Blaaderen, A., Colloids get complex, *Science*, **301**, 470 (2003).

[2] Li, F., Josephson, D. P. & Stein, A. Colloidal Assembly: The Road from Particles to Colloidal Molecules and Crystals. *Angew. Chem. Int. Ed.* **50,** 360–388 (2011).

[3] Velev, O. D. & Gupta, S. Materials Fabricated by Micro- and Nanoparticle Assembly – The Challenging Path from Science to Engineering. *Adv. Mater.* **21,** 1897–1905 (2009).

[4] Duguet, E., Désert, A., Perro, A. & Ravaine, S. Design and elaboration of colloidal molecules: an overview. *Chem. Soc. Rev.* **40,** 941 (2011).

[5] Sacanna, S. & Pine, D. J. Shape-anisotropic colloids: Building blocks for complex assemblies. *Curr. Opin. Colloid Interface Sci.* **16,** 96–105 (2011).

[6] Glotzer, S. C. & Solomon, M. J. Anisotropy of building blocks and their assembly into complex structures. *Nat. Mater.* **6,** 557–562 (2007).

[7] Yi, G.-R., Pine, D. J. & Sacanna, S. Recent progress on patchy colloids and their self-assembly. *J. Phys. Condens. Matter* **25,** 193101 (2013).

[8] Wang, Y. *et al.* Colloids with valence and specific directional bonding. *Nature* **491,** 51–55 (2012).

[9] The calculation proceeds as follows: let us consider a parallelized system, composed of one thousand wells (a number compatible with the actual capabilities of microfluidic technology) each of them incorporating the adequate number of particles with the appropriate type for obtaining AB_4 type structures. This system produces

1000 colloidal molecules every 10^3 seconds. With an intermolecular distance of 1 µm, one needs 10^9 molecules to obtain a solid sample of 1 mm^3, which takes 10^9 seconds, i.e 30 years.

[10] Koh, Y. K., Yip, C. H., Chiang, Y.-M. & Wong, C. C. Kinetic Stages of Single-Component Colloidal Crystallization. *Langmuir* **24,** 5245–5248 (2008).

[11] Wong, S., Kitaev, V. & Ozin, G. A. Colloidal Crystal Films: Advances in Universality and Perfection. *J. Am. Chem. Soc.* **125,** 15589–15598 (2003).

[12] Crane, N. B., Onen, O., Carballo, J., Ni, Q. & Guldiken, R. Fluidic assembly at the microscale: progress and prospects. *Microfluid. Nanofluidics* **14,** 383–419 (2013).

[13] Yi, G.-R. *et al.* Generation of Uniform Colloidal Assemblies in Soft Microfluidic Devices. *Adv. Mater.* **15,** 1300–1304 (2003).

[14] Carlo, D. D., Irimia, D., Tompkins, R. G. & Toner, M. Continuous inertial focusing, ordering, and separation of particles in microchannels. *Proc. Natl. Acad. Sci.* **104,** 18892–18897 (2007).

[15] Dino Di Carlo, J. F. E. Equilibrium separation and filtration of particles using differential inertial focusing. *Anal. Chem.* **80,** 2204–11 (2008).

[16] Gerstner, E. Microfluidics: Solutions for assembly. *Nat. Phys.* **7,** 98–98 (2011).

[17] Schneider, T. M., Mandre, S. & Brenner, M. P. Algorithm for a Microfluidic Assembly Line. *Phys. Rev. Lett.* **106,** 094503 (2011).

[18] Malloggi, F., Pannacci, N., .Attia, R., Monti, F., Willaime, H., Cabane, B., Poncet, F., Monodisperse Colloids Synthesized with Nanofluidic Technology. *Langmuir* **26,** 2369–2373 (2010).

[19] Willaime, H., Barbier, V., Kloul, L., Maine, S., Tabeling, P., Arnold Tongues in a Microfluidic Droplet Emitter, *Phys. Rev. Lett*. **96,** 054501 (2006)

[20] Poulin, P., Nallet, F., Cabane, B. & Bibette, J. Evidence for Newton Black Films between Adhesive Emulsion Droplets. *Phys. Rev. Lett.* **77,** 3248–3251 (1996).

[21] Poulin, P. & Bibette, J. Wetting of Emulsions Droplets: From Macroscopic to Colloidal Scale. *Phys. Rev. Lett.* **79,** 3290–3293 (1997).

[22] Evans, E. & Sackmann, E. Translational and rotational drag coefficients for a disk moving in a liquid membrane associated with a rigid substrate. *J. Fluid Mech.* **194,** 553–561 (1988).

[23] Eri, A. & Okumura, K. Viscous drag friction acting on a fluid drop confined in between two plates. *Soft Matter* **7,** 5648–5653 (2011).

[24] Beatus, T., Tlusty, T. & Bar-Ziv, R. Phonons in a one-dimensional microfluidic crystal. *Nat. Phys.* **2,** 743–748 (2006).

[25] Beatus, T., Bar-Ziv, R. & Tlusty, T. Anomalous Microfluidic Phonons Induced by the Interplay of Hydrodynamic Screening and Incompressibility. *Phys. Rev. Lett.* **99,** 124502 (2007).

[26] Cui, B., Diamant, H., Lin, B. & Rice, S. A. Anomalous Hydrodynamic Interaction in a Quasi-Two-Dimensional Suspension. *Phys. Rev. Lett.* **92,** 258301 (2004).

[27] Champagne, N., Lauga, E. & Bartolo, D. Stability and non-linear response of 1D microfluidic-particle streams. *Soft Matter* **7,** 11082 (2011).

[28] Bhattacharya, S., Blawzdziewicz, J. & Wajnryb, E. Far-field approximation for hydrodynamic interactions in parallel-wall geometry. *J. Comput. Phys.* **212,** 718–738 (2006).

[29] Uspal, W. E. & Doyle, P. S. Scattering and nonlinear bound states of hydrodynamically coupled particles in a narrow channel. *Phys. Rev. E* **85,** 016325 (2012).

[30] Shen, B., Leman, M., Reyssat, M. & Tabeling, P. Dynamics of a small number of droplets in microfluidic Hele–Shaw cells. *Exp. Fluids* **55,** 1–10 (2014).

[31] Meng, G., Arkus, N., Brenner, P.,M., Manoharan, V.N., *Science*, **327**, 560 (2010).

[32] Z Li, AM Leshansky, LM Pismen, P Tabeling, *arXiv preprint* arXiv:1405.1923

[33] Shui, L., Van den Berg, A., Eijkel, J.C.T., Scalable attoliter monodisperse droplet formation using multiphase nano-microfluidics, *Microfluid Nanofluid*, **11**, 87 (2011).

SUPPLEMENTARY INFORMATION

Supplementary Material 1 : Component droplets of a cluster production

When the plug-like droplet produced at the T-junction reaches at the step, it will break into smaller spherical droplets. The experimental results suggest that for a fixed geometry, it exists a corresponding critical volume (V^*), below which there is no break-up, the narrowing process cannot be completed, i.e. the tongue's width couldn't reach the critical width to have the fast pinch off, Rayleigh plateau instability. Above this volume, the droplet can further break into several smaller droplets at the 3D step according to the initial plug volume. As a result, we can have one droplet with a satellite droplet, two droplets, two droplets with a satellite etc. The corresponding critical radius R^* is mainly dictated by the height $h1$. Empirically this corresponding critical radius R^* is around 2.5 times the height of the first layer $h1$, this founding is confirmed by other studies (ref). The devil's staircase is observed when the number of the droplets is an integer (N = 1, 2, 3 etc.) for the curve of number of droplets as a function of the plug volume (Fig. 2). The devil's staircase in mathematical analysis refers to any singular function in general. This 3D step emulsification shows the behavior similar to the frequency locking phenomena which gives rise to the devil's staircase. When the plug volume is close to 2 times of the critical volume, for instance 1.95 V^* or 2.05 V^*, in both cases it tends to break to 2 equal sized droplets (0.975 V^* or 1.025 V^* respectively) instead of one droplet with one big satellite droplet (1.95 V^*) or two droplets with one tiny droplet (2.05 V^*). Similar reasoning works for other integer N = 3, 4, 5 etc.

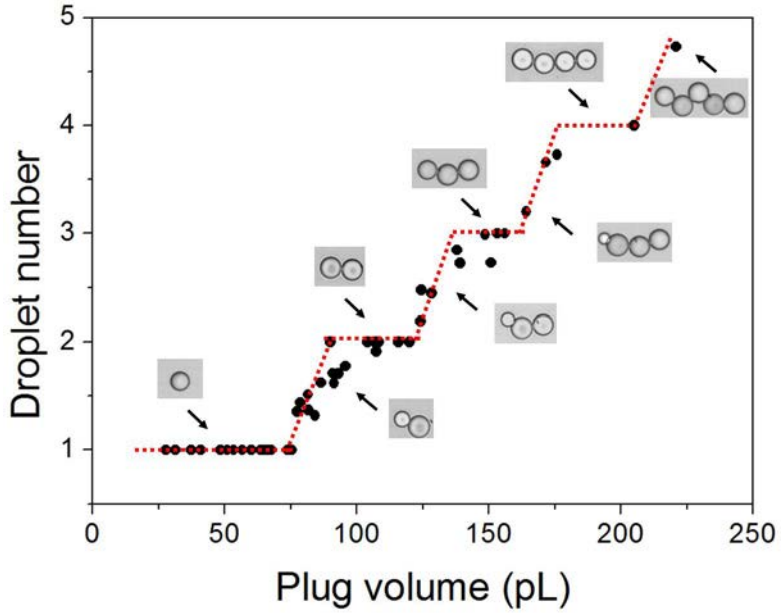

Supplementary Figure 1: Devil's staircase of droplets production. Droplet number as a function of Plug volume for microfluidic system (W=50μm, h_1=10μm).

Supplementary Material 2: Role of the control flow

The control flow changes the initial configuration of the cluster at the step, along with the distances between successive clusters in the SA channel. This is shown in the Figure below, for triplets. Here we maintain the pressures of the dispersed and continuous phases constant (resp. equal to 38 and 11 mbar), and we increase the pressure P_C at the control entries.

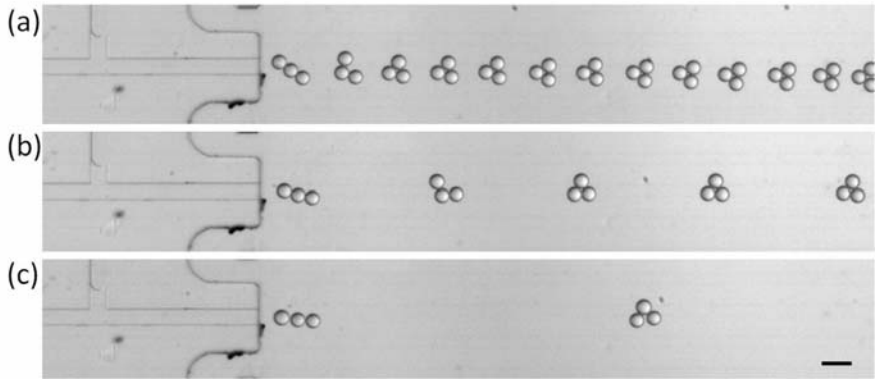

Supplementary Figure 2: Spacing control between the clusters in SA channel. Different configurations observed at various P_c, in a system where W=50μm, h_1=10μm, h_2=160μm. (a) P_C= 20mbar. The distance between clusters is 100μm. (b) P_C= 80mbar. The distance between clusters is 400μm. (c) P_C= 120mbar. The distance between clusters is 1100 μm. The scale bar is 100μm.

As the pressure at the control entries raises up, the orientation of the cluster at the entry tends to align with the mean flow, while, in the meantime, the distances between two successive trimers in the SA channel increase, as the result of mass conservation.

Supplementary Material 3: Numerical simulation

We used the commercial COMSOL Multiphasics software to simulate the flow in the microfluidic device shown in Fig 1a-1b .From the velocity field we extract the streamline, the curve which, at a given instant t, is tangent to the velocity vector. We plot the streamlines coming from the middle height of the confined inlet channel (see Figure 3-1). We see a centering of the streamlines after a length on the order of the height (L~hsa). The convective flux coming from the step channel confirms the centering effect.

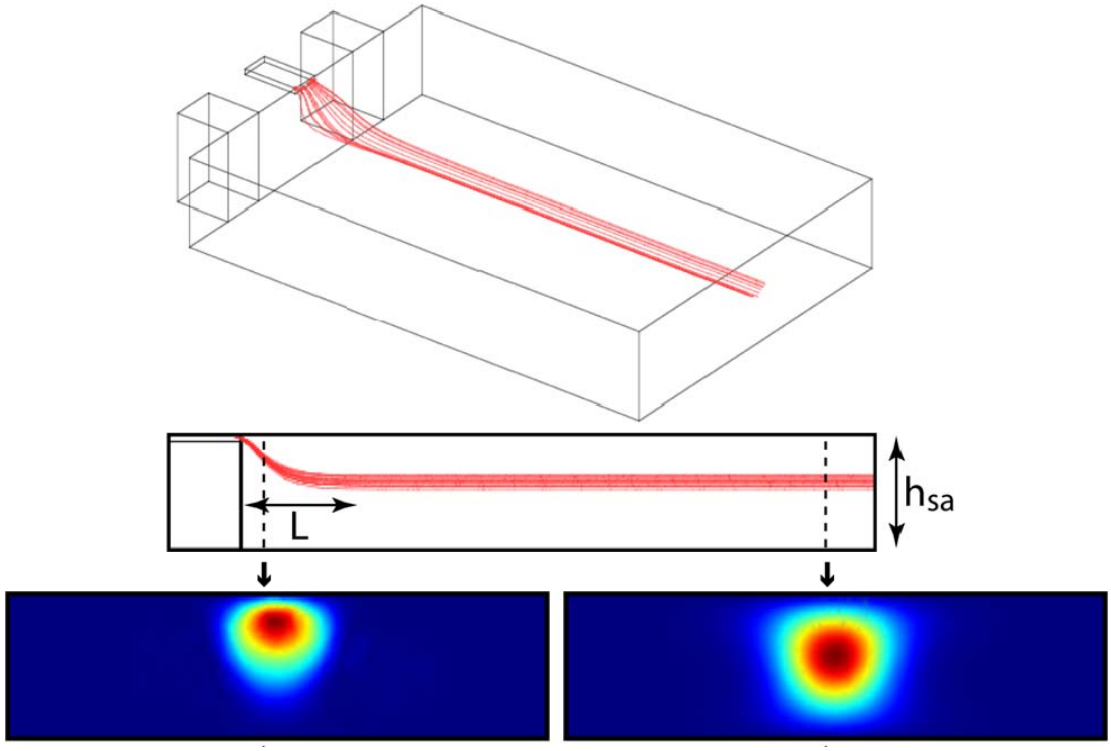

Supplementary Figure 2: Streamlines and convective flux from the middle inlet channel.

Supplementary Material 4: Theory

The model we consider is based on the system of equations obtained in Ref X, in which the two dimensional movement of a system of N identical droplets, whose speeds are different from that at infinity is analysed. In our case, the balance of forces that lead to the system of equations governing the dynamics of the droplets is supplemented by two terms, one expressing the adhesion force between two droplets in contact ant the other, corresponding to a short range repulsive force, which prevents droplet interpenetration. Under such conditions, the system reads:

$$\boldsymbol{U}_i = \beta \boldsymbol{U}_\infty + \beta \sum_{j \neq i} (1-\beta)\left(\left(\frac{R}{r_{ij}}\right)^2 \boldsymbol{U}_\infty - 2\left(\frac{R}{r_{ij}}\right)^2 \boldsymbol{e}_{ij}(\boldsymbol{e}_{ij}.\boldsymbol{U}_\infty)\right) + \sum_{j \neq i} \frac{A\beta}{72\pi\eta}\left(\left(\frac{1}{r_{ij}-2R}\right)^2 + F_{ij}\right)\boldsymbol{e}_{ij}$$

in which U_i is the dimensionless speed of droplet i (in which $\tilde{r}_i$ is its position, and $\tilde{t}$ the dimensionless time), e_∞ the unit vector projected onto the mean flow at infinity, ß the reduction factor of the cluster speed (due to friction against the wall, as discussed in the paper), $\tilde{r_{ij}}$ the separation vector between droplets i and j, Fij a repulsive short range term that prevents droplet interpenetration; its expression is:

$$F_{ij} = \left(\frac{1}{r_{ij}-2R}\right)^{13}$$

To obtain the dimensionless equations (1), on introduces the following dimensionless quantities.

$$\widetilde{U_i} = \frac{\boldsymbol{U}_i}{\beta(1-\beta)U_\infty}, \quad \widetilde{r_{ij}} = \frac{r_{ij}}{R} \text{ and } \tilde{t} = \frac{\beta(1-\beta)U_\infty t}{R}$$

Placing ourselves in the frame of referenceβU_∞, and adimensionalizing the system, one finally gets the following system of equations:

$$\widetilde{\boldsymbol{U}_i^*} = \sum_{j \neq i} (\left(\frac{1}{\widetilde{r_{ij}}}\right)^2 \boldsymbol{e}_\infty - 2\left(\frac{1}{\widetilde{r_{ij}}}\right)^2 \boldsymbol{e}_{ij}(\boldsymbol{e}_{ij}.\boldsymbol{e}_\infty))] + \sum_{j \neq i} \frac{A}{72\pi\eta U_\infty R^2(1-\beta)}\left(\left(\frac{1}{\widetilde{r_{ij}}-2}\right)^2\right)\boldsymbol{e}_{ij} + \boldsymbol{G}_{ij}$$

5.6 Conclusion

Using the same hydrodynamics self-assembly mechanism discovered with our microfluidic device, we have shown, in this chapter, lots of interesting results by simply varying the fluids applied to the systems. In the sticky clusters part, we discussed the influence of surfactants and salts on the adhesion of droplets. We demonstrated that through altering the physico-chemistry of formulation, the adhesion could be reinforced and the cluster's properties could be further tuned. With our approach, the adhesion can be increased either by depletion or by van der Waal force. In the hybrid clusters, magnetic and non magnetic clusters part, we succeeded in bringing anisotropy to the clusters by integrating additional functionalities to our microfluidic chips. Clusters containing droplets of different chemical compositions (dye or magnetic particles) were synthesized. In particular, the hybrid magnetic clusters allows to develop directional reaction. By introducing solidifiable liquid as the dispersed phase, we obtained particle clusters from droplet clusters by sol-gel reaction. These features of new clusters are potentially interesting to access new microstructured colloidal materials.

Chapter 6

Conclusion

In this thesis, we have studied the transport and self-assembly of droplets in microfluidic devices and we have discovered a novel mechanism that assembles droplets into monodispersed clusters in a deterministic manner within our microfluidic device.

Two main contributions have been made in this Ph.D. study:

(1) We carried out a quantitative analysis of the dynamics of a small number of droplets in Hele-Shaw cells. By analyzing basic situations where non trivial phenomena occur, theoretical descriptions could confronted in detail, at a quantitative level, to the experiment. We established an approximate form of the governing equations of the droplet system. This leads to a system of minimal complexity, easy to compute. With the help of microfluidic techniques, we conducted the experimental investigation. We considered the cases N = 1, 2 and 3 droplets and analyzed the influence of the side walls. We compared the model to the experiments and analyzed the discrepancies. As a whole, the model provides a correct picture even if the droplets are close enough.

(2) Assisted with the hydrodynamic dipolar interactions, we succeeded to produce an ensemble of elementary structures of great diversity, using a continuous flow process (by opposition to the batch process used in the field). We have synthesized a rich ensemble of micrometric structures with controlled anisotropies (geometrical, chemical, magnetic) in 2D and 3D, as well as spirals. Many of them have capabilities, from a structural standpoint, to develop directional interactions. The synthesis are achieved rapidly (a few seconds), under high throughput conditions, with almost one hundred percent yields, three critical conditions that, coupled with the complexity level that is accessible, opens a new pathway towards the elaboration of functional colloidal materials of sizes appropriate for industrial applications.

The clusters we produced can conceivably be incorporated into large assemblies to obtain a material. By far the most interesting direction for future work would be the stabilization of the cluster integrity, their extraction from the chip and their final assembly.

Stabilization should not raise any particular difficulty, owing to the considerable range of possibilities that are available in terms of surfactant chemistry, photocurable materials, polymerization techniques ...

The solidification of droplet clusters could be realized with various kinds of reactions, such as free-radical polymerization, ionic crosslinking etc.

The final assembly of the clusters can be done by drying, with or without electric or magnetic field, adding a few hours to the overall process. The fact that, in principle, the droplet chemistry can be changed at will, along with their physical properties (refraction index, electrical conductivity, magnetic susceptibility,...) should greatly facilitate the realization of these steps and, in the meantime, enable the development of interesting

functionalities.

Bibliography

[1] Claudia Simone Plüisch and Alexander Wittemann. Shape-tailored polymer colloids on the road to become structural motifs for hierarchically organized materials. *Macromolecular Rapid Communications*, 34(23-24):1798–1814, 2013.

[2] Birger Lange, Nadine Metz, Muhammad Nawaz Tahir, Friederike Fleischhaker, Patrick Theato, Heinz-Christoph Schröder, Werner E. G. Müller, Wolfgang Tremel, and Rudolf Zentel. Functional polymer-opals from core–shell colloids. *Macromolecular Rapid Communications*, 28(20):1987–1994, October 2007.

[3] Thomas Hellweg. Towards large-scale photonic crystals with tuneable bandgaps. *Angewandte Chemie International Edition*, 48(37):6777–6778, September 2009.

[4] Antti-Pekka Hynninen, Job H. J. Thijssen, Esther C. M. Vermolen, Marjolein Dijkstra, and Alfons van Blaaderen. Self-assembly route for photonic crystals with a bandgap in the visible region. *Nature Materials*, 6(3):202–205, March 2007.

[5] Wei Cheng, Jianjun Wang, Ulrich Jonas, George Fytas, and Nikolaos Stefanou. Observation and tuning of hypersonic bandgaps in colloidal crystals. *Nature Materials*, 5(10):830–836, October 2006.

[6] T. Gorishnyy, C. K. Ullal, M. Maldovan, G. Fytas, and E. L. Thomas. Hypersonic phononic crystals. *Physical Review Letters*, 94(11):115501, March 2005.

[7] F. Yan and W. A. Goedel. A simple and effective method for the preparation of porous membranes with three-dimensionally arranged pores. *Advanced Materials*, 16(11):911–915, 2004.

[8] Arne Thomas, Frederic Goettmann, and Markus Antonietti. Hard templates for soft materials: Creating nanostructured organic materials†. *Chemistry of Materials*, 20(3):738–755, 2008.

[9] Yaw Koon Koh, Chan Hoe Yip, Yet-Ming Chiang, and Chee Cheong Wong. Kinetic stages of single-component colloidal crystallization. *Langmuir*, 24(10):5245–5248, 2008.

[10] Sean Wong, Vladimir Kitaev, and Geoffrey A. Ozin. Colloidal crystal films: advances in universality and perfection. *Journal of the American Chemical Society*, 125(50):15589–15598, November 2003.

[11] G. vonFreymann, S. John, V. Kitaev, and G. A. Ozin. Enhanced coupling to slow photon modes in three-dimensional graded colloidal photonic crystals. *Advanced Materials*, 17(10):1273–1276, 2005.

[12] Melanie L. Mastronardi, Florian Maier-Flaig, Daniel Faulkner, Eric J. Henderson, Christian Kübel, Uli Lemmer, and Geoffrey A. Ozin. Size-dependent absolute quantum yields for size-separated colloidally-stable silicon nanocrystals. *Nano Letters*, 12(1):337–342, January 2012.

[13] Ludovico Cademartiri and Vladimir Kitaev. On the nature and importance of the transition between molecules and nanocrystals: towards a chemistry of "nanoscale perfection". *Nanoscale*, 3(9):3435, 2011.

[14] Judith E. G. J. Wijnhoven and Willem L. Vos. Preparation of photonic crystals made of air spheres in titania. *Science*, 281(5378):802–804, August 1998.

[15] Florent Malloggi, Nicolas Pannacci, Rafaele Attia, Fabrice Monti, Pascaline Mary, Herve Willaime, Patrick Tabeling, Bernard Cabane, and Pascal Poncet. Monodisperse colloids synthesized with nanofluidic technology. *Langmuir*, 26(4):2369–2373, 2010.

[16] Shin-Hyun Kim, Su Yeon Lee, Gi-Ra Yi, David J. Pine, and Seung-Man Yang. Microwave-assisted self-organization of colloidal particles in confining aqueous droplets. *Journal of the American Chemical Society*, 128(33):10897–10904, 2006.

[17] Orlin D. Velev, Abraham M. Lenhoff, and Eric W. Kaler. A class of microstructured particles through colloidal crystallization. *Science*, 287(5461):2240–2243, March 2000.

[18] G.-R. Yi, T. Thorsen, V.n. Manoharan, M.-J. Hwang, S.-J. Jeon, D.j. Pine, S.r. Quake, and S.-M. Yang. Generation of uniform colloidal assemblies in soft microfluidic devices. *Advanced Materials*, 15(15):1300–1304, 2003.

[19] Gi-Ra Yi, Seog-Jin Jeon, Todd Thorsen, Vinothan N. Manoharan, Stephan R. Quake, David J. Pine, and Seung-Man Yang. Generation of uniform photonic balls by template-assisted colloidal crystallization. *Synthetic Metals*, 139(3):803–806, October 2003.

[20] A. D. Dinsmore, Ming F. Hsu, M. G. Nikolaides, Manuel Marquez, A. R. Bausch, and D. A. Weitz. Colloidosomes: Selectively permeable capsules composed of colloidal particles. *Science*, 298(5595):1006–1009, November 2002.

[21] Orlin D. Velev and Shalini Gupta. Materials fabricated by micro- and nanoparticle assembly – the challenging path from science to engineering. *Advanced Materials*, 21(19):1897–1905, 2009.

[22] Paul F. Noble, Olivier J. Cayre, Rossitza G. Alargova, Orlin D. Velev, and Vesselin N. Paunov. Fabrication of "hairy" colloidosomes with shells of polymeric microrods. *Journal of the American Chemical Society*, 126(26):8092–8093, 2004.

[23] Mirjam E. Leunissen, Christina G. Christova, Antti-Pekka Hynninen, C. Patrick Royall, Andrew I. Campbell, Arnout Imhof, Marjolein Dijkstra, René van Roij, and Alfons van Blaaderen. Ionic colloidal crystals of oppositely charged particles. *Nature*, 437(7056):235–240, September 2005.

[24] Krassimir P. Velikov, Christina G. Christova, Roel P. A. Dullens, and Alfons van Blaaderen. Layer-by-layer growth of binary colloidal crystals. *Science*, 296(5565):106–109, April 2002.

[25] Robert J. Macfarlane, Byeongdu Lee, Matthew R. Jones, Nadine Harris, George C. Schatz, and Chad A. Mirkin. Nanoparticle superlattice engineering with DNA. *Science*, 334(6053):204–208, October 2011.

[26] Zuocheng Zhou, Qingfeng Yan, Qin Li, and X. S. Zhao. Fabrication of binary colloidal crystals and non-close-packed structures by a sequential self-assembly method. *Langmuir*, 23(3):1473–1477, January 2007.

[27] Eli Yablonovitch. Inhibited spontaneous emission in solid-state physics and electronics. *Physical Review Letters*, 58(20):2059–2062, 1987.

[28] David Lindley. Landmarks—the birth of photonic crystals. *Physics*, 6:94, 2013.

[29] Martin Maldovan and Edwin L. Thomas. Diamond-structured photonic crystals. *Nature Materials*, 3(9):593–600, September 2004.

[30] F. García-Santamaría, H.t. Miyazaki, A. Urquía, M. Ibisate, M. Belmonte, N. Shinya, F. Meseguer, and C. López. Nanorobotic manipulation of microspheres for on-chip diamond architectures. *Advanced Materials*, 14(16):1144–1147, 2002.

[31] Vinothan N. Manoharan and David J. Pine. Building materials by packing spheres. *MRS Bulletin*, 29(02):91–95, 2004.

[32] David G. Grier. From dynamics to devices: Directed self-assembly of colloidal materials. *MRS Bulletin*, 23(10):21–23, 1998.

[33] Costas D. Maranas and Christodoulos A. Floudas. A global optimization approach for lennardjones microclusters. *The Journal of Chemical Physics*, 97(10):7667–7678, November 1992.

[34] L. T. Wille. Searching potential energy surfaces by simulated annealing. *Nature*, 324(6092):46–48, November 1986.

[35] Chuanming Zong. *Sphere Packings*. Springer, August 1999.

[36] Alfons van Blaaderen. CHEMISTRY: Colloidal molecules and beyond. *Science*, 301(5632):470–471, July 2003.

[37] Alfons van Blaaderen. Materials science: Colloids get complex. *Nature*, 439(7076):545–546, 2006.

[38] Etienne Duguet, Anthony Désert, Adeline Perro, and Serge Ravaine. Design and elaboration of colloidal molecules: an overview. *Chemical Society Reviews*, 40(2):941–960, January 2011.

[39] Amar B. Pawar and Ilona Kretzschmar. Fabrication, assembly, and application of patchy particles. *Macromolecular Rapid Communications*, 31(2):150–168, January 2010.

[40] Erik W. Edwards, Dayang Wang, and Helmuth Möhwald. Hierarchical organization of colloidal particles: From colloidal crystallization to supraparticle chemistry. *Macromolecular Chemistry and Physics*, 208(5):439–445, March 2007.

[41] Stefano Sacanna and David J. Pine. Shape-anisotropic colloids: Building blocks for complex assemblies. *Current Opinion in Colloid & Interface Science*, 16(2):96–105, 2011.

[42] John C. Crocker. Turning away from high symmetry. *Science*, 327(5965):535–536, January 2010.

[43] Pablo F. Damasceno, Michael Engel, and Sharon C. Glotzer. Predictive self-assembly of polyhedra into complex structures. *Science*, 337(6093):453–457, July 2012.

[44] Karol Miszta, Joost de Graaf, Giovanni Bertoni, Dirk Dorfs, Rosaria Brescia, Sergio Marras, Luca Ceseracciu, Roberto Cingolani, René van Roij, Marjolein Dijkstra, and Liberato Manna. Hierarchical self-assembly of suspended branched colloidal nanocrystals into superlattice structures. *Nature Materials*, 10(11):872–876, November 2011.

[45] Sharon C. Glotzer and Michael J. Solomon. Anisotropy of building blocks and their assembly into complex structures. *Nature Materials*, 6(8):557–562, 2007.

[46] Fan Li, David P. Josephson, and Andreas Stein. Colloidal assembly: The road from particles to colloidal molecules and crystals. *Angewandte Chemie International Edition*, 50(2):360–388, 2011.

[47] Y. Mao, M. E. Cates, and H. N. W. Lekkerkerker. Depletion force in colloidal systems. *Physica A: Statistical Mechanics and its Applications*, 222(1–4):10–24, 1995.

[48] S. Sacanna, W. T. M. Irvine, P. M. Chaikin, and D. J. Pine. Lock and key colloids. *Nature*, 464(7288):575–578, March 2010.

[49] Henk N. W. Lekkerkerker and Remco Tuinier. *Colloids and the Depletion Interaction*. Springer, May 2011.

[50] Guangnan Meng, Natalie Arkus, Michael P. Brenner, and Vinothan N. Manoharan. The free-energy landscape of clusters of attractive hard spheres. *Science*, 327(5965):560–563, January 2010.

[51] Sho Asakura and Fumio Oosawa. On interaction between two bodies immersed in a solution of macromolecules. *The Journal of Chemical Physics*, 22(7):1255–1256, December 2004.

[52] Stefano Sacanna, William T. M. Irvine, Laura Rossi, and David J. Pine. Lock and key colloids through polymerization-induced buckling of monodisperse silicon oil droplets. *Soft Matter*, 7(5):1631–1634, February 2011.

[53] Daniela J. Kraft, Ran Ni, Frank Smallenburg, Michiel Hermes, Kisun Yoon, David A. Weitz, Alfons van Blaaderen, Jan Groenewold, Marjolein Dijkstra, and Willem K. Kegel. Surface roughness directed self-assembly of patchy particles into colloidal micelles. *Proceedings of the National Academy of Sciences*, 109(27):10787–10792, July 2012.

[54] Patrick M. Johnson, Carlos M. van Kats, and Alfons van Blaaderen. Synthesis of colloidal silica dumbbells. *Langmuir*, 21(24):11510–11517, November 2005.

[55] M. Ibisate, Z. Zou, and Y. Xia. Arresting, fixing, and separating dimers composed of uniform silica colloidal spheres. *Advanced Functional Materials*, 16(12):1627–1632, 2006.

[56] Allison M. Yake, Rocco A. Panella, Charles E. Snyder, and Darrell Velegol. Fabrication of colloidal doublets by a salting outquenchingfusing technique. *Langmuir*, 22(22):9135–9141, October 2006.

[57] Joseph J. McDermott and Darrell Velegol. Simple fabrication of metallic colloidal doublets having electrical connectivity. *Langmuir*, 24(8):4335–4339, 2008.

[58] Adeline Perro, Stéphane Reculusa, Serge Ravaine, Elodie Bourgeat-Lami, and Etienne Duguet. Design and synthesis of janus micro- and nanoparticles. *Journal of Materials Chemistry*, 15(35-36):3745, 2005.

[59] Andreas Walther and Axel H. E. Müller. Janus particles. *Soft Matter*, 4(4):663, 2008.

[60] Frederik Wurm and AndreasF.M. Kilbinger. Polymeric janus particles. *Angewandte Chemie International Edition*, 48(45):8412–8421, October 2009.

[61] Liang Hong, Angelo Cacciuto, Erik Luijten, and Steve Granick. Clusters of charged janus spheres. *Nano Letters*, 6(11):2510–2514, November 2006.

[62] Stefano Sacanna, Laura Rossi, and David J. Pine. Magnetic click colloidal assembly. *Journal of the American Chemical Society*, 134(14):6112–6115, 2012.

[63] V. Garcés-Chávez, R. Quidant, P. J. Reece, G. Badenes, L. Torner, and K. Dholakia. Extended organization of colloidal microparticles by surface plasmon polariton excitation. *Physical Review B*, 73(8):085417, 2006.

[64] Pei Yu Chiou, Aaron T. Ohta, and Ming C. Wu. Massively parallel manipulation of single cells and microparticles using optical images. *Nature*, 436(7049):370–372, 2005.

[65] Hyundoo Hwang, Youn-Hee Park, and Je-Kyun Park. Optoelectrofluidic control of colloidal assembly in an optically induced electric field. *Langmuir*, 25(11):6010–6014, 2009.

[66] Mirjam E. Leunissen, Hanumantha Rao Vutukuri, and Alfons van Blaaderen. Directing colloidal self-assembly with biaxial electric fields. *Advanced Materials*, 21(30):3116–3120, 2009.

[67] Jeffrey R. Millman, Ketan H. Bhatt, Brian G. Prevo, and Orlin D. Velev. Anisotropic particle synthesis in dielectrophoretically controlled microdroplet reactors. *Nature Materials*, 4(1):98–102, January 2005.

[68] Jianping Ge, Le He, James Goebl, and Yadong Yin. Assembly of magnetically tunable photonic crystals in nonpolar solvents. *Journal of the American Chemical Society*, 131(10):3484–3486, March 2009.

[69] D. Zerrouki, J. Baudry, D. Pine, P. Chaikin, and J. Bibette. Chiral colloidal clusters. *Nature*, 455(7211):380–382, September 2008.

[70] Randall M. Erb, Hui S. Son, Bappaditya Samanta, Vincent M. Rotello, and Benjamin B. Yellen. Magnetic assembly of colloidal superstructures with multipole symmetry. *Nature*, 457(7232):999–1002, 2009.

[71] Paul L. Biancaniello, Anthony J. Kim, and John C. Crocker. Colloidal interactions and self-assembly using DNA hybridization. *Physical Review Letters*, 94(5):058302, 2005.

[72] Anthony J. Kim, Paul L. Biancaniello, and John C. Crocker. Engineering DNA-mediated colloidal crystallization. *Langmuir*, 22(5):1991–2001, 2006.

[73] Faisal A. Aldaye and Hanadi F. Sleiman. Dynamic DNA templates for discrete gold nanoparticle assemblies: control of geometry, modularity, write/erase and structural switching. *Journal of the American Chemical Society*, 129(14):4130–4131, 2007.

[74] Sung Yong Park, Abigail K. R. Lytton-Jean, Byeongdu Lee, Steven Weigand, George C. Schatz, and Chad A. Mirkin. DNA-programmable nanoparticle crystallization. *Nature*, 451(7178):553–556, January 2008.

[75] Mirjam E. Leunissen, Rémi Dreyfus, Roujie Sha, Tong Wang, Nadrian C. Seeman, David J. Pine, and Paul M. Chaikin. Towards self-replicating materials of DNA-functionalized colloids. *Soft Matter*, 5(12):2422, 2009.

[76] Colin J. Loweth, W. Brett Caldwell, Xiaogang Peng, A. Paul Alivisatos, and Peter G. Schultz. DNA-based assembly of gold nanocrystals. *Angewandte Chemie International Edition*, 38(12):1808–1812, 1999.

[77] Etienne Duguet, Anthony Désert, Adeline Perro, and Serge Ravaine. Design and elaboration of colloidal molecules: an overview. *Chemical Society Reviews*, 40(2):941, 2011.

[78] Yufeng Wang, Yu Wang, Dana R. Breed, Vinothan N. Manoharan, Lang Feng, Andrew D. Hollingsworth, Marcus Weck, and David J. Pine. Colloids with valence and specific directional bonding. *Nature*, 491(7422):51–55, November 2012.

[79] Louis C. Brousseau III, James P. Novak, Stella M. Marinakos, and Daniel L. Feldheim. Assembly of phenylacetylene-bridged gold nanocluster dimers and trimers. *Advanced Materials*, 11(6):447–449, 1999.

[80] Novak Jp and Feldheim Dl. Assembly of phenylacetylene-bridged silver and gold nanoparticle arrays. *Journal of the American Chemical Society*, 122(16):3979–3980, 2000.

[81] James P. Novak, Charles Nickerson, Stefan Franzen, and Daniel L. Feldheim. Purification of molecularly bridged metal nanoparticle arrays by centrifugation and size exclusion chromatography. *Analytical Chemistry*, 73(23):5758–5761, 2001.

[82] Dana R. Breed, Raymond Thibault, Fang Xie, Qian Wang, Craig J. Hawker, and David J. Pine. Functionalization of polymer microspheres using click chemistry. *Langmuir*, 25(8):4370–4376, 2009.

[83] Yadong Yin, Yu Lu, and Younan Xia. Assembly of monodispersed spherical colloids into one-dimensional aggregates characterized by well-controlled structures and lengths. *Journal of Materials Chemistry*, 11(4):987–989, 2001.

[84] Y. Yin and Y. Xia. Self-assembly of monodispersed spherical colloids into complex aggregates with well-defined sizes, shapes, and structures. *Advanced Materials*, 13(4):267–271, 2001.

[85] Y Yin, Y Lu, B Gates, and Y Xia. Template-assisted self-assembly: a practical route to complex aggregates of monodispersed colloids with well-defined sizes, shapes, and structures. *Journal of the American Chemical Society*, 123(36):8718–8729, September 2001.

[86] Y. Xia, Y. Yin, Y. Lu, and J. McLellan. Template-assisted self-assembly of spherical colloids into complex and controllable structures. *Advanced Functional Materials*, 13(12):907–918, 2003.

[87] O. D. Velev, K. Furusawa, and K. Nagayama. Assembly of latex particles by using emulsion droplets as templates. 1. microstructured hollow spheres. *Langmuir*, 12(10):2374–2384, January 1996.

[88] Bernard P. Binks and Tommy S. Horozov. *Colloidal Particles at Liquid Interfaces*. Cambridge University Press, August 2006.

[89] Vinothan N. Manoharan, Mark T. Elsesser, and David J. Pine. Dense packing and symmetry in small clusters of microspheres. *Science*, 301(5632):483–487, July 2003.

[90] G.-R. Yi, T. Thorsen, V.n. Manoharan, M.-J. Hwang, S.-J. Jeon, D.j. Pine, S.r. Quake, and S.-M. Yang. Generation of uniform colloidal assemblies in soft microfluidic devices. *Advanced Materials*, 15(15):1300–1304, 2003.

[91] Djamal Zerrouki, Benjamin Rotenberg, Sébastien Abramson, Jean Baudry, Cécile Goubault, Fernando Leal-Calderon, Dave J. Pine, and Jérome Bibette. Preparation of doublet, triangular, and tetrahedral colloidal clusters by controlled emulsification. *Langmuir*, 22(1):57–62, January 2006.

[92] G.-R. Yi, V. N. Manoharan, E. Michel, M. T. Elsesser, S.-M. Yang, and D. J. Pine. Colloidal clusters of silica or polymer microspheres. *Advanced Materials*, 16(14):1204–1208, 2004.

[93] Bo Peng, Frank Smallenburg, Arnout Imhof, Marjolein Dijkstra, and Alfons van-Blaaderen. Colloidal clusters by using emulsions and dumbbell-shaped particles: Experiments and simulations. *Angewandte Chemie International Edition*, 52(26):6709–6712, 2013.

[94] Patrick Tabeling. *Introduction to Microfluidics*. Oxford University Press, November 2005.

[95] Linas Mazutis, John Gilbert, W Lloyd Ung, David A Weitz, Andrew D Griffiths, and John A Heyman. Single-cell analysis and sorting using droplet-based microfluidics. *Nature Protocols*, 8(5):870–891, April 2013.

[96] David J. Beebe, Glennys A. Mensing, and Glenn M. Walker. Physics and applications of microfluidics in biology. *Annual Review of Biomedical Engineering*, 4(1):261–286, 2002.

[97] Carl Hansen and Stephen R Quake. Microfluidics in structural biology: smaller, faster... better. *Current Opinion in Structural Biology*, 13(5):538–544, October 2003.

[98] Delai L. Chen, Cory J. Gerdts, and Rustem F. Ismagilov. Using microfluidics to observe the effect of mixing on nucleation of protein crystals. *Journal of the American Chemical Society*, 127(27):9672–9673, 2005.

[99] Carl L. Hansen, Emmanuel Skordalakes, James M. Berger, and Stephen R. Quake. A robust and scalable microfluidic metering method that allows protein crystal growth by free interface diffusion. *Proceedings of the National Academy of Sciences*, 99(26):16531–16536, December 2002.

[100] Jing-Tao Wang, Juan Wang, and Jun-Jie Han. Fabrication of advanced particles and particle-based materials assisted by droplet-based microfluidics. *Small*, 7(13):1728–1754, 2011.

[101] Eugenia Kumacheva and Piotr Garstecki. *Microfluidic Reactors for Polymer Particles*. John Wiley & Sons, February 2011.

[102] Tharwat F. Tadros. *Emulsion Formation and Stability*. John Wiley & Sons, September 2013.

[103] Bernard P. Binks. *Modern Aspects of Emulsion Science*. Royal Society of Chemistry, January 1998.

[104] Dimiter N. Petsev. *Emulsions: Structure, Stability and Interactions: Structure, Stability and Interactions*. Academic Press, October 2004.

[105] Fernando Leal-Calderon, Véronique Schmitt, and Jerôme Bibette. *Emulsion Science: Basic Principles*. Springer, August 2007.

[106] Andrew S. Utada, Alberto Fernandez-Nieves, Howard A. Stone, and David A. Weitz. Dripping to jetting transitions in coflowing liquid streams. *Physical Review Letters*, 99(9):094502, 2007.

[107] Andrew S. Utada, Alberto Fernandez-Nieves, Jose M. Gordillo, and David A. Weitz. Absolute instability of a liquid jet in a coflowing stream. *Physical Review Letters*, 100(1):014502, January 2008.

[108] Edward Kang, Su-Jung Shin, Kwang Ho Lee, and Sang-Hoon Lee. Novel PDMS cylindrical channels that generate coaxial flow, and application to fabrication of microfibers and particles. *Lab on a Chip*, 10(14):1856, 2010.

[109] Todd Thorsen, Richard W. Roberts, Frances H. Arnold, and Stephen R. Quake. Dynamic pattern formation in a vesicle-generating microfluidic device. *Physical Review Letters*, 86(18):4163–4166, 2001.

[110] Piotr Garstecki, Michael J. Fuerstman, Howard A. Stone, and George M. Whitesides. Formation of droplets and bubbles in a microfluidic t-junction—scaling and mechanism of break-up. *Lab on a Chip*, 6(3):437, 2006.

[111] Shelley L. Anna, Nathalie Bontoux, and Howard A. Stone. Formation of dispersions using "flow focusing" in microchannels. *Applied Physics Letters*, 82(3):364–366, January 2003.

[112] Piotr Garstecki, Howard A. Stone, and George M. Whitesides. Mechanism for flow-rate controlled breakup in confined geometries: A route to monodisperse emulsions. *Physical Review Letters*, 94(16):164501, 2005.

[113] Chunfeng Zhou, Pengtao Yue, and James J. Feng. Formation of simple and compound drops in microfluidic devices. *Physics of Fluids (1994-present)*, 18(9):092105, September 2006.

[114] Yung-Chieh Tan, Vittorio Cristini, and Abraham P. Lee. Monodispersed microfluidic droplet generation by shear focusing microfluidic device. *Sensors and Actuators B: Chemical*, 114(1):350–356, March 2006.

[115] Andrew Woodward, Terence Cosgrove, Joussef Espidel, Paul Jenkins, and Neil Shaw. Monodisperse emulsions from a microfluidic device, characterised by diffusion NMR. *Soft Matter*, 3(5):627, 2007.

[116] Shinji Sugiura, Mitsutoshi Nakajima, and Minoru Seki. Preparation of monodispersed polymeric microspheres over 50 m employing microchannel emulsification. *Industrial & Engineering Chemistry Research*, 41(16):4043–4047, 2002.

[117] Shinji Sugiura, Mitsutoshi Nakajima, Naoyuki Kumazawa, Satoshi Iwamoto, and Minoru Seki. Characterization of spontaneous transformation-based droplet formation during microchannel emulsification. *The Journal of Physical Chemistry B*, 106(36):9405–9409, September 2002.

[118] Shinji Sugiura, Mitsutoshi Nakajima, and Minoru Seki. Effect of channel structure on microchannel emulsification. *Langmuir*, 18(15):5708–5712, 2002.

[119] Shinji Sugiura, Mitsutoshi Nakajima, and Minoru Seki. Prediction of droplet diameter for microchannel emulsification: prediction model for complicated microchannel geometries. *Industrial & Engineering Chemistry Research*, 43(26):8233–8238, 2004.

[120] Emory M. Chan, A. Paul Alivisatos, and Richard A. Mathies. High-temperature microfluidic synthesis of CdSe nanocrystals in nanoliter droplets. *Journal of the American Chemical Society*, 127(40):13854–13861, October 2005.

[121] Craig Priest, Stephan Herminghaus, and Ralf Seemann. Generation of monodisperse gel emulsions in a microfluidic device. *Applied Physics Letters*, 88(2):024106, January 2006.

[122] Venkatachalam Chokkalingam, Stephan Herminghaus, and Ralf Seemann. Self-synchronizing pairwise production of monodisperse droplets by microfluidic step emulsification. *Applied Physics Letters*, 93(25):254101, December 2008.

[123] Daisuke Saeki, Shinji Sugiura, Toshiyuki Kanamori, Seigo Sato, Sukekuni Mukataka, and Sosaku Ichikawa. Highly productive droplet formation by anisotropic elongation of a thread flow in a microchannel. *Langmuir*, 24(23):13809–13813, 2008.

[124] Katherine J. Humphry, Armand Ajdari, Alberto Fernández-Nieves, Howard A. Stone, and David A. Weitz. Suppression of instabilities in multiphase flow by geometric confinement. *Physical Review E*, 79(5):056310, 2009.

[125] Rémi Dangla, Etienne Fradet, Yonatan Lopez, and Charles N. Baroud. The physical mechanisms of step emulsification. *Journal of Physics D: Applied Physics*, 46(11):114003, March 2013.

[126] Ralf Seemann, Martin Brinkmann, Thomas Pfohl, and Stephan Herminghaus. Droplet based microfluidics. *Reports on Progress in Physics*, 75(1):016601, January 2012.

[127] G. F. Christopher and S. L. Anna. Microfluidic methods for generating continuous droplet streams. *Journal of Physics D: Applied Physics*, 40(19):R319, October 2007.

[128] Charles N. Baroud, Francois Gallaire, and Rémi Dangla. Dynamics of microfluidic droplets. *Lab on a Chip*, 10(16):2032–2045, July 2010.

[129] J K Nunes, S S H Tsai, J Wan, and H A Stone. Dripping and jetting in microfluidic multiphase flows applied to particle and fiber synthesis. *Journal of physics D: Applied physics*, 46(11), March 2013.

[130] Demetrios T. Papageorgiou. On the breakup of viscous liquid threads. *Physics of Fluids (1994-present)*, 7(7):1529–1544, July 1995.

[131] Jens Eggers. Nonlinear dynamics and breakup of free-surface flows. *Reviews of Modern Physics*, 69(3):865–930, 1997.

[132] Jeremy L. Steinbacher and D. Tyler McQuade. Polymer chemistry in flow: New polymers, beads, capsules, and fibers. *Journal of Polymer Science Part A: Polymer Chemistry*, 44(22):6505–6533, November 2006.

[133] W. Engl, R. Backov, and P. Panizza. Controlled production of emulsions and particles by milli- and microfluidic techniques. *Current Opinion in Colloid & Interface Science*, 13(4):206–216, 2008.

[134] C. A. Serra and Z. Chang. Microfluidic-assisted synthesis of polymer particles. *Chemical Engineering & Technology*, 31(8):1099–1115, 2008.

[135] Dhananjay Dendukuri and Patrick S. Doyle. The synthesis and assembly of polymeric microparticles using microfluidics. *Advanced Materials*, 21(41):4071–4086, 2009.

[136] Zhihong Nie, Shengqing Xu, Minseok Seo, Patrick C. Lewis, and Eugenia Kumacheva. Polymer particles with various shapes and morphologies produced in continuous microfluidic reactors. *Journal of the American Chemical Society*, 127(22):8058–8063, 2005.

[137] S. Takeuchi, P. Garstecki, D. B. Weibel, and G. M. Whitesides. An axisymmetric flow-focusing microfluidic device. *Advanced Materials*, 17(8):1067–1072, 2005.

[138] Jeremy L. Steinbacher, Rebecca W. Y. Moy, Kristin E. Price, Meredith A. Cummings, Chandrani Roychowdhury, Jarrod J. Buffy, William L. Olbricht, Michael Haaf, and D. Tyler McQuade. Rapid self-assembly of coreshell organosilicon microcapsules within a microfluidic device. *Journal of the American Chemical Society*, 128(29):9442–9447, 2006.

[139] Elizabeth Quevedo, Jeremy Steinbacher, and D. Tyler McQuade. Interfacial polymerization within a simplified microfluidic device: capturing capsules. *Journal of the American Chemical Society*, 127(30):10498–10499, 2005.

[140] Robert F. Shepherd, Jacinta C. Conrad, Summer K. Rhodes, Darren R. Link, Manuel Marquez, David A. Weitz, and Jennifer A. Lewis. Microfluidic assembly of homogeneous and janus colloid-filled hydrogel granules. *Langmuir*, 22(21):8618–8622, October 2006.

[141] A. S. Utada, E. Lorenceau, D. R. Link, P. D. Kaplan, H. A. Stone, and D. A. Weitz. Monodisperse double emulsions generated from a microcapillary device. *Science*, 308(5721):537–541, April 2005.

[142] Wonje Jeong, Jeongyun Kim, Sunjeong Kim, Sanghoon Lee, Glennys Mensing, and David. J. Beebe. Hydrodynamic microfabrication via?on the fly? photopolymerization of microscale fibers and tubes. *Lab on a Chip*, 4(6):576, 2004.

[143] Won Je Jeong, Jeong Yun Kim, Jaebum Choo, Eun Kyu Lee, Chang Soo Han, David J. Beebe, Gi Hun Seong, and Sang Hoon Lee. Continuous fabrication of biocatalyst immobilized microparticles using photopolymerization and immiscible liquids in microfluidic systems. *Langmuir*, 21(9):3738–3741, 2005.

[144] Bruno G. De Geest, John Paul Urbanski, Todd Thorsen, Jo Demeester, and Stefaan C. De Smedt. Synthesis of monodisperse biodegradable microgels in microfluidic devices. *Langmuir*, 21(23):10275–10279, November 2005.

[145] Patrick C. Lewis, Robert R. Graham, Zhihong Nie, Shengqing Xu, Minseok Seo, and Eugenia Kumacheva. Continuous synthesis of copolymer particles in microfluidic reactors. *Macromolecules*, 38:4536–4538, 2005.

[146] Shengqing Xu, Zhihong Nie, Minseok Seo, Patrick Lewis, Eugenia Kumacheva, Howard A. Stone, Piotr Garstecki, Douglas B. Weibel, Irina Gitlin, and George M. Whitesides. Generation of monodisperse particles by using microfluidics: Control over size, shape, and composition. *Angewandte Chemie*, 117(5):734–738, 2005.

[147] Shingo Okushima, Takasi Nisisako, Toru Torii, and Toshiro Higuchi. Controlled production of monodisperse double emulsions by two-step droplet breakup in microfluidic devices. *Langmuir*, 20(23):9905–9908, November 2004.

[148] Dhananjay Dendukuri, Kim Tsoi, T. Alan Hatton, and Patrick S. Doyle. Controlled synthesis of nonspherical microparticles using microfluidics. *Langmuir*, 21(6):2113–2116, March 2005.

[149] Sebastian Seiffert, Mark B. Romanowsky, and David A. Weitz. Janus microgels produced from functional precursor polymers. *Langmuir*, 26(18):14842–14847, September 2010.

[150] Sebastian Seiffert and David A. Weitz. Controlled fabrication of polymer microgels by polymer-analogous gelation in droplet microfluidics. *Soft Matter*, 6(14):3184, 2010.

[151] Keng-Shiang Huang, Tzung-Heng Lai, and Yu-Cheng Lin. Manipulating the generation of ca-alginate microspheres using microfluidic channels as a carrier of gold nanoparticles. *Lab on a Chip*, 6(7):954–957, June 2006.

[152] Kwang Ho Lee, Su Jung Shin, Yongdoo Park, and Sang-Hoon Lee. Synthesis of cell-laden alginate hollow fibers using microfluidic chips and microvascularized tissue-engineering applications. *Small*, 5(11):1264–1268, 2009.

[153] Kan Liu, Hui-Jiang Ding, Jing Liu, Yong Chen, and Xing-Zhong Zhao. Shape-controlled production of biodegradable calcium alginate gel microparticles using a novel microfluidic device. *Langmuir*, 22(22):9453–9457, October 2006.

[154] Shinji Sugiura, Tatsuya Oda, Yasuhiko Izumida, Yasuyuki Aoyagi, Mitsuo Satake, Atsushi Ochiai, Nobuhiro Ohkohchi, and Mitsutoshi Nakajima. Size control of calcium alginate beads containing living cells using micro-nozzle array. *Biomaterials*, 26(16):3327–3331, 2005.

[155] Hong Zhang, Ethan Tumarkin, Raheem Peerani, Zhihong Nie, Ruby May A. Sullan, Gilbert C. Walker, and Eugenia Kumacheva. Microfluidic production of biopolymer microcapsules with controlled morphology. *Journal of the American Chemical Society*, 128(37):12205–12210, September 2006.

[156] W.-H. Tan and S. Takeuchi. Monodisperse alginate hydrogel microbeads for cell encapsulation. *Advanced Materials*, 19(18):2696–2701, September 2007.

[157] Hong Zhang, Ethan Tumarkin, Ruby May A. Sullan, Gilbert C. Walker, and Eugenia Kumacheva. Exploring microfluidic routes to microgels of biological polymers. *Macromolecular Rapid Communications*, 28(5):527–538, March 2007.

[158] Ethan Tumarkin and Eugenia Kumacheva. Microfluidic generation of microgels from synthetic and natural polymers. *Chemical Society Reviews*, 38(8):2161–2168, July 2009.

[159] Wenjie Lan, Shaowei Li, Yangcheng Lu, Jianhong Xu, and Guangsheng Luo. Controllable preparation of microscale tubes with multiphase co-laminar flow in a double co-axial microdevice. *Lab on a Chip*, 9(22):3282, 2009.

[160] Mohana Marimuthu, Sanghyo Kim, and Jeongho An. Amphiphilic triblock copolymer and a microfluidic device for porous microfiber fabrication. *Soft Matter*, 6(10):2200, 2010.

[161] Abel L. Thangawng, Peter B. Howell Jr, Jeffrey J. Richards, Jeffrey S. Erickson, and Frances S. Ligler. A simple sheath-flow microfluidic device for micro/nanomanufacturing: fabrication of hydrodynamically shaped polymer fibers. *Lab on a Chip*, 9(21):3126, 2009.

[162] Baoguo Wang, Ho Cheung Shum, and David A Weitz. Fabrication of monodisperse toroidal particles by polymer solidification in microfluidics. *Chemphyschem: a European journal of chemical physics and physical chemistry*, 10(4):641–645, March 2009.

[163] Aiping Fang, Cédric Gaillard, and Jean-Paul Douliez. Template-free formation of monodisperse doughnut-shaped silica microparticles by droplet-based microfluidics. *Chemistry of Materials*, 23(21):4660–4662, November 2011.

[164] Aiping Fang, Charlie Gosse, Cédric Gaillard, Xuan Zhao, and Joëlle Davy. Tuning silica particle shape at fluid interfaces. *Lab on a chip*, 12(23):4960–4963, December 2012.

[165] Nathan B. Crane, Onursal Onen, Jose Carballo, Qi Ni, and Rasim Guldiken. Fluidic assembly at the microscale: progress and prospects. *Microfluidics and Nanofluidics*, 14(3-4):383–419, March 2013. WOS:000315299100001.

[166] Su Eun Chung, Wook Park, Sunghwan Shin, Seung Ah Lee, and Sunghoon Kwon. Guided and fluidic self-assembly of microstructures using railed microfluidicchannels. *Nature Materials*, 7(7):581–587, 2008.

[167] Su Eun Chung, Yoonseok Jung, and Sunghoon Kwon. Three-dimensional fluidic self-assembly by axis translation of two-dimensionally fabricated microcomponents in railed microfluidics. *Small*, 7(6):796–803, March 2011.

[168] Paul Abbyad, Rémi Dangla, Antigoni Alexandrou, and Charles N. Baroud. Rails and anchors: guiding and trapping droplet microreactors in two dimensions. *Lab on a Chip*, 11(5):813, 2011.

[169] Jing Xu, Byungwook Ahn, Hun Lee, Linfeng Xu, Kangsun Lee, Rajagopal Panchapakesan, and Kwang W. Oh. Droplet-based microfluidic device for multiple-droplet clustering. *Lab on a Chip*, 12(4):725–730, January 2012.

[170] Anthony K. Au, Hoyin Lai, Ben R. Utela, and Albert Folch. Microvalves and micropumps for BioMEMS. *Micromachines*, 2(2):179–220, May 2011.

[171] Catherine M Pemble and Bruce C Towe. A miniature shape memory alloy pinch valve. *Sensors and Actuators A: Physical*, 77(2):145–148, October 1999.

[172] Douglas B. Weibel, Adam C. Siegel, Andrew Lee, Alexander H. George, and George M. Whitesides. Pumping fluids in microfluidic systems using the elastic deformation of poly(dimethylsiloxane). *Lab on a Chip*, 7(12):1832, 2007.

[173] Douglas B. Weibel, Maarten Kruithof, Scott Potenta, Samuel K. Sia, Andrew Lee, and George M. Whitesides. Torque-actuated valves for microfluidics. *Analytical Chemistry*, 77(15):4726–4733, 2005.

[174] Patrick M. Pilarski, Sophia Adamia, and Christopher J. Backhouse. An adaptable microvalving system for on-chip polymerase chain reactions. *Journal of Immunological Methods*, 305(1):48–58, October 2005.

[175] Narayan Sundararajan, Dongshin Kim, and Andrew A Berlin. Microfluidic operations using deformable polymer membranes fabricated by single layer soft lithography. *Lab on a chip*, 5(3):350–354, March 2005.

[176] Vincent Studer, Giao Hang, Anna Pandolfi, Michael Ortiz, W. French Anderson, and Stephen R. Quake. Scaling properties of a low-actuation pressure microfluidic valve. *Journal of Applied Physics*, 95(1):393–398, January 2004.

[177] Kazuo Hosokawa and Ryutaro Maeda. A pneumatically-actuated three-way microvalve fabricated with polydimethylsiloxane using the membrane transfer technique. *Journal of Micromechanics and Microengineering*, 10(3):415, September 2000.

[178] William H Grover, Alison M Skelley, Chung N Liu, Eric T Lagally, and Richard A Mathies. Monolithic membrane valves and diaphragm pumps for practical large-scale integration into glass microfluidic devices. *Sensors and Actuators B: Chemical*, 89(3):315–323, 2003.

[179] Marc A. Unger, Hou-Pu Chou, Todd Thorsen, Axel Scherer, and Stephen R. Quake. Monolithic microfabricated valves and pumps by multilayer soft lithography. *Science*, 288(5463):113–116, April 2000.

[180] Bozhi Yang and Qiao Lin. A latchable microvalve using phase change of paraffin wax. *Sensors and Actuators A: Physical*, 134(1):194–200, 2007.

[181] Jong-Chul Yoo, Y. J. Choi, C. J. Kang, and Yong-Sang Kim. A novel polydimethylsiloxane microfluidic system including thermopneumatic-actuated micropump and paraffin-actuated microvalve. *Sensors and Actuators A: Physical*, 139(1–2):216–220, September 2007.

[182] Daniel Irimia and Mehmet Toner. Cell handling using microstructured membranes. *Lab on a Chip*, 6(3):345, 2006.

[183] W. van der Wijngaart, D. Chugh, E. Man, J. Melin, and G. Stemme. A low-temperature thermopneumatic actuation principle for gas bubble microvalves. *Journal of Microelectromechanical Systems*, 16(3):765–774, June 2007.

[184] Dong Eun Lee, Steve Soper, and Wanjun Wang. Design and fabrication of an electrochemically actuated microvalve. *Microsystem Technologies*, 14(9-11):1751–1756, October 2008.

[185] Govind V. Kaigala, Viet N. Hoang, and Christopher J. Backhouse. Electrically controlled microvalves to integrate microchip polymerase chain reaction and capillary electrophoresis. *Lab on a Chip*, 8(7):1071, 2008.

[186] Stephen C. Jacobson, Sergey V. Ermakov, and J. Michael Ramsey. Minimizing the number of voltage sources and fluid reservoirs for electrokinetic valving in microfluidic devices. *Analytical Chemistry*, 71(15):3273–3276, 1999.

[187] Richard B. M. Schasfoort, Stefan Schlautmann, Jan Hendrikse, and Albert van den Berg. Field-effect flow control for microfabricated fluidic networks. *Science*, 286(5441):942–945, October 1999.

[188] Lin Gui and Jing Liu. Ice valve for a mini/micro flow channel. *Journal of Micromechanics and Microengineering*, 14(2):242, February 2004.

[189] Charles N. Baroud, Jean-Pierre Delville, François Gallaire, and Régis Wunenburger. Thermocapillary valve for droplet production and sorting. *Physical Review E*, 75(4):046302, 2007.

[190] Qing Yu, Joseph M. Bauer, Jeffrey S. Moore, and David J. Beebe. Responsive biomimetic hydrogel valve for microfluidics. *Applied Physics Letters*, 78(17):2589–2591, April 2001.

[191] Chenwei Liu, Joong Yull Park, Yugong Xu, and SangHoon Lee. Arrayed pH-responsive microvalves controlled by multiphase laminar flow. *Journal of Micromechanics and Microengineering*, 17(10):1985, October 2007.

[192] Robin H. Liu, Justin Bonanno, Jianing Yang, Ralf Lenigk, and Piotr Grodzinski. Single-use, thermally actuated paraffin valves for microfluidic applications. *Sensors and Actuators B: Chemical*, 98(2–3):328–336, March 2004.

[193] Hansang Cho, Ho-Young Kim, Ji Yoon Kang, and Tae Song Kim. How the capillary burst microvalve works. *Journal of Colloid and Interface Science*, 306(2):379–385, 2007.

[194] Jerry M. Chen, Po-Chun Huang, and Mou-Gee Lin. Analysis and experiment of capillary valves for microfluidics on a rotating disk. *Microfluidics and Nanofluidics*, 4(5):427–437, May 2008.

[195] Michael T. Tolley, Mekala Krishnan, David Erickson, and Hod Lipson. Dynamically programmable fluidic assembly. *Applied Physics Letters*, 93(25):254105, December 2008.

[196] Ed Gerstner. Microfluidics: Solutions for assembly. *Nature Physics*, 7(2):98–98, 2011.

[197] Tobias M. Schneider, Shreyas Mandre, and Michael P. Brenner. Algorithm for a microfluidic assembly line. *Physical Review Letters*, 106(9):094503, 2011.

[198] Henrik Bruus. *Theoretical Microfluidics*. OUP Oxford, January 2008.

[199] G. K. Batchelor. *An Introduction to Fluid Dynamics*. Cambridge University Press, February 2000.

[200] Sir Horace Lamb. *Hydrodynamics*. University Press, 1916.

[201] Louis Melville Milne-Thomson. *Theoretical Hydrodynamics*. Dover Publications, 1996.

[202] Etienne Guyon, Jean Pierre Hulin, and Luc Petit. *Hydrodynamique physique*. EDP Sciences, 2001.

[203] J. Happel and H. Brenner. *Low Reynolds Number Hydrodynamics: With Special Applications to Particulate Media*. Springer, September 1983.

[204] Brian J. Kirby. *Micro- and Nanoscale Fluid Mechanics: Transport in Microfluidic Devices*. Cambridge University Press, July 2010.

[205] G. K. Batchelor and J. T. Green. The hydrodynamic interaction of two small freely-moving spheres in a linear flow field. *Journal of Fluid Mechanics*, 56(02):375–400, 1972.

[206] Tsevi Beatus, Roy H. Bar-Ziv, and Tsvi Tlusty. The physics of 2d microfluidic droplet ensembles. *Physics Reports*, 516(3):103–145, 2012.

[207] Bianxiao Cui, Haim Diamant, Binhua Lin, and Stuart A. Rice. Anomalous hydrodynamic interaction in a quasi-two-dimensional suspension. *Physical Review Letters*, 92(25):258301, 2004.

[208] Tsevi Beatus, Tsvi Tlusty, and Roy Bar-Ziv. Phonons in a one-dimensional microfluidic crystal. *Nature Physics*, 2(11):743–748, November 2006.

[209] Tsevi Beatus, Roy Bar-Ziv, and Tsvi Tlusty. Anomalous microfluidic phonons induced by the interplay of hydrodynamic screening and incompressibility. *Physical Review Letters*, 99(12):124502, September 2007.

[210] N. J. A. Sloane, R. H. Hardin, T. D. S. Duff, and J. H. Conway. Minimal-energy clusters of hard spheres. *Discrete & Computational Geometry*, 14(1):237–259, December 1995.

[211] Jie Xu and Daniel Attinger. Drop on demand in a microfluidic chip. *Journal of Micromechanics and Microengineering*, 18(6):065020, June 2008. arXiv: 0912.2905.

[212] Zong'an Li, Liya Hou, Weiyi Zhang, and Li Zhu. Preparation of PDMS microfluidic devices based on drop-on-demand generation of wax molds. *Analytical Methods*, 6(13):4716–4722, June 2014.

[213] Hao Gu, Chandrashekhar U. Murade, Michael H. G. Duits, and Frieder Mugele. A microfluidic platform for on-demand formation and merging of microdroplets using electric control. *Biomicrofluidics*, 5(1), March 2011.

[214] Aurélien Duboin. Ecoulements de fluides complexes en présence d'interfaces dans des systèmes microfluidiques. page 87, 2013.

[215] David W. Inglis, John A. Davis, Robert H. Austin, and James C. Sturm. Critical particle size for fractionation by deterministic lateral displacement. *Lab on a Chip*, 6(5):655, 2006.

[216] Masumi Yamada and Minoru Seki. Hydrodynamic filtration for on-chip particle concentration and classification utilizing microfluidics. *Lab on a Chip*, 5(11):1233–1239, October 2005.

[217] M. D. Vahey and J. Voldman. An equilibrium method for continuous-flow cell sorting using dielectrophoresis. *Analytical Chemistry*, 80(9):3135–3143, May 2008.

[218] Thomas Franke, Adam R. Abate, David A. Weitz, and Achim Wixforth. Surface acoustic wave (SAW) directed droplet flow in microfluidics for PDMS devices. *Lab on a Chip*, 9(18):2625–2627, September 2009.

[219] Ghulam Destgeer, Kyung Heon Lee, Jin Ho Jung, Anas Alazzam, and Hyung Jin Sung. Continuous separation of particles in a PDMS microfluidic channel via travelling surface acoustic waves (TSAW). *Lab on a Chip*, 13(21):4210–4216, October 2013.

[220] M. P. MacDonald, G. C. Spalding, and K. Dholakia. Microfluidic sorting in an optical lattice. *Nature*, 426(6965):421–424, November 2003.

[221] Jean-Christophe Baret, Oliver J Miller, Valerie Taly, Michaël Ryckelynck, Abdeslam El-Harrak, Lucas Frenz, Christian Rick, Michael L Samuels, J Brian Hutchison, Jeremy J Agresti, Darren R Link, David A Weitz, and Andrew D Griffiths. Fluorescence-activated droplet sorting (FADS): efficient microfluidic cell sorting based on enzymatic activity. *Lab on a chip*, 9(13):1850–1858, July 2009.

[222] A. C. Siegel, D. A. Bruzewicz, D. B. Weibel, and G. M. Whitesides. Microsolidics: Fabrication of three-dimensional metallic microstructures in poly(dimethylsiloxane). *Advanced Materials*, 19(5):727–733, March 2007.

[223] J. Cooper McDonald and George M. Whitesides. Poly(dimethylsiloxane) as a material for fabricating microfluidic devices. *Accounts of Chemical Research*, 35(7):491–499, 2002.

[224] Jean-Christophe Galas, Denis Bartolo, and Vincent Studer. Active connectors for microfluidic drops on demand. *New Journal of Physics*, 11(7):075027, July 2009.

[225] Tsevi Beatus, Tsvi Tlusty, and Roy Bar-Ziv. Phonons in a one-dimensional microfluidic crystal. *Nature Physics*, 2(11):743–748, November 2006.

[226] Nicolas Champagne, Eric Lauga, and Denis Bartolo. Stability and non-linear response of 1d microfluidic-particle streams. *Soft Matter*, 7(23):11082, 2011.

[227] Tsevi Beatus, Roy Bar-Ziv, and Tsvi Tlusty. Anomalous microfluidic phonons induced by the interplay of hydrodynamic screening and incompressibility. *Physical Review Letters*, 99(12), September 2007. arXiv:1008.1473 [physics].

[228] J. Bławzdziewicz M Baron. Hydrodynamic crystals: collective dynamics of regular arrays of spherical particles in a parallel-wall channel. *Physical review letters*, 100(17):174502, 2008.

[229] William E. Uspal and Patrick S. Doyle. Collective dynamics of small clusters of particles flowing in a quasi-two-dimensional microchannel. *Soft Matter*, 8(41):10676–10686, October 2012.

[230] Evan Evans and Erich Sackmann. Translational and rotational drag coefficients for a disk moving in a liquid membrane associated with a rigid substrate. *Journal of Fluid Mechanics*, 194:553–561, 1988.

[231] S. Bhattacharya, J. Blawzdziewicz, and E. Wajnryb. Far-field approximation for hydrodynamic interactions in parallel-wall geometry. *Journal of computational physics*, 212(2):718–738, 2006.

[232] Haim Diamant. Hydrodynamic interaction in confined geometries. *Journal of the Physical Society of Japan*, 78(4):041002, April 2009. arXiv:0812.4971 [cond-mat, physics:physics].

[233] V. Barbier, H. Willaime, P. Tabeling, and F. Jousse. Producing droplets in parallel microfluidic systems. *Physical Review E*, 74(4):046306, October 2006.

[234] Denis Bartolo, Guillaume Degré, Philippe Nghe, and Vincent Studer. Microfluidic stickers. *Lab on a chip*, 8(2):274–279, February 2008.

[235] Jacques Goulpeau, Daniel Trouchet, Armand Ajdari, and Patrick Tabeling. Experimental study and modeling of polydimethylsiloxane peristaltic micropumps. *Journal of Applied Physics*, 98(4):044914–044914–9, 2005.

[236] Ayako Eri and Ko Okumura. Viscous drag friction acting on a fluid drop confined in between two plates. *Soft Matter*, 7(12):5648–5653, June 2011.

[237] S. van der Graaf, T. Nisisako, C. G. P. H. Schroën, R. G. M. van der Sman, and R. M. Boom. Lattice boltzmann simulations of droplet formation in a t-shaped microchannel. *Langmuir*, 22(9):4144–4152, 2006.

[238] Joshua D. Tice, Adam D. Lyon, and Rustem F. Ismagilov. Effects of viscosity on droplet formation and mixing in microfluidic channels. *Analytica Chimica Acta*, 507(1):73–77, 2004.

[239] Natalie Arkus, Vinothan N. Manoharan, and Michael P. Brenner. Minimal energy clusters of hard spheres with short range attractions. *Physical Review Letters*, 103(11):118303, September 2009.

[240] Dudley Albert Schowalter William Raymond William Bailey Russel, Saville. *Colloidal dispersions*. Cambridge Univ. Press, Cambridge [u.a., 1991.

[241] N. D. Denkov, D. N. Petsev, and K. D. Danov. Interaction between deformable brownian droplets. *Physical Review Letters*, 71(19):3226–3229, November 1993.

[242] Ivan B. Ivanov, Krassimir D. Danov, and Peter A. Kralchevsky. Flocculation and coalescence of micron-size emulsion droplets. *Colloids and Surfaces A: Physicochemical and Engineering Aspects*, 152(1–2):161–182, 1999.

[243] Ivan B. Ivanov, Krassimir D. Danov, and Peter A. Kralchevsky. Flocculation and coalescence of micron-size emulsion droplets. *Colloids and Surfaces A: Physicochemical and Engineering Aspects*, 152(1–2):161–182, 1999.

[244] Dan Guo, Guoxin Xie, and Jianbin Luo. Mechanical properties of nanoparticles: basics and applications. *Journal of Physics D: Applied Physics*, 47(1):013001, January 2014.

[245] R. Aveyard, B. P. Binks, J. Esquena, P. D. I. Fletcher, R. Buscall, and S. Davies. Flocculation of weakly charged oilwater emulsions. *Langmuir*, 15(4):970–980, 1999.

[246] Robert I Feigin and Donald H Napper. Depletion stabilization and depletion flocculation. *Journal of Colloid and Interface Science*, 75(2):525–541, 1980.

[247] P. G. de Gennes. Polymer solutions near an interface. adsorption and depletion layers. *Macromolecules*, 14:1637–1644, November 1981.

[248] J. Bibette. Depletion interactions and fractionated crystallization for polydisperse emulsion purification. *Journal of Colloid and Interface Science*, 147(2):474–478, 1991.

[249] Soon-Chul Kim, Soong-Hyuck Suh, and Baek-Seok Seong. Effect of polymer size and chain length on depletion interactions between two colloids. *The Journal of Chemical Physics*, 127(11):114903, September 2007.

[250] Michael P. Aronson. The role of free surfactant in destabilizing oil-in-water emulsions. *Langmuir*, 5(2):494–501, March 1989.

[251] P. Poulin and J. Bibette. Adhesion between pure and mixed surfactant layers. *Langmuir*, 15(14):4731–4739, 1999.

[252] P. Poulin and J. Bibette. Adhesion of water droplets in organic solvent. *Langmuir*, 14(22):6341–6343, October 1998.

[253] Jessamine Ng Lee, Cheolmin Park, and George M. Whitesides. Solvent compatibility of poly(dimethylsiloxane)-based microfluidic devices. *Analytical Chemistry*, 75(23):6544–6554, 2003.

[254] Thomas E. Furia. *CRC Handbook of Food Additives, Second Edition*. CRC Press, January 1973.

[255] Hans Schott. Hydrophile-lipophile balance and cloud points of nonionic surfactants. *Journal of Pharmaceutical Sciences*, 58(12):1443–1449, 1969.

[256] Harned, G and Owen, B. Physical chemistry of solutions of electrolytes [russian translation]. *IL, Moscow*, page 485, 1952.

[257] E. D. Goddard, O. Harva, and T. G. Jones. The effect of univalent cations on the critical micelle concentration of sodium dodecyl sulphate. *Transactions of the Faraday Society*, 49(0):980–984, January 1953.

[258] R. A. Robinson and R. H. Stokes. Tables of osmotic and activity coefficients of electrolytes in aqueous solution at 25 c. *Transactions of the Faraday Society*, 45(0):612–624, January 1949.

[259] J. Bibette, D. Roux, and B. Pouligny. Creaming of emulsions: the role of depletion forces induced by surfactant. *Journal de Physique II*, 2(3):401–424, March 1992.

[260] J. Bibette, D. Roux, and F. Nallet. Depletion interactions and fluid-solid equilibrium in emulsions. *Physical Review Letters*, 65(19):2470–2473, November 1990.

[261] T. A. Bleasdale and G. J. T. Tiddy. Surfactant liquid crystals. In D. M. Bloor and E. Wyn-Jones, editors, *The Structure, Dynamics and Equilibrium Properties of Colloidal Systems*, number 324 in NATO ASI Series, pages 397–414. Springer Netherlands, January 1990.

[262] P. Poulin and J. Bibette. Wetting of emulsions droplets: From macroscopic to colloidal scale. *Physical Review Letters*, 79(17):3290–3293, October 1997.

[263] Janos Fendler. *Catalysis in Micellar and Macromoleular Systems*. Elsevier, December 1975.

[264] John H Clint. *Surfactant aggregation*. Blackie ; Chapman and Hall, Glasgow; New York, 1992.

[265] Rubingh, DN and Mittal, KL. Solution chemistry of surfactants. *vol*, pages 337–354, 1979. http://library.wur.nl/WebQuery/clc/124146.

[266] J. Santhanalakshmi and S. I. Maya. Solvent effects on reverse micellisation of tween 80 and span 80 in pure and mixed organic solvents. *Proceedings of the Indian Academy of Sciences - Chemical Sciences*, 109(1):27–38, February 1997.

[267] Samuel Kaufman and Curtis R Singleterry. Micelle formation by sulfonates in a nonpolar solvent. *Journal of Colloid Science*, 10(2):139–150, 1955.

[268] Foyeke O. Opawale and Diane J. Burgess. Influence of interfacial properties of lipophilic surfactants on water-in-oil emulsion stability. *Journal of Colloid and Interface Science*, 197(1):142–150, January 1998.

[269] S. M. Nelson and R. C. Pink. Solutions of metal soaps in organic solvents. part IV. direct-current conductivity in solutions of some metal oleates in toluene. *Journal of the Chemical Society (Resumed)*, (0):4412–4417, January 1954.

[270] senja paasimaa. Factors affecting water solubility in oils. *vaisala news*, 2005.

[271] S. Ardizzone, G. Gabrielli, and P. Lazzari. Adsorption of methylene blue at solid/liquid and water/air interfaces. *Colloids and surfaces. A, Physicochemical and engineering aspects*, 76(C):149–157, 1993. S. Ardizzone, G. Gabrielli,P. Lazzari.

[272] Bjørn-Ivar Haukanes and Catrine Kvam. Application of magnetic beads in bioassays. *Nature Biotechnology*, 11(1):60–63, January 1993.

[273] Hun Lee, Linfeng Xu, Byungwook Ahn, Kangsun Lee, and Kwang W. Oh. Continuous-flow in-droplet magnetic particle separation in a droplet-based microfluidic platform. *Microfluidics and Nanofluidics*, 13(4):613–623, October 2012.

[274] Kai Zhang, Qionglin Liang, Sai Ma, Xuan Mu, Ping Hu, Yiming Wang, and Guoan Luo. On-chip manipulation of continuous picoliter-volume superparamagnetic droplets using a magnetic force. *Lab on a Chip*, 9(20):2992, 2009.

[275] D. J. Sellmyer and Ralph Skomski. *Advanced Magnetic Nanostructures*. Springer, July 2006.

[276] Basarab G. Hosu, Károly Jakab, Péter Bánki, Ferenc I. Tóth, and Gabor Forgacs. Magnetic tweezers for intracellular applications. *Review of Scientific Instruments*, 74(9):4158–4163, August 2003.

[277] Zhou Ye, Eric Diller, and Metin Sitti. Micro-manipulation using rotational fluid flows induced by remote magnetic micro-manipulators. *Journal of Applied Physics*, 112(6):064912, September 2012.

[278] Eric Diller. Micro-scale mobile robotics. *Foundations and Trends in Robotics*, 2(3):143–259, 2011.

[279] Jianing Zha and Hans Roggendorf. Sol–gel science, the physics and chemistry of sol–gel processing, ed. by c. j. brinker and g. w. scherer, academic press, boston 1990, xiv, 908 pp., bound—ISBN 0-12-134970-5. *Advanced Materials*, 3(10):522–522, October 1991.

[280] Thibaud Coradin, Michel Boissière, and Jacques Livage. Sol-gel chemistry in medicinal science. *Current medicinal chemistry*, 13(1):99–108, 2006.

[281] Rosaria Ciriminna, Alexandra Fidalgo, Valerica Pandarus, François Béland, Laura M. Ilharco, and Mario Pagliaro. The sol–gel route to advanced silica-based materials and recent applications. *Chemical Reviews*, 113(8):6592–6620, 2013.